Ultrafast lasers in the femtosecond regime : generation, amplification and measurement

Pedro Oliveira

▶ **To cite this version:**

Ultrafast lasers in the femtosecond regime: generation, amplification and measurement

Pedro Bernardino Machado Andrade Oliveira

2012
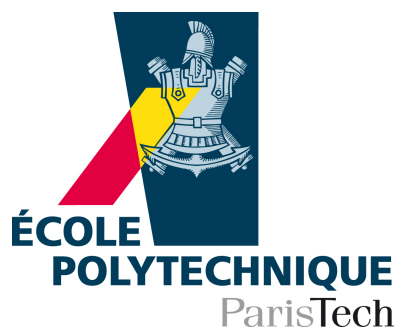
Supervisors

Helder Manuel Paiva Rebelo Cerejo Crespo,

Professor Auxiliar@Department of Physics and Astronomy

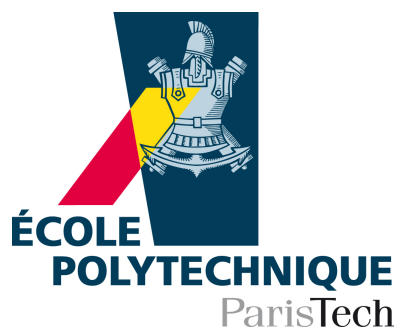Faculty of Sciences of the University of Porto

Frédérika Augé-Rochereau,

Professor@École Nationale Supérieure de Techniques Avancées ParisTech

École Polytechnique

Abstract

It is intuitive that with new tools to analyze nature, new domains can be explored. Ultrafast electromagnetic fields are one of those tools, as they allow the probing of matter on new time scales, both for new applications and for basic research. However they are on their own right an important phenomenon that deserves to be analyzed, studied and probed.

This work is divided in two parts one that deals with the generation and amplification of ultrashort pulses the second with the diagnostics of these lasers. We present a home-built tunable, narrow spectrum CPA amplification chain. We study the features of optical parametric amplification in several configurations. We made simulations regarding the amplification of a seed pulse that is angularly chirped, we also make some analytical calculations based on the same principle. Two mode-locked oscillators are presented one is a sub-12 fs laser oscillator used to produce the seed of the amplification chain, the second is a sub-6 fs laser oscillator. We describe the first laser oscillator in great detail. We devise and discuss models that can explain the parameters of the sub-cavity and the ability of these lasers to enter into mode-locking (ML), we compare the simulation results precise experimental measures made on the sub-6 fs oscillator.

The measurement of ultrafast phenomena is also very challenging because their time scale is too short for common electronic devices. We have examined known measurements, such as third order cross correlations (TOCC) and interferometric second order autocorrelations (IAC) and obtained new analysis methods and new facts that broaden their usefulness. In particular, we have fully reconstructed the spectral phase of a pulse using an IAC trace and its power spectrum. We also prove that the existence of a TOCC plus an intensity autocorrelation is sufficient to retrieve the intensity profile of a pulse we present initial results on reconstruction algorithms, that might be able to do this with a high temporal contrast. We end this thesis with a study on simulation and implementation of a new configuration for single shot correlation measurements.

Keywords – Ultrafast nonlinear optics; Ultrashort lasers; Three-wave mixing; Interferometric autocorrelators; Optimization algorithm; Genetic algorithm; Variational calculus; Third order cross correlation; Single shot measurements; Optical Amplification.

Resumo

O aparecimento de novas ferramentas de análise da natureza faz com que novos domínios desta possam ser explorados. Os campos eletromagnéticos ultra-rápidos são uma dessas ferramentas, e têm provado a sua utilidade. No entanto, estes campos são fenómenos que por si próprios merecem ser estudados.

Apresentamos uma cadeia de amplificação ótica com uma banda espectral curta e sincronizável. Assim como um estudo aprofundado sobre a amplificação ótica paramétrica em diversas configurações, sobretudo quando o impulso a ser amplificado apresenta um espectro *chirpado* angularmente. Analisamos também dois osciladores laser que permitem a geração de impulsos ultracurtos, comparamos e expomos os detalhes experimentais destes osciladores e um novo modelo de cálculo para determinar a habilidade destes osciladores entrarem em blocagem de modos em função dos parâmetros geométricos da sub-cavidade existente no interior do laser.

Lasers ultra-curtos têm durações cuja escala de tempo é mais rápida que a da eletrónica tradicional, e a segunda parte desta tese trata destas medidas. Aqui analisamos correlações cruzadas de terceira ordem e autocorrelações interferométricas de segunda ordem. A partir das autocorrelações interferométricas e da densidade espectral foi possível obter a reconstrução completa do campo elétrico. Provamos também que o facto de termos em simultâneo as correlações cruzadas de terceira ordem e a autocorrelação intensiométrica é suficiente para a reconstrução do perfil de intensidade do impulso, e apresentamos alguns algoritmos que conseguiriam realizar esta tarefa. Posteriormente apresentamos um estudo, que inclui simulações e experiências, de uma nova configuração para medição de autocorrelações utilizando um só impulso.

Palavras-chave – Ótica não linear ultra-rápida; Lasers ultra-curtos; Processos de mistura a três ondas; Autocorrelador interferométrico de segunda ordem; Algoritmos de otimização; Algoritmos genéticos; Cálculo variacional; Correlação cruzada de terceira ordem; Medições em evento único; Amplificação ótica.

Resumé

Il est intuitif qu'avec de nouveaux outils, il devient possible d'explorer de nouveaux domaines de la physique. Les champs électromagnétiques ultra-rapides sont l'un de ces outils, ils permettent de sonder la matière à de nouvelles échelles de temps, à la fois pour développer de nouvelles applications et pour la recherche fondamentale. Néanmoins, ces champs constituent en eux-mêmes un phénomène méritant d'être analysé et étudié.

Le travail présenté ici est divisé en deux parties, dont la première s'occupe de la génération et amplification de lasers ultracourtes. L'amplification paramétrique optique est discutée dans les différentes configurations, notamment dans le cas où le signal a une dérivé angulaire spectrale. On discute aussi deux oscillateurs à blocage de mode en phase. Ont présente aussi une nouvelle manière d'étudier son comportement en fonction des dimensions de la sous-cavité.

La mesure de ces phénomènes représente également un défi en raison de l'échelle temporelle extrêmement réduite à laquelle ces phénomènes se produisent, échelle bien trop petite pour des méthodes de mesure traditionnelles. Dans ce manuscrit, nous avons abordé deux techniques de mesure bien connues: l'autocorrélation interférométrique (IAC) du second ordre et la corrélation croisée du 3ème ordre (TOCC). Avec l'IAC et une mesure de la puissance spectrale du champ, il est possible de reconstruire intégralement le champ électrique tandis que le TOCC associé à l'autocorrélation en intensité détermine le profil en intensité de manière unique, et ont présente des algorithmes que font la reconstruction avec un haut contraste. Nous avons par ailleurs étudié la réalisation d'une nouvelle configuration de corrélateur croisé monocoup.

Mots-clés – Optique ultra-rapide non-linéaire; Laser ultra-bref; Mélange à trois ondes; Algorithme d'optimisation; Calcul variationnel; Corrélateur croisée de troisième ordre; Autocorrélation interférométrique; Mesures monocoup; Amplification optique.

Asato Ma Sat Gamaya

Take me from what is untrue to what is true

WHAT SCIENCE SHOULD BE ALL ABOUT

Acknowledgements

Lokah Samastah Sukhino Bhavantu

May all the beings in all the universes be happy

I am very thankful to all the people I have come across on this long path that was my PhD thesis. In particular I must thank my parents and my brother that always had to endure me, which I know is not always an easy task.

The second recognition must go to my supervisors that have guided my research work, Helder Crespo and Frédérika Augué-Rochereaux. Um muito obrigado ao Helder, et un merci bien a Frédérika.

Doing a PhD thesis in two places at once, I have not only discussed science and technology with a lot of people, but sometimes it made me wonder if my probability density function was not localized but actually had two maxima in two very faraway places (to the reviewers of this work we kindly ask you to ignore this last phrase). At the very least, it seems like a double life, which sometimes becomes a triple life (don't ask). Both in Portugal and in France there are quite a lot of people you meet at work and help you in every way they can; of this people I must thank, I highlight Alexandra Agra Amorim in Portugal and Armindo dos Santos in France. Among many other things, Alexandra helped me to put this thesis in its final form, a task actually performed during her vacations (many times during the night), this tells us something about the character and stamina of such a person. Armindo has received me in France and in his work-home and helped me whenever I asked and even when I needed but didn't ask.

I must thank Gilles Cheriaux for the time he spent with me, and for what he taught me on Ti:sapphire lasers, mainly oscillators. I thank Guy Hamoniaux for what he taught me and for what he tried to teach me, actually Guy and I had very interesting discussions about the third order crosscorrelator, and I must say that a lot of what I learned on this subject was fruit of these discussions. I thank Fabio Giambruno for the initial work we did together in Ti:sapphire laser oscillators, and for the discussions on OPCPA. I thank the crowd at LOA, Laura Antonucci, Fatima, Pascal, Charles, Pierre, Amar,

Gilles, Rodrigo, Aurélie, Amandine, Frédéric, Brigitte, Jean-Philipe, Stéphan, Anna et Antoine, I apologize if I forgot someone (I know I did), but you are just too many.

I must thank Professor Luís Miguel Bernardo all the teachings he gave me about optics and lasers. It was a pleasure to be in the laboratory with Francisco Silva and Miguel Miranda, they always had interesting and relevant things to say about the last results in ultrafast science. I thank João Luis Silva for the useful discussions about simulations. To Ana Sofia Silva, Cledson Santana Lopes and David Schmool, I wish them the best of luck in fingering out the processes behind ultrafast magnetization, it was a pleasure to work with you, and I only wish I could have spent more time with you. I thank Miguel Macau for his participation in the work we did together. I thank Francisco Carpinteiro, and the people from the mechanics workshop, for all their support. I am sure I am forgetting someone in Portugal too, I am sorry.

A debt of gratitude to the people that accepted to be in jury of my PhD thesis. I thank Olivier Albert not only because he belongs to the jury, but also because of the useful discussions we had during my PhD, Olivier corrected my ideas of polarization in uniaxial crystals. Maybe more than anyone else, I must thank the two rapporteurs, Gonçalo Figueira and Olivier Uteza, for the time and effort they will consecrate to this thesis.

Newton once said: "if I see far it is because I stand on the shoulders of giants" I myself have been lift up by a string of professors to which I also owe a debt of gratitude, this string of professors and researchers is too long to be entirely accounted for, however the Professors at FCUP, João Bessa Sousa, José Luis dos Santos, and Antonio Pereira Leite come to mind without any effort, as do several professors from École Polytechnique, Antigoni Alexandrou, Françoise Masnou, and Patrick Mora.

Last but not least I thank Angelina Heft, my friends and my Yoga people.

To all of you, I bow my head in gratitude.

Nomenclature

ASE   Amplified Spontaneous Emission

BBO crystal β-Barium Borate crystal

BS   Beam Splitter

CCD   Charge Coupled Device

CPA   Chirped Pulse Amplification

CW   Continuous Wave

DCM   Double-Chirped Mirror

DFG   Difference Frequency Generation

FFT   Fast Fourier Transform

FISH   Full Information from a Single Hologram: spatially and temporally resolved intensity and phase evaluation device:

FROG   Frequency Resolved Optical Gating

FWHM   Full Width at Half Maximum

GRENOUILLE   Grating-Eliminated No-nonsense Observation of Ultrafast Incident Laser Light E-fields

GRIN   Graded-Index

HV   High Voltage

IA   Intensity Autocorrelation

IAC	Interferometric Autocorrelation
IFFT	Inverse Fast Fourier Transform
KLM	Kerr Lens Modelocking
ML	Modelocking
MOSAIC	Modified Spectrum Auto-Interferometric Correlation
OC	Output coupler
OPA	Optical Parametric Amplification
OPCPA	Optic Parametric Chirped Pulse Amplification
OPF	Optical Parametric Fluorescence
OR	Optical Rectification
PCF	Photonic Crystal Fiber
PD	Photodiode
PM	Photomultiplier
PSO	Particle Swarm Optimization
RPSO	Repulsive Particle Swarm Optimization
SFG	Sum Frequency Generation
SHAC	Second Harmonic Autocorrelation
SHG	Second Harmonic Generation
SPIDER	Spectral Phase Interferometry for Direct Electric-field Reconstruction
SPM	Self Phase Modulation
SSCC	Single Shot Third Order Cross Correlator

SSIA	Single Shot Intensity Autocorrelator
SVE	Slowly Varying Envelope
THG	Third Harmonic Generation
TOCC	Third Order CrossCorrelations
TOIAC	Third Order Interferometric Autocorrelation
TWM	Three Wave Mixing

List of Figures

List of Tables

Contents

Contents

Thesis overview and context

The developments in laser technology over the last 50 years have allowed for ultrafast and ultra-intense lasers. Lasers, with peak power on the PW level and durations as short as 67 attoseconds have been reported [1–4]. These facts bring new tools to the physicist table that can be used to probe reality with an unprecedented accuracy and in unprecedented regimes [5, 6].

This thesis exposes the result of my PhD work throughout its duration. My doctoral studies were based on the ultrafast nonlinear optics and the development of tools to work with lasers which pulse durations are in the femtosecond (fs) regime. This thesis is divided into two parts: in the first part we concern ourselves with the production of ultrafast pulses in a passive ML oscillator and with the amplification of those pulses, particularly OPCPA amplification. The second part of these thesis deals with diagnostics of ultrashort laser pulses.

Before describing the systems that we have studied we make a quick introduction (Chap. (1)) to three wave mixing (TWM) which we use through out the thesis. We treat the coupled propagation equations of TWM (Sec.1.4) and solve them in the case of optical parametric amplification (OPA). Also with TWM in mind we discuss noncollinear phase-matching (Sec. (1.5)) and the characteristics lengths of this process (Sec. (1.2)). We also discuss some features of optical amplification in this introduction (Sec. (1.3) and Sec. (1.4)).

Chirped pulse amplification (CPA) and optical parametric chirped pulse amplification (OPCPA) are well developed techniques that have allowed an unprecedented increase in laser power [7–10]. There are two pump sources normally considered for OPCPA amplification of Ti:Sapphire laser sources, the doubled glass solid state lasers and a doubled Ti:Sapphire lasers, which gives rise to a non-degenerate and to a degenerate OPCPA, we discuss these two approaches.

Very recently, there has been several attempts to increase the spectral bandwidth of OPCPA lasers using an angularly chirped seed [11–15]. This configuration gives one more degree of freedom to the system which might allow the system to be more flexible and to increase the bandwidth of the amplified signal it might also allow for a greater tolerance of the pump wavelength which might might be interesting when the pump is obtained by doubling a Ti:Sapphire laser system.

We use non-collinearity and spatial chirp to enhance the gain, simulation and analytical calculations are presented (Sec. (2.2)). We use the characteristics of a Ti:Sapphire laser as a seed pulse and the BBO crystal as an amplification medium. This kind of approach, gives the configuration an additional

degree of freedom which has the potential either to increase the amplified bandwidth of the system, to improve the energy extraction from the pump and to improve the tolerance of the system to the pump bandwidth. However it also has some inherent problems such as the subsequent angular and temporal compression that is needed in order to make this a useful laser system. We also present a tunable, small bandwidth CPA laser system, based on Ti:Sapphire that was built in *Laboratoire d'Optique Appliquée* (LOA), this is a millijoule amplification system, in which the spectrally selective optics placed inside the regenerative amplifier narrow and select the output spectrum (Sec. (2.5)).

The Ti:Sapphire lasers have been the dominant ultrafast laser technology [16–18]. Particularly Ti:Sapphire oscillators have been the most common form of technology to obtain laser pulses with sub-100fs to few cycle laser pulses, in the near infrared. Passive mode-locked (ML) Ti:Sapphire have been explored at length (simulations, experiments, models) in articles [19–31] and PhD thesis [32, 33]. There are several critical factors to consider when designing a mode lock oscillator, among them the most paramount are the spectral phase accumulated in a round trip around the cavity and the configuration of the sub-cavity. This last parameter determines the mode inside the Ti:Sapphire crystal which works at the same time as a nonlinear medium and as gain medium. The configuration of the sub-cavity is going to determine the stability of the laser and the competition between the free running (CW) and the ML configuration of the laser.

In this thesis we present in detail a sub-15 fs ML oscillator that was built in LOA. We also discuss several models that pinpoint the optimal configuration of the sub-cavity for ML operation. We compare the obtained results with the results obtained with another Ti:Sapphire oscillator (sub-6 fs) that was built in *Universidad Complutense de Madrid*. We discuss the thermal lens in great detail as well as the transition between the CW and ML operation, this are the two unknowns that the model has. We confirmed the model that we use with the second laser that we have presented. The model that we have developed is a purely spatial model we do not consider the temporal/spectral dynamic of the oscillator.

The second part of this thesis concerns itself with temporal diagnostics of ultrashort laser pulses. There are a number of diagnostics to evaluate the temporal profile of ultrashort pulses, some of these diagnostics require that we take 2D temporal and spectral information on the same measurement like frequency resolved optical gating (FROG) [34–36], spectral phase interferometry for direct electric-field reconstruction (SPIDER) [37, 38], and second-harmonic dispersion scans (D-scan) [39] these diagnostics are used to retrieve the pulse temporal profile. Other diagnostics are based on 1D measurements such as third order cross-correlations (TOCC) [40–44], intensity autocorrelations (IA) [45], interferometric autocorrelations (IAC) [46] and spectral intensity measurements, these last diagnostics are easy to implement, and many times used for preliminary measurements of the pulse characteristics. In the second part of this thesis I try to use this last measurements to retrieve the as much information as possible. We actually reconstruct the pulse profile using a combination of measurements, our objective is to enhance the usefulness of these last diagnostics and make them viable tools to measure the temporal profile of ultrafast pulses.

Interferometric autocorrelations have been used since 1985 [46] to characterize the temporal profile of laser pulses. Naganuma et al. proved that together with the spectral intensity profile they completely define the pulse temporal profile [47]. However, as remarked by Trebino in [36], the method of retrieving the intensity profile of the pulse presented by Naganuma et al. was not applicable to the reconstruction of ultrashort pulses (as we confirmed in Sec.(4.4)). Not only there was no reconstruction method available, but also the IAC traces seamed not very sensitive to variations in the spectral shape has proved by Chung and Wiener [48] in 2001 (see the beginning of Chap. (4) for further details). Because of these reasons the IAC diagnostics was merely used as preliminary diagnostics of ultrashort pulses and not to reconstruct the pulse shape. In 2002 by Hyraiama et al. [49], applied a frequency filter to the IAC trace and created the new spectrally modified interferometric autocorrelation (MOSAIC), this proved to be a highly sensitive diagnostic to changes in the spectral phase.

In this work we discuss at length the sensitivity of the IAC and MOSAIC traces to changes in the spectral phase (Secs.(4.1) and (4.2)) in order systematically verify the sensitivity of these diagnostics to changes in the spectral phase and draw qualitative and quantitative conclusions. Following this study we present several methods to reconstruct the spectral phase using these measurements. We reconstruct the spectral the intensity profile of several experimental measurements of sub-8 fs and sub-5 fs pulses. We estimate the uncertainty that can be due to the reconstruction method that we use, which is clearly smaller than the uncertainty due to the experimental measurement. We also discuss several algorithms that failed to reconstruct the pulse using these measurements, we think this is useful because it will narrow the kind of algorithms to be used in the future. Using experimental measurements we also used two methods to define the spectral phase and compare the results obtained by both approaches. One of the methods is to define the phase as a Taylor series (which as classically been the description of the spectral phase for ultrashort pulses [50]) another approach uses a point per point approach, we concluded that this second approach as been more successful in reproducing the experimental measurements that were made.

We envision that it is possible to apply this method to the reconstruction of the pulse profile for longer pulses, as long as the second harmonic autocorrelation can be retrieved from these measurements (see Sec. (4.3)). Furthermore we also conceive the possibility that this method may be used for single shot measurements if three measurements are made simultaneously, the measurements of the field spectrum, the SH spectrum and the intensity autocorrelation (there are several commercial devices used to make this last measurement [51, 52]).

TOCC is used in a different context of IAC. IAC is conceived to measure the pulse intensity profile and the spectral phase of the pulse, it is used for low contrast measurements (up to one order of magnitude), it is used for almost every kind of femtosecond laser to know the pulse shape duration and peak power. TOCC is conceived to analyze the pulse temporal profile with a high dynamic range (12 orders of magnitude) [40–44], this is only important in high power laser systems. Due to this fact the time window that needs to be measured is also different, for a fs pulse the time window of the

IAC measurement has to be within the fs time scale, beyond this window the intensity of the pulse is smaller than the noise. When considering a TOCC measurement however the FWHM duration of the pulse is not important because the pulse is measured in a logarithmic scale, the information retrieved from a TOCC trace is the existence and magnitude of pre and post pulses and the dynamic contrast of the pulse within a time windows of hundreds of ps, up to 1 ns. Beyond this time scale other measurement techniques can be used [53]. In this work we discuss the features that are normally retrieved from a TOCC trace, as well as some features on the measurement device itself.

We prove that the combination of IA plus TOCC univocally defines the intensity profile of the laser. This is interesting because with this we can completely define the intensity using two diagnostics that can be taken with a high dynamic contrast [40, 54]. To the best of our knowledge this is the first time this proof has been published, however, as in the IAC case, there is an intermediary step between the analytical proof and the application to experimental measurements, which is to find a method that takes both measurements and retrieves the intensity profile from them. We take one of the retrieval methods that we used when retrieving spectral phase from the IAC trace (slightly modified) trace and apply it to this problem, obtaining some preliminary results the reconstruct the pulse with a dynamic range of $10^4 - 10^5$. This new property might not be interesting evaluate the pre post pulses or even the background amplified spontaneous emission (ASE), however it might be applicable to retrieve the pedestal of the pulse, where more complicated features may exist.

When dealing with high power, single shot laser pulses or even low repetition rate laser systems it becomes imperative to have a diagnostic that analysis the temporal profile of the pulse in one shot. Sweeping diagnostics are not appropriate, not only due to practical reasons of getting a data point per shot, but also because these systems present more thermal noise[1] which in turn make the intensity profile of the pulse vary from shot to shot. Single shot intensity autocorrelators have been used for some time [55–58], we propose a different single shot intensity autocorrelator based on the superposition of two sagittal focal lines of astigmatic mirrors, these allows the system to integrate the pulse profile over one of the directions of the spatial profile giving a more accurate measurement of the temporal profile of the pulse. We built and tested this configuration for an intensity autocorrelator. We compare the features of this correlator with the classical intensity autocorrelator which uses two tilted beams converging in a SH crystal.

However when dealing with high power ultrafast lasers one of the most important measures is the TOCC that gives us a high dynamic contrast of the pulse profile. Recently there have been several devices proposed to serve as a single-shot TOCC [57–63]. We make our own proposal for a single-shot TOCC based on the same delay process, we also propose a system to control the SH profile by controlling the phase-matching conditions in the SH generation. We present simulations on this device.

This PhD was done in a mix regime, in the context of the group ELF (*Études des Laser Femtosec-*

---

[1]Many of these systems have an higher peak power than laser systems with a high repetition rate.

onde), later group LHP (*Laser Haute Puissance*) at LOA (*Laboratoire d'Optique Appliquée*) which is situated in the *École Polytechnique*, in Paris, France, and also in the group CLOQ (*Centro de Lasers e Óptica Quântica*), later Ultrafast Lasers and Magnetodynamics Spectroscopies group which belongs to IFIMUP (Instituto de Física dos Materiais da Universidade do Porto), we worked at a laboratory situated in FCUP (*Faculdade de Ciências da Universidade do Porto*), in Portugal.

Part I.

Generation and amplification of ultrashort pulses

1. Introduction to three wave mixing and optical amplification

In this chapter we study three wave mixing at length, and introduce optical amplification, particularly optical parametric amplification (OPA), which is a three wave mixing process.

Second harmonic generation (SHG), difference frequency generation (DFG) and sum frequency generation (SFG) are all forms of three wave mixing (TWM). OPA is based in DFG and some of the diagnostics presented here are based on SHG or SFG and so we must study these processes in order to know the validity of their nonlinearities.

TWM happens in a non-centrosymmetric medium with a nonzero second order nonlinearity [64]. Normally two initial waves (ω_1, ω_2) mix inside a crystal originating a third wave which may have a frequency that is the the sum or difference of the previous frequencies: $\omega_0 = \omega_2 \pm \omega_1$. This relation between frequencies is compulsory in order to conserve the energy of the ensemble. The virtual energy levels can be seen in Fig. (1.1).

We have SHG if $\{\omega_1, \omega_1\} \Rightarrow \omega_0 = 2\omega_1$, optical rectification (OR) if $\{\omega_1, -\omega_1\} \Rightarrow \omega_0 = \omega_1 - \omega_1$, SFG if $\{\omega_1, \omega_2\} \Rightarrow \omega_0 = \omega_1 + \omega_2$ and DFG if $\{\omega_1, -\omega_2\} \Rightarrow \omega_0 = \omega_1 - \omega_2$.

This chapter is divided in several sub-chapters where each corresponds to a specific subject.

➤ In Sec. (1.1) we introduce the TWM coupled equations.

➤ Sec. (1.2) discusses standard normalizations of the parametric equations that lead us to the characteristic values in TWM.

➤ Sec. (1.3) very briefly describes chirped pulse amplification (CPA).

➤ Sec. (1.4) treats the optical parametric amplification (OPA) and the classical approaches to it, namely plane wave approximation.

➤ Sec. (1.5) treats phase matching in 3-wave interaction.
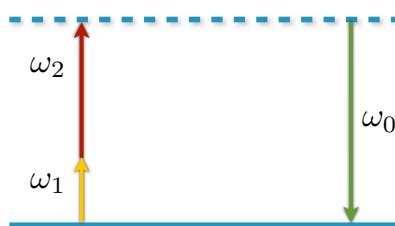
Figure 1.1.: Representation of the virtual energy levels on a TWM configuration where $\omega_0 = \omega_1 + \omega_2$.

1.1. TWM propagation equations

Let's consider a loss-less medium with second order nonlinear effects. Three waves propagate in this medium in which walk-off, group velocity mismatch and dispersion are negligible, we use a plane wave approximation, which entails a SVE approximation in which we must consider that our amplitude obeys the following condition (referential of propagation moving with the group velocity of the pulse):

$$\left(\frac{\partial}{\partial z} - \frac{2}{v_r} \frac{\partial}{\partial \tau} \right) A_j(\mathbf{r}, \tau) \ll \frac{1}{k_j} A_j(\mathbf{r}, \tau). \tag{1.1}$$

In this case the amplitude of the waves propagating in the medium can be described by the following equations [64, 65]:

$$
\begin{aligned}
\frac{\partial A_0(\mathbf{r}, \tau)}{\partial z} &= i \frac{\omega_0^2}{2k_0 c^2} \chi_{eff}^{(2)} A_1(\mathbf{r}, \tau) A_2(\mathbf{r}, \tau) \; e^{-i\Delta kz} \\
\frac{\partial A_1(\mathbf{r}, \tau)}{\partial z} &= i \frac{\omega_1^2}{2k_1 c^2} \chi_{eff}^{(2)} A_0(\mathbf{r}, \tau) \overline{A_2}(\mathbf{r}, \tau) \; e^{i\Delta kz} \\
\frac{\partial A_2(\mathbf{r}, \tau)}{\partial z} &= i \frac{\omega_2^2}{2k_2 c^2} \chi_{eff}^{(2)} A_0(\mathbf{r}, \tau) \overline{A_1}(\mathbf{r}, \tau) \; e^{i\Delta kz}
\end{aligned}
\tag{1.2}
$$

in which $\chi_{eff}^{(2)}$ is the second order nonlinearity coefficient, $\Delta k = k_0 - k_1 - k_2$ is the phase-mismatch, $A_i, \omega_i, k_i, i = \{1, 2, 3\}$ are the amplitude, frequency and wave-vector of the three waves in the non-linear medium; z is the propagation direction.

It is possible to decompose any wave in an ensemble of plane waves; we can do this using a Fourier transform, in which case we will get:

$$A_i(\mathbf{r}, \tau) = \mathscr{F}_{x,y,t} \left\{ \mathscr{A}_{\mathbf{i}}(\mathbf{k_T}, \Omega, z) \right\}. \tag{1.3}$$

Please remember that $\mathbf{k_T}$ is the transverse coordinate of the Fourier pair of (x, y), and Ω is not the angular frequency of the electric field but the Fourier transform of the amplitude, the two are related by: $\Omega = \omega - \omega_i$, in which ω_i is the carrier frequency of the ith wave.

Imputing this into the coupled equations will give us:

$$\frac{\partial \mathscr{A}_0(\mathbf{k_T^0}, \Omega, z)}{\partial z} = \frac{i\omega_0^2 \chi_{eff}^{(2)}}{2k_0 cos(\alpha)c^2} \iiint \mathscr{A}_1(\mathbf{k_T^1}, \Omega - \Delta, z)\overline{\mathscr{A}_2(\mathbf{k_T^2}, \Delta, z)}e^{-i\Delta k(\Omega, \Delta)z}\delta(\mathbf{k_T^0} - \mathbf{k_T^1} - \mathbf{k_T^2})d\Delta d\mathbf{k_T^1}\mathbf{k_T^2}$$

$$\frac{\partial \mathscr{A}_1(\mathbf{k_T^1}, \Omega, z)}{\partial z} = \frac{i\omega_0^2 \chi_{eff}^{(2)}}{2k_0 cos(\alpha)c^2} \iiint \mathscr{A}_0(\mathbf{k_T^0}, \Omega - \Delta, z)\overline{\mathscr{A}_2(\mathbf{k_T^2}, \Delta, z)}e^{-i\Delta k(\Omega, \Delta)z}\delta(\mathbf{k_T^0} - \mathbf{k_T^1} - \mathbf{k_T^2})d\Delta d\mathbf{k_T^0}\mathbf{k_T^2}$$

$$\frac{\partial \mathscr{A}_2(\mathbf{k_T^2}, \Omega, z)}{\partial z} = \frac{i\omega_0^2 \chi_{eff}^{(2)}}{2k_0 cos(\alpha)c^2} \iiint \mathscr{A}_0(\mathbf{k_T^0}, \Omega - \Delta, z)\overline{\mathscr{A}_1(\mathbf{k_T^1}, \Delta, z)}e^{-i\Delta k(\Omega, \Delta)z}\delta(\mathbf{k_T^0} - \mathbf{k_T^1} - \mathbf{k_T^2})d\Delta d\mathbf{k_T^0}\mathbf{k_T^1}$$

$$(1.4)$$

In which the phase mismatch is given by: $\Delta k(\Omega, \Delta) = k_3(\Omega) - k_1(\Omega - \Delta) - k_2(\Omega)$, where $k_i(\Omega)$ is the z component of the wave vector, for the correspondent component. For more details on the function $\delta(\mathbf{k_T^0} - \mathbf{k_T^1} - \mathbf{k_T^2})$ see Sec. (1.5). Remember that here we are still in the paraxial approximation, but the equation above could easily be adapted to any non-paraxial case as we do this in Chap. (5).

1.2. Normalization of the coupled equations

Before exploring TWM any further we normalize the equations, this will facilitate the calculations further on and give the characteristic values of the system, normalizations are useful when simulating any physical system. There are several possible normalizations. We can normalize the quantities involved using the initial values of the pulse, such as duration or amplitude. However a more common and more useful normalization is to use the characteristics of the medium and the nonlinearity coefficients. We can normalize all the equations leaving no coefficients, by using (see appendix for more details):

$$A_0 = \frac{2c^2\sqrt{k_1 k_2}}{\omega_1 \omega_2 \chi_{eff}^{(2)}} B_0 e^{-i\Delta k^{(2)}z} \tag{1.5}$$

$$A_1 = \frac{2c^2\sqrt{k_0 k_2}}{\omega_0 \omega_2 \chi_{eff}^{(2)}} B_1 \tag{1.6}$$

$$A_2 = \frac{2c^2\sqrt{k_0 k_1}}{\omega_0 \omega_1 \chi_{eff}^{(2)}} B_2 \tag{1.7}$$

Using this normalization all the coefficients in the coupled propagation (Eq. (1.2)) vanish.

The coefficients B_i are not adimensional, they have the units of distance, but now it is easier to

normalize. We normalize the length and the amplitude using a referential B_r which may be the most intense beam, in the case of OPA, optical rectification or Optical Parametric Fluorescence (OPF) $B_r = B_0$. In SHG $B_r = B_1 = B_2$. In SFG the referential B_r can be a combination of the B_i related to both original beams like for instance $B_r = \sqrt{B_1 B_2}$.

In any case we may find a normalized amplitude by the the factor $A_i \to B_i / B_r$ and the length $z \to z / B_r$.

$$
\begin{aligned}
B_i &\to B_i B_r \\
z &\to z / B_r
\end{aligned}
\tag{1.8}
$$

The nonlinear length ($L_{NL} = B_r^{-1}$) for OPA or parametric fluorescence is given by:

$$
L_{NL} = \frac{2c^2 \sqrt{k_1 k_2}}{\omega_1 \omega_2 \chi_{eff}^{(2)} A_0(0)},
\tag{1.9}
$$

or by the more useful expression:

$$
L_{NL}^{OPA} = \frac{1}{2\pi \chi_{eff}^{(2)}} \sqrt{\frac{2\varepsilon_0 c n_0 n_1 n_2 \lambda_1 \lambda_2}{I_0(0)}}.
\tag{1.10}
$$

In SHG we only have two coupled equations which simplifies the problem, in this case beam 1 is equal to beam 2 ($\omega_0 = 2\omega_1 = 2\omega_2$, $\chi_0^{(2)} = \chi_1^{(2)} = \chi_2^{(2)}$):

$$
L_{NL}^{SH} = \frac{\lambda_1 n_1}{2\pi \chi_{eff}^{(2)}} \sqrt{\frac{\varepsilon_0 n_0 c}{I_1(0)}} \cos(\alpha_0) \cos(\alpha_1).
\tag{1.11}
$$

For SFG we have (using the same assumption concerning the nonlinear susceptibility):

$$
L_{NL}^{SFG} = \frac{1}{\pi \chi_{eff}^{(2)}} \sqrt{\varepsilon_0 c n_0 n_1 n_2 \lambda_0 \cos(\alpha_0)} \sqrt[4]{\frac{\lambda_1 \lambda_2 \cos(\alpha_1) \cos(\alpha_2)}{I_1(0) I_2(0)}}.
\tag{1.12}
$$

In general, for any case where we normalize using one beam the normalization becomes

$$
L_{NL} = \frac{1}{2\pi \chi_{eff}^{(2)}} \sqrt{\frac{2\varepsilon_0 c n_0 n_1 n_2 \lambda_0 \lambda_1 \lambda_2}{I_r(0) \lambda_r}}.
\tag{1.13}
$$

By normalizing the z coordinate found in Eq. (1.2) we obtain a new quantity S related to the phase-mismatch defined as:

$$S = \Delta k L_{NL}. \tag{1.14}$$

We conclude that in TWM, the energy transfer between pulses is going to be determined by the value of L_{NL}, S, and the propagating distance (z). Using Eq. (1.8), the coupled equations become:

$$\begin{aligned} \frac{\partial B_0}{\partial z} &= i \left(B_1 B_2 + S B_0 \right) \\ \frac{\partial B_1}{\partial z} &= i \ B_0 \overline{B}_2 \\ \frac{\partial B_2}{\partial z} &= i \ B_0 \overline{B}_1 \end{aligned} \tag{1.15}$$

We could also normalize the z coordinate using the phase-mismatch value in which case only a constant term would be present in the equations.

An unconventional normalization would be to take the length of the crystal (L_{cr}) and obtain a characteristic amplitude which could normalize the amplitude of the fields, and this would give us an indication of the critical amplitude of the nonlinear process. If one of the beams is dominant (OPA, OPF) we can obtain this critical intensity by inverting Eq. (1.13),

$$I_c = \frac{1}{4\pi^2 \left(\chi_{eff}^{(2)} \right)^2} \frac{2\varepsilon_0 c n_0 n_1 n_2 \lambda_0 \lambda_1 \lambda_2}{L_{cr}^2 \lambda_r}. \tag{1.16}$$

1.3. CPA, chirped pulse amplification

We will restrain from describing CPA in great detail. CPA is the dominant form of short pulse laser amplification since its invention in 1985 [7]. CPA works by first stretching the pulse in time before amplification, (hopefully keeping the pulse spectral shape and width) and after amplification the pulse is re-compressed. This scheme avoids damage and nonlinear effects in the amplification medium. From the wide range of studies done on CPA we highlight the following [7, 66, 67]. For a contextualization of laser amplification techniques, please see [68].

1.4. Optical parametric amplification and optical chirped pulse amplification

OPA and optic parametric chirped pulse amplification (OPCPA) is the single subject of several PhD theses [69–72]. We found it appropriate to expose the classical features of OPA in this introductory chapter. We have seen the DFG phase matching conditions Sec. (1.5). In fact OPA is the same thing as DFG. In OPA the main objective is to amplify a weak signal, a seed. For this effect we use the

high energy beam to transfer energy to the signal. This creates a byproduct that is the idler, basically a beam whose frequency is the difference between the frequencies of the other two beams.

Using the notation above, the pump beam is represented by the subscript zero, the signal beam is represented by one and the idler beam by two.

OPA was the subject of one of the first articles in nonlinear optics [73], where the coupled equations are solved, this is the basis of DFG or SFG.

We have seen the characteristic nonlinear length Eq. (1.13) and the normalized coupled equations, Eq. (A.6), lets now solve these equations and discuss their solutions. In the following sub-sections we solve the parametric equations in a low pump depletion approximation and in the case where no idler exists but we have pump depletion. In the appendix for this chapter, we present two other cases, "no phase-mismatch" and "no idler input", and the general solution for the parametric equations in any case, but please note that this last case is applicable to any TWM not only OPA.

1.4.1. Low pump depletion

In a low pump depletion, we consider a configuration where the pump amplitude stays the same. Consequentially the derivative of the pump amplitude is zero and so we just work with two coupled equations, the first two expressions in Eq. (1.2). The resolution is given in the appendix:

$$A_1(z) = A_1(0) \left[\cosh(\gamma z) + i \frac{\Delta k}{2\gamma} \sinh(\gamma z) \right] e^{i \frac{\Delta kz}{2}}$$

$$A_2(z) = i \sqrt{\frac{n_1 \lambda_1 \cos(\alpha_1)}{n_2 \lambda_2 \cos(\alpha_2)}} \overline{A}_1(0) \frac{\Delta k}{2\gamma} \sinh(\gamma z) e^{i \frac{\Delta kz}{2}} \tag{1.17}$$

$$\gamma^2 = L_{NL}^{-2} - \left(\frac{\Delta k}{2} \right)^2$$

where γ^{-1} is the characteristic length for this propagation.

The complete equations that include the case when the propagation starts with 3 beams are given in several classical textbooks (see [64]). We do not use this expression because in most cases the idler is not inputted at the beginning of the nonlinear medium. Notice that when $L_{NL} > \frac{2}{|\Delta k|}$, there is no amplification. The hyperbolic functions transform themselves into sinusoidal functions and we have an oscillatory behavior of the amplitude. In this regime the amplification increases exponentially as seen in Fig. (1.2). We obtain an amplification that can be quickly characterized using Table (1.1).

Amplification is only possible when the intensity surpasses the threshold intensity that is given by:

$$I_0 > \frac{2\Delta k n_0 n_1 n_2 c}{\chi_{eff} \omega_0 \omega_1 \omega_2 \varepsilon_0}. \tag{1.18}$$

The classic signal amplification gain is given by:

$$G_1 = 1 + \left(\frac{1}{L_{NL}\gamma}\right)^2 \sinh^2(\gamma z).$$ (1.19)

The idler amplification normalized to the initial value of the signal is

$$G_2 = \left(\frac{1}{L_{NL}\gamma}\right)^2 \sinh^2(\gamma z).$$ (1.20)
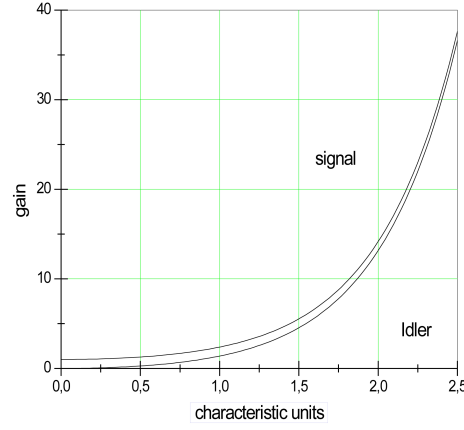
Figure 1.2.: Gain in a low pump depletion approximation for the idler and signal beams as a function of the propagation distance normalized by γ^{-1}.

Distance (in nonlinear length units)	Gain
1.83	10
5.5	10^4
6.4	10^5
7.25	10^6
8.2	10^7
9.8	10^8

Table 1.1.: Amplification of the signal pulse intensity as a function of the nonlinear length in a perfect phase matching condition.

The phase of the pulse, which is important for the compression of the amplified pulses in OPA and OPCPA [74], is given by:

$$\tan\left(\phi_1 - \phi_1(0) - \frac{\Delta k}{2}z\right) = \frac{\tan\left(\frac{\Delta k}{2}z\right) + \frac{\Delta k}{2\gamma}\tanh(\gamma z)}{1 - \frac{\Delta k}{2\gamma}\tanh\left(\frac{\Delta k}{2}z\right)\tanh(\gamma z)}.$$ (1.21)

1. Introduction to three wave mixing and optical amplification

The idler phase is given by

$$\phi_2 = \pi/2 - \phi_1 + \frac{\Delta kz}{2}. \tag{1.22}$$

However, it is easy to understand that with an exponential amplification, we are in a situation where the pump depletion becomes important, in which case the approximations that was done initially are no longer valid.

There are some differences between the solutions for DFG and SFG, in low pump depletion approximation; the solution for SFG is presented later on.

1.4.2. Exact solutions of the coupled equations with pump depletion, no idler input

We have now to consider all the terms in Eq. (A.6), normalized as follows:

$$\begin{aligned}
\frac{\partial B_0}{\partial z} &= i\ B_1 B_2\ \exp\left(-i\Delta kz\right) \\
\frac{\partial B_1}{\partial z} &= i\ B_0 \overline{B}_2\ \exp\left(i\Delta kz\right) \quad . \\
\frac{\partial B_2}{\partial z} &= i\ B_0 \overline{B}_1\ \exp\left(i\Delta kz\right)
\end{aligned} \tag{1.23}$$

Before solving the equations themselves we should find some constants that are possible to gather from the coupled wave equations. We explain how to obtain this constants in the appendix. We obtain:

$$\begin{aligned}
m_0 &= |B_1|^2 - |B_2|^2 \\
m_1 &= |B_0|^2 + |B_2|^2, \\
m_2 &= |B_0|^2 + |B_1|^2
\end{aligned} \tag{1.24}$$

and

$$\begin{aligned}
\Gamma_0 &= |B_0||B_1||B_2|\cos\Theta + \frac{\Delta k}{2}|B_0|^2 \\
\Gamma_1 &= |B_0||B_1||B_2|\cos\Theta - \frac{\Delta k}{2}|B_1|^2 \quad , \\
\Gamma_2 &= |B_0||B_1||B_2|\cos\Theta - \frac{\Delta k}{2}|B_2|^2
\end{aligned} \tag{1.25}$$

where $\Theta = \phi_0 - \phi_1 - \phi_2 + \Delta kz$.

This constants are not independent among themselves (there are 3 independent constants, chosen among these two groups, for instance $m_0 = m_2 - m_1, \frac{\Delta k}{2} m_0 = \Gamma_1 - \Gamma_2$). This constants are related to the energy of the TWM system [69].

16

With this constants we can obtain each one of the coupled equations as one variable differential equation, as follows:

$$
\begin{aligned}
\left(\frac{\partial |B_0|}{\partial z}\right)^2 &= (m_2 - |B_0|^2)(m_1 - |B_0|^2) - \frac{(\Gamma_0 - \frac{\Delta k}{2}|B_0|^2)^2}{|B_0|^2}, \\
\left(\frac{\partial |B_1|}{\partial z}\right)^2 &= (m_2 - |B_1|^2)(|B_1|^2 - m_0) - \frac{(\Gamma_1 + \frac{\Delta k}{2}|B_1|^2)^2}{|B_1|^2}, \\
\left(\frac{\partial |B_2|}{\partial z}\right)^2 &= (m_1 - |B_2|^2)(m_0 + |B_2|^2) - \frac{(\Gamma_2 + \frac{\Delta k}{2}|B_2|^2)^2}{|B_2|^2}.
\end{aligned}
\tag{1.26}
$$

We may solve one of the equations and resolve the other variable propagation equations using the constants given in Eq. (1.24).

If we have no idler before propagation, $B_2(0) = 0$. In this case $\Gamma_2 = 0$, $\Gamma_0 = \frac{\Delta k}{2}|B_0(0)|^2$ and $\Gamma_1 = -\frac{\Delta k}{2}|B_1(0)|^2$, resolving the amplitude evolution equations (Eq.(1.26)) we obtain two support variables $\left(\delta = \left|\frac{B_1(0)}{B_0(0)}\right|^2\right)$:

$$
\begin{aligned}
\gamma_1 &= \left[\frac{1-\delta-S}{2} + \sqrt{\left(\frac{1-\delta-S}{2}\right)^2 + \delta}\right] \\
\gamma_2 &= \left[\frac{\delta+S-1}{2} + \sqrt{\left(\frac{1-\delta-S}{2}\right)^2 + \delta}\right] \\
S &= \left(\frac{\Delta k}{2|B_0(0)|}\right)^2
\end{aligned}
\tag{1.27}
$$
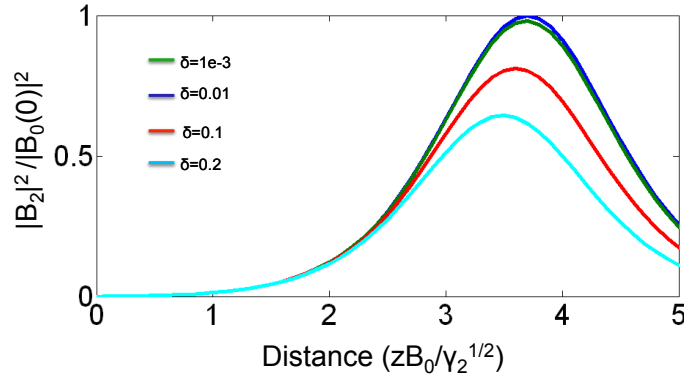
Figure 1.3.: Beam 2, square amplitude for several values of δ for the same value of $\delta = 1e^{-3}$.

In the limit where $\delta \to 0$ and $S \to 0$, we have $\gamma_1 \to 1$, $\gamma_2 \to 0$. The amplitude evolution becomes:

$$
\begin{aligned}
|B_0| &= |B_0(0)|\sqrt{1 - \gamma_1^2 + \gamma_1^2 sn^2(|B_0(0)|\alpha z + K(\frac{\gamma_1}{\gamma_2+\gamma_1})|\frac{\gamma_1}{\gamma_2+\gamma_1})} \\
|B_1| &= |B_0(0)|\sqrt{\delta + \gamma_1^2 cn^2(|B_0(0)|\alpha z + K(\frac{\gamma_1}{\gamma_2+\gamma_1})|\frac{\gamma_1}{\gamma_2+\gamma_1})} \\
|B_2| &= |B_0(0)||\gamma_1|cn(|B_0(0)|\alpha z + K(\frac{\gamma_1}{\gamma_2+\gamma_1})|\frac{\gamma_1}{\gamma_2+\gamma_1})|
\end{aligned}
\tag{1.28}
$$

where *K* is the complete elliptic integral of the first kind, *sn* the Jacobi sinus and *cn* the Jacobi cosines. All the information on the properties of this functions can be viewed in [75]. Here α is a support variable given by:

$$\alpha = \sqrt{(\gamma_2 + \gamma_1)}. \tag{1.29}$$

These equations are applicable to any case where one of the constants Γ_i equals zero. We can use these equations in order to evaluate OPA systems because in general OPA occurs with no initial idler but with phase mismatch.
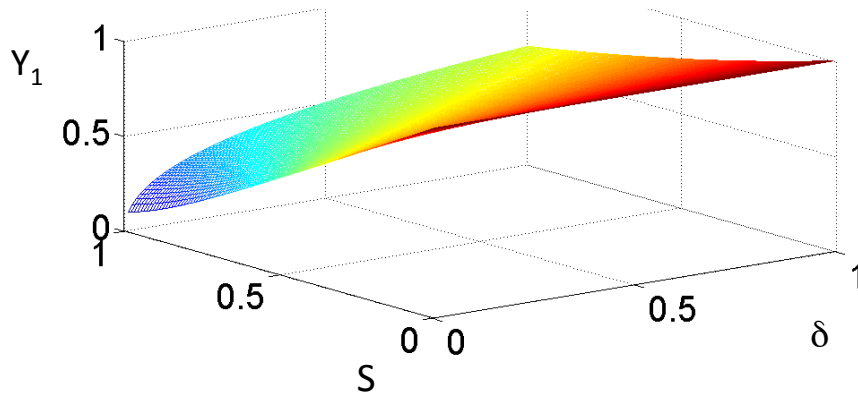
Figure 1.4.: Maximum conversion of the idler square amplitude given by the parameter γ_1 as a function of the phase mismatch parameter S and the intensity ratio parameter δ.

In Fig. (1.4) we see that for the maximum conversion the dependence is bigger in S than δ.
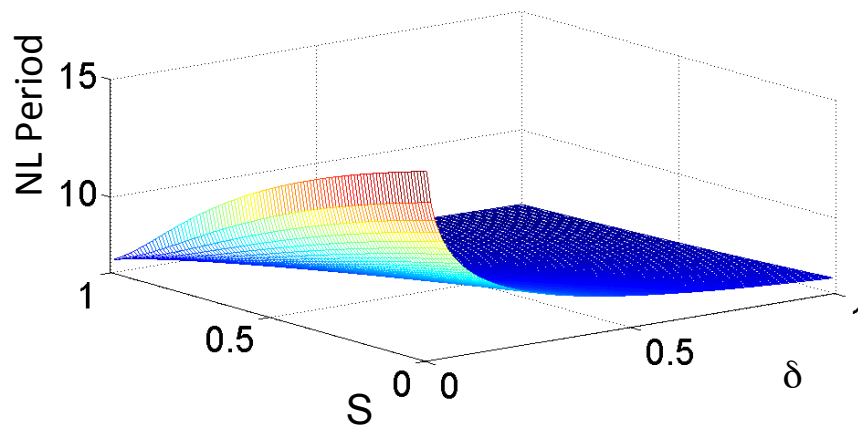
Figure 1.5.: The period of the nonlinear process as a function of the parameter γ_1, as a function of the phase mismatch parameter S and the intensity ratio parameter δ. We have a bigger dependence on δ than on S.

The characteristic length in this particular situation can be given by:

$$\gamma_{NL}^{-1} = \frac{1}{|B_0(0)|\alpha} = \frac{1}{|B_1(0)|\sqrt{(1-\delta-S)^2+4\delta}} \tag{1.30}$$

The signal intensity gain is given by:

$$|B_1| = 1 + \frac{\gamma_1^2}{\delta} cn^2(|B_0(0)|\alpha z + K(\frac{\gamma_1}{\gamma_2+\gamma_1})|\frac{\gamma_1}{\gamma_2+\gamma_1}) \tag{1.31}$$

In the case where $\Gamma_2 = 0$ the evolution of the phase of each pulse is given by the solution to the following equations (see appendix for more detail):

$$\frac{\partial \phi_0}{\partial z} = \frac{\Delta k}{2}\frac{|B_2|^2}{|B_0|^2} \quad , \quad \frac{\partial \phi_1}{\partial z} = \frac{\Delta k}{2}\frac{|B_2|^2}{|B_1|^2} \quad , \quad \frac{\partial \phi_2}{\partial z} = \frac{\Delta k}{2} \tag{1.32}$$

The resolution of this is quite strait forward, it results in incomplete Jacobi elliptic integrals of the third kind [75],

$$\phi_0 = -\frac{\Delta k}{2}z + \frac{1}{1-\gamma_1^2}\frac{\Delta k}{2|B_0|\alpha}\Pi\left(\frac{\gamma_1^2}{1-\gamma_1^2}; am\left(|B_0(0)|\alpha z + K(\frac{\gamma_1}{\gamma_2+\gamma_1})|\frac{\gamma_1}{\gamma_2+\gamma_1}\right)|\frac{\gamma_1}{\gamma_2+\gamma_1}\right)$$

$$\phi_1 = \frac{\Delta k}{2}z - \frac{\delta}{\delta+\gamma_1^2}\frac{\Delta k}{2|B_0|\alpha}\Pi\left(\frac{\gamma_1^2}{\delta+\gamma_1^2}; am\left(|B_0(0)|\alpha z + K(\frac{\gamma_1}{\gamma_2+\gamma_1})|\frac{\gamma_1}{\gamma_2+\gamma_1}\right)|\frac{\gamma_1}{\gamma_2+\gamma_1}\right) \tag{1.33}$$

$$\phi_2 = \frac{\Delta k}{2}z$$

where *am* function is the Jacobi amplitude function [75, 76].

1.4.3. Optical chirped pulse amplification OPCPA

Optical chirped pulse amplification, OPCPA, is a mix between OPA and CPA. We use OPA with a chirped pulse as a seed, after amplification the pulse is re-compressed thus avoiding the damage threshold and third order nonlinearities during amplification and obtaining short pulses.

The idea of amplification using OPA and chirped pulses avoiding damage in the materials, nonlinear effects and enabling better efficiencies in terms of the net efficiency over all the wavelengths, has been proposed by Dubietis et al. [77] and then re-developed by I. N. Ross [8, 78], and as we claimed above there are several PhD thesis which sole subject is OPCPA.

Using OPCPA instead of CPA has several advantages but also drawbacks, we normally compare it with CPA laser chains which are the fully developed technological competitor, there are few other amplification techniques with comparable properties.

The main difference between CPA and OPCPA is that CPA is based on pumping a material to an excited state which results in an energy storage. OPCPA is based upon the mixing of two waves (that create a third wave, the idler) and the energy transfer between the beams. The first process has inherent thermal effects and this will not be the case in OPCPA.

CPA depends on the electronic structure of the amplification medium to obtain the spectral frequencies which may be amplified, the spectral amplification shape. In OPCPA this depends on the phase-matching conditions inside the nonlinear crystal. Due to this fact, in OPCPA the allowed amplification bandwidth, (and tunability) is much larger then in CPA. In OPCPA we normally have a higher gain per pass (100000$\times$ has been observed), which might at first sight, indicate a better contrast. The main inconvenient in OPCPA is that due to the fact that OPA is a nonlinear process, OPCPA tends to be more unstable than CPA, and actually more unstable than the pump and the seed beams. In order to decrease these instabilities several vibration control and active stabilization methods have to be designed [79].

1.4.4. Spectral bandwidth and shape

In the section above, we have given the resolution of the propagation equations for OPA in a quasi plane wave approximation, however in reality this is just an approximation to a real OPCPA process. In order to have short pulses after amplification we need to be aware of the limitations in the spectral bandwidth which can be measured using the equations of the previous section for each spectral component. Doing this we will know which wavelengths can be amplified.

There are several classical studies [8] that approach the phase matching condition in linear and nonlinear configurations of the signal and pump beam. Normally the phase-mismatch can be compensated for by adjusting the non-collinear angle between signal and pump, several schemes profit from this property to obtain *nJ* level, $3.8\,fs$ pulses and sub-7 fs amplified pulses.

The spectral bandwidth is not solely dependent on the geometry of the trio, pump, signal and idler. In a situation where we have a small signal amplification, with an increase in amplification the amplified bandwidth is going to decrease. Saturation tends to increase the spectral bandwidth [71].

In order to have an idea of the amplification bandwidth and magnitude in a collinear and non-collinear case, using a small gain amplification or considering the depletion of the pump, we present the gain profile in these four cases in Fig. (1.6) and Fig. (1.7). The analysis is made for a pump pulse at 532 nm and a seed pulse at 800 nm, which is a classical example. The pump beam before amplification is a 5 ns pulse with 70 mJ energy and a peak intensity of approximately $0.2\,GW/cm^2$, and the seed pulse is a ps pulse with 0.7 mJ and a peak intensity of approximately of $1.9\,MW/cm^2$, both beams with a size of 3 mm. We are dealing with a classic Type I phase-matching in a BBO crystal. In this case the nonlinear length L_{NL} will be $3.6\,mm$ and we consider a path length of $15\,mm$.

For a small gain amplification, this results on average amplifications, on the order of ~ 336 times for the collinear case and ~ 470 times for the non-collinear case, as well as a bandwidth of 3.9 nm in the collinear case and 154 nm in the non-collinear case.
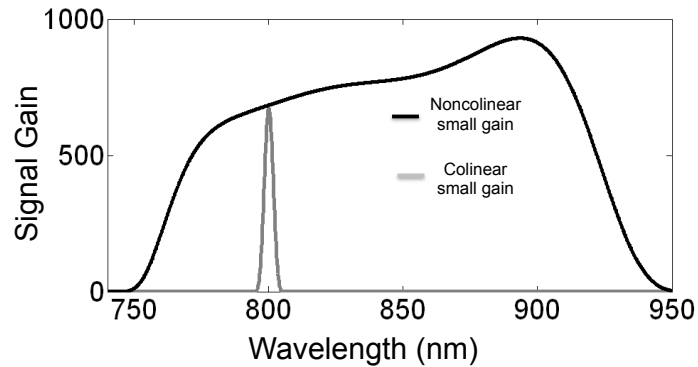
Figure 1.6.: Frequency dependence of the signal gain as a function of the wavelength for the collinear and non-collinear case.

It is important to notice that the small gain amplification is a parametric amplification independent on the seed intensity, and so the data related to the energy and intensity of the seed pulse given above do not play any role in this calculation, and we may consider that this would be the amplification in a case where the signal pulse intensity would be much less then the pump intensity.
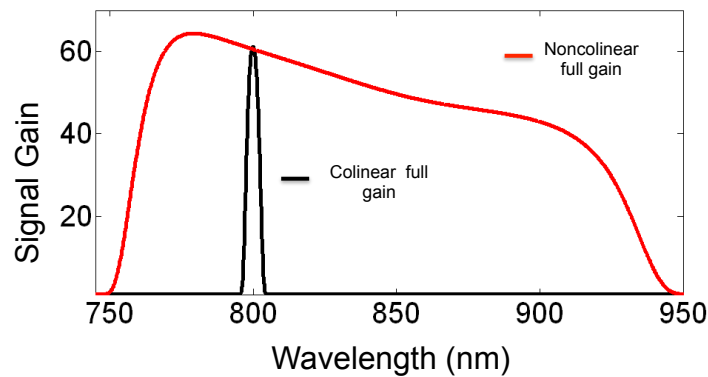
Figure 1.7.: Signal gain in the case where we consider amplification with pump depletion, in the collinear and the non-collinear cases. When calculating this graph we considered a single spectral linewidth for the pump with a top hat temporal profile for both pulses and a top hat spectral profile for the seed.

The pump depletion amplification is highly dependent on the pump intensity, on the seed intensity and on the beam path, and the results are not so reliable because we considered an uniform seed spectrum at the entry of the nonlinear medium. For the values given above, we obtain approximately 5 nm FWHM bandwidth in the collinear case and 163 nm in the non-collinear case. The amplification values obtained are on the order of 35 times.

In conclusion we may say that non-collinear phase matching gives us an additional degree of freedom that enables amplification of pulses of large spectral bandwidth, for low gain and high gain configurations.

1.4.5. Walk-off

An important factor in OPCPA is the walk-off effect, which is due to the fact that in an anisotropic crystal, the intensity and the phase do not propagate in the same direction. For more information on this effect please consult [70].

1.4.6. Contrast in OPA/OPCPA

The contrast is a very important aspect of amplified laser systems, specially in high power laser systems. Peak powers of hundreds of terawatts can mean that pre-pulses, at the order of 10^{-6}, are already sufficient to damage the material, ionize a gas or any other effect in the sample which could randomize the result of an experiment of laser matter interaction.

In CPA laser chains the contrast is limited by the spontaneous emission that is amplified on the subsequent amplification media (ASE - amplified spontaneous emission). When several amplifiers are used the noise is also amplified – in fact it works similarly to noise amplification in electronic circuits and so it obeys its general rules of using the less noisier amplifiers first and the noisier amplifiers at the end.

In a single amplifier considering that the noise inputted by unit of length is given by n and that the gain is given by G, the noise in the amplification is given by:

$$N(z) = \frac{n}{G} \left(e^{Gz} - 1 \right).$$

(1.34)

However the contrast is not only dependent on the ASE. We also have to consider coherent effects which might be due to imperfections in the compression, spectral modulations or simply partial reflections in the optics. This may create pre- and post-pulses which may damage the contrast.

The contrast in OPCPA has been the subject of many studies [43, 69, 70, 80]. In principle, OPA is a technique where the material does not absorb the light and so spontaneous emission (and so ASE) does not exist, but we have parametric fluorescence that might in some cases have the same effect, when the pump and the seed interact the parametric fluorescence diminishes considerably (pump depletion). However in a standard situation the pump duration is longer than the seed pulse, which means that when only the pump is present the parametric fluorescence is going to increase considerably.

1.4.7. B integral

The B integral is the measure of the third order nonlinear effect, and both CPA and OPCPA have problems with this. Keeping the effect of the third order nonlinearity low means keeping the higher order nonlinear effects low and the peak intensities below the damage threshold. Third order nonlinearities can be a nuisance when compressing a pulse, but they also allow for pulse compression in some special cases [81], however normally they introduce a spectral phase that is difficult to compensate [70, 82]. Another effect of third order nonlinearities is the self-focusing of the laser, where the beam profile in a nonlinear medium can create a parabolic refraction index which may simulate the effect of a lens at the center of the beam and focus it into a spot. This may create hot spots, which may damage the optics in the system.

Even if fiber amplifiers with B integrals as high as 16 have been reported (without nuisances to pulse re-compression) [83] it is known that B integral above 1 modifies the spatial profile due to self-focusing, and so high power laser systems are designed to have a B integral below 2 [84].

The B integral is the total phase shift due to the third order nonlinear coefficient and is given by

$$B = \frac{2\pi}{\lambda} \int n_2 I(z) dz. \tag{1.35}$$

It is intuitive that a low B means that the spectrum will only be slightly modified and also that the spectral phase will be easier to compensate. OPA has normally a low value of the B integral, (one order of magnitude lower than CPA, [70]) because the nonlinear medium is short. For low pump depletion, it can be approximated by

$$B = \frac{2\pi}{\lambda_s} n_2 I_S(0) \left[\frac{L}{2} + \sinh\left(\frac{\gamma L}{2} \right) \right]. \tag{1.36}$$

1.5. Phase matching and Manley-Rowe relations in the three wave mixing

Phase matching is the wave equivalent to momentum conservation in particle/mechanical physics. In linear optics, when two photons collide, nothing happens due to the linearity of the Maxwell equations, *i.e.*, photons do not interact with each other. In nonlinear optics, a collision of two or more photons may entail an interaction and the creation of new photons. The overall momentum and energy of the photons has to be conserved during propagation.

In any collision the conservation of two quantities (energy and momentum) must be preserved. When we have a mechanical collision we consider that mass has also to be conserved, however mass

conservation does not make much sense in linear/nonlinear optics. If we consider that mass can be related with the quantity of photons (as quantity of matter) it is clear that, in nonlinear optics, the Manley-Rowe relations exhibit the properties of mass conservation.[1]

These properties can be deduced properly by integrating the coupled propagation equations (Eq. (1.2)). Other way to get the Manley-Rowe relations is to analyze the energy diagrams associated with these collisions. For instance, considering Fig. (1.1) we see that the gain in ω_3 is the loss in ω_2 and ω_1, and that the gain in ω_1 is also the gain in ω_2. This can be translated by:

$$\Delta N_3 = -\Delta N_2 = -\Delta N_1,\tag{1.37}$$

where ΔN_i is the variation of the number of photons at ω_i. If we consider the mass to be the energy of a photon then we get the energy conservation as an equivalent condition. If we consider the mechanical equivalent of the TWM the SFG, where two classical bodies form another all together, we would have to assume we would have to obey the conservation relations, in other words, we would have at the same time a perfect elastic collision and a perfectly inelastic one:

$$
\begin{aligned}
\vec{p}_3 &= \vec{p}_1 + \vec{p}_2 \\
m_3 &= m_1 + m_2 \\
E_3 &= E_1 + E_2
\end{aligned}
\qquad\Longleftrightarrow\qquad
\frac{p_3^2}{m_3} = \frac{p_1^2}{m_1} + \frac{p_2^2}{m_2}
\tag{1.38}
$$

Using a direct mathematical calculation we obtain:

$$\left(\frac{p_3}{m_3}\right)^2 = \left(\frac{p_1}{m_1}\right)^2 + \left(\frac{p_2}{m_2}\right)^2 - 2\,p_1 p_2 cos(\alpha),\tag{1.39}$$

where α is the angle between $\vec{p}_1$ and $\vec{p}_2$. Treating it analytically, we get:

$$\frac{p_2}{m_2} = \frac{p_1}{m_1}exp(i\alpha)\tag{1.40}$$

which does not make a lot of sense for classical body mechanics.

Considering $\vec{p} = \hbar\vec{k}$, the wave mechanics equivalent of momentum and energy conservation can be viewed as:

$$\left(\vec{k}_3, \omega_3\right) = \left(\vec{k}_1, \omega_1\right) + \left(\vec{k}_2, \omega_2\right),\tag{1.41}$$

---

[1]If we consider the inertial mass there is another way to establish a parallel with mass in photons, which is to use the Einstein energy equation, making the mass conservation equivalent to energy conservation.

which is the phase matching condition and the energy transfer between pulses. However, Eq. (1.28) tells us that part of the energy transfer may be reversed after a distance that is equal to the inverse of the phase mismatch, meaning that we have energy transfer even if we do not have perfect phase matching. This distance is

$$z_{PM} = \frac{\pi}{\triangle k} \tag{1.42}$$

in which, $\triangle \vec{k} = \vec{k}_3 - \vec{k}_2 - \vec{k}_1$. This phase mismatch is discussed in detail. It is important to notice that, at first, we do not know the direction of all the three vectors. In a difference frequency generation (DFG) we do not know $\vec{k}_2$ or $\vec{k}_1$ and in a sum frequency generation (SFG) the $\vec{k}_3$ is unknown. However we know the length of the unknown vector even if we do not know its direction. When the existing beams are collinear this problem seems to be algebraic. However in a non-collinear scheme, doubts may arise on how to define the third vector's direction.

In the case of a particle collision with a wall, or with the interface between two media (frictionless collision) the momentum parallel to the interface between the media remains constant. However the momentum perpendicular to the wall or the interface can change. Similarly, when three waves interact in a nonlinear medium, the momentum does not change parallel to the interface of the linear/nonlinear medium. In other words the phase-mismatch vector is perpendicular to the linear medium/nonlinear medium interface. A scheme of phase-matching for a DFG between fields 3 and 1 is given in Fig. (1.8).
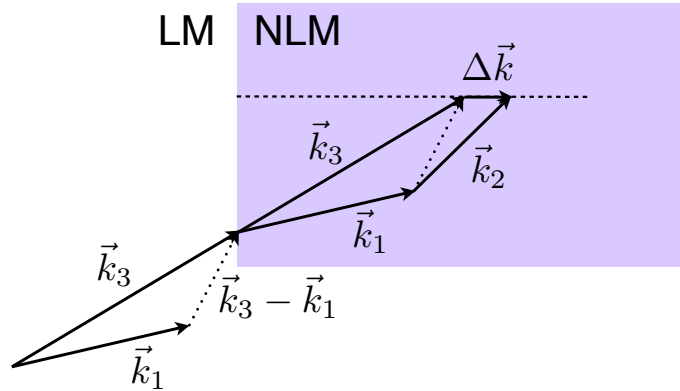
Figure 1.8.: Representation of the momentum vectors, $\vec{k}_1, \vec{k}_2, \vec{k}_3$ where $\omega_3 = \omega_1 + \omega_2$. Beam 2 is created as a DFG of beams 3 and 1.

Alternatively we can look at this differentially and say that we must find the the vector that minimizes the Hamiltonian factor (the Hamiltonian of a three wave mixing is proportional to $\int E_3\overline{E_2E_1}$):

$$\int\!\!\int\!\!\int_V \exp\left\{i\Delta\vec{k}\cdot\vec{r}\right\}dV \tag{1.43}$$

25

From this equation we can see that the integration in the direction of the interface is an integration over the width of the interface ($w_{interface}$, in a plane wave approximation this would be an infinite crystal) or the size of the beam. It is clear that the integration over this length would make the phase-mismatch zero on this direction, with an allowed phase-mismatch that would be proportional to $(2\pi/w_{interface})$. For information on practical ways of ensuring phase matching we advise the consultation of [69].

1.5.1. Type I phase matching in a uniaxial crystal, an example

This has been discussed by a wide range of authors, and thus we will be overlooking the basics. In an uniaxial crystal we have one preferential axis and a plane perpendicular to this axis where the index is the same over the entire plane. We have then two normal refraction indexes, one in a plane which is called ordinary plane, and the other in a perpendicular axis called extraordinary axis where the propagation is normal as well. The refraction index is given by:

$$\frac{1}{n^2(\omega)} = \frac{\cos^2(\theta)}{n_o^2(\omega)} + \frac{\sin^2(\theta)}{n_e^2(\omega)} \tag{1.44}$$

Type I phase matching in an uniaxial crystal means that we have two mixing waves (the low frequency waves, ω_1, ω_2) whose electric fields are within the ordinary plane and the high frequency wave ω_3 which electric field is within the extraordinary plane (or with a a certain angle θ), in this case $o + o \rightarrow e$. For a Type II phase matching the waves are organized in a configuration $o + e \rightarrow o$.

Normally we are working in a situation where, at the entry of the nonlinear medium (in this case a crystal), there are only two beams meaning that there is a third beam being created either by SFG or by DFG. Using this fact and the phase matching conditions (phase matching perpendicular to the interaction surface null) we can calculate the direction from where the beam originates (the propagation axis is considered to be z). In the DFG case the azimuthal angle of the third beam is given by:

$$\phi_2 = \arctan\left(\frac{k_3^y - k_1^y}{k_3^x - k_1^x}\right). \tag{1.45}$$

In the case of SFG we get:

$$\phi_3 = \arctan\left(\frac{k_2^y + k_1^y}{k_2^x + k_1^x}\right) \tag{1.46}$$

The axial angle for DFG is given by:

$$\theta_2 = \arcsin\left(\sqrt{\frac{\left(k_3^y - k_1^y\right)^2 + \left(k_3^x - k_1^x\right)^2}{|\mathbf{k}_2|^2}}\right) \tag{1.47}$$

and for SFG we have:

$$\theta_3 = \arcsin\left(\sqrt{\frac{\left(k_1^y + k_2^y\right)^2 + \left(k_1^x + k_2^x\right)^2}{|\mathbf{k}_3|^2}}\right) \tag{1.48}$$

In the case where we have three beams mixing from the start we have to remember that we have to integrate in x and y and for a plane wave this integral is a delta function of $\Delta k^{x,y}$. Using the equations above, we determined the third beam direction using the two input beams within a $\chi^{(2)}$ medium. The magnitude of this third beam is determined by its refraction index by way of the expression $\frac{2\pi n}{\lambda}$. The refraction index is determined using the electric field polarization.

We can now try to find the conditions over which we have null phase matching. For a collinear beam we have:

$$k_3 = k_1 + k_2 \tag{1.49}$$

Using Eq. (1.49) and Eq. (1.44) we obtain (using $\frac{1}{\lambda_3} = \frac{1}{\lambda_1} + \frac{1}{\lambda_2}$):

$$\theta = \arccos\left(\sqrt{\frac{\lambda_3^{-2}\left(\frac{n_o^2(\lambda_1)}{\lambda_1^2} + \frac{n_o^2(\lambda_2)}{\lambda_2^2} + 2\frac{n_o(\lambda_1)n_o(\lambda_2)}{\lambda_1\lambda_2}\right)^{-1} + n_e^{-2}(\lambda_3)}{n_o^{-2}(\lambda_3) - n_e^{-2}(\lambda_3)}}\right). \tag{1.50}$$

For a non-collinear case we get:

$$\theta = \arccos\left(\sqrt{\frac{\lambda_3^{-2}\left(\begin{array}{c}\frac{n_o^2(\lambda_1)}{\lambda_1^2} + \frac{n_o^2(\lambda_2)}{\lambda_2^2} - \frac{n_o(\lambda_1)}{n_o(\lambda_2)}\frac{\lambda_2}{\lambda_1}\sin^2\alpha + \\ +2\frac{n_o(\lambda_1)n_o(\lambda_2)}{\lambda_1\lambda_2}\left(\cos\alpha\sqrt{1 - \left(\frac{n_o(\lambda_1)}{n_o(\lambda_2)}\frac{\lambda_2}{\lambda_1}\sin\alpha\right)^2}\right)\end{array}\right)^{-1} + n_e^{-2}(\lambda_3)}{n_o^{-2}(\lambda_3) - n_e^{-2}(\lambda_3)}}\right), \tag{1.51}$$

where α is the angle between $\mathbf{k_1}$ and $\mathbf{k_3}$.

1.6. Final remarks

We use this chapter as an introduction to three wave mixing. We use the characteristic nonlinear length and the solution of the propagation equations in Chap. (3) and in Chap. (4).

We discuss the phase-matching conditions in an uniaxial crystal which we will use in Chap. (2) and in Chap. (5).

We also discuss some features of amplification, we calculate the difference in spectral gain in a low pump depletion approximation and with pump depletion observing in Figs. (1.6) and (1.7), that in the case where pump depletion is important the spectrum broadens.

2. Study of optical amplification – angularly chirped pulses for spectral gain bandwidth enlargement in OPCPA and presentation of a CPA chain with a detailed discussion and modelization of a laser oscillator

In this chapter we expose two techniques of optical amplification. There is an high interest on optical amplification for practical applications and for basic scientific research. In recent studies, Mourou et al. [85, 86] have envisioned that the Schwinger value could be approached using laser amplification. This would give rise to an entire new field of study. Here we present two basic studies of laser amplification. We present OPCPA simple schemes in a purely theoretical study and afterwards a detailed description of a CPA chain. We also expose a detailed study of a Ti:Sapphire laser oscillator with theoretical and experimental details. In fact, we present simulations of a laser oscillator that do not consider the temporal/spectral issues but actually discuss the evolution of the spatial characteristics of a pulse inside the oscillator.

This study was done with a Ti:Sapphire laser in mind. In this chapter, the OPCPA is obtained with a seed pulse centered at 800 nm, the nonlinear medium is a BBO crystal, in a type I phase matching configuration.

OPA was presented in the introductory Chap. 1, we worked with a SVE/quasi plane wave approximation OPA where the evolution of the beam may be resolved by the coupled equations (Eq. (1.2)). We will use this approximation in every simulation, using the methods given in Sec. (1.4) of the introduction. A Fourier decomposition of the field is used as well as a low pump depletion approximation.

OPCPA/OPA implies three pulses, the signal pulse seeded by an existing beam centered at ω_s, which is normally the pulse to be amplified, the pump pulse that has the highest frequency ω_p and a third pulse, the idler, with a frequency that is the difference of the frequencies between the two previous pulses, $\omega_I = \omega_p - \omega_s$. It is basically DFG in which the pulse with the smallest wavelength transfers energy to the low frequency pulses.

2. Study of optical amplification

In OPA, the energy is not stored in the medium and so the thermal effects on the crystal are much smaller than in a classical CPA configuration. The gain per crystal length can be larger than in CPA techniques. However, OPCPA's most interesting feature is a gain profile controlled by the geometry and temporal/spectral profile of the pulses.

The phase matching considerations are very important in order to have short pulse amplification. Indeed, the phase match determines the spectral gain bandwidth which has to be as large as possible for fs amplification. In this chapter, we are going to research some alternative phase-matching configurations to enlarge the spectral bandwidth of the gain profile. In fact, the OPCPA enables amplification of sub-6 fs without spectral filters [8]. The pulses amplified bandwidth is normally bigger in a OPCPA scheme than in a classical CPA because, in the latter, the gain bandwidth is constrained by the emission spectrum of the amplification medium.

The spectral gain bandwidth is going to depend on the gain itself, not only on the geometrical configuration of the pulses. It is well known that the spectral gain bandwidth decreases with an increase in gain. In a high gain configuration (without phase-matching considerations $L_{NL} \gg \Delta k^{-1}$), the spectral gain bandwidth ($\Delta \lambda_{1/2}^s$) is given by Eq. (2.1), where G is the maximum gain and λ_S, λ_I, λ_P are the wavelengths of the signal, idler and pump respectively. This equation is written considering that pump is far from depletion. If this is not the case, an enlarged gain bandwidth can be expected as it can be seen the introductory chapter:

$$\Delta \lambda_{1/2}^s \approx 2\sqrt{\lambda_S \lambda_I} \frac{1}{1 - \frac{\ln 2}{\ln G}} \sqrt{\frac{\lambda_S \lambda_I}{\lambda_P^2} \frac{1}{1 - \frac{\ln 2}{\ln G}} - 1}. \qquad (2.1)$$

The gain bandwidth in frequency ($\Delta f_{1/2}$) is also limited by the velocity mismatch that may exist between pulses [87]. It is possible to represent this in a Gaussian approximation to the pulses, as a function of the velocity of the signal v_s and the velocity of the pump v_p by:

$$\Delta f_{1/2} = \frac{4\ln 2}{\left| v_s^{-1} - v_p^{-1} \right|} \sqrt{\frac{g}{L}}, \qquad (2.2)$$

where g is the gain per unit of length, and L is the length of the medium.

Since the first proposals for a OPCPA amplification, the spectral bandwidth that could be amplified has been studied. Ian Ross et al. [8] have proved that a non-collinear amplification would enable a larger bandwidth than a collinear configuration. The optimal non-collinear angle (angle between the signal and pump beams) has been calculated. This "magic" angle tends to give the biggest spectral gain profile bandwidth, because at this angle the phase-mismatch first derivative is null.

In this chapter we explore the spectral gain in different situations, not only in a non-collinear phase-matching but also in a configuration where the pulses are spatially chirped. This increases the degrees

of freedom of the problem and allows the phase-matching to be done over a wider spectral bandwidth.

Apart from the spectral bandwidth, the geometrical configuration can also favor others factors such as the beam pointing stability and tolerance to the pump wavelength, in other words, the non-collinear angle/phase-matching angle configuration may allow for an insensibility to these factors. However the non-collinear angle with which insensitivity to the pump wavelength is maximal is not the same angle where we have the maximum signal gain bandwidth. However, seen that an extra degree of freedom (the spatial chirp) exists, it is possible to widen the gain bandwidth with one factor and beam pointing stability with the other. This is quite important because it is known that stability is one of the most critical aspects of OPCPA, instability in the system can also be due to several other factors like temporal jitter [80].

Two pump wavelength configurations will be presented, for a non degenerated problem and for a degenerated/quasi-degenerated problem in Sec. (2.1), we will discuss the influence that these two configurations have on the amplified bandwidth.

Afterwards, in Sec. (2.2), we will give a simple analytical approach of spatially chirped pulses, followed by some simulations using chirped pulses, in Sub-Sec. (2.2.2).

In Sec. (2.3), we present in detail a Ti:Sapphire oscillator. We discuss the dispersion management that is necessary for mode-locking (ML), the astigmatism inside the laser and its spectral profile. We then present simulations of the ML cavity, a detailed discussion of the thermal lens in play and of the spot size, as well as the the consequences of the sub-cavity configuration, the thermal lens and the Kerr lens on the ML operation. In this section, we try to identify the best sub-cavity configuration to have a ML operation and discuss the methods we can use to determine the propensity to ML. We end this section with an experimental scheme of one of the cavity stability zones and where the ML operation was preformed.

The ML oscillator described in Sec. (2.3) was used to seed a CPA chain, we describe this CPA chain in Sec. (2.5). This amplified laser included a regenerative amplifier and a 4-pass amplifier, the regenerative amplifier has a set of two prisms inside the cavity that will help to select the bandwidth of the output. This system will not only help to select the central wavelength but also to reduce the FWHM of the spectrum, which was our objective here.

2.1. OPCPA gain bandwidth in a non-degenerative configuration versus a degenerative situation

As we already have referred in the beginning of this section, we consider a seed laser with wavelengths around $800\,nm$, which is approximately the central wavelength of a Ti:Sapphire laser. We consider two options in what concerns the pump laser, our options are dependent on the available

2. Study of optical amplification

solid state lasers with wavelengths smaller than 800 nm. There are available pump lasers near 500 *nm*, either doubled solid state lasers like Nd:glass (phosphate glasses 527 *nm* and silicate glasses 531 *nm*), Nd:YAG (532 *nm*), Nd:VO4 (532 *nm*), Nd:YLF (523/526 *nm*) and Nd:YCOB (530 *nm*), or rare earth doped fiber lasers at doubled communications wavelength. Another approach is to use a doubled Ti:Sapphire laser near 400 *nm*. The second approach results in a degenerated or quasi degenerated DFG.

In a degenerative configuration, the angle between pump and seed that maximizes the amplified bandwidth is zero (Eq. (2.7)) and the phase-matching angle θ is 29º. For a 500 *nm*, this means an internal non-collinear angle of 2.7º and a phase-matching angle θ of 25º. By coincidence this angle is similar to the walk-off angle.

It is intuitive that a degenerative OPA situation will result in a quadratic phase matching curve, because the idler and the signal are not distinguishable (type I phase-matching) and so going to the left or right of the central wavelength is the same. In a non-degenerated case, the phase mismatch curve will not be parabolic, the FWHM gain bandwidth will be bigger but the spectral gain profile will be more irregular.
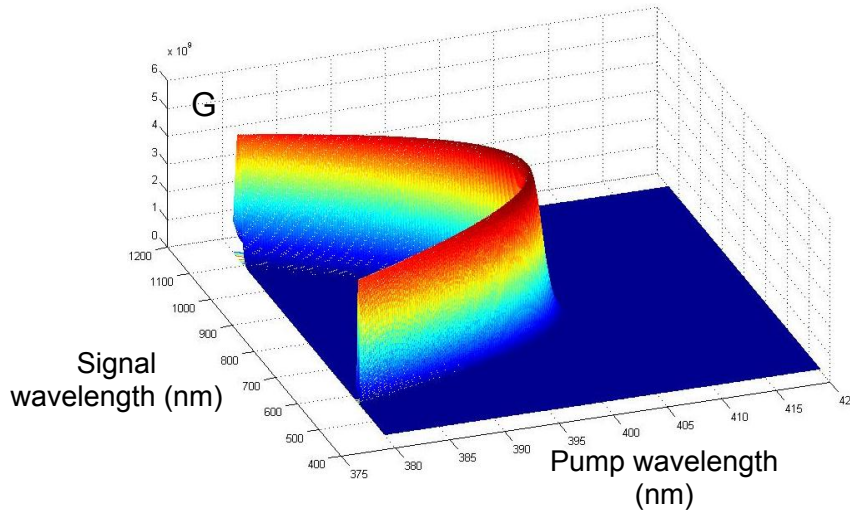
Figure 2.1.: Gain profile in small pump depletion approximation as a function of signal and pump wavelength, in a degenerated case.

In Fig. (2.1) we represent the gain as a function of the pump and signal wavelengths. The parabolic profile that is due to a parabolic phase-mismatch seen in Fig. (2.1) is an obstacle to a large gain spectral bandwidth. In the profile of Fig. (2.1), we see that the top of the gain is clearly defined by the phase-matching condition, and that there is no sensitivity to the wavelengths apart from the phase-matching itself. If we obey the phase matching condition for the central wavelengths, changing the non-collinear angle is the equivalent to turn the gain profile around the central wavelength. From this, we see that the worst possible condition for the pump wavelength insensibility will

be when the spectral gain bandwidth is the smallest. Fig. (2.1) clearly shows a parabolic profile and an insensitivity of the gain to the pulses wavelength. This picture was obtained using a PM configuration for a degenerative configuration, $\alpha = 0$ and $\theta = 29, 18°$, a crystal length of $2\,mm$ and a pump intensity of $5 \times 10^{10}W/cm^2$. In a non-degenerative configuration (532 nm/800 nm) however, the phase-matching conditions are not symmetric for the idler and signal pulses, the idler is going to be centered at $1.59\mu m$. The gain is given by Fig. (2.2). In this situation the phase-mismatch has a cubic shape in the signal-pump wavelength diagram. This picture was obtained using a PM configuration for a non-degenerative configuration, $\alpha = 2.38$ and $\theta = 23.8°$ and a crystal length of $15\,mm$ and a pump intensity of $2 \times 10^{12}W/cm^2$.
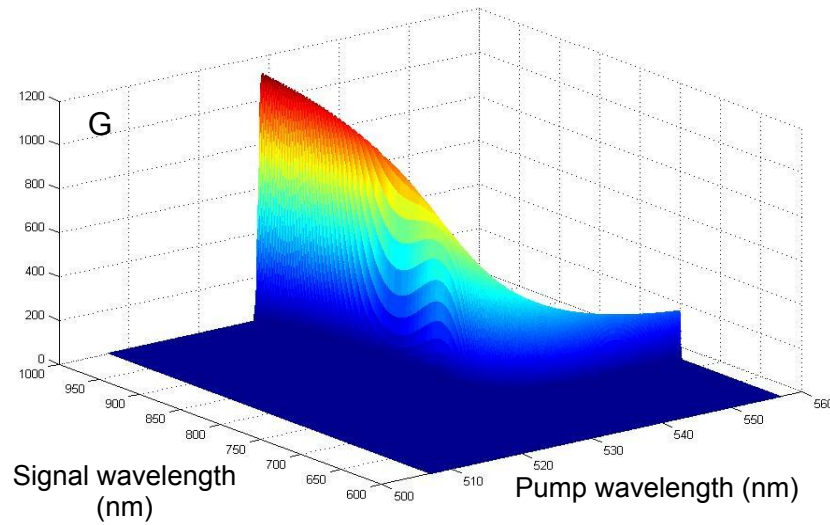
Figure 2.2.: Gain in a small pump depletion approximation as a function of signal and pump wavelength, in a non-degenerated configuration.

2.2. OPA phase matching adjustments using an angular chirped signal

In this section, we study OPA phase matching conditions when the signal has an angular chirp. Having an angular or spatial chirp in the signal, gives us one more degree of freedom, which may be used to have a bigger bandwidth, a bigger beam pointing stability or an insensibility the the pump bandwidth. We can have mixed situations where we adjust the two degrees of freedom, the non-collinear angle and the spatial chirp, to obey two different conditions, for instance the insensibility to the pump bandwidth and spectral bandwidth maximization.

From Fig. (2.3) (where we represent the angles α, β, γ) we deduce the following equations that will be used further on:

$$k_P^2 = k_S^2 + k_I^2 + 2k_S k_I \cos(\beta) \tag{2.3}$$

$$k_S^2 = k_P^2 + k_I^2 - 2k_P k_I \cos(\gamma) \tag{2.4}$$

$$k_I^2 = k_P^2 + k_S^2 - 2k_P k_S \cos(\alpha) \tag{2.5}$$
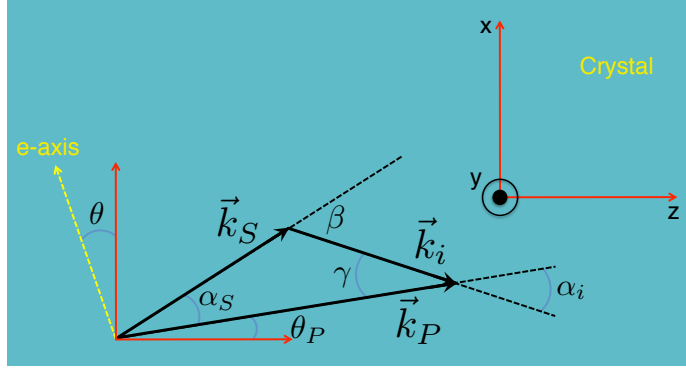
Figure 2.3.: Phase matching configuration inside the crystal with the three vectors important for phase matching and the important angles for phase-matching.

2.2.1. Spectral Bandwidth maximization

We have seen above that the spectral bandwidth depends on several factors. Here we consider solely the phase matching condition in the crystal, which is the most crucial factor. The maximum bandwidth conditions for a non spatially chirped pulses may be given by adjusting the phase matching and the non-collinear angle. We start with a known phase matching condition, stated above in Eq. (2.5).

In order to increase the spectral bandwidth, we have to have tolerance to the frequency of the signal ω_S, changing the frequency of the signal will also imply changing the frequency of the idler ω_I, since the pump frequency is considered to be constant and since we have a fixed relation between the three frequencies that is given by: $\omega_P = \omega_S + \omega_I$. The relation between the two varying frequencies will be given by $\frac{d\omega_I}{d\omega_S} = -1$ or $\frac{dk_I}{dk_S} = -\frac{n_{gI}}{n_{gS}}$. We use Eq. (2.5) in order to study the tolerance to the seed frequency. We chose this equation because, when altering the wave vector of the seed, the angle α is the only one that stays constant. The result is given by:

$$k_P \cos(\alpha) v_{gS}^{-1} = k_s v_{gS}^{-1} + k_I v_{gI}^{-1} \tag{2.6}$$

Where v_{gS} and v_{gI} are the group velocities of the signal and the idler. From this simple equation it is easy to deduce the following non-collinear angle:

$$\cos(\beta) = \frac{n_{gI}}{n_{gS}} \tag{2.7}$$

or

$$\alpha_{EXT} = \arcsin\left(\frac{k_i}{k_p} \sin\left(\arccos\left(\frac{n_{gI}}{n_{gS}}\right)\right)\right) \tag{2.8}$$

Where n_{gS} and n_{gI} are the group refractive index for the signal and the idler, this calculation had already been done in [8]. In here we can try a different approach by considering a spatial chirp. We will define our linear chirp as follows:

$$LC = \frac{d(-\cos(\alpha))}{d\omega_S} \simeq \alpha \frac{d\alpha}{d\omega_S} \tag{2.9}$$

Using this relation we re-deduce the equations above deriving Eq. (2.5) but considering that α is no longer constant with ω_S, but instead, that $\cos(\alpha)$ derivative is constant.

$$k_P v_{gS}^{-1} \cos(\alpha) - k_P k_S LC = k_s v_{gS}^{-1} + k_I v_{gI}^{-1} \tag{2.10}$$

As we have two degrees of freedom, we can differentiate the equation once more and obtain a second derivative condition:

$$k_P k_S'' \cos(\alpha) - 2k_P v_{gS}^{-1} LC = v_{gS}^{-2} - v_{gI}^{-2} + k_S k_S'' - k_I k_I'' \tag{2.11}$$

Combining the two equations, we arrive at the following formula for the spatial chirp:

$$LC = \frac{v_{gS}^{-2} - v_{gI}^{-2} - k_I \left[k_I'' + k_S'' \frac{v_{gI}}{v_{gS}}\right]}{k_P \left(2 v_{gS}^{-1} + k_S k_S'' v_{gS}\right)} \tag{2.12}$$

The ideal non-collinear angle also changes, and is given by the following formula:

$$\cos(\alpha) = \frac{k_S + k_I \frac{v_{gS}}{v_{gI}}}{k_P} + v_{gS} k_S LC \tag{2.13}$$

It might be more practical to put these expressions on the following form, where the spatial chirp is

2. Study of optical amplification

given by:

$$LC = \frac{n_{gS}}{ck_P} \frac{\left(k_I b + (\frac{n_{gI}}{n_{gS}})^2 - 1\right)}{2 + \frac{\lambda_S^2}{n_{gS}^2} n_S''} \tag{2.14}$$

where $n_S'' = \frac{d^2 n}{d\lambda^2}\Big|_{\lambda_S}$ and the angle between $\vec{k}_I$ and $\vec{k}_S$ may be given as $\cos(\beta) = \frac{n_{gI}}{n_{gS}} + \frac{k_P k_S}{k_I} v_{gS} LC$, where b is given by $b = \frac{d^2 k_I}{dk_S^2} = \frac{1}{2\pi n_{gS}} \left[\frac{n_{gI}}{n_{gS}} n_S'' \lambda_S^3 - n_I'' \lambda_I^3 \right]$ and $n_I'' = \frac{d^2 n}{d\lambda^2}\Big|_{\lambda_I}$.

These are the conditions that allow spatial chirp and the angle between the pump and the seed to enlarge the spectral gain bandwidth. Please beware that these results do not work in a degenerated configuration (sin that situation $LC = 0$). We may see this by equaling idler to signal, the parameter b will be zero and $\left(\frac{n_{gI}}{n_{gS}}\right)^2 = 1$, the spatial chirp would be zero. However this may mean that, if we define the spatial chirp differently, the results might be different, in reality because the optimal angle for a degenerated situation is zero the definition of LC in Eq. (2.9) will automatically mean $LC = 0$ even if $\frac{d\alpha}{d\omega}$ is not.

We could use the relations in [8] to obtain combined effects, for instance the condition to have tolerance in the pump wavelength that is expressed by Eq. (2.15) and Eq. (2.16) may be combined with the first order derivative condition in Eq. (2.10), in order to obtain at the same time an insensibility to the pump wavelength and a wider spectral bandwidth.

$$\cos(\gamma) = \frac{n_{gI}}{n_{gP}} \tag{2.15}$$

$$k_P = k_S \cos(\alpha) + k_I \frac{n_{gI}}{n_{gP}} \tag{2.16}$$

where n_{gP} is the group refraction index of the pump. The combination of the Eqs. (2.16) and (2.10) gives:

$$LC = \frac{n_{gS}}{c} \left[\frac{1}{k_S^2} \left[k_P - k_I \frac{n_{gI}}{n_{gP}} \right] - \frac{1}{k_P} - \frac{k_I}{k_p^2 k_s^2} \frac{n_{gI}}{n_{gS}} \right] \tag{2.17}$$

2.2.2. OPCPA simulations using spatially chirped pulses

We did several calculations in order to determine the ability of spatial chirp to increase the gain spectral bandwidth. We did this using the non-degenerated configuration using a pump with a wavelength of $532\,nm$ and the degenerated case with a pump wavelength of $400\,nm$. The biggest

spectral bandwidth was obtained in the second case.

In our simulations, we used a low pump depletion approximation and summed the electric field of a virtual seed at different wavelengths; the considered intensities as well as the crystal length are the ones that were used in Sec. (2.1). The seed signal non-collinear angle depended on the wavelength according to the formula: $\alpha(\lambda) = \alpha_0 + (\lambda - \lambda_0) \times L$, the central wavelength λ_0 is $800\,nm$. For a pump with a wavelength of $400\,nm$ a sweep the central non-collinear angle α_0 (please note that α_0 is the angle between the pump and the seed signal at λ_0) and of the angular chirp L was done, the FWHM of the spectral gain is given in Fig. (2.4).
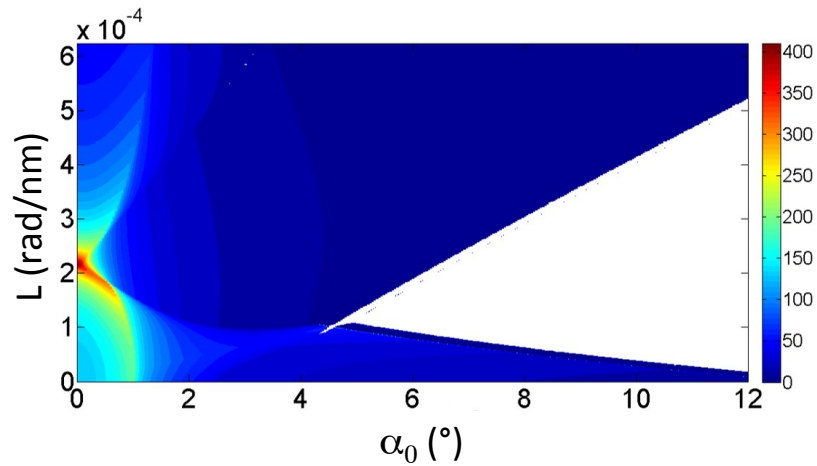
Figure 2.4.: FWHM of the spectral gain as a function of the non-collinear angle and the angular chirp, with the color scale given in nanometers.

We may see that parameters which maximize the FWHM of the spectral gain are $L = 2.2 \times 10^{-4}\,rad/nm$ and $\alpha_0 = 0°$. We use this parameters to calculate the spectral gain and phase. The result can be found in Fig. (2.5). The spectral gain is going to have a FWHM of $450\,nm$ centered at $850\,nm$.
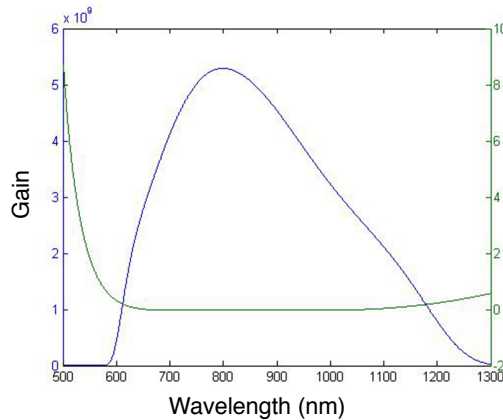
Figure 2.5.: (blue) Gain in function of the wavelength for a pump at $400\,nm$ and a seed centered at $800\,nm$, (green) spectral phase accumulated due to OPA for each wavelength.

A similar simulation was presented by Cardoso et al. [12, 13]. They used a different relation between the non-collinear angle and the wavelength, a different pump and seed wavelengths as well as a sweep over different parameters, but the idea was also to use spatial chirp in order to increase the bandwidth of the gain spectral. They also concluded that the degenerated case presented a bigger spectral gain bandwidth than the non-degenerate case.

2.3. Ti:Sapphire oscillator

We built and simulated a Ti:Sapphire mode-locked oscillator. The laser is designed to have a spectral bandwidth of $150\,nm$. The dispersion compensation is constituted by a set of chirped mirrors plus two fused silica prisms. By combining these two compensation schemes, the objective was to have at the same time a spectral emission between 750 and 900 nm, a high stability due to the reduced dimensions of the cavity and the flexibility to adjust the spectral profile at will.

The passive mode-lock (ML) involved here is called Kerr lens mode-locking (KLM), due to the Kerr effect introduced in the Ti:Sapphire crystal that is also the gain medium. In broad terms what we have is a positive gain feedback of the most intense pulses, that will lock the modes of the oscillator cavity.

If we have a Kerr medium inside a cavity, the radiation will be affected by the Kerr effect which is a third order nonlinear effect. Because of this non-linearity, peaks in the intensity propagating inside the cavity will be more affected by the Kerr nonlinearity than the CW component. These peaks will suffer a two part effect, a combination of self phase modulation (SPM), that enlarges the pulses spectrum and modifies its spectral phase, plus a lens effect that is due to the spatial profile of the beam inside the cavity. In a properly aligned cavity, the resulting Gaussian profile will either increase or decrease the beam size, depending on the observed position, and on the overall configuration of the cavity. If we have a way of selecting a beam of a certain size, then we can create an enhancing mechanism for that beam, which has a specific size.

In practice, we either put an aperture at edge of the cavity and select the smallest beam in the back mirror, by increasing the loss of the other modes, or we decrease the pump size inside the gain medium and increase the gain for the mode with the smallest size in the crystal. In the first case, we are dealing with an "hard aperture mode-lock", in the second with "soft aperture mode-lock". In order to have pulses with a duration of a few femtoseconds, dispersive effects have to be taken into consideration. In fact, if a pulse passes through a set of dispersive optics, its duration will enlarge. The shorter the Fourier transform of the pulse (bigger spectral bandwidth) the more the duration will increase. This will decrease the Kerr effect suffered by the beam which, in turn, will decrease the spectral bandwidth and the KLM stability.

In order to avoid this, we have to control the dispersion and, more specifically, we have to decrease

the pulse duration by compensating the spectral phase introduced by the dispersive optics (it will increase the pulse intensity, which in turn focus the beam due to the Kerr lens, and will increase the Kerr effect).

The issue of sub-two-cycle radiation directly from a Ti:Sapphire oscillator have been reported [88, 89]. Please note that sub-cycle laser pulse propagation would be theoretically impossible[1], however this does not mean that sub-cycle pulses are not possible in a certain time-space point [90]. It simply means that their propagation as a sub-cycle pulse is not possible [91], which means that the issue of KLM lasers is on the edge of what is physically possible. The locking mechanism in KLM is not spontaneous. Initially, the laser is in a CW mode, it only enters into a mode-lock configuration if a perturbation in the optical set starts the feedback mechanism. This perturbation may be a slight "bump" in one optical component of the cavity or in the optical table where it is assembled. In the first versions of KLM oscillators, one mirror was attached to a shaker that perturbed the cavity into mode-locking [30, 92]. Some of the more recent oscillators are stable enough not to need this artifice. The laser we describe in this section is one of those devices, where a single "bump" in the cavity is enough to mode-lock it.

Because there are some very good academic presentations on the basic theory inherent to these oscillators [93, 94], we do not debate it any further. Suffice to say that the stability of this oscillators is assured by the locking mechanism, that is due to the phase introduced by the linear dispersion and nonlinear dispersion. This mechanism is stable and it allows frequency measurements with a precision of 10^{19} over 100 THz [95], or frequency combs with sub-mHz spectral linewidth [96].

This type of oscillators have been widely reported by several authors. The first proposals and analyzes of Kerr medium on mode-lock/Q-switch lasers were done in the 1970's [97–99]. The spectroscopic and laser characteristics of Ti:Sapphire were studied in the 1980's [100, 101] and the firsts Kerr lens mode-locking lasers appeared in the early 1990's [19, 23, 29, 102–104]. Since then they have been explored by numerous authors, both in experimental studies and simulations. Several commercial Ti:Sapphire femtosecond lasers are available (see list in [105]) and fundamental research on the Ti:Sapphire mode-lock oscillator continues [21, 27, 106].

The most stable and first described Ti:Sapphire are hard aperture lasers. When compared to a soft aperture, the conditions that enable mode-lock operation are not so strict, and so it is presumably easier to achieve self starting mode-lock in the first case [29]. However self starting mode-locking as been achieved in both cases for asymmetric cavities[31, 107]. Self-starting mode-locking [20] depends on the nonlinearity of the cavity itself and can be achieved by introducing additional nonlinear elements into the cavity [108].

Early authors, reported oscillators where dispersion compensation was exclusively made by a set of two prisms inside the cavity, these prisms compensate the dispersion caused by the intracavity

---

[1]By definition the DC component of a sub-cycle pulse is different from zero. A DC component of a electric field cannot be propagated.

medium [19]. However the advent of chirped mirrors [109] has enable the design of oscillators in which spectral phase compensation is done on the basis of these mirrors and wedge plates [110]. Using chirped mirrors has several advantages: larger spectral bandwidth, more compact oscillators [32, 111] and, in a prismless oscillator, the coupling between amplitude/beam pointing and the carrier envelope phase is also eliminated [28]. However, having prisms inside the cavity allows the spectral intensity profile to be more flexible.

The exact model that we develop to calculate the oscillator beam size had not been presented previously. In this model, we do not include the temporal and spectral features of the resonating pulse. We find a coherent model, that determines beam propagation inside the cavity considering the pump size, the thermal lens and the Kerr lens. The sub-cavity is constituted by two curved mirrors plus the doped Ti:Sapphire crystal. It is well known that the exact dimensions of this sub-cavity are essential to the cavity dynamics, and so we use our model to make a 2D sweep of the sub-cavity dimensions that can be controlled experimentally.

The ability of a laser to enter into a mode-lock configuration and the stability of this configuration may be evaluated using the Kerr lens mode-locking parameter [93, 107, 112]. There are several formulas for this parameter that are discussed here. Another interesting feature is to see which configuration leads to a smaller mode-lock beam size; this beam size will translate into a bigger SPM and to a larger spectral bandwidth. With this model, we accurately predicted the results of a similar laser that is presented in [106]. For a reference on a Ti:Sapphire laser model that considers only the temporal propagation inside the cavity please consult [32].

2.3.1. Oscillator laser description

A general scheme of the laser oscillator is given in Fig. (2.6).

The dimensions of the cavity are presented in Tab. (2.1). The lens that focus the pump laser in the gain medium has a $+70\,mm$ focal length. The pump laser is a Millennia 532 nm CW, DPSS Lasers-5W, and the pump power used was $3.28\,W$. The Ti:Sapphire crystal has a 0.15% concentration of Ti$_2$O$_3$ and a thickness of $4.5\,mm$.

OC-M2	20.70 cm		MC1-M3	38.50 cm
M2-M1	17.20 cm		M3-M4'	56.00 cm
M1-MC2	23.70 cm		M3-P1	14.55 cm
MC1-MC2	10.75 cm		P1-P2	24.80 cm
CR-MC2	5.30 cm		P2-M4	17.25 cm
CR-MC1	5.10 cm		CR length	4.5 mm

Table 2.1.: Dimensions of the oscillator.

E is a descendent crossed polarization elevator with two 45° degrees mirrors with a distance between

them of around $9.5\,cm$; it brings the beam from a height of $16.2\,cm$ to a height of $7.5\,cm$, that is the height in which the laser is built. The MG1 and MG2 are two dielectric mirrors (@532 nm), MG1 has a fine adjustment that can be quantified.

MC1 and MC2 have both a $50\,mm$ focal distance and both reflect in the $800\,nm$ region and transmit approximately 99.7% @532 nm. MC1 has the reference Z0805033, and MC2 has Z0805031 (Layertech mirrors). These mirrors have a reflectivity of at least 99.8% from $630\,nm$ to $1010\,nm$. We present the transmission and GDD of these mirrors in the appendix Figs. (B.1) and (B.2), the typical combined GDD introduced by this mirrors is -160 fs^2@800 nm. The mirrors transmission at $532\,nm$ is approximately 99.7%, this is important because they must transmit the green pumping light, that is collinear to the laser beam, in the sub-cavity. The output coupler (OC) transmittance is 10% with a bandwidth from $700\,nm$ to $900\,nm$, the transmittance profile can be found in the annex, Fig. (B.3). The GDD introduced on the reflected beam by the output coupled is negligible, Fig. (B.4).
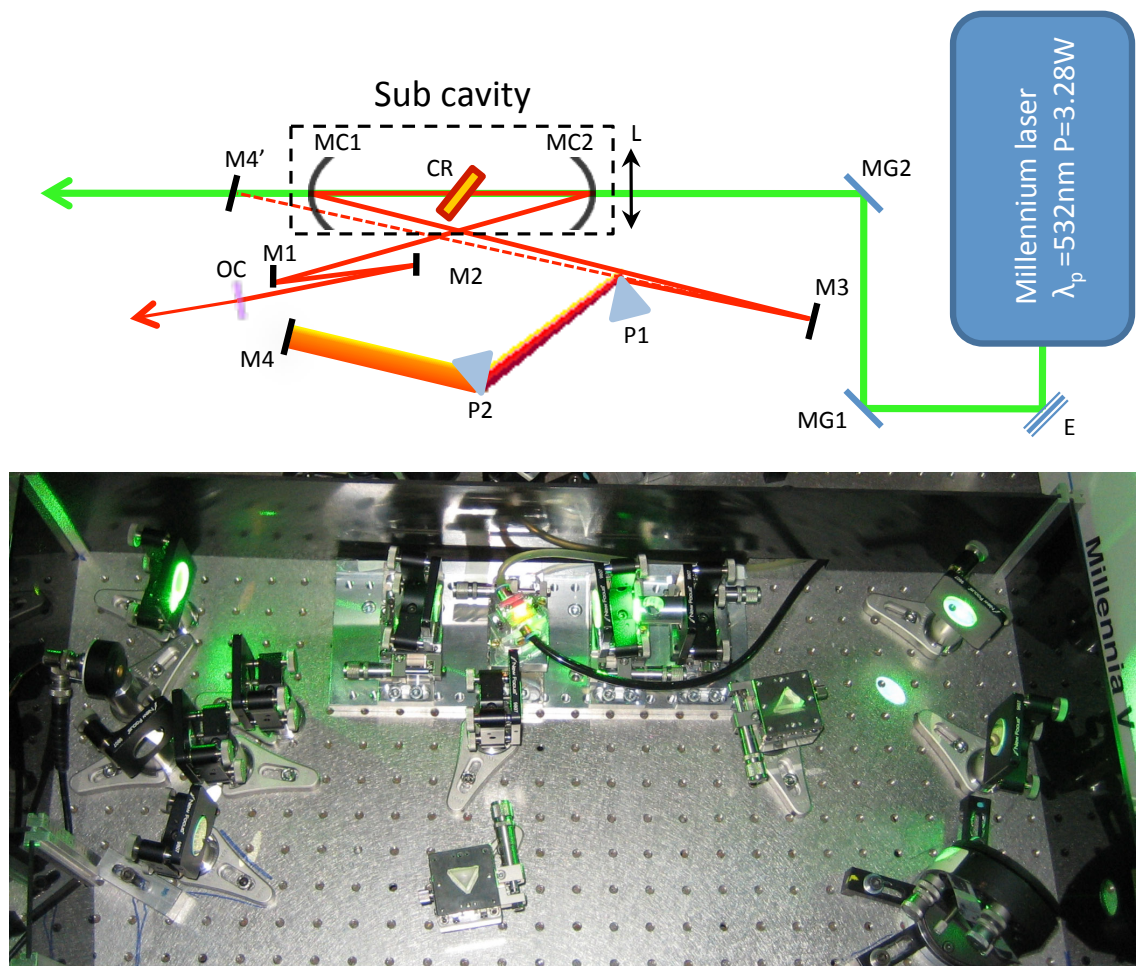
Figure 2.6.: (top) Laser oscillator cavity scheme, with plane mirrors M1, M2, M3, M4, and the plane silver mirror M4', output coupler OC, prisms P1, and P2, sub-cavity mirrors MC1 and MC2, transport mirrors MG1 and MG2, elevator E and focal lens L. (bottom) Photo of the cavity.

The mirrors on the arm of the output coupler M1 (reference Z0102037), and M2 (reference Z0102041), (Layertec mirrors) are configured for high transmission $600 - 900\,nm$ at zero degrees. The sum of both mirrors GDD is approximately $-100\,fs^2$@800 nm, the GDD of each mirror oscillates, however the oscillations cancel each other, and so the combined GDD is near flat.

Mirrors M3 (G0304008) and M4 (G1003015) have GDD profiles similar to M1 and M2 (with smoother oscillations) and a combined GDD of $-100\,fs^2$@$800\,nm$. M4 has a reflectivity higher than 99.8% for $630 - 1010\,nm$ and M3 from $650 - 1040\,nm$. The transmission and GDD data of these mirrors can be found in the annex, Figs. (B.5), (B.6), (B.7), (B.8), and (B.9).

The prisms are made with fused silica, and with roughly $15\,mm$ length, they are designed in such a way that the minimal deviation angle is also the Brewster angle, which gives an apex angle of $\sim 58º$. The total cavity length is approximately 1.669 m for the prismless cavity configuration and 1.675 m for the cavity with prisms.

The mirror M4' is a support mirror only used in alignment. When first assembling the oscillator, the cavity is first aligned using the pump light reflected by MC1, the prism P1 is pushed back in order for the light to go through to M4' that reflects the light back to the crystal. This reflected laser passes trough the crystal and a small part is reflected to the other arm of the cavity (by MC2) we use this light to align the mirrors in the other side of the cavity until the OC, which reflects the light back into the crystal. We can also align the cavity using the fluorescence of the Ti:Sapphire, mainly on the arm of the OC (which sometimes is convenient if we do not see the pump light due to the $< 0.3\%$ of reflectivity of the subcavity concave mirrors). At this point the laser can enter a continuous wave regime (CW) and by shear coincidence this laser configuration can also mode-lock without the prisms inserted, with a small spectrum. It is easier to have the laser in CW because the sub-cavity configuration is not so demanding, only some sub-cavity configurations are favorable for a ML regime (see the cavity stability models below). After having laser light the prisms are inserted in a minimum deviation angle (with the prisms inserted the pump light is no longer reflected back to the crystal), and the back mirror M4 is placed so that it reflects the light to the crystal, until we have laser light in the cavity

2.3.2. Astigmatism compensation

The Ti:Sapphire crystal is placed at Brewster angle, this means that the beam will be different in the tangential and sagittal planes. In fact, the crystal is not only acting as the gain/propagation medium but it has an intrinsic astigmatic lens (because of gain guiding and thermal lens) that is the combination of the Kerr lens, created by the laser pulse itself, and a thermal lens, due to the pump pulse intensity profile. The Kerr lens only exists when the pulse is mode-locked.

We use the folding of the cavity in order to compensate for the astigmatism in the nonlinear medium. More specifically, we use the extra distance traveled by the beam in the sagittal plane to compensate

the difference in the focal length of the astigmatic curved mirror of the sub-cavity (if both mirrors are equal $d_s - 2f_s = d_t - 2f_t$). This will give the expression[2]:

$$\cos^2 \theta + \frac{Nt}{R} \cos \theta = 1 \tag{2.18}$$

where θ is the incidence angle on the curved mirror, R is the curvature radius of the mirrors, t the thickness of the crystal and N is a parameter dependent on the refraction index (n): $N = \sqrt{n^2 + 1} \frac{n^2 - 1}{n^4}$. Applying Eq. (2.18) gives us an angle of 8.07º.

In practice, we first aligned the cavity without any prisms, even without prisms the cavity was able to ML, and so it is possible to have a cavity with two important characteristics: no prisms and a Kerr lens. It is with this cavity that we adjust the folding angle by minimizing the astigmatism of this output beam. The fact that we do not have to readjust the prisms makes it easier to align, because there are less degrees of freedom and the fact that there is a Kerr lens allows us to try to compensate the astigmatism introduced by the Kerr lens as well. We start with a folding angle of 15°, and we corrected (decreased) it observing the astigmatism at the output mirror, the final angle was near 7.5º. This ML configuration as 50 nm bandwidth.

Using a simple model, explained below, and the commercial program *WinLase,* we find the stability for the tangential and sagittal plane in function of one of the sub-cavity dimensions. We adjust the folding angle in order to obtain the same stability values in both planes, for the point where passive Kerr lens mode locking should occur, this angle is 7.2º.

2.3.3. Dispersion control

As we said above, we included prisms and chirped mirrors in the cavity in order to have: a better dispersion control, to allow the size of the cavity to be smaller, which results in a cavity that is more stable, and also in the flexibility that allows active dispersion control and so an adjustable spectral intensity profile. It is hard to modulate the dispersion inside the cavity, the mirror and prism introduce a spectral phase which is easy to calculate however the nonlinear Kerr medium, the Ti:Sapphire crystal, introduces a temporal dispersion which is hard to modulate and it is dependent on the pulse inside the crystal. A theoretical detailed study on the intracavity dispersion in this oscillator is given by Giambruno in his PhD thesis [113].

The first prism (P1) insertion controls the amount of material (amount of fused silica) the beam passes through. If we take into consideration the Fermat principle, it is easy to see that the second prism is a wavelength selector. In minimal insertion, the dispersion induced by the prisms is given by [92]:

---

[2]This expression was taken from [93].

$$\left.\frac{d^2\phi}{d\omega^2}\right|_{prisms} \simeq 527.4 - 21.1L_p \quad [fs^2] \tag{2.19}$$

Where L_p is the distance between the prisms, in cm. This results in a null dispersion for $L_p \simeq 25\,cm$, negative for bigger distances and positive for smaller distances. It must be clear that this is the value for minimum beam insertion in the first prism. The insertion has a positive chirp and for each millimeter of fused silica inserted into the beam path the round trip accumulates more $126\,fs^2$ of dispersion.

From this we see that the dispersion introduced by the prisms in the scheme given above is slightly positive, $+4\,fs^2$. It would be impossible to ML this laser without chirped mirrors. In fact, in order to compensate the linear dispersion of $2 \times 4.5\,mm$ of sapphire plus air without chirped mirrors the distance between prisms would have to be above $49.7\,cm$ [92].

In our case the sum of the negative GDD due to the chirped mirrors in a cavity round trip is approximately -700 fs^2@$800\,nm$, the output coupler has a positive dispersion of ~ $+5\,fs^2$@$800\,nm$. At $700\,nm$ the output coupler has ~ $+10\,fs^2$ and the chirped mirrors have ~ $-580\,fs^2$.

The positive GDD due to a round trip in air and in the Ti:Sapphire is ~ $+673$ fs^2@800 nm, which combined with the mirror values gives $\sim -22\,fs^2$@$800\,nm$ of GDD in an entire round trip of the cavity. The same value for 700 nm is ~ $+103\,fs^2$. Please be aware that the insertion of the fused silica that is $+126\frac{fs^2}{mm\,of\,insertion}$@$800$ nm, is not counted as well as the nonlinear phase due to the Kerr effect.

Let us now start to describe what we did in practice. The mirrors here exchanged in the search for a larger spectrum, although the dispersion seemed to change and the insertion of P1 to get the same spectrum would have to be different, we did not find any qualitative difference in terms of FWHM in large spectrums. The spectrum modulations that appear at some circumstances were observed in all the cases, no matter how the mirrors were distributed in the oscillator. We also tried several distances between prisms. We explored the region between $33\,cm$ and $21.6\,cm$ of prism to prism distance. At the extremes of these distances, the oscillator became unstable and it was quite difficult to ML. The actual distance between prisms of $24.8\,cm$ is not critical because we obtain similar spectrums with distances between $23.5\,cm$ and $26\,cm$.

The final stable configuration had an output power of $0.35\,W$ (ML configuration), which signifies $3.93\,nJ$ per pulse and $0.3\,W$ in a free running configuration. The spectral bandwidth FWHM was $150\,nm$ in a logarithmic scale and $100\,nm$ in a linear scale. The insertion between prisms is such that the distance between reflections in P1 is $9\,mm$ and in P2 is $3\,mm$. The spectrum is shown in Fig. (2.7).

For a cavity with prisms, the spectrum depends on the position of the prisms. The spectrum was easily found from $650\,nm$ to $950\,nm$, most of these spectrums were either unstable or there FWHM was smaller than $100\,nm$. We remind the reader that the output coupler worked between $700\,nm$ and

$900\,nm$ and so the part of the spectrum that is below $700\,nm$ passes only once in the oscillator and it is simply due to the SPM in the gain medium, in other words, it is not resonant.
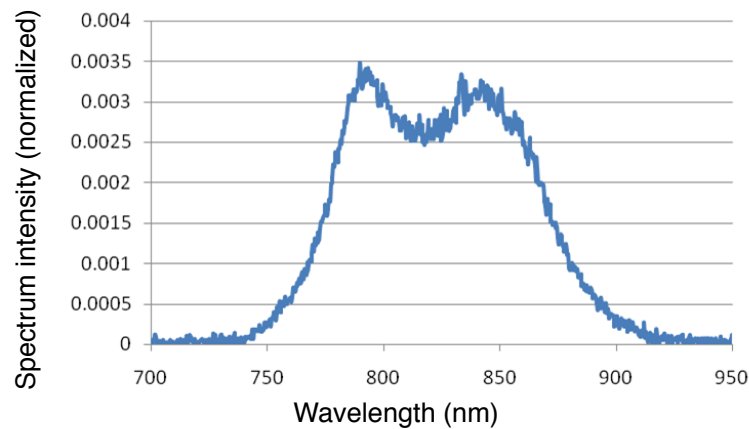
Figure 2.7.: Laser oscillator spectrum.

Some stable configurations presented spectral shapes which, in a logarithmic scale, had a FWHM that exceeded the FWHM of Fig. (2.7). However these FWHM in linear scale did not exceed $50\,nm$, a scheme of this spectrum is presented in the appendix (see Fig. (B.10)). This spectrum may be obtained just by moving the prisms, namely by inserting a higher quantity of glass with P2, this will increase the round trip cavity gain at lower wavelengths.

2.3.4. Cavity stability model in cw and in mode-lock

Calculating the stability of the laser using ABCD matrices is a well known method that is detailed in several academic courses [114, 115]. We use this tool in order to evaluate the spatial characteristics (curvature radius and mode size) in the laser, both in the CW mode and in ML. We consider only the spatial effects in a Gaussian and paraxial approximation. This is a strait forward calculation if we consider a CW mode, the laser stability and size do not depend on the pulse intensity, only on the other intracavity elements.

If we assume this, we have to estimate the thermal lens to completely reconstruct the ABCD matrix of the cavity and in doing so, to reconstruct the laser beam characteristics. However even in CW mode, it is difficult to make a precise estimate of the pump size. In order to have a good estimate for the pump size, we may compare it to the beam size. In other words, in order to assure a properly distributed gain profile the pump size cannot be smaller than the infrared mode size, otherwise the actual beam size is smaller and the beam cannot be resonant in the same cavity. On the other hand, if the pump size is too big, the gain decreases because the population inversion decreases. In conclusion, if the thermal lens is important, the beam size associated has to be comparable to the pump size. We could then devise an algorithm to estimate which pump size adapts to the beam size. Experimentally, we

move the pump beam size by adjusting the lens that focus the pump on the gain medium.

In a mode-lock regime, we will have at least 3 positive feedback regimes: the intensity of the laser in the gain medium will impact the Kerr and thermal lens and in consequence this will affect the size of the beam that will impact its intensity. Also, the intensity will affect the spectral profile due to the SPM of the Kerr effect, that extra spectral component, if compressed by the dispersion control mechanism, will increase the intensity itself. Moreover the average gain in a mode-lock configuration will be bigger, because the spatial profile of the laser will be smaller than the spatial profile of the pump.

If we would want to completely simulate what happens in a mode-lock laser we would have to simulate the temporal part of the mechanism and the small increase in average gain that takes place due to a better mode matching. However we will only simulate the spatial part of the mechanism assuming that the power of the beam is the one observed experimentally, the way the beam reaches this power is not our concern. The calculation will be self consistent, we will not guess the size of the beam profile inside the crystal, but the obtained profile will be consistent with the beam power and with the effects this power creates in the crystal.

2.3.4.1. Thermal and Kerr lens in a GRIN medium

Before calculating the stability profile of the cavity, let us study the effects presented in the nonlinear medium. We will not study the temporal effects, only the spatial effects in a steady state. The thermal lens introduced by the pump exists no matter the mode that the cavity finds itself in, however the Kerr effect is only important if the laser is in a mode-locked state. Please note that the Kerr lens is due to a nonlinear effect and in a CW mode neither the pump nor the resonant laser have enough peak power to induce a Kerr lens.

The pump laser is going to be absorbed by the Ti:Sapphire crystal, assuring population inversion, but also heating the crystal. This heat is going to create a gradient in the temperature distribution of the crystal, it is this effect that is going to produce a lens effect. It is important to clarify that it is the temperature gradient that creates the thermal lens and not the pump laser itself. Indeed, in order to have a thermal lens, the beam size can be bigger than the pump size and this is only possible because it is the thermal gradient that creates the lens.

Within the framework of a very simple model, the thermal lens power is going to be given by Eq. (2.20).

$$f_{th}^{-1} = \frac{1}{n}\left[\frac{dn}{dT} + (n-1)(1+v)\alpha_T + \frac{1}{2}n^3\alpha_T p_{eff}\right]\frac{\eta_{th}I_{abs}}{K}\frac{1}{1+2\left(\frac{w_L}{w_P}\right)^2},\qquad(2.20)$$

where:

➤ *n* is the refraction index, corrected for the nonlinear Kerr effect, $n = n_0(\lambda) + n_2 I_L$,

➤ $\frac{dn}{dT}$ the variation of the index with temperature,

➤ I_{abs} the intensity of the beam absorbed by the crystal, $I_{abs} = \frac{P_{abs}}{\pi w_p^2}$, w_p the pump diameter in the crystal, P_{abs} average pump power that is absorbed by the crystal,

➤ n_{th} the part of the absorbed pump that is converted into heat,

➤ *K* the thermal capacity of the crystal,

➤ *v* the Poison coefficient,

➤ α_T the thermal expansion coefficient,

➤ p_{eff} the strain-optic effective constant,

➤ w_P the the size of the pump beam,

➤ w_L the size of the laser beam.

In order to obtain this formula, we first make a parabolic approximation to the temperature profile [116–118], and then take the value of this approximation and calculate the optical path deformation due to this effect [119, 120].

Most studies do not account for the correction term that adjusts the laser beam to the pump beam, $\frac{1}{1+2\left(\frac{w_L}{w_P}\right)^2}$, which is the same to consider that the temperature gradient is calculated using a linewidth heat source and a cooling at the hedges of the crystal. However the heat source is not a line, the pump that heats the crystal has a Gaussian shape, with a size is similar to the size of the laser beam. In order to consider the mode adaptation of both beams, the difference between the ideal lens and the real optical path difference has to be considered as an aberration. This is masterly done by Fan et al. in [121], where we see that Eq. (2.20) is valid as long as $2 > w_L/w_P > 0$. The expression would be different for a top hat spatial profile pump beam.

This formula takes into account that the optical path is deformed not only by the temperature gradient effect on the refraction index $\frac{dn}{dT}$ [116] but also the crystal deformation due to the temperature gradient, $\alpha_T(1+v)(n-1)$ [120], this includes the window deformation.

The refraction index dependence on the strain applied to the crystal is given by $\frac{1}{2}n^3\alpha_T p_{eff}$ [122, 123]. The photoelastic component is not due to the temperature profile but to the intensity profile, and it is a fast contribution to the thermal lens. For the Ti:Sapphire, the photoelastic effect is still understudied. In a recent study, Zheng et al. [124] have measured one of the strain-optic tensor components of Ti:Sapphire and concluded that the transitory photoelastic lens could account for 27% of the total thermal lens.

The study of this phenomena is obviously important but the lack of data on the subject simply does

not allow for a concrete evaluation of the thermal lens in our case. Zheng et al. [124] have evaluated the coefficient $p_{31} = -0.03 \pm 0.01$. With this coefficient, the contribution of the photoelastic effect to the thermal lens would be $\sim 3.5\%$, however this photoelastic coefficient is not pertinent to our case because the polarization is not within the c-axis of the crystal[3]. In [125], Reintjes et al. have measured the strain-optic coefficients of sapphire. We note that the coefficient $p_{31} = 0.032$ that was obtained in [125] has an absolute value that is similar to the value obtained by Zheng et al. [124].

If we take the other components of Ti:Sapphire to be the same as the sapphire, with $p_{eff} = p_{11}$, we have a contribution by the photoelastic effect that is 29% of the total thermal lens, if we take the coefficients of Cr:Sapphire [123] the correspondent value will be 27%. However the fact that $\frac{dn}{dT}$ is not calculated considering an explicit photoelastic component, we may say that this component is included in $\frac{dn}{dT}$.

In some studies [116, 118], the window medium deformation is estimated in other manner: $\frac{2\alpha_T r_0(n-1)}{L}$ where L is the beam path in the crystal and r_o is the radius of the deformed part due to the temperature gradient.

We have to be aware that this considers the strain of the heat/cold source and not the strain of the crystal mount, or the response of the mount to the deformations due to heat. In order to have a more exact model to the thermal effect deformation of the beam path, we would have to take into consideration the astigmatic pump profile, the absorption and the propagation of the pump due to its own thermal lens [126].

The real effects of thermal deformation of the optical path do not form a perfect lens or a quadratic index GRIN medium, several computational models and experimental work [126–130] were done in order to have more precise figure of the thermal load in the optical path. However this would exponentially increase the complexity of the problem and, as we have refereed above, with this model we completely explained the experimental results for another laser that can be found in [106].

In order to determine the absorbed pump power, we use the absorption coefficient α (measured for a crystal with the same doping percentage [4]) and the formula,

$$P_{abs} = P_{pump}\left(1 - \exp\left[-\alpha L\right]\right). \tag{2.21}$$

In order to know the part of the absorbed power that is converted into heat, we have to consider the ways in which this power can be discharged: spontaneous emission and stimulated emission by the

---

[3]In fact, we blindly considered the expression given in [121] for the optical path difference, but it is our opinion that the photoelastic effect should be treated apart from the thermal effect, when the model includes the mismatch between the beams. In other words, the optical path difference of the first two effects is simply given by the temperature distribution, the last effect however is dependent on the light intensity distribution in the crystal and should be accounted as such. In a Ti:Sapphire the photoelastic effect is still not well known so we will not dwell on this.
[4]Absorption depends on the doping of the crystal.

infrared laser. Classically this fraction is given by Eq. (2.22).

$$\eta_{th} = 1 - \eta_p \left[(1 - \eta_l) \eta_r \frac{\lambda_p}{\lambda_f} + \eta_l \frac{\lambda_p}{\lambda} \right], \tag{2.22}$$

where η_p is the pump quantum efficiency, η_r is the radiative efficiency of the florescence, η_l is the fraction of photons that decays due to stimulated emission, and λ_p, λ_f are the pump and fluorescence wavelengths.

The Kerr lens is originated by the ML beam on itself. It is the effect of the spatial Gaussian intensity profile, combined with the Kerr effect [50]. The focal distance is going to be dependent on the beam size, w_L, the laser intensity, I_L and is given by:

$$f_{Kerr} = \frac{w_L^2}{4n_2 I_L L}, \tag{2.23}$$

where n_2 is the nonlinear refraction index and L is the beam path inside the crystal, which for a crystal of thickness L_c and corrected refraction index of $n = n_0(\lambda) + n_2 I_L$ is $L = \frac{L_c}{\cos(\arcsin(\frac{\sin(\arctan(n))}{n}))}$.

We could consider these lenses on the center of the laser medium, however we have to be aware that these lenses come from considering a quadratic dependence on the temperature and intensity profile of the laser beam. We can simulate the lens effect and the propagation in a single matrix if we consider a GRIN medium. The GRIN medium is going to have a refraction index given by:

$$n_i = n \left(1 - \frac{1}{2} \gamma^2 r^2 \right) \tag{2.24}$$

The parameter γ is given by $\gamma^2 = \gamma_T^2 + \gamma_K^2$. The thermal γ_T and Kerr γ_K GRIN coefficients are related to the focal distances given above by $\gamma_i^2 = \frac{2}{f_i L}$.

Estimations for the thermal and Kerr lens

We use the values given in the literature. Please note that depending on the chosen literature the values change, for instance depending on the author [105, 130–134] we find different values of $\frac{dn}{dT}$ in the ordinary axis: $12.6 \times 10^{-6} K^{-1}$, $13.6 \times 10^{-6} K^{-1}$, $8.5 \times 10^{-6} K^{-1}$, $18 \times 10^{-6} K^{-1}$. A more critical situation is the determination of thermal conductivity of the crystal where we find in the ordinary plane $K = 52^{W}/_{m.K}$ in [132] but most authors present a value around $K = 34^{W}/_{m.K}$. As we have not measured the entire set of characteristics, we do not know the precise values.

We use: pump quantum efficiency is 1, the radiative florescence quantum efficiency is 0.81, the central wavelength of the florescence is 750nm [135], $\frac{dn}{dT} = 12.6 \times 10^{-6} K^{-1}$ [123], $\alpha_T = 4.6 \times$

2. Study of optical amplification

$10^{-6} K^{-1}$, $\nu = 0.25$, $K = 35\,W/m.K$, $n_2 = 3.45 \times 10^{-20}\,m^2/W$ [105]. We measured an absorption coefficient of $\alpha = 3.22 \pm 0.05\,cm^{-1}$ which is within the values presented in the literature for 0.15% Titanium doping.

The pump quantum efficiency is nearly perfect ($\eta_p = 1$), in order to obtain the ratio of photons that are emitted by stimulated emissionη_l, we consider the rate at which they are emitted by stimulated emission ($S_{abs}\frac{I_L\lambda_L}{hc}$) and the rate for spontaneous emission ($\frac{1}{\eta_r\tau_d}$) this gives:

$$\eta_l = \frac{S_{abs}\frac{I_L\lambda_L}{hc}}{S_{abs}\frac{I_L\lambda_L}{hc} + \frac{1}{\eta_r\tau_d}}. \tag{2.25}$$

The values found in literature for the decay time is $3.2\,\mu s$ and for the absorption section is $4.1 \times 10^{-23}\,m^2$.

Our ML laser emission is centered at $824\,nm$ with a average power of $0.35\,W$ which with a repetition rate of $89\,MHz$ means a pulse energy of $3.93\,nJ$. The Fourier limited duration is $\sim 12\,fs$, considering some simple calculations (we used the Eq. (D.6) given in the introduction). We estimate an average duration inside the crystal of $24\,fs$. Which gives an approximate peak power of $1.6\,MW$ inside the crystal.

In our simulations, we will not have to estimate the transversal dimensions of the laser inside the crystal however in order to estimate the Kerr lens we might consider it to be around $40\,\mu m$ (sagittal plane), we will check later the validity of this estimation.

These values will give a Kerr lens of $\sim +22\,mm$ (we consider an effective section between the sagittal and tangential planes), this should not be taken in the strict sense it is rather an indicative value. We note, that although most values are reliable the laser spot size in the crystal is only estimated, the Kerr lens has a fourth power dependence on this parameter, it is easy to be mistaken by one order of magnitude.

In order to estimate the thermal lens we calculate the fraction of absorbed pump that is converted to thermal energy, which is 0.35, please be aware that the fraction of photons that is not converted by stimulated emission is on the order of 10^{-2} which means that a very good approximation is simply the energy difference between the pump and the signal ($\frac{\lambda - \lambda_p}{\lambda}$).

The absorbed pump power is estimated at $2.52\,W$ (we consider 5% losses between the reflection and diffusion). Furthermore the pump size is estimated to be $40\,\mu m$, in the sagittal plane (we consider an aperture given by the pump focal length). Considering this, the value for the thermal lens is $\sim +10\,cm$ (considering the difference between the sagittal and tangential planes).

The dependence on the laser size is not as pronounced as in the case of the Kerr lens (for w_L in the same order of magnitude of w_P), however there is a square dependence on the pump size, so the values given here are simply rough estimates of the real values.

2.3.4.2. Cavity stability profile ABCD equations and mode-lock parameters
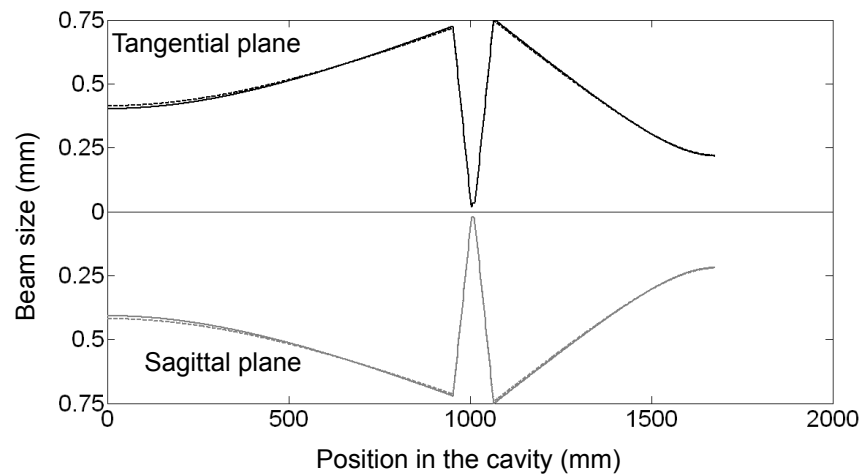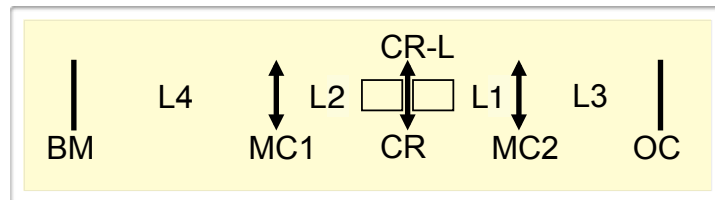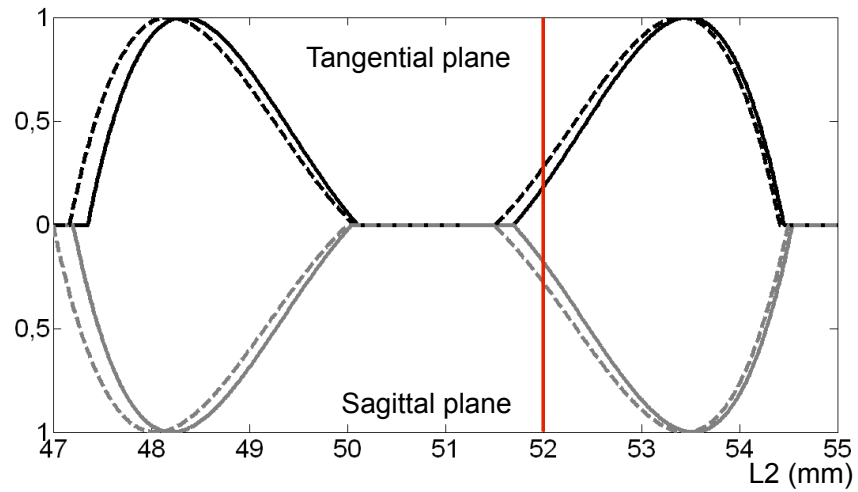
Figure 2.8.: *WinLase* calculation of the ML cavity (traced line) and the CW cavity (continuous line). (top) Stability results, with the normal ML position marked with a double line; (Middle) simple scheme of the simplified cavity; (Bottom) Beam size as a function of the position in the cavity.

We ignore the existence of prisms in the cavity and consider that there are simply two big arms one with $61.6\,cm$ that goes from MC2 until the output coupler ($L_3 = \overline{MC2OC} = 61.6\,cm$) and the other with $95.1\,cm$ (the biggest arm can also be considered to exist without prisms in which case it will have $94.5\,cm$ in length) that goes from MC1 until the back mirror ($L_4 = \overline{MC1BM} = 95.1\,cm$).

2. Study of optical amplification

The two arms in the sub-cavity are more difficult to determine, they are measured over the table and have uncertainty of some millimeters and a length of approximately $50\,mm$ (the focal distance of the curved mirrors).

We designate $L_1 = \overline{MC2CR}$ and $L_2 = \overline{MC1CR}$ (very approximate experimental values of $51\,mm$ and $53\,mm$). We will sweep these two arms of the sub-cavity. It is known that the cavity stability is very sensitive to the sub-cavity dimensions but the sensibility to the other values is not as great. In other words, the big arms measurements have a precision that allows us to determine the stability profile of the laser but not the sub-cavity measurements.

With the values given above, we may construct a simple cavity. In a first approximation, we use the program *Winlase* that will give us the stability profile that may be found in Fig. (2.8). However we may develop our own calculations and retrieve more information from it. Most of the propagation ABCD matrices may be found in [93] and are reproduced in the appendix to this chapter. However the propagation through a Kerr medium in a Brewster angle has to be deduced. In the sagittal plane this is a simple propagation in a Kerr medium:

$$\begin{bmatrix} \cos(\gamma_s L) & \frac{\sin(\gamma_s L)}{n\gamma_s} \\ -n\gamma_s \sin(\gamma_s L) & \cos(\gamma_s L) \end{bmatrix},\tag{2.26}$$

where γ_S is the GRIN medium total coefficient in the sagittal plane.

In the tangential plane, the entry into a medium placed at the Brewster angle is described by the matrix $\begin{bmatrix} n & 0 \\ 0 & 1/n \end{bmatrix}$, the inverted matrix describes the exit of the same medium. In the tangential plane the propagation through the crystal may be described by the following matrix:

$$\begin{bmatrix} \cos(\gamma_t L) & \frac{\sin(\gamma_t L)}{n^3\gamma_t} \\ -n^3\gamma_t \sin(\gamma_t L) & \cos(\gamma_t L) \end{bmatrix},\tag{2.27}$$

where γ_t is the GRIN medium total coefficient in the tangential plane.

Please note that we prefer to maintain the propagation in the medium divided in tangential and sagittal plane, the GRIN medium indexes are also divided because the effect is different for both axes. Please remember that the size in the sagittal plane (w_s) and the size in the tangential plane (w_t) are related by the following formula:

$$w_t \simeq n w_s \tag{2.28}$$

In order to calculate the laser intensity inside the crystal, we have to consider both axis: $I_L = P_L/\pi w_s w_t$ which for a well compensated astigmatism would be: $I_L \sim P_L/\pi n w_s^2$. Please note that in a CW mode, there is no coupling between the sagittal and tangential modes.

The thermal lens that affects the tangential and the sagittal plane is also different, we approximate this using the GRIN coefficient of Eq. (2.29).

$$\gamma_{th,s-t}^2 = \frac{2}{nL}\left[\frac{dn}{dT} + (n-1)(1+v)\alpha_T\right]\frac{\eta_{th}P_{abs}}{\pi K w_{P,s-t}^2}\frac{1}{1+2\left(\frac{w_{s-t}}{w_{P,s-t}}\right)^2}. \tag{2.29}$$

Please be aware that $n_P/n_L = 1.0066$ and so the astigmatism is introduced by the pump beam itself and not by the correction introduced by the aberration. In order to correctly find the GRIN thermal coefficient, we would have to solve a 2D head equation.

The Kerr GRIN coefficients in the sagittal and tangential plane are given by:

$$\begin{aligned}\gamma_{kerr,s}^2 &= \frac{8n_2 P_L L}{\pi L w_s^3 w_t}\\ \gamma_{kerr,t}^2 &= \frac{8n_2 P_L L}{\pi L w_s w_t^3}\end{aligned} \tag{2.30}$$

Considering this, we obtain the ABCD matrix of the laser oscillator round trip which is going to be the multiplication of the ABCD matrices of all elements. From half a crystal to half, a crystal we have:

$$\begin{aligned}ABCD_{roundtrip,i} &= [CR_i]\,[P(L_1)]\,[CM_i]\,[P(2L_4)]\,[CM_i]\,\times\\ &\times\,[P(L_1)]\,[CR_i]^2\,[P(L_2)]\,[CM_i]\,[P(2L_3)]\,[CM_i]\,[P(L_2)]\,[CR_i]\end{aligned} \tag{2.31}$$

As we said in the appendix, $[CR_i]$ designates the propagation matrix through half a crystal in the plane i, the sagittal or tangential plane. $[P(L_j)]$ is the propagation matrix over a length of air L_j and the matrix $[CM_i]$ represents the bouncing in one curved mirror.

As seen above, the thermal and Kerr lens are going to be dependent on the size and power of the laser beam. The thermal lens depends on the pump power and is only going to be slightly affected by the beam size, however the Kerr lens is dependent on the laser power and its beam size. In consequence, the GRIN medium is going to affect the propagation ABCD matrix that is going to affect the beam size, which affects the GRIN medium so there is a loop effect between the beam size and the Kerr effect.

For a CW laser, this effect is small because there is no Kerr lens but in ML, this is not the case. This process, that constitutes a part of the Kerr lens mode-locking mechanism, is going to end up with a certain laser power. We do not have to simulate this laser power because we have measured the energy output and we can estimate the pulse duration inside the crystal, from the pulse spectrum outside the cavity [136], as we have done above. Using these facts, we design a feedback cycle (Fig. (2.9)) that will result in a beam profile consistent with the beam power in a ML configuration. All lasers start in a CW configuration and so we do not expect a reproducible and stable ML cavity if

that cavity does not allow a stable CW. In practice this is not so, because once in ML the cavity can go to a configuration where no CW operation is possible but where it is possible to have a ML pulse. However if we want a reliable laser, this is not practical.
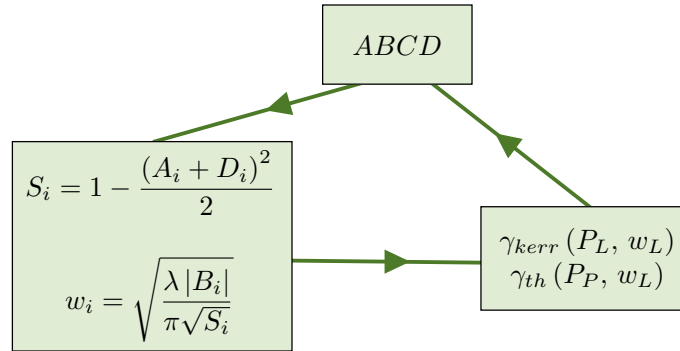
Figure 2.9.: Feedback cycle used to find a laser spatial profile that is consistent with the mode-locked power laser; it is repeated until a convergency of 5% is achieved, the laser proves to be unstable, or the cycle is repeated 100 times.

In this system we have several approximations:

➤ In order to consider the same GRIN medium parameter throughout the medium, we consider the pump and infrared beam sizes to be constant inside the crystal. The beam size used to calculate the GRIN propagation parameter γ_i is the beam size in the geometric center of the crystal. This is a good approximation because in the zone where passive mode-locking is expected, the beam waist is not inside the crystal.

➤ We consider that the power of both lasers is constant, which is not true for either the resonant or the pump laser. The pump is absorbed in the propagation, we used Eq. (2.21). The laser power increases with the increase in the nonlinear Kerr effect, because the duration deceases, we do not know exactly how, some measurements are presented in [136]. We will make some calculations where the intensity increases from a CW to a ML configuration.

➤ The pulse duration inside the crystal is constant.

➤ The pulse duration is an average estimation from the linear dispersion values and the measured pulse duration.

➤ The pump beam size is simply going to be estimated and not measured, this is probably the roughest estimation.

Despite this limitations, the simulation will give us an idea of the beam size inside the crystal, the stability of the oscillating cavity as well as the best zone for ML the laser. It will allow us to determine the sensibility that our system has to changes in its configuration.

The ML parameter

It is difficult to evaluate the ability of a laser to enter a ML configuration. It is difficult to obtain a parameter that distinguishes a configuration where ML is easily achieved and another where it is difficult to obtain ML. In [107], Cerullo et al. have defined a parameter that was proportional to the loss inside the cavity when a Kerr lens was introduced. This parameter was defined for a hard aperture configuration and it reflects the difference in mode size due to the Kerr lens:

$$ML_P^0 = \left(\frac{1}{w} \frac{dw}{dP} \right)_{P=0} \tag{2.32}$$

This simple parameter reflects the change in size due to the increase in power, then for a hard aperture the size of the mode should be taken in the place where the aperture exists, in the back mirror. This is the mostly used ML parameter [137]. In our case however, the ML is in a soft aperture mode. What we should evaluate is the mode inside the crystal. The mode size in the crystal is astigmatic, which was not the case in the back mirror of the cavity, and so we have to redefine the ML parameter as:

$$ML_P^0 = \left(\frac{1}{\sqrt{w_s w_t}} \frac{d\sqrt{w_s w_t}}{dP} \right)_{P=0} \tag{2.33}$$

It is obvious however that an approximation of what happens at low power may fully not represent the climb up in power that exists in the ML process (please remember that in a CW configuration the peak power of the laser is 6 orders of magnitude smaller than in the ML).

Let us remember that, in order to have ML, the laser cavity has to be near an unstable point and that the Kerr lens is introduced in the cavity and assures a bigger stability. However the introduction of this Kerr effect may in fact destroy the stability of the cavity in some sub-cavity configurations, and so there are zones where the parameter of Eq. (2.33) is maximized, but where it is not possible to obtain ML at all because the cavity is unstable. In [93], we find another definition for the ML parameter. We adapt this definition and redefine a new ML parameter in Eq. (2.34):

$$ML_P = \frac{1}{\sqrt{w_s\big|_{(P=0)} w_t\big|_{(P=0)} w\big|_{(P=P_{ML})} w_t\big|_{(P=P_{ML})}}} \frac{w_s\big|_{(P=P_{ML})} w_t\big|_{(P=P_{ML})} - w_s\big|_{(P=0)} w_t\big|_{(P=0)}}{P_{ML}/P_c}, \tag{2.34}$$

where P_{ML} is the peak power of the laser in a ML configuration and $P_c = \lambda^2/2\pi n_2 n_0^2$ is the critical power for self focusing. Please notice that this ML parameter is adimensional. The concept behind this parameter is simple, we compare the mode size in a ML configuration and in a CW configuration. This parameter however also poses some problems. Mainly it is difficult to find the ML configuration beam size that satisfies a cavity with the correspondent Kerr effect.

2. Study of optical amplification

Above in this section, we have exposed an algorithm that enabled us to find the ML size, however, as we are going to discuss in this section, this is not the only way to find the beam size in a mode-locking configuration.

Other definitions of ML parameters are discussed by Grace et al. in [112], this several proposals are based on a gain/loss comparison of both modes. Grace et al. do not consider any thermal lenses but considers instead a gain guiding due to the pump Gaussian profile.

Results without a thermal lens

Let us consider that there is no thermal lens inside the crystal. For a CW mode this means that there is no difference on the position of the crystal. We make a sweep over the dimensions of the sub-cavity, we sweep over L_1 and over $z = L_1 + L_2$. The beam size[5] for such a CW laser is given in Fig. (2.10).
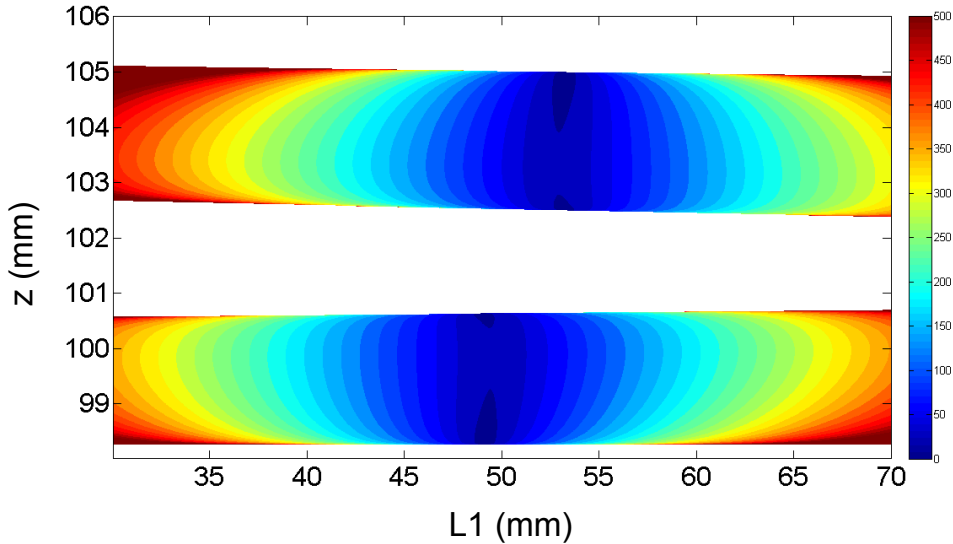
Figure 2.10.: CW beam size (in μm) as a function of the cavity configuration (in *mm*).

We may notice that the beam size is almost independent of L_1; this is obvious because without any lens, moving the crystal inside the cavity does not have any effect on the propagation matrix between the two curved mirrors. The slight slope in Fig. (2.10) is due to a change in L_3 and L_4 when we move the curved mirrors.

In order to do this calculation, we consider that the cavity is centered in the configuration expressed above and that every move in L_1 and L_2 will have a consequent effect in L_3 and L_4. However this effect changes the beam size by less than 3% and we could chose to maintain L_3 and L_4 constant, no qualitative results would change.

---

[5]All the beam sizes presented here are effective spot sizes in the tangential and sagittal planes $w = \sqrt{w_s w_t}$ taken at the geometrical center of the crystal.

In order to evaluate the ability to ML, we implement a infinitesimal power increase (10^{-8} of the actual laser peak power) of the laser that is going to give a differential Kerr contribution in the gain medium. Due to the fact that this perturbation is small, the algorithm exposed in Fig. (2.9) converges after the first or second loop.

The size of the beam with this small perturbation is used to calculate the derivative in Eq. (2.33). The resulting ML parameter is found in Fig. (2.11).
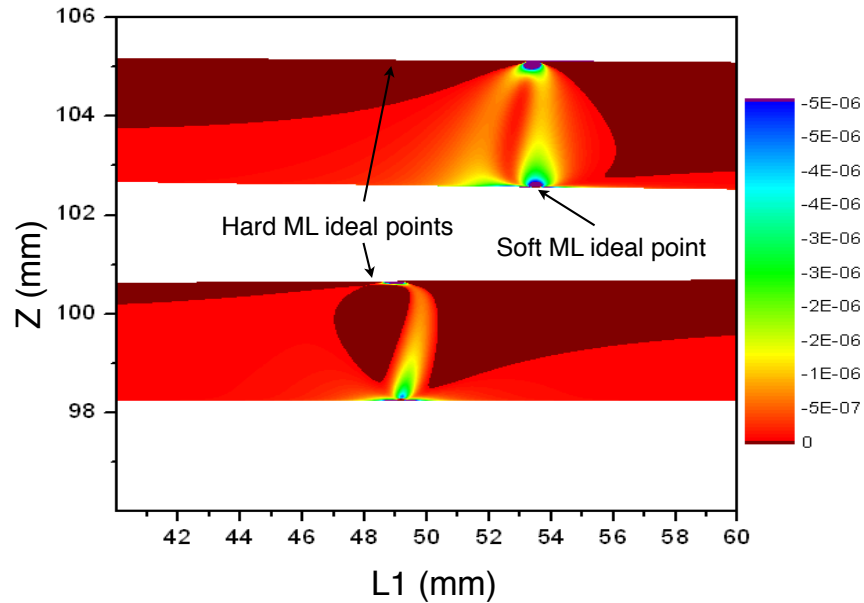
Figure 2.11.: ML parameter for zero power as a function of the sub-cavity dimensions (in *mm*). The color scale indicated on the right of the contour plot is expressed in W^{-1}. The soft aperture and hard aperture ML positions are indicated.

Please notice that in order to have soft aperture ML, the beam size with the Kerr lens has to be smaller than the beam size without the Kerr lens, and so the ML parameter has to be negative. In Fig. (2.11) we can clearly see the zone where ML should occur, it is not only on the interior of the second zone but it is also on a very specific location of the crystal.

The ideal point for ML obtained in Fig. (2.11). may be a point where ML is not possible because the Kerr lens, characteristic of ML, may destroy the stability in this specific point. In order to determine the ML size, to evaluate the stability of the ML laser and then to calculate the ML parameter as given by Eq. (2.11) we apply the algorithm given in Fig. (2.9).

Our initial guess for the beam size is the beam size in CW mode, the logic is to have a CW configuration in which a Kerr lens is introduced, and try to adapt the Kerr lens to the beam size and vice versa. The results are given in Fig. (2.12).
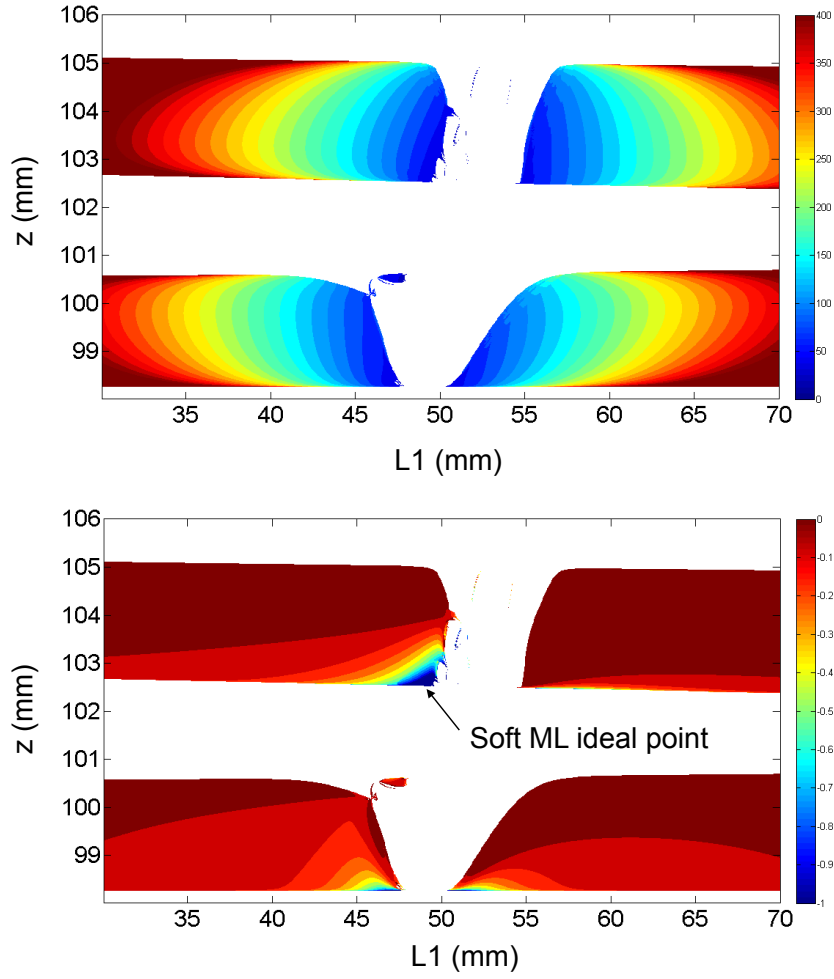
Figure 2.12.: (Top) ML beam size (in μm) as a function of the cavity dimensions (in *mm*). (bottom) the ML parameter as given by Eq. (2.34). The soft aperture ML ideal sub-cavity configuration is indicated.

The structure near to the ideal ML point is a hint, it might be possible to have stability in regions that do not present stability in Fig. (2.12), because they might have been awry calculated by the algorithm of Fig. (2.9).

We try another method to find the beam size in a ML configuration. We start from the CW configuration and gradually increase the power inside the cavity. We did this in 20 linear steps, and at each step we apply the algorithm of Fig. (2.9) until convergency is achieved. The idea behind this algorithm is to simulate the gradual power buildup inside the cavity. The results are given in Fig. (2.13). We may see that the complicated structure disappears, however as we do not simulate the buildup of power inside the cavity we do not know if this is the correct assumption.

In order to test the possible beam sizes that would make a stable ML cavity, we re-adapt the algorithm of Fig. (2.9). We use a second algorithm that is exposed in Fig. (2.14). For every (z, L_1) point this

algorithm consists in:

1. We start with the CW values for the beam size in the tangential and sagittal planes.

2. We calculate the GRIN coefficients with these beam sizes.

3. We calculate the ABCD matrix.

4. We recalculate the spot size.

5. If the cavity is stable we memorize the beam size for both planes ($w_M = w_i$).

6. With the spot size we recalculate the GRIN lens and continue to the next cycle.

7. If the cavity is unstable we try $w_L = f^b w_M$.

8. We recalculate the GRIN coefficients and if the cavity is stable we memorize the spot sizes.

9. At each failed attempt $b = b + 1$.
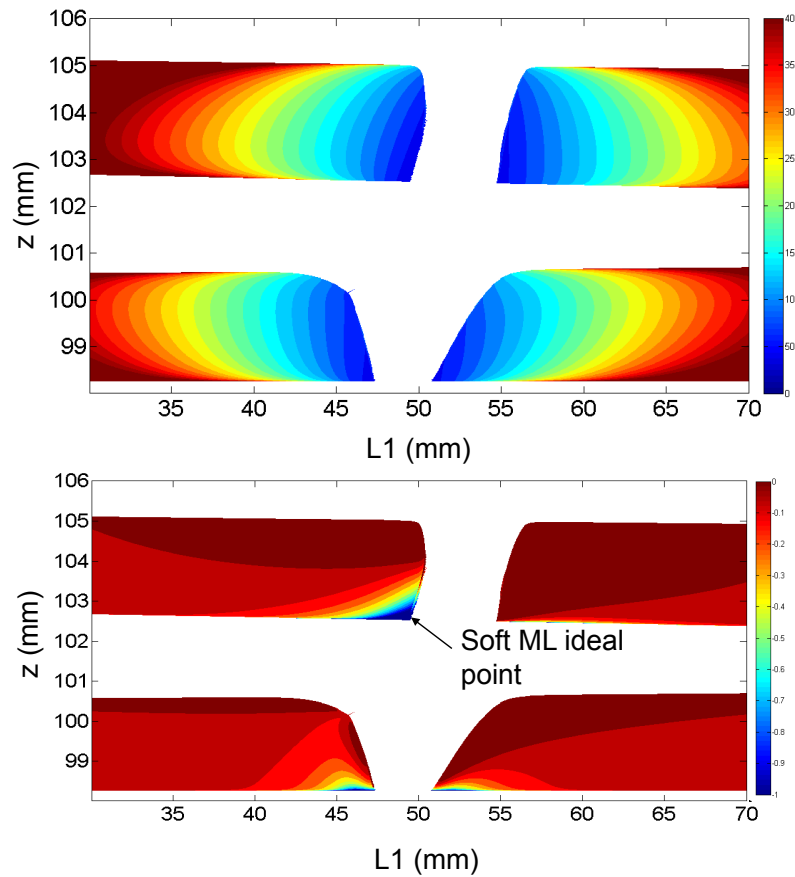
Figure 2.13.: (Top) ML beam size (in μm) as a function of the cavity dimensions (in *mm*); (Bottom) the ML parameter as given by Eq. (2.34). The soft aperture ML position is indicated.

2. Study of optical amplification

We impose a limit for the trial spot size and if no trial spot size makes the cavity stable the cavity is considered to be unstable in that point. If we want to test the stability of spot sizes which are larger than the memorized spot, then $f > 1$, if we want to test the stability of smaller spot sizes, then $f < 1$.
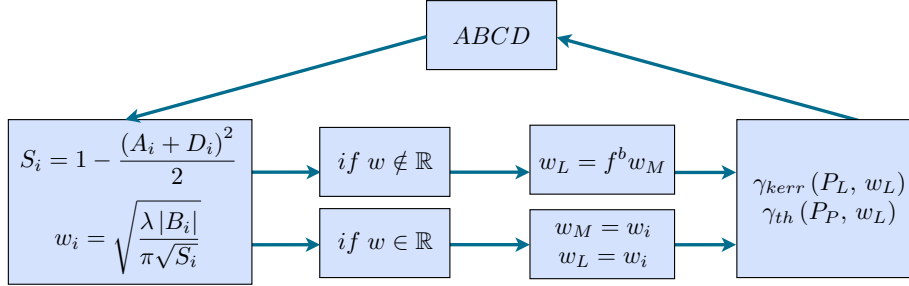
Figure 2.14.: Alternative algorithm to find the ML beam size.

We tried this second algorithm with $f = 0.99$ (lower limit for the beam size is $3\mu m$), the results are presented in Fig. (2.15).
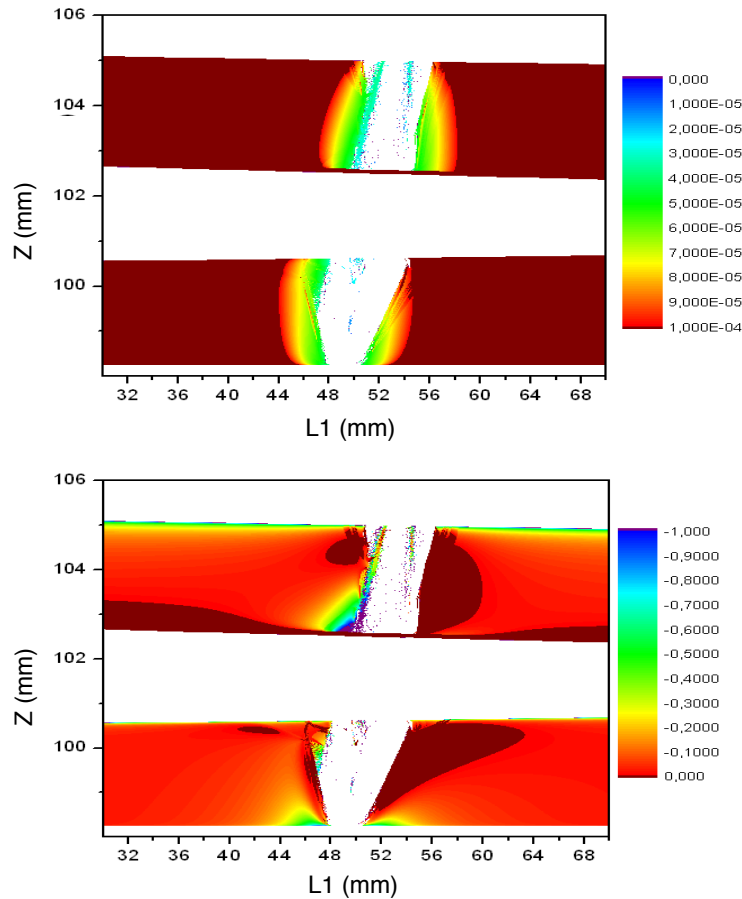
Figure 2.15.: (Top) ML beam size (in m) as a function of the cavity dimensions (in mm); (Bottom) the ML parameter as given by Eq. (2.34).

We may clearly see that this algorithm finds new stable points that had not been found before. The algorithm finds a strait line of optimal isolated points near the optimal ML point, this straight line appears for a constant value of L_2. At this point, we have to warn the reader that it is not compulsory that the values obtained by this method are possible, the path to get this values might not exist. However it is possible that this point might exist, the effect of bistability in Kerr lens ML lasers is well known, which means that the path to ML is not unique. Observing the line on the bottom of the second stability zone in Fig. (2.15), we can distinctly see that our spot size search algorithm is not perfect.

We have also tried the same algorithm but with $f = 1.01$ (upper beam size limit of $300 \mu m$). With these parameters, the results did not improve what we had obtained with the first search algorithm (Fig. (2.9)) and so we conclude that in order to find stability in points that are not stable with the first algorithm we must search smaller beam sizes.

Constant thermal lens in the cavity

Here we consider that there is a thermal lens. We consider a pump with a spot size of $40 \mu m$ in the sagittal plane, which gives an effective spot size of $53 \mu m$. With this pump size we use Eq. (2.20), however for the effects of the thermal lens we consider that the beam size is equal to the pump size. This will give us a thermal focal length of $52.5 \, cm$ and $16.6 \, cm$ for the tangential and sagittal planes respectively.
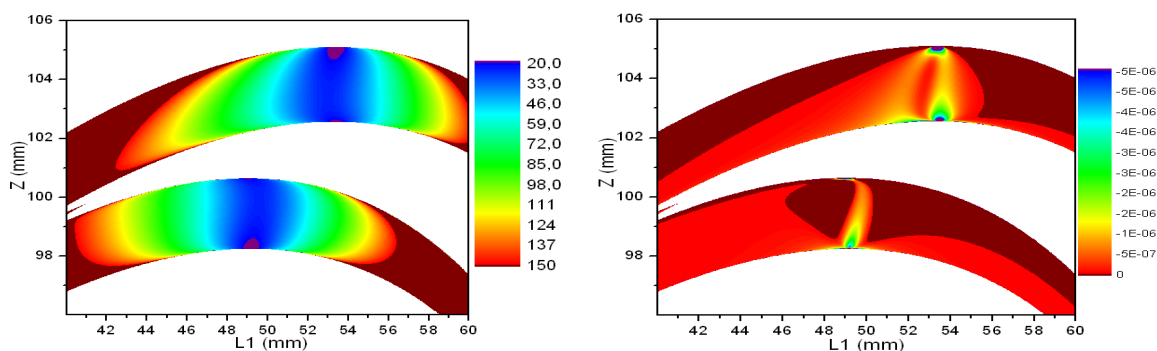
Figure 2.16.: (Top) CW beam size (in μm) as a function of the cavity dimensions (in *mm*); (Bottom) the ML parameter (in W^{-1}) as given by Eq. (2.34).

We compute the CW beam size as we did in the previous section and calculate the ML parameter as given by Eq. (2.33), the results are presented in Fig. (2.16).

The stability profile bends due to the thermal lens. Comparing Figs. (2.10) and (2.16), it is clear that the bending is done around the configuration that leads to the smallest beam size. The zone we had pointed out in Fig. (2.16), as ideal for soft aperture ML operation and where the CW beam has the

smallest size, seams to be remain ideal for ML operation independently of the thermal lens.

Using the algorithm of Fig. (2.9), we calculate the ML parameter as given by Eq. (2.34). The results are given in Fig. (2.17). With this configuration, we can clearly see that the ideal ML sub-cavity dimensions are given at the point we signal with an "X".
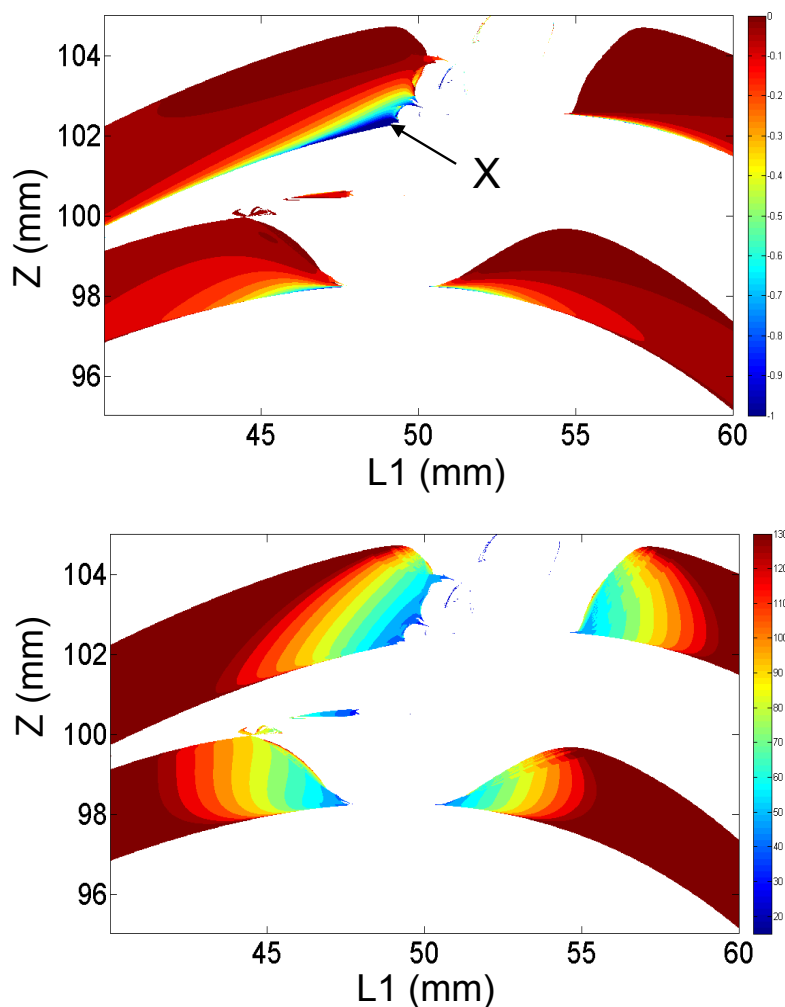
Figure 2.17.: (Bottom) ML beam size (in μm) as a function of the cavity dimensions (in *mm*); (Top) the ML parameter as given by Eq. (2.34).

Applying the second algorithm, we find the results presented in Fig. (2.18). In Fig. (2.18) the "X" position does not change. However the region where L_2 is constant that we had observed in Fig. (2.15) when no thermal lens existed appears when we use this algorithm and it also seams to be a position favorable for ML operation. In this region, the ML seams to be stable.

The results do not fundamentally change between this two search algorithms but in this second algorithm there are more stable points around "X".

The results obtained are primarily due to the thermal lens that we considered and to the astigmatism of this lens. The astigmatism of the thermal lens compensates the cavity in the sagittal and tangential planes and allows the cavity to be stable in points that would not be stable otherwise. Because we have not solved the heat equation for the astigmatic pump beam, our thermal GRIN coefficient might not be the best approximation possible, however some laser designers include a small tilt in the lens that focus the pump in order to compensate the astigmatism of the output beam [92].
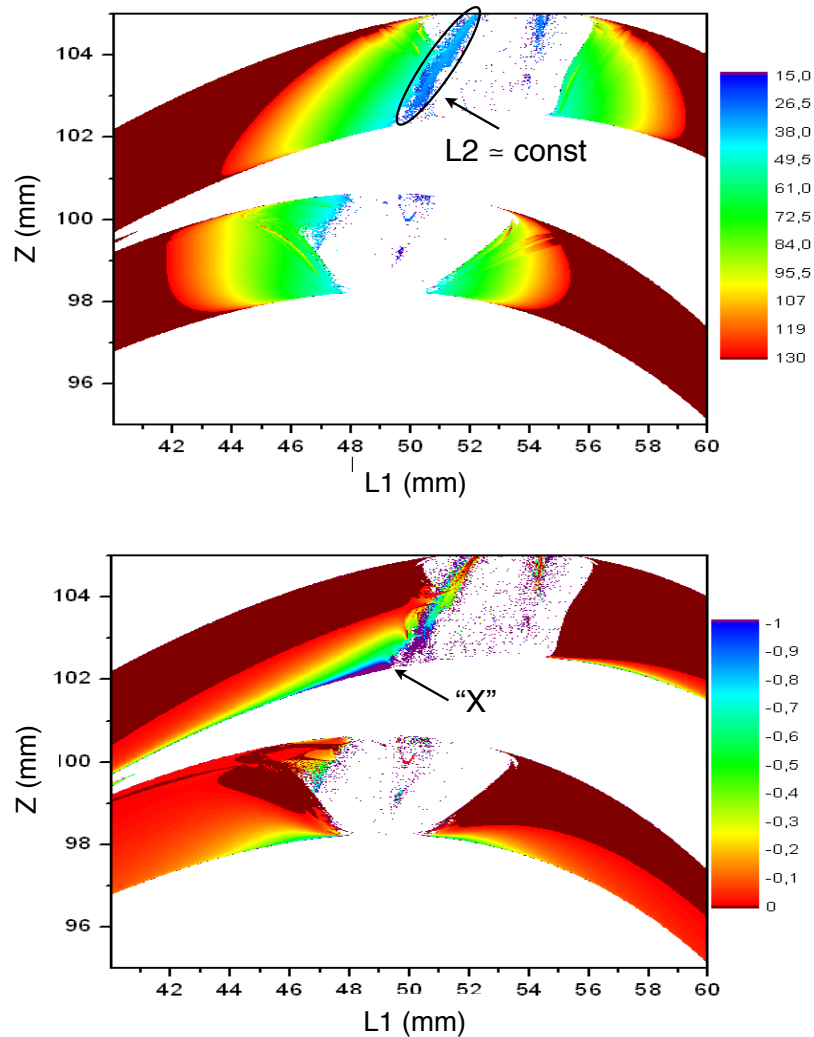
Figure 2.18.: (Top) ML beam size (in μm) as a function of the sub-cavity dimensions (in *mm*); (Bottom) the ML parameter as given by Eq. (2.34).

Constant pump size in the cavity

Here we consider that there is a thermal lens. However it is not the thermal lens that is constant, but the pump spot size. A pump spot size of $53\,\mu m$ is considered. The model for the thermal lens is given in the previous sub-subsection, in this model the thermal GRIN coefficient varies with the

2. Study of optical amplification

spot size of the intracavity laser, please note that this dependence exists only because, the aberration minimizing focal length depends on the spot size of the laser itself. According to this, the changes in the thermal focal length are not dependent on a thermal adaptation but only on the spot size. For this reason, we can include this thermal lens in the cavity and in the search algorithm without any loss in generality. In the previous paragraphs, only the Kerr component of the GRIN coefficient was adapted, here the thermal lens is also going to be adapted to the change in spot size.
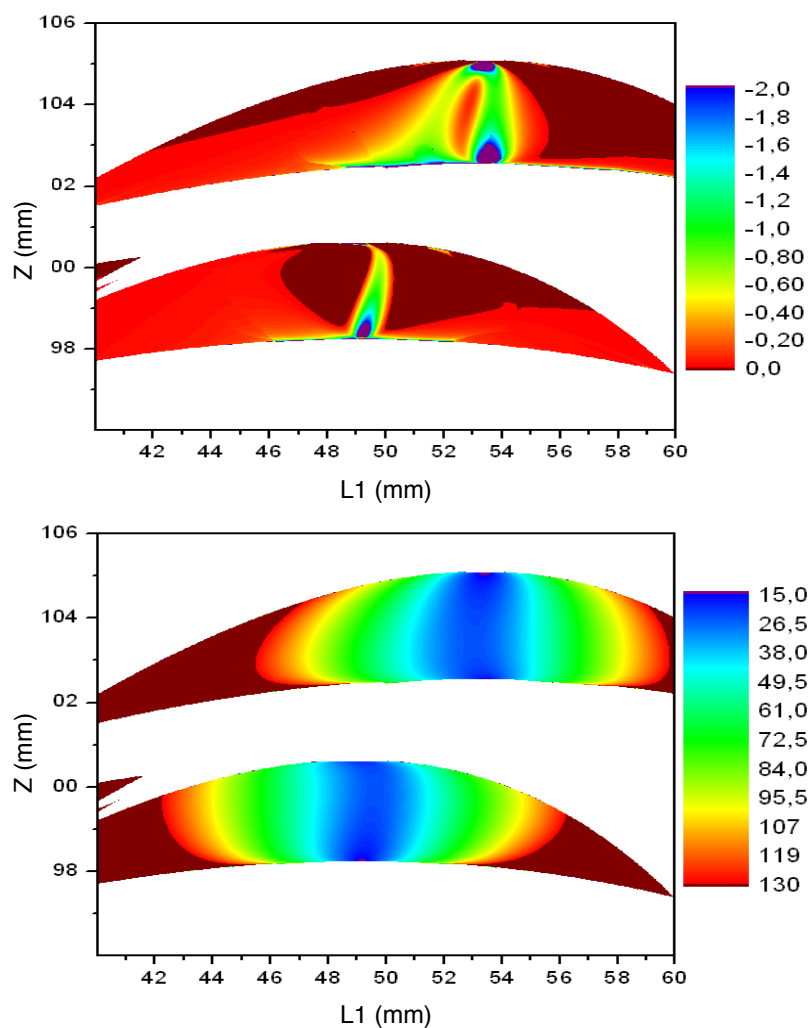
Figure 2.19.: (Bottom) CW beam size (in μm) as a function of the sub-cavity dimensions (in *mm*); (Top) the ML parameter at zero power (MW^{-1}).

We compute the results for a CW laser, and then calculate the ML parameter at zero power. With this we obtain Fig. (2.19). Here, we see that the introduction of a variable thermal lens creates some differences in the cavity stability profile. We find however the same specific point that is ideal for ML and that we had already seen in Fig. (2.16).

In further simulations, we concluded that if the pump spot size would have been smaller, thermal lens

model would influence the ideal ML sub-cavity configuration. In fact, we see that the contribution for the mode locking process may be due not only to the Kerr lens, but there might be some contribution of the thermal lens variation with the spot size of the beam, but only if the pump size would be smaller than $10\,\mu m$.
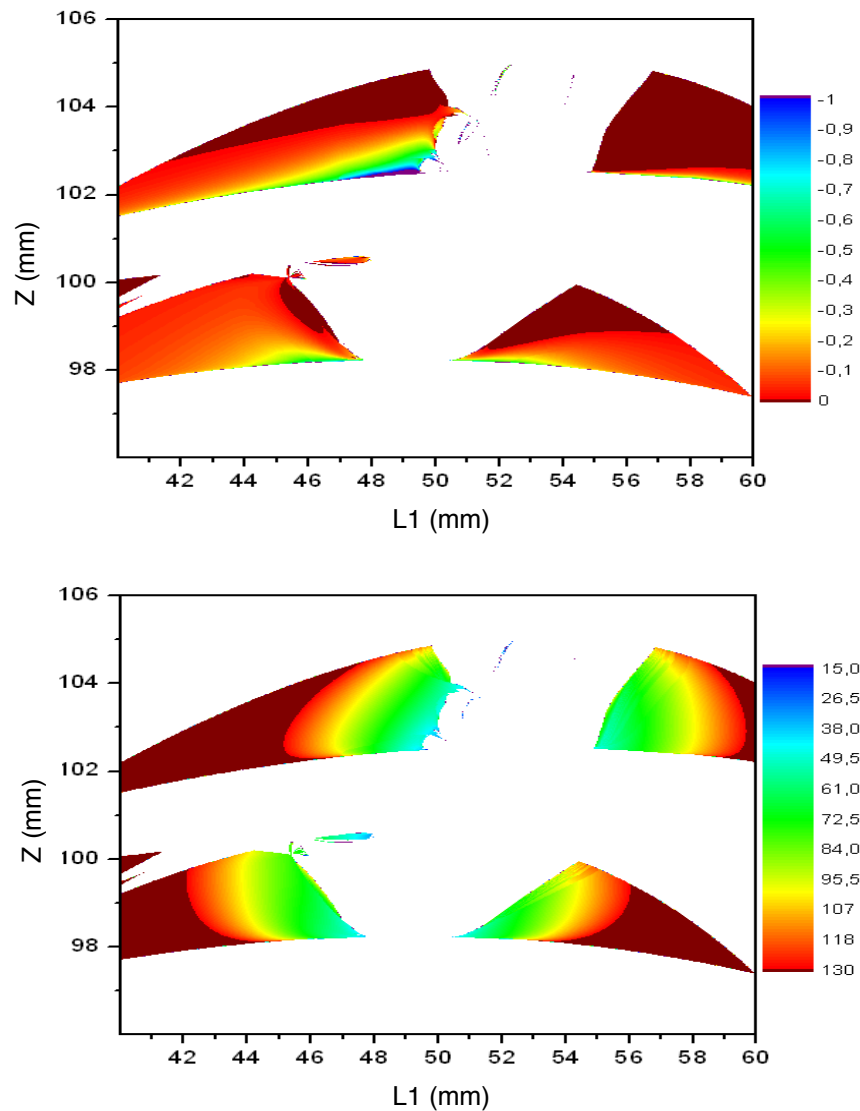
Figure 2.20.: (Bottom) ML beam size (in μm) as a function of the sub-cavity dimensions (in *mm*); (Top) the ML parameter.

We calculated the spot size in a ML configuration according the algorithms of Fig. (2.9) and Fig. (2.14) and obtained the results presented in Fig. (2.20) and in Fig. (2.21) correspondingly. From Figs. (2.20) and (2.21) it is evident that the search algorithm, or the path between CW and ML regimes, is important. As we had seen before, there are distinct differences between the ML parameter obtained by the two search algorithms.

If we compare Fig. (2.20) with Fig. (2.17), we may see that ML ideal point of operation is similar in both cases and that a thermal lens with such a big focal length does not affect the ideal point for ML. In other words, we find that, in this case, the ML ideal region does not depend on the aberration of the thermal lens (or a size miss match between the pump and the resonant beam).
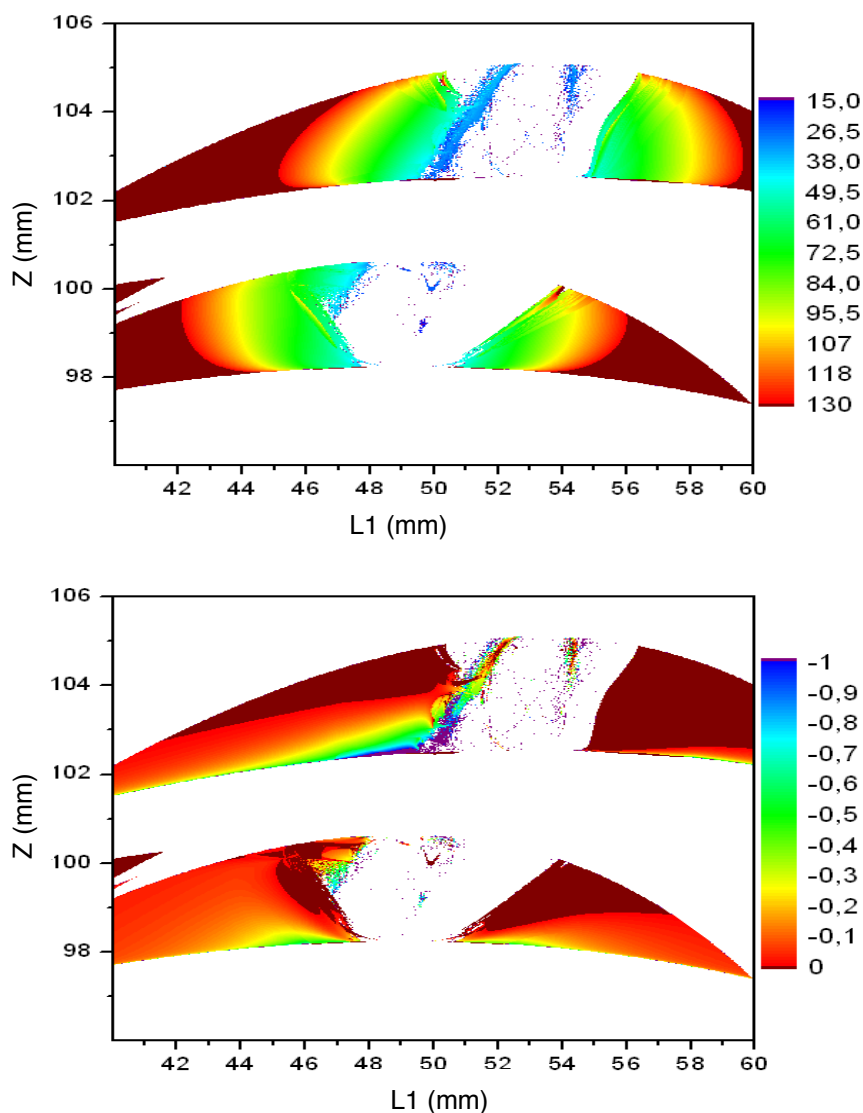
Figure 2.21.: (Top) ML beam size (in *µm*) as a function of the sub-cavity dimensions (in *mm*); (Bottom) the ML parameter.

One of the approximations of these calculations is to consider that the ML beam power is constant for all sub-cavity configurations, which means that both the output energy and the duration of the pulse are considered to be constant (this is intrinsic on our algorithms because we do not calculate neither the temporal pulse evolution nor the gain in the resonator). In order to evaluate the effect of this approximation, we redid the calculations using a longer pulse with $100\,fs$. The calculation were

done with the algorithm of Fig. (2.9) and with the algorithm of Fig. (2.14). The results are presented in Fig. (2.22). Here we see that for a configuration where the pulse intensity is smaller the conditions for ML are easier to achieve because the focal length of the Kerr lens is bigger. Such a configuration could be achieved by managing the dispersion over a small spectral bandwidth. We may say that, for a small spectral bandwidth the conditions for a ML operation are not so strict. In fact we see that, with the second algorithm, the gap between the left and right side of the second stability zone almost closes.
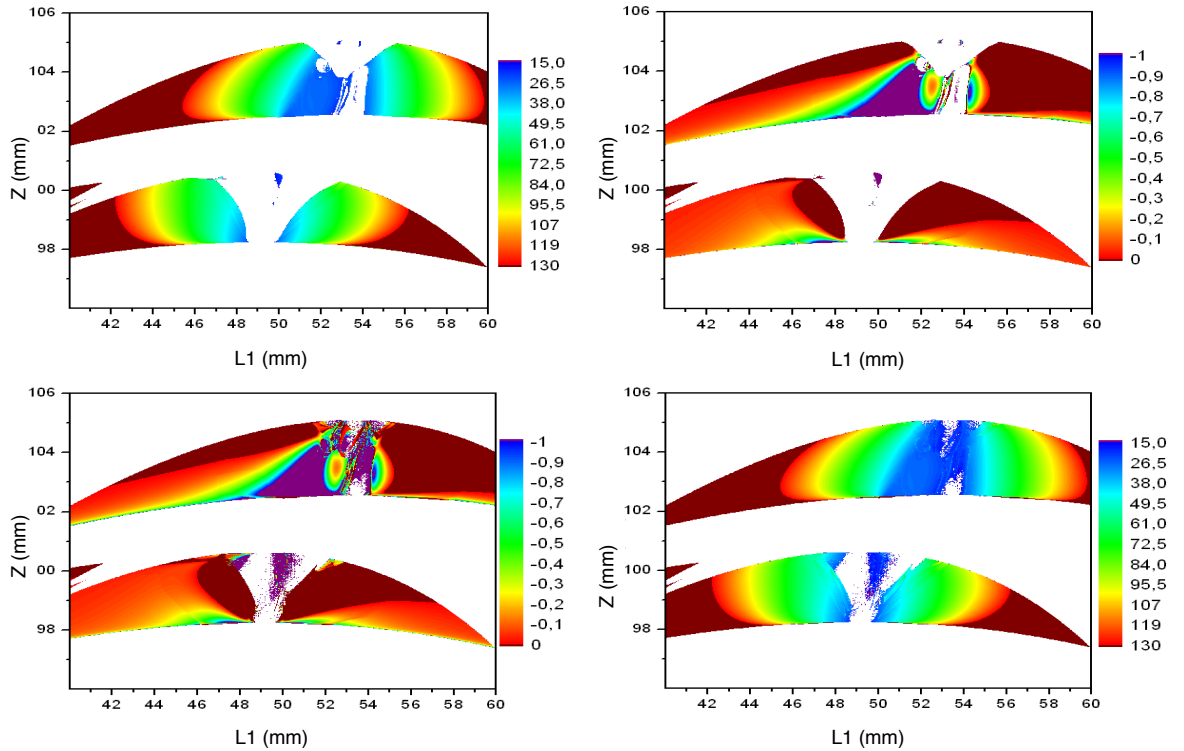
Figure 2.22.: (Bottom) ML beam size (in μm) as a function of the sub-cavity dimensions (in *mm*); (Top) the ML parameter of Eq. (2.34). On the left, the results are obtained using the algorithm of Fig. (2.9), and on the right the algorithm of Fig. (2.14). We maintained the color-scale of the ML parameter to facilitate the comparison with Figs. (2.20) and (2.21).

Adaptable pump size in the cavity

We have refereed above that the ML intrinsic mechanism does not affect the pump mode directly. However when we are aligning the laser, we tend to optimize the power output of the laser by changing the position of the lens that focus the pump in the gain medium. In reality part of what we are doing is a match between the pump and beam sizes, which will assure a homogeneous gain throughout the crystal. We try to simulate this effect by adapting the pump size to the beam size. As we did in the previous approaches, we treat the CW mode first, adapting the spot size of the pump and the CW mode, only afterwards we considered a ML configuration. We do not adapt the pump

mode to the ML mode, the reason for this will be explained later on.

In an initial attempt to match the CW beam and the pump, we inspired ourselves in the algorithm of Fig. (2.9). We used the recursive algorithm that is exposed in Fig. (2.23). For each (L_1, z) point, we start with a certain pump spot size ($200 \, \mu m$) and calculate the GRIN thermal coefficient and the ABCD matrix. From this we calculate the beam size and equal the pump size to the beam spot size. We recalculate the GRIN thermal coefficient and again equal the spot size inside the crystal to the pump spot size, and so on.

In our case the algorithm fails to converge to a certain spot size at every (L_1, z) point, at every point the cycle resulted in a cavity with a non-stable configuration. This means that, if we attempt to do the same with a ML lens inside the cavity we would have a convergency to a non-stable configuration, and that is why we do not adapt the size of the pump in a ML configuration.
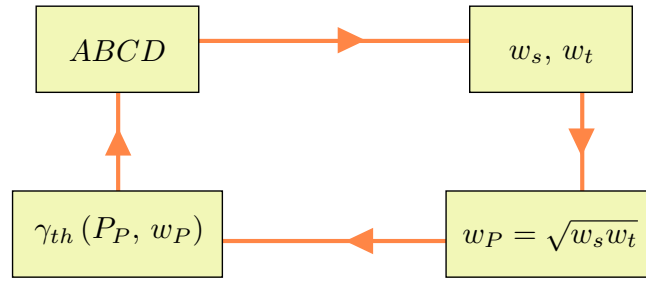
Figure 2.23.: First algorithm tried to obtain a match of spot sizes between the laser and the pump beam.

After this attempt, we decided to follow another approach, based on the fact that it is reasonable to assume that the pump spot size in the crystal is less than $132 \, \mu m$ (effective spot size, sagittal spot size $100 \mu m$), because bigger spot sizes (with a $3 \, W$ pump) do not allow population inversion. So, for every sub-cavity configuration (L_1, z), we did a sweep of the pump beam size (100 points), and for every pump spot size we calculated the beam spot size. We then calculated the difference between the two using Eq. (2.35). In here we consider a thermal GRIN coefficient of Eq. (2.29), considering however that the spot sizes were matched.

$$\delta w = 2 \frac{w_P - \sqrt{w_s w t}}{w_P + \sqrt{w_s w t}} \tag{2.35}$$

We memorized the pump size and the correspondent beam spot size that minimized δw. We take this spot size to be the spot size in a CW configuration. As we did previously, the ML parameter of Eq. (2.33) is calculated using an infinitesimal Kerr lens (we use Eq. (2.30) but with a laser peak power 10^{-10} of the actual laser peak power). The results are presented in Fig. (2.24).

Please note that there seams to exist four stability zones connected to each other. From Fig. (2.24) (c) we can also see that the agreement between pump sizes is obtained only in a limited zone (the

green zone), the zones that are not purple are defined by $|\delta w| < 50\%$. In fact this means that the CW operation in this laser is only possible while the pump/beam size remains bigger than the "guessed" $53\,\mu m$ (considering the pump power and absorption coefficients that we establish here). The two zones where the size agreement seams possible are coincident with the two zones studied in the previous sections.

In the other zones we obtain stability because the thermal lens bends the stability zones but the resulting beam spot sizes are not coincident with the pump spot size, this is a characteristic of this specific laser, in the laser presented in [106] this is not so.

In Fig. (2.24) (d) the ML parameter, that seams to enable ML operation is placed in regions where the pump size is substantially smaller than the beam size, and on the edge of the stability zone. Notice that this is in a zone implies a strong thermal lens, so we may see a favorable effect if an oscillator allows a strong thermal lens, which implies a smaller beam size in the cavity.
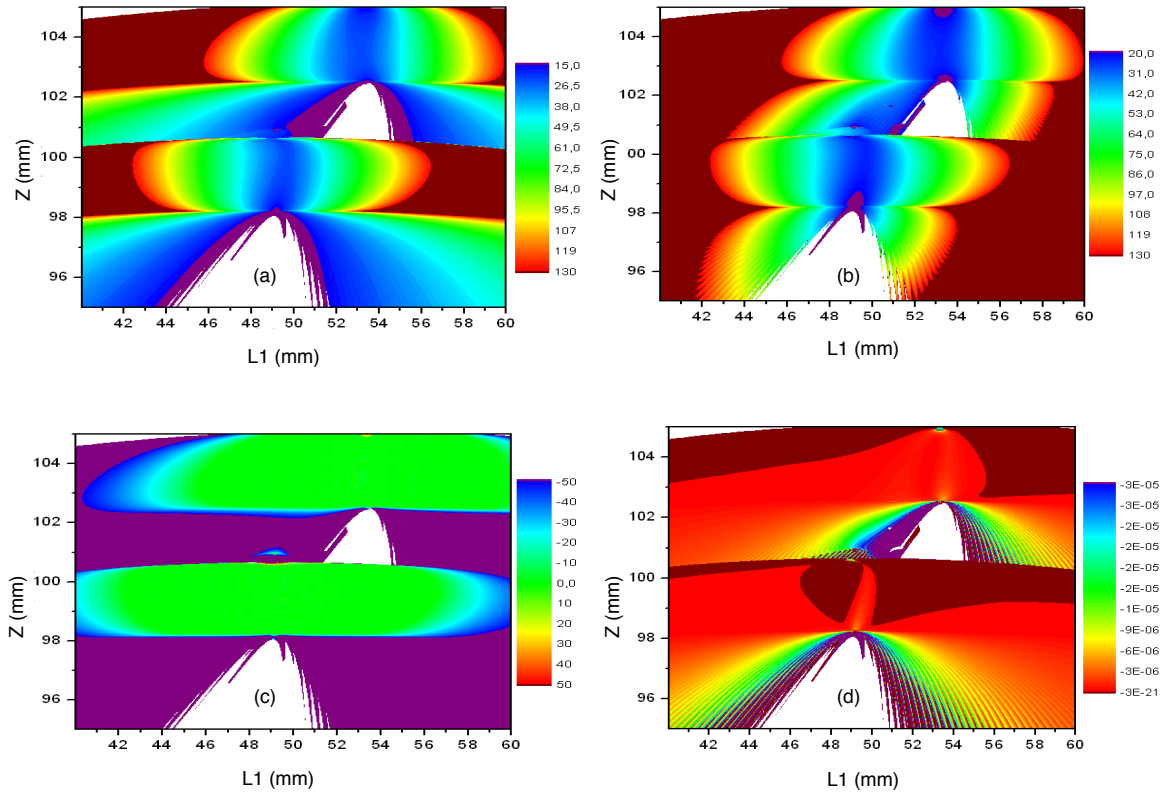
Figure 2.24.: Results of the algorithm that adapts the pump size to the spot size. (a) pump spot size, in μm; (b) the CW mode spot size, in μm; (c) the difference between the two using δw, in percentage (zero means there is no difference); (d) the ML parameter as given by Eq. (2.33) in W^{-1}.

We use both algorithms (Figs. (2.9) and (2.14)) to calculate the mode in a ML configuration, from this we calculated the ML parameter in both cases. The results can be seen in Fig. (2.25).

2. Study of optical amplification

In Fig. (2.25) the zones where the pump size does not fit the beam mode size are not stable. The results are similar to the results we had when the pump size was not adapted. In Fig. (2.25) (a) and (b) we see once again, that the algorithm presented in Fig. (2.9) does not find a stable ML configuration in the sub-cavity configuration where the spot size is smaller, and also as we have seen before this algorithm that seems to mimic the ML process does not find a stable configuration where the second algorithm we present does.
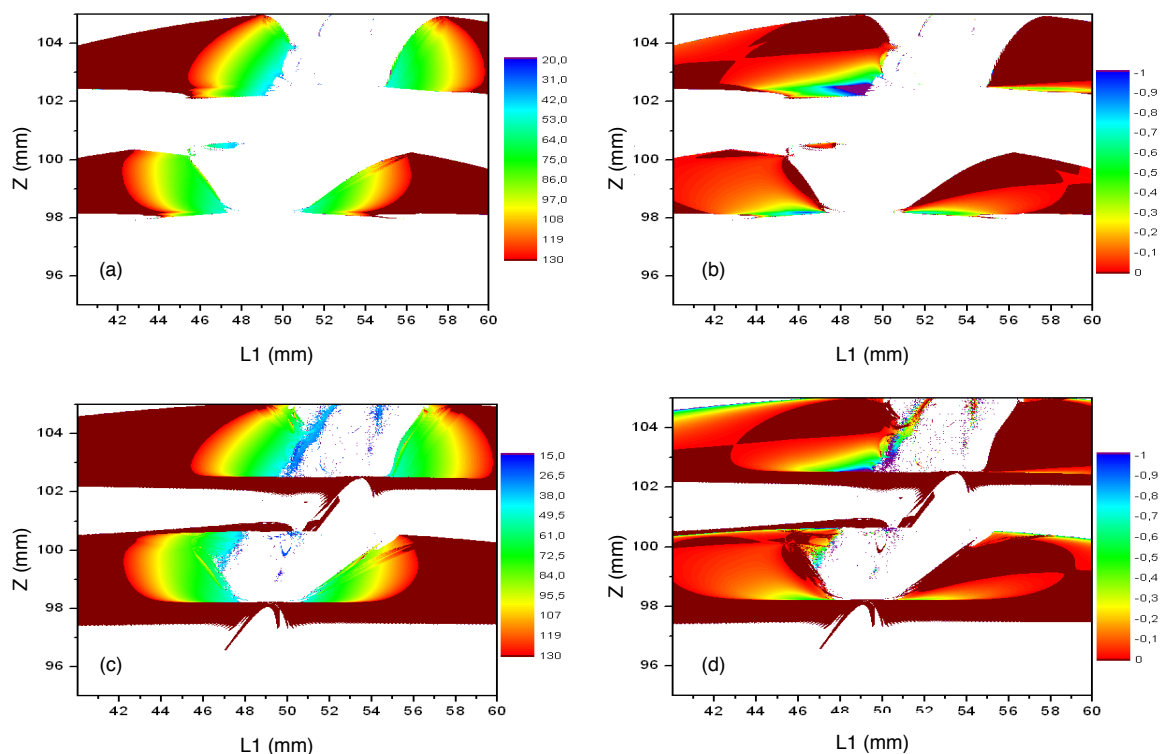
Figure 2.25.: ML using an adaptable pump size. (a) ML spot size (μm) and (b) ML parameter as calculated by the algorithm in Fig. (2.9); (c) ML spot size (μm) and (d) ML parameter as calculated by the algorithm in Fig. (2.14).

It is important to point out the difference between the actual ML mechanism and the first presented algorithm, in an actual laser the laser peak power increases with the decrease in duration and mode adaptation, in our algorithm the Kerr lens is introduced with a constant laser power. In Fig. (2.25) (c) and (d) we present the results of the ML operation using the second algorithm of Fig. (2.14).

It is clear that this algorithm finds stability where the other algorithm does not, a negative ML parameter is found in a region with a reduced spot, however it is clear that in this region there are only isolated points of stability. We then tried different algorithms to retrieve the ML laser configuration, we evolved the laser power step by step (200 steps linear scale), and memorized the last stable configuration as we increase the laser power, for this calculation we started the laser beam size as the CW beam size. The results from this calculation are presented in Fig. (2.26).
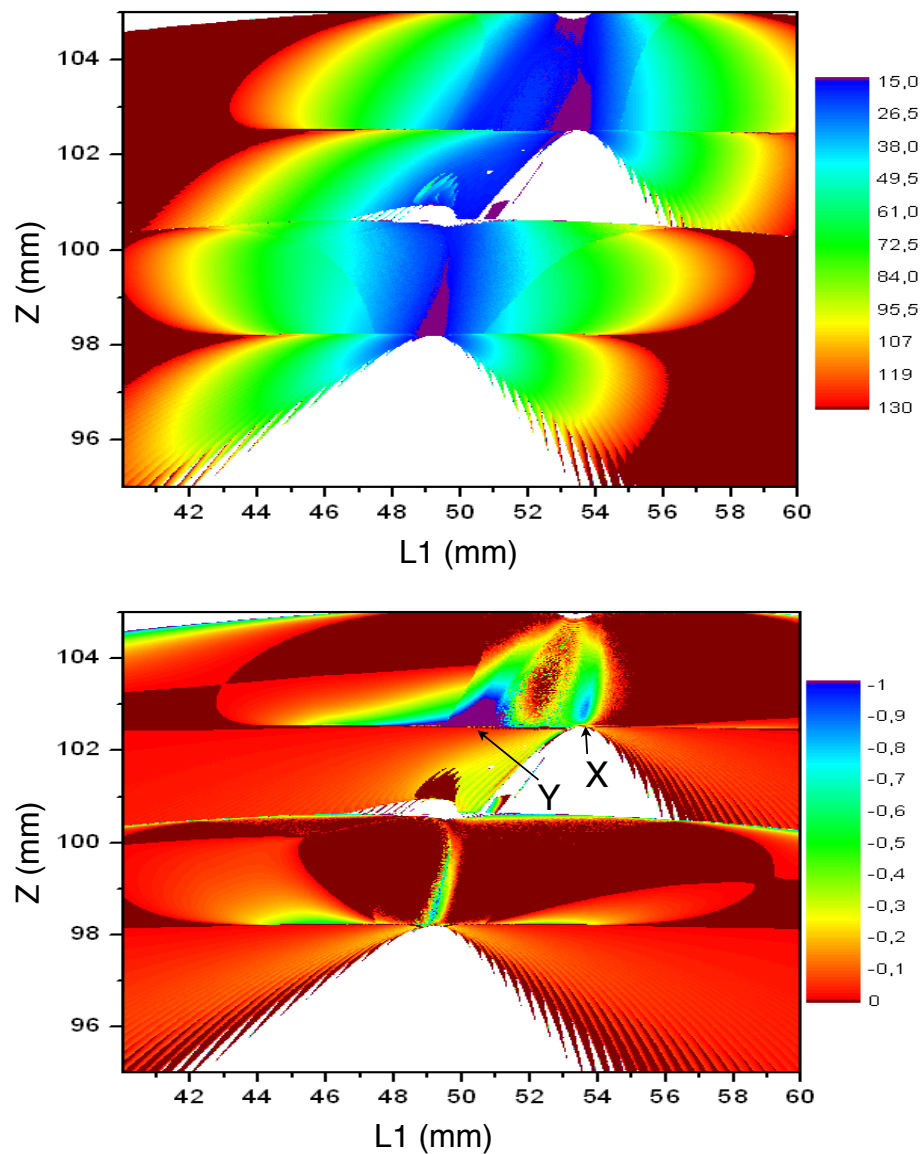
Figure 2.26.: ML using an adaptable pump size and an ever increasing cavity intensity. (Top) ML spot size
(μm) and (Bottom) ML parameter.

From Fig. (2.26), we see that considering a slow evolution of the laser power until the cavity is no
longer stable gives us the region that is best suited for ML (marked with a "Y"). This region is near
the "X" region that we saw in other models. In fact, the "Y" region can already be perceived in the
previous models, but not so marked as in this one. This result is important because in the previous
models we considered the laser power to be the same for every region and this is simply not the case
in an actual laser oscillator.

We developed another model in which, the intracavity power was increased exponentially. We used
10 points one order of magnitude apart from each other up until the actual intracavity power, however

at each increase in power, we applied the algorithm of Fig. (2.14), searching at each point a stable ML configuration. The results are presented in Fig. (2.27).
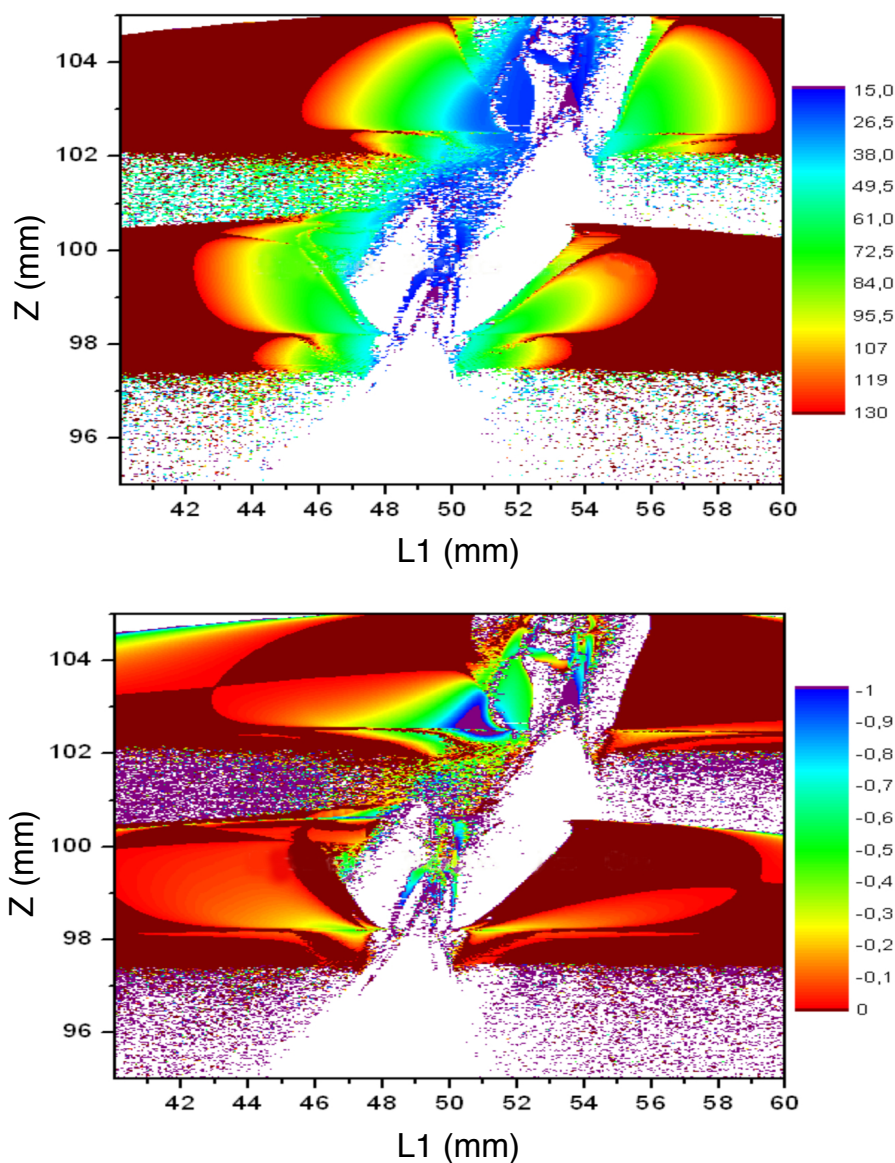
Figure 2.27.: ML using an adaptable pump size, evolving the intracavity power and at the same time using a beam size search algorithm. (Top) ML spot size (μm) and (Bottom) ML parameter.

From Fig. (2.27) we see the regions that favor ML can be presented where the size of the beam is small but that this is not done in a continuum of points but it is highly sensitive to the position itself. We tried one last algorithm that reproduced the experimental results of [106], and that gives similar results to the ones presented in Fig. (2.27).

We considered the algorithm of Fig. (2.14) but only one loop for every point. The results from this algorithm are very similar to the results obtained in Fig. (2.27) even if we have no physical

explanation that exposes the close relation between them.
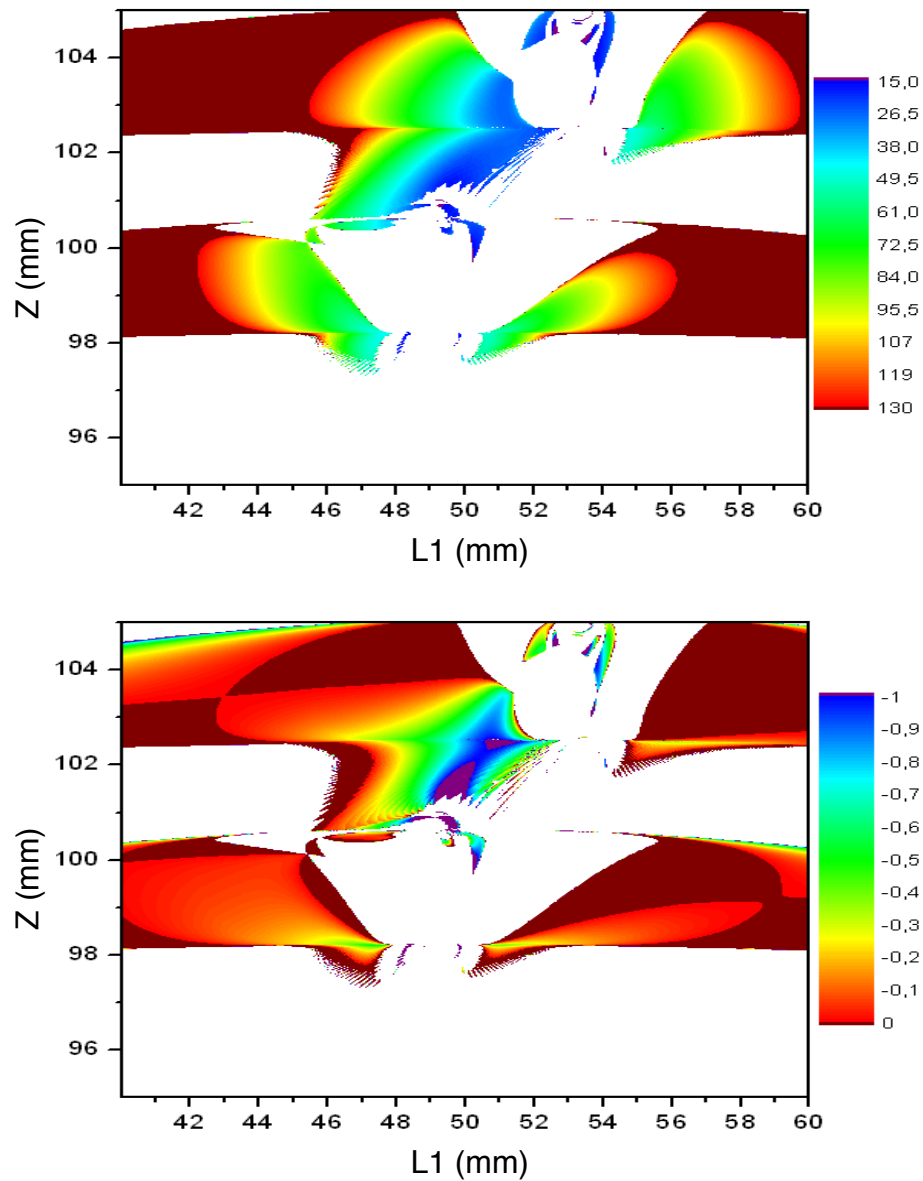
Figure 2.28.: ML using an adaptable pump size, and one loop of the algorithm in Fig. (2.14). (Top) ML spot size (μm) and (Bottom) ML parameter.

2.3.5. Mode-locking beyond the expected parameters

In the experimental setup we obtained mode-locking on the lower edge of the second stability region. This is to be expected, however we also obtained ML not only for the smallest length of the stability region (position R1) but also after the maximum of stability, more specifically in the position R2 that may be seen in Fig. (2.29).
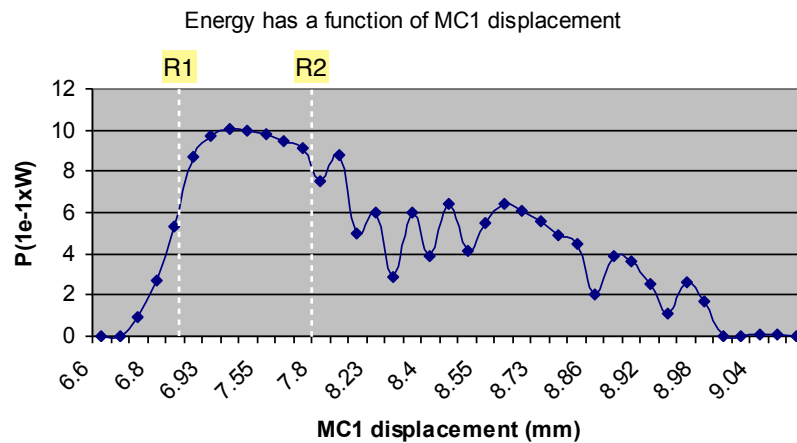
Figure 2.29.: Laser oscillator output power as a function of the sub-cavity position. The positions R1 and R2 are two positions where the ML occurred.

2.4. Sub-6 fs ultrafast mode-locked laser

Here we make a brief description of a Sub-6 fs ultrafast mode-locked laser (4.8 fs Fourier limited). We used this oscillator to calibrate the model we obtained. Our objective is to compare both oscillators and clearly state what changes from one case to the next.
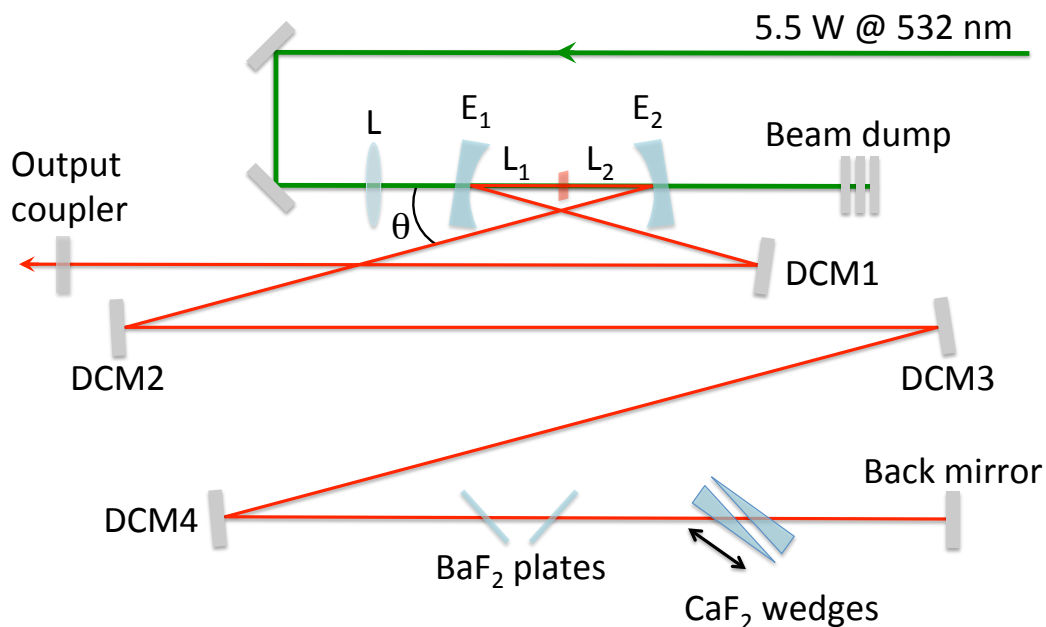
Figure 2.30.: Cavity of sub-6 fs oscillator, DCM1, DCM2, DCM3, DCM4 are chirped mirrors, θ is the folding angle, L1 and L2 are the distances of the sub-cavity.

This oscillator is designed to have a smaller pulse duration. The dispersion compensation is made over a larger spectrum and we use a smaller crystal ($L_c = 1.9\,mm$) in order to decrease the dispersion on the round trip of the cavity.

In order to compensate for a smaller crystal the Titanium doping is increased so that the absorption coefficient goes to $\alpha = 5 \pm 0.4\,cm^{-1}$ the pump power is also increased to $P_{pump} = 5.5W$. The average pulse duration inside the crystal is 18 fs (calculations are done using the same principles as before), the OC transmission is only 2%. The design of the cavity is given in Fig. (2.30).

The two concave mirrors in the sub-cavity have a focal length of $37.5\,mm$, the length of the bigger harm (between the E2 and the back mirror) is of $1315\,mm$, the length of the smallest arm (between E1 and the output coupler) is of $503\,mm$. The folding angle is set to 5.8°, we tried to match the beam on the sagittal and on the tangential plane, we use the same reasoning as in the last laser to obtain the ideal folding angle.

Apart from the Crystal and the doubled chirped mirrors (DCM) we also have two BaF2 plates and two CaF2 wedges, the wedges are assembled in a translation stage that allows us to finely tune the dispersion inside the cavity. The SPM effect in this case is such that the output spectrum can go from 650 nm to 1125 nm while the output coupler has a flat transmission from 605 nm to 925 nm.

In other words there is a part of the spectrum which half-life time in the cavity is smaller than the half-life time of the central part of the spectrum, which is only made possible due to the strong SPM inside the crystal that creates frequency components at each round-trip (see Fig. 2.31).
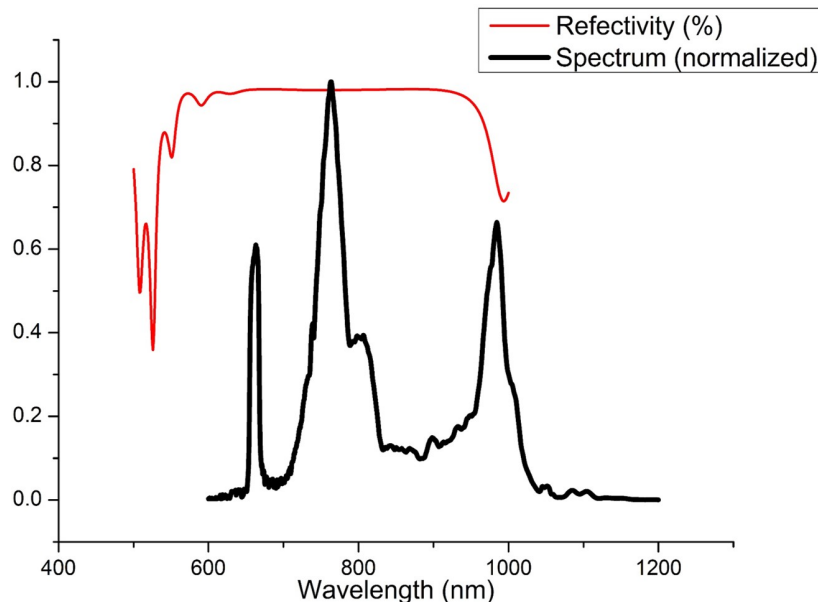
Figure 2.31.: Spectral intensity (black) at the output of the oscillator and reflectivity (red) of the output coupler.

2. Study of optical amplification

Let us first observe the ML parameter and the beam size without any thermal lens, as we referred before, without the thermal lens, there is no optical component that depends on the pump size. Using this we can observe the size of the beam without interference of the pump. We present the size of the CW beam, of the ML beam and of the ML parameter given by Eq. (2.34).

We recall that all the beam sizes presented here are beam sizes taken at the center of the crystal. The ML results are obtained using Fig. (2.9). The differences between this model and the model represented by Fig. (2.14), are qualitatively the same in the two lasers (if no thermal lens is used).
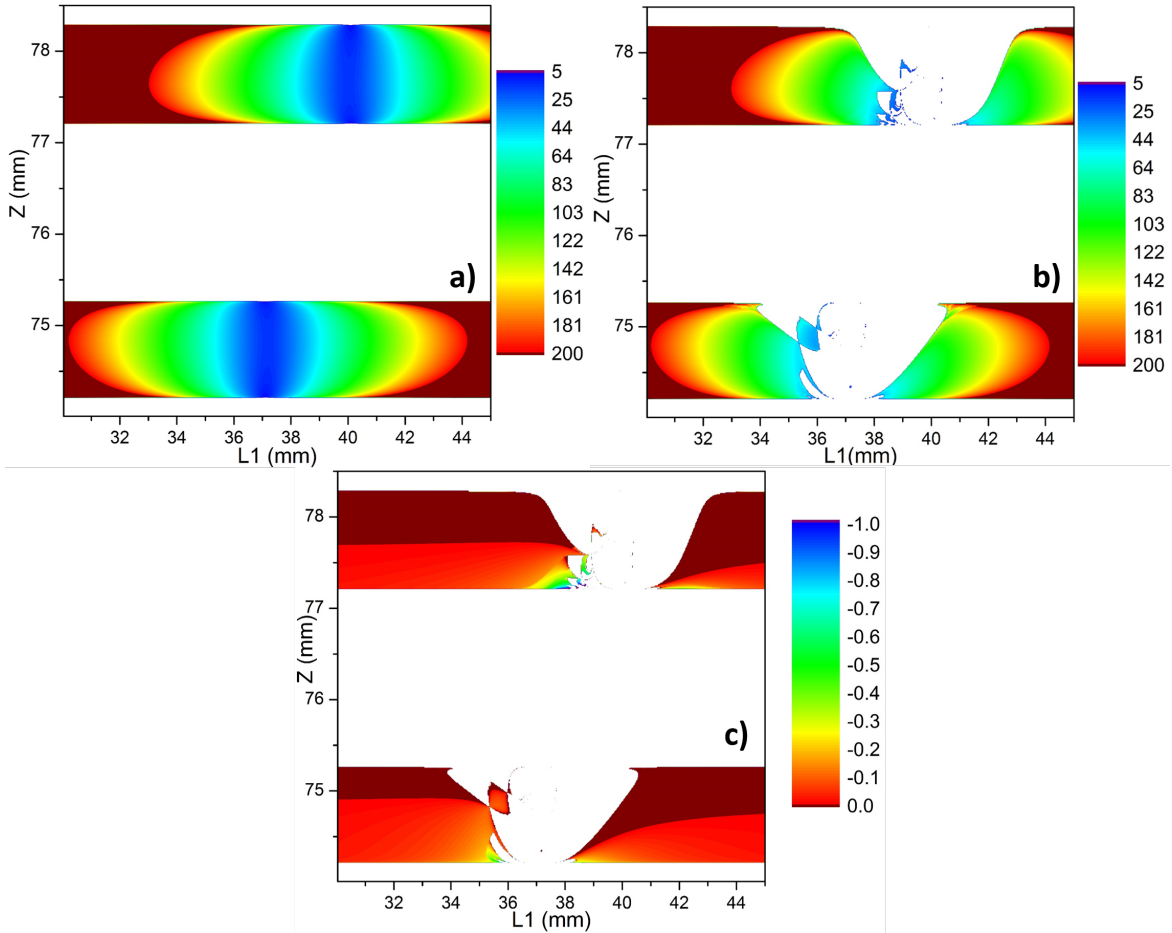
Figure 2.32.: a) CW beam size (μm), b) ML beam size (μm), c) ML parameter as given by Eq. (2.34). ML results obtained using the algorithm of Fig. (2.9).

Comparing Fig. (2.32) with Fig. (2.12) (consider the scale) we can clearly see that the size of the beam is smaller in this second oscillator, this means that the size of the pump will have to be smaller to match the size of the beam. This is obviously not a linear system, we have to apply the feedback mechanism of Fig. (2.23) in order to obtain the pump size that adapts itself to the CW mode, from there we determine the ML parameter as defined by Eq. (2.33). We present the results in Fig. (2.33).

We can clearly see that the zone where we have an agreement between both beams is now flexed

due to the bigger thermal lens created by the smaller pump size. We can clearly see that due to the thermal lens the stability zones are bent in such away that the second stability zone drops into the first stability zone, it is in the meeting between these two zones that we find the X point, which is also in a zone where we find agreement between both beam sizes.
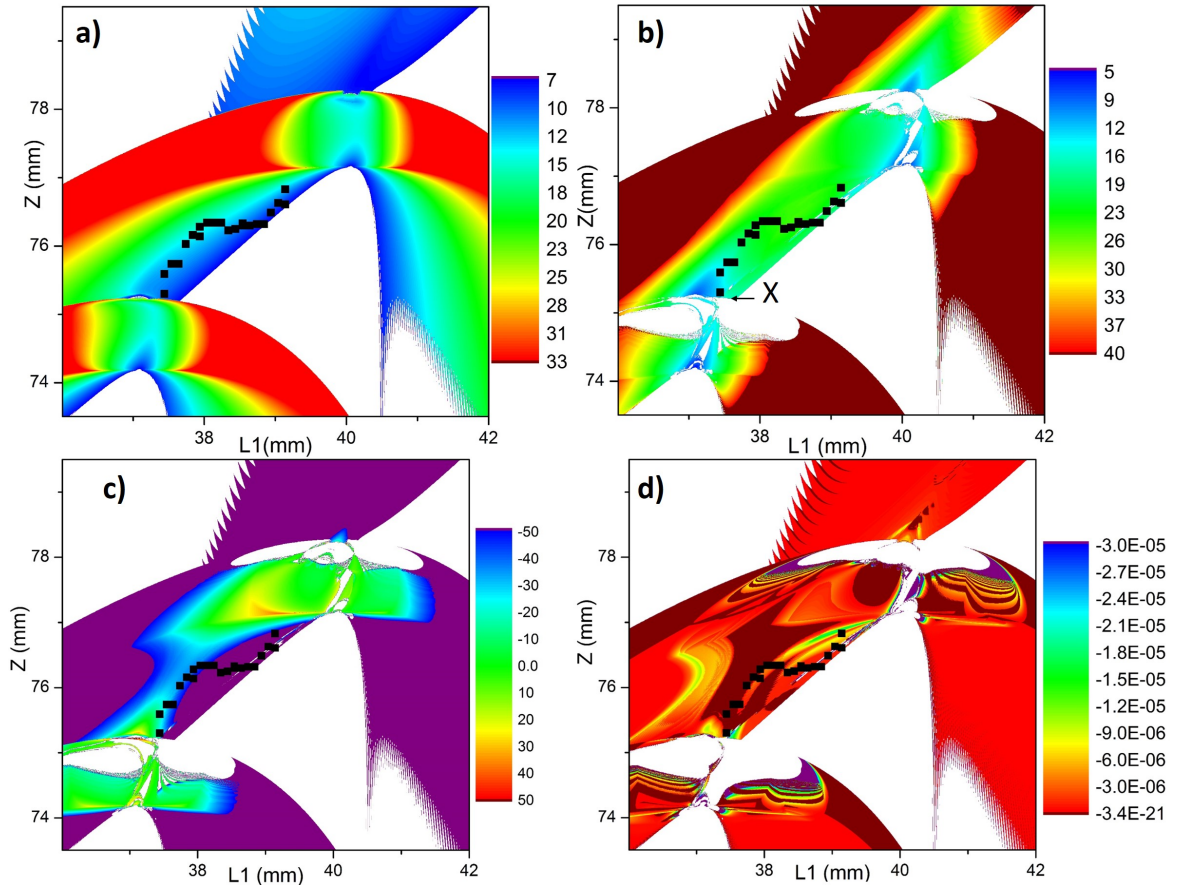
Figure 2.33.: Results of the algorithm that adapts the pump size to the spot size. (a) pump spot size, in μm; (b) the CW mode spot size, in μm; (c) the difference between the two using δw, in percentage (zero means there is no difference); (d) the ML parameter as given by Eq. (2.33) in W^{-1}. Experimental points are shown in black; the "X" refers to the point where the largest spectrum was found.

We apply the last algorithm we used with the first laser using the cycle of Fig. (2.14) only once to the CW laser (which stability profile was already obtained using an adaptive pump size that is given by the algorithm of Fig. 2.23) and obtain the results given by Fig. (2.34).
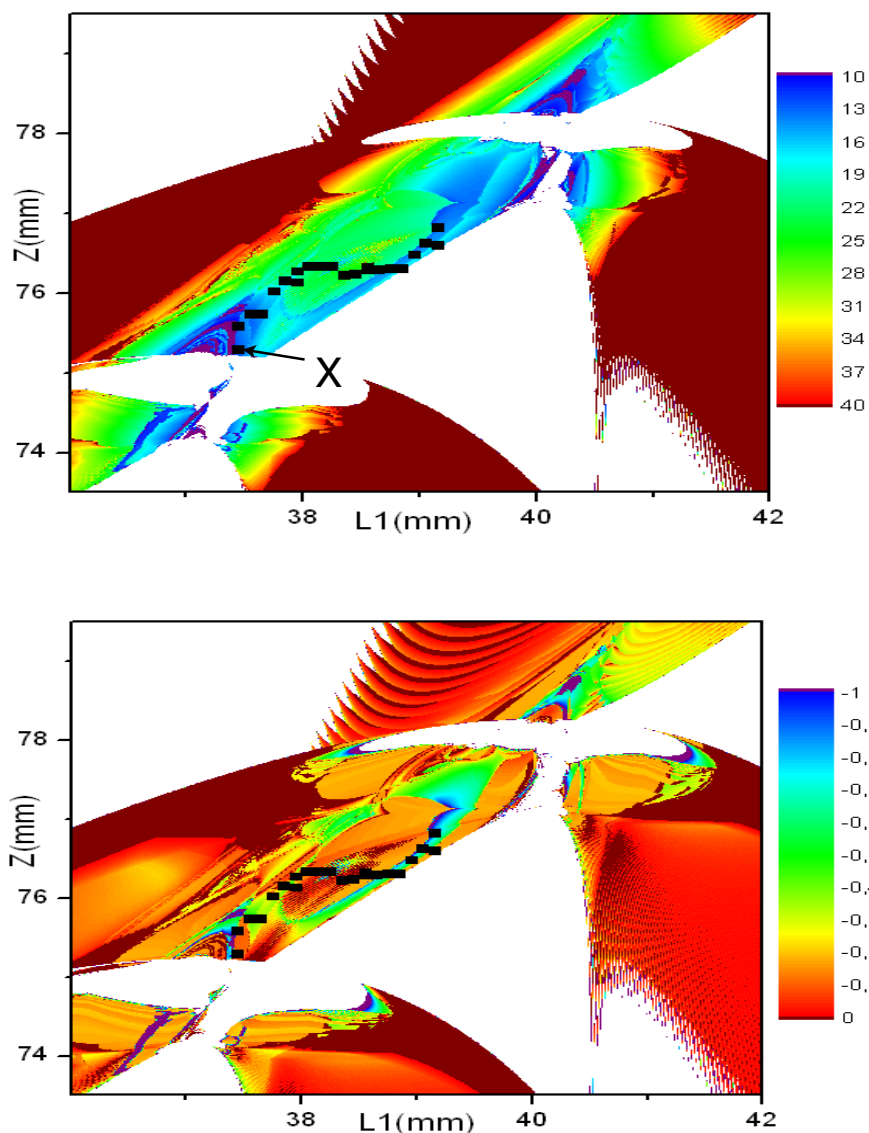
Figure 2.34.: ML using an adaptable pump size and a search mechanism that consisted of one loop of the algorithm presented in Fig. (2.14) for each point. (above) ML spot size (μm) and (below) ML parameter. Experimental points are shown in black; the "X" refers to the point where the largest spectrum was found.

The experimental points in the last two sets of figures are data points on a line in which ML operation was easy to find, the X point marks the position where the shortest pulse could be obtained. It is easy to see that at this point corresponds to the smallest beam size inside the zones where ML is possible, both beams sizes are in agreement and the second stability zone finds the first stability zone, the first stability zone is not stable in this zone probably because the thermal lens is too big for the cavity to be stable.

This last oscillator is scheduled for publication [106].

2.5. CPA laser chain for OPCPA pump and seed

We have designed and implemented a CPA laser chain intended at serving a OPCPA system with a pump and a seed synchronized in time. After having some trials done on a similar system [70], we wanted to improve the concept. The general scheme and the main components are represented in Fig. (2.35).
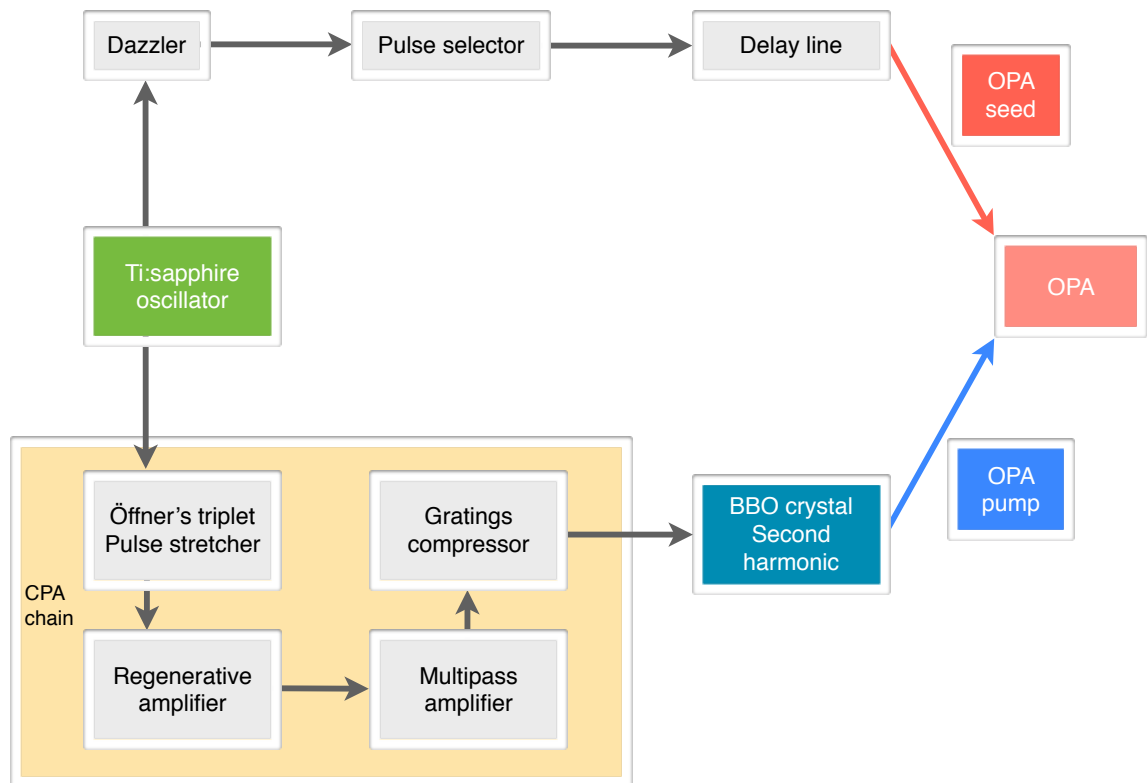
Figure 2.35.: General scheme of the OPA system. The output of a Ti:Sapphire oscillator is divided in two: the transmitted part is going to be selected and stretched to serve as a OPA seed, the reflected part is going to be amplified in a CPA chain and frequency doubled to serve as the OPA pump.

In theory, the advantage of having the pump and the seed originated from the same oscillator would be a perfect time synchronization. However the beam path through the CPA laser chain (and probably thermal fluctuations) has resulted in too many fluctuations so the wave mixing was unstable and no viable characterization of the OPA could be done. Giving this, we will only expose the characteristics of the CPA laser chain. Due to the CPA chain characteristics, a *Fastlite* acousto-optic programmable dispersive filter was used to stretch the pulse, afterwards a pulse selection by two polarizers and a Pockels cell and a delay line were added in order to allow temporal synchronization and to avoid the secondary pulses. These secondary pulses leaked from the regenerative amplifier, they passed through the optics of the stretcher and are back reflected into the seed of the OPA by the oscillator mirrors. Due to the 10^7 gain of the regenerative amplifier, the leaked pulses that pass through all this

optics are more intense than the seed pulse itself. In order to avoid this, we introduce the delay line, the length of this delay line is roughly equivalent to 5 round trips in the cavity.

This OPA will be a quasi degenerate OPA because the central wavelength is not maintained in the CPA chain. The characteristic SH efficiency is approximately 37%. We used a 5 mm thick BBO crystal in a type I phase-matching configuration. We did not improve the results obtained by Renault et al. [70] and so we do not present any OPA results.

Due to the results obtained by Renault et al. [70], the CPA chain was designed to have a small spectral bandwidth at the output. Two things are important, that we have a flexible central wavelength in order to avoid a degenerate wave mixing and a small spectral width. It is well known that the chirp of both waves will influence the OPA process, and that there is a perfect chirp relation which maintains a small phase mismatch throughout the wave-mixing. Here we try to have a narrow spectral profile, not to improve the efficiency of the wave mixing but to improve the stability of the process. In order to achieve this goal, we use a spectral selective regenerative amplifier. In reality we used a set of prisms inside the cavity that allow us to select the part of the spectrum to be analyzed. Other authors also used a spectral filter inside a regenerative amplifier [138]. This was also used in the pump of a OPCPA scheme, the objective in this case was to improve the contrast of the pulse, by filtering the pump pulse [139], this group used a volume Bragg grating to filter the pump inside its regenerative cavity.

2.5.1. Öffner triplet stretcher and holographic diffraction grating compressor

The dispersion of the CPA chain is going to be controlled by a Öffner triplet [140] at the beginning of the chain and by a holographic diffraction grating compressor [50] at the end of the chain.

Because this is a CPA chain and because we are trying to amplify a pulse with a $1\,nm$ spectrum, it is difficult to stretch the pulse. Then it is difficult to avoid a high B integral or damage threshold intensities. Please remember that CPA is based on highly chirped pulses and so if we expand Eq. (D.6) for pulses with high values of chirp, we will get a linear proportionality between the pulse duration and spectral width[6]. In order to address this problem, we use holographic gratings. These gratings allow a high groove density of $2200\,{}^{lines}\!/_{mm}$.

The stretcher as two curved mirrors and a holographic grating, a detailed description of the device can be found in [141]. The concave mirror as a curvature ray of $1000\,mm$ and the convex mirror half that value. This results in an introduced chirp of $2.3 \times 10^7\,fs^2$. For a spectrum of 15 nm this means that the pulse will be on the ns scale, however for a 1 nm pulse this means that the pulse has less than

---

[6]For a highly chirped pulse with a quadratic spectral phase and with a spectral bandwidth of $\Delta\omega$, the pulse duration $\Delta\tau$ is given by:

$$\Delta\tau \sim chirp \times \Delta\omega. \tag{2.36}$$

100 ps. A thorough discussion on the impact of this spectral narrowing in the damage threshold of the Pockets cell of the regenerative amplifier can be found in [70].

Due to the high groove density, the optics in the stretcher system cannot encompass the entire spectral bandwidth of the oscillator. In fact, by changing the angle of incidence in the holographic grating, we can select the spectrum at the output of the stretcher.

The compressor has two parallel holographic diffraction gratings [142] with the same number of grooves as the stretcher compressor. The gratings are placed roughly 90 cm away from each other. An intensity autocorrelator was used at the output of the compressor, in order to minimize the duration of the pulse by adjusting the compressor. The compressor has a overall efficiency of 50%.

2.5.2. Millijoule regenerative amplifier with spectral filter

The trials done by Renault et al. [70] demonstrated that it was important to decrease the spectral width of the pump pulse used in the OPCPA. There are several ways to do this. Renault used a slit in the pulse stretcher after the oscillator. We tried a different approach and used prisms in the regenerative amplifier cavity in order to obtain a shorter spectrum. This angularly dispersive component will allow us to select which spectral component is resonant in the cavity.
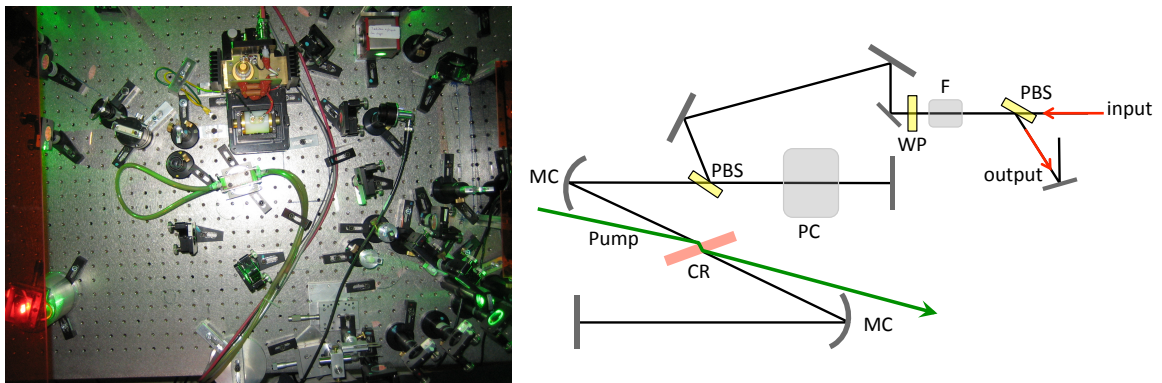
Figure 2.36.: Regenerative amplifier photo with two prisms inside (left) and a scheme of the cavity without prisms (right). PC - Pockels cell, PBS - polarization beam splitter, F - Faraday rotator, WP - half-wave plate, CR - crystal placed at the Brewster angle, MC - curved mirrors.

In a regenerative amplifier, the seed pulse is inputted into the cavity using a polarization based system. The seed pulse turns inside the cavity passing through the amplification medium that is a $20\,mm$ Ti:Sapphire crystal. At the output, we obtain a pulse amplified at the millijoule level. The crystal is placed at the Brewster angle in order to avoid losses. The pump laser is a Nd:YLF laser emitting at $527\,nm$ with a output energy of $8\,W$ at $1\,KHz$ ($8mJ/pulse$).

The polarization system that controls the input/output in the cavity is described here. It is helpful to

follow the description below using Fig. (2.36):

➤ Before the cavity itself, we have an optical isolator, that is composed by the following elements:

- a Polarization beam splitter, that reflects light with a vertical polarization and transmits light with a horizontal polarization;

- a Faraday rotator that rotates the incoming light 45° and the outgoing light by -45°;

- a half-wave plate that changes the polarization of light by 45°;

These elements will turn the polarization of a horizontally polarized beam at the way into the cavity making the polarization vertical. On the way out of the cavity the vertical polarization remains unchanged through the Faraday rotator plus the half-wave plate and is reflected by the polarization beam splitter.

➤ A polarization beam splitter makes the coupling between the input and the output beam. It will reflect the vertically polarized light and transmit the horizontally polarized light inside the amplification cavity.

➤ In order to trap the light inside the cavity the Pockels cell has two modes. In the open mode the Pockels cell will work as a quarter wave plate, it will turn the polarization to a circular state in one passage and to a horizontal state in the second passage. This horizontally polarized beam will be amplified within the cavity. In this configuration, the cavity is open because, if the cell does not change mode, the beam will be amplified by two passages in the Ti:Sapphire crystal before exiting.

➤ In order to close the cavity, the Pockels cell changes its mode and starts working as a half wave plate, this will allow the beam to be trapped inside the cavity. In one passage through the Pockels cell, the beam polarization shifts to vertical, in the second passage the beam polarization turns horizontal. The horizontally polarized beam stays in the cavity.

➤ In order to open the cavity again and let the pulse exit the cavity, the Pockels cell mode changes: it starts working as a quarter-wave plate.With a double passage thought the beam polarization becomes vertical.

➤ This vertically polarized beam will exit the cavity through the polarization beam splitter. It will pass through the half wave and the Faraday rotator, the polarization remains vertical and it will exit the optical isolator through the first polarization beam splitter.

Please notice that this opening and closing mechanism also selects the pulses to be amplified. The Pockels cell works at a kHz repetition rate and is coupled with the oscillator repetition rate. It works as a pulse selector decreasing the repetition rate from 89 MHz to approximately 1 kHz. In

other words, at each millisecond, the cavity will close, trapping the pulse inside during amplification and releasing it after 144 ns approximately (the round trip inside the regenerative amplifier cavity is approximately 12 ns).

The collimation of the beam in this oscillator is very important. In a standard regenerative amplifier the rear mirror is curved and the cavity is constituted only by three mirrors, two curved ones with the same focal length and a third plane mirror. It is near this third mirror that the Pockels cell and the polarization beam splitter are placed. In this zone of the cavity, the beam will be slightly collimated. This will help the coupling of the beam into the cavity. The fact that the beam is collimated will also assure that there is no damage to the Pockels cell. In our case we want to use prisms inside the cavity. In order to do this we need a collimated arm to implement the set of prisms, that's the reason why we have to have two collimated arms in the cavity, one for the Pockels cell and the other for the prisms set.

In order to do an ABCD analysis of the cavity, the biggest difficulty is to evaluate the thermal lens because of the pump radius. In order to do this, we proceeded similarly to what we did in the previous section. In order to obtain an adequate pump radius, we used the beam size inside the cavity and considered that the pump size was the beam size. First we considered no thermal lens. From this, we obtained the beam size inside the cavity. Using the formulas for the thermal lens that are given above, we calculated the thermal lens and inputted it into the cavity. We repeated the procedure several times, until the size of the beam inside the cavity converged. We were able to do this because the thermal lens effect in this cavity is small. The beam size converged around $207\,\mu m$ (sagittal plane) and the thermal lens around $33\,cm$. Experimentally the pump focal lens was moved in order to optimize the output energy.

In reality, the thermal lens will have a small effect on the stability of the cavity, on the beam size and on the collimation of the beams inside the cavity. Indeed, any thermal lens larger than 250 mm will have a very small effect on the cavity dynamics. We used $8\,W$ pump power, however as seen in Fig. (2.36), the pump is recycled using a folding mirror and a curved mirror, this allows the total pump intensity to be approximately $8.5\,W$.

PC	50 mm
PC cavity arm	510 mm
MC-CR (PC side)	338 mm
CR-MC (prism side)	332 mm
prism cavity arm	345 mm

Table 2.2.: Approximate dimensions of regenerative amplifier cavity.

We calculated the incidence angle in the curved mirrors using Eq. (2.18). The angle given was 7.6°, we used this angle in the experimental setting. The rest of the cavity approximate dimensions are given in Tab. (2.2). Please note that this setup was changed while we here optimizing the output

beam, and so the values are not exact values. The focal lens of the curved mirror is 250 mm.

Using the data above we calculate the beam size inside the cavity, the results are presented in Fig. (2.37), we use the commercial program *WinLase* in order to obtain results.
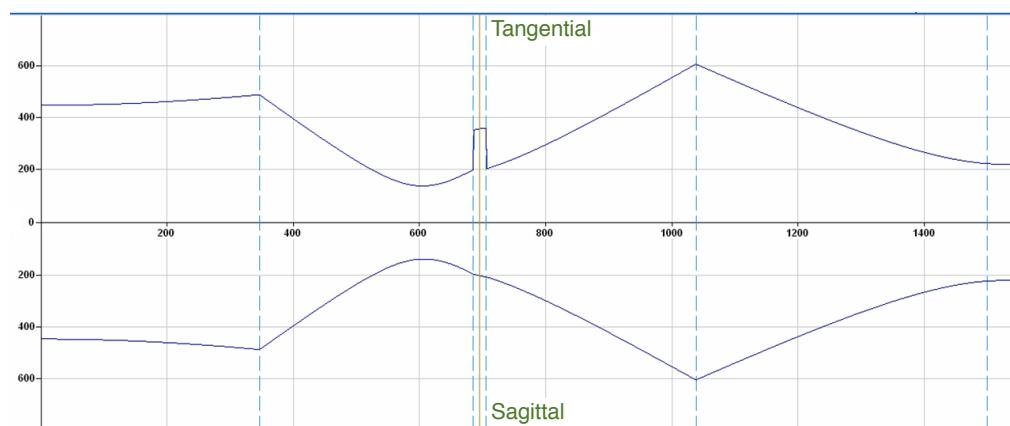
Figure 2.37.: Scheme of the size of the beam inside the regenerative amplifier cavity, with values given in *μm*.

Of course when compared to the oscillator cavity, the stability of this cavity is not crucial. In reality the seed pulse only turns in the cavity 10-14 times. The back mirror intensity and the output beam are represented in Fig. (2.38). This results were gathered with the smallest spectral width.
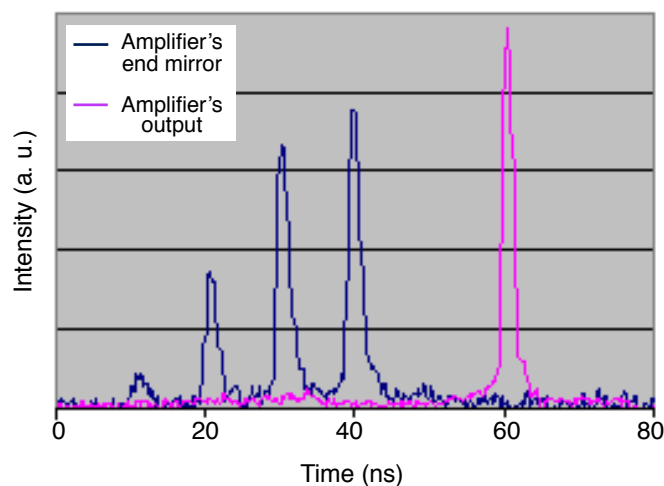
Figure 2.38.: Amplification inside the cavity. The amplifier's end mirror measurement and the output pulse measured by a *Thorlabs* photodiode.

We now analyze the spectral features of this amplifier. It is well known that CPA can originate spectral narrowing, this is actually true for wide spectral shapes because of the gain spectral profile, however for very thin spectral shapes, saturation might enlarge the spectral bandwidth of the

amplified pulse. As we have seen in the previous subsection, the Öffner triplet stretcher can be used to select a part of the spectrum, the exit of the stretcher has approximately 15nm FWHM. The regenerative amplifier cavity is by itself an oscillator with a characteristic spectral shape. In Fig. (2.39) we can clearly see the 3 spectral curves. We can clearly see the effect of saturation in the spectral shape and an increase in the width of the pulse spectrum, the output spectrum FWHM is 19 nm.
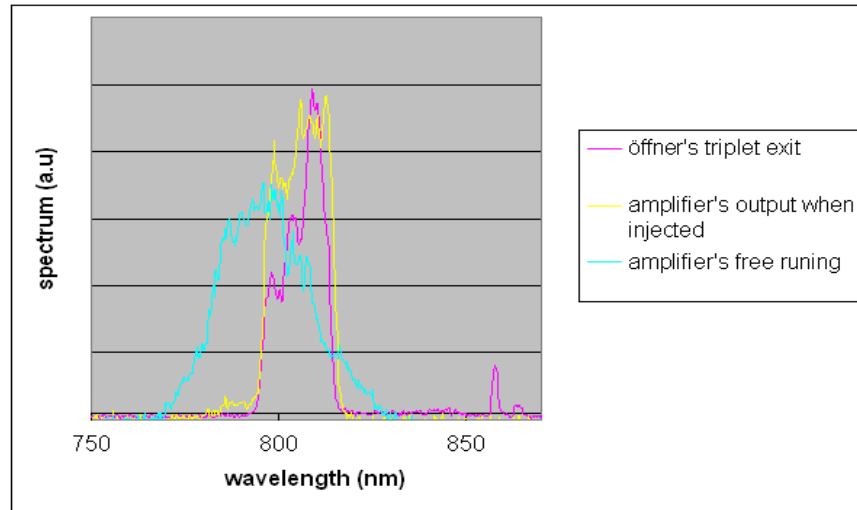
Figure 2.39.: Regenerative amplifier's characteristic spectra without any prisms.

Remember that even without the seed injection the laser is still pulsed because the Pockels cell opens and closes at a 1 kHz rate. As it is to be expected the ideal open/close time of the Pockels cell is not the same for a free running laser and for an injected laser. In a prismless configuration, if we optimize the round trip time in order to obtain the maximum amplification (9 round trips), we obtain $1.35\,mJ/pulse$. The injection coming from the stretcher has $5\,mW\,@\,89\,MHz$, or $56\,pJ/pulse$.
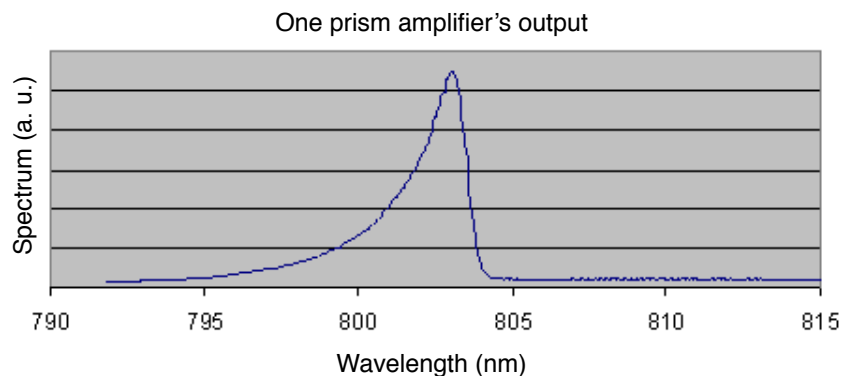
Figure 2.40.: Output spectrum of the regenerative amplifier using one prism inside the cavity.

We used one prism in the cavity and obtained the characteristic result seen in Fig. (2.40). The

amplified pulses had a spectrum with a FWHM of $1.7\,nm$ and is centered at $803\,nm$, with an energy of $950\,\mu J/pulse$. In this configuration, the spectrum can be adjusted. We report that the central wavelength can be shifted, approximately $5\,nm$, with an output energy that does not go below $780\,\mu J/pulse$.

Due to the characteristics of this system, it would be expectable to obtain an important ASE at the edges of the spectral profile. In order to avoid this, and in order to narrow the spectral profile, we use two razor blades (curved edges) near the back mirror. With these razor blades, we were able to obtain a minimum of $1.2\,nm$ spectral width, with $700\,\mu J$, but the configuration is clearly unstable. We then used two prisms inside the cavity, the characteristics result can be viewed in Fig. (2.41).

In Fig. (2.41) a) we see that the output spectrum is the superposition of the input spectrum and the free running cavity spectrum. Controlling these two spectrum we obtain the spectrum to be amplified. We can clearly see that the longer wavelengths will tend to emit even if there is no seed at those wavelengths. In order to avoid this, a razor blade is placed in position. This razor blade avoids the free running laser emission at those wavelengths deceasing the ASE.

(a)   (b)
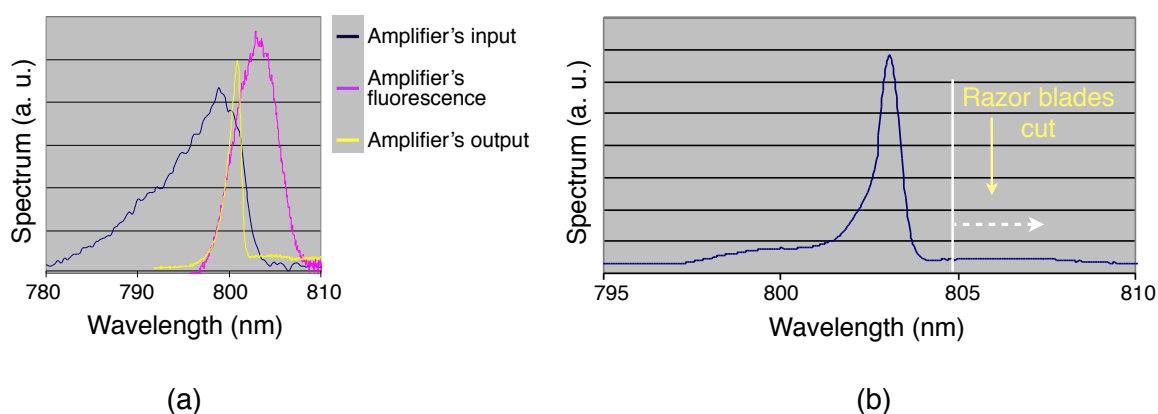
Figure 2.41.: Output spectrum of the regenerative amplifier using two prisms inside the cavity. (a) the input, free run and output spectrum, (b) the output spectrum cut by razor blades.

The results in this configuration are as follows. The output energy is 1mJ and the characteristic spectrum FWHM varies between 0.8 and 1.1 nm. We report that during thermalisation the spectrum FWHM may vary by a few tenths of nanometers. The energy of the pulse remains constant. Characteristically the total gain of the regenerative amplifier is 10^7.

2.5.3. Multipass amplifier

The following amplifier is a multipass amplifier, the polarization in this amplifier will always be vertical, the Ti:Sapphire crystal is $10\,mm$ thick and is coated to decrease the reflections in its surface.

The multipass amplifier has no curved mirrors or lenses, it only uses the thermal lens inside the crystal in order to maintain the beam size controlled. In theory it works like a cavity, the beam bounces of a first mirror with a slight divergence, it arrives at the crystal that will work as a lens and it bounces into a second mirror. In this mirror, we find the waist of the beam which is then reflected back into the crystal and so on. In truth, this worked well for the first 4 passages through the crystal. We tried a fifth passage for which we used a divergent lens (f= -1000 mm) that helped us with another amplifier passage, however no amplification was achieved during this passage. We only used 4 amplification stages.
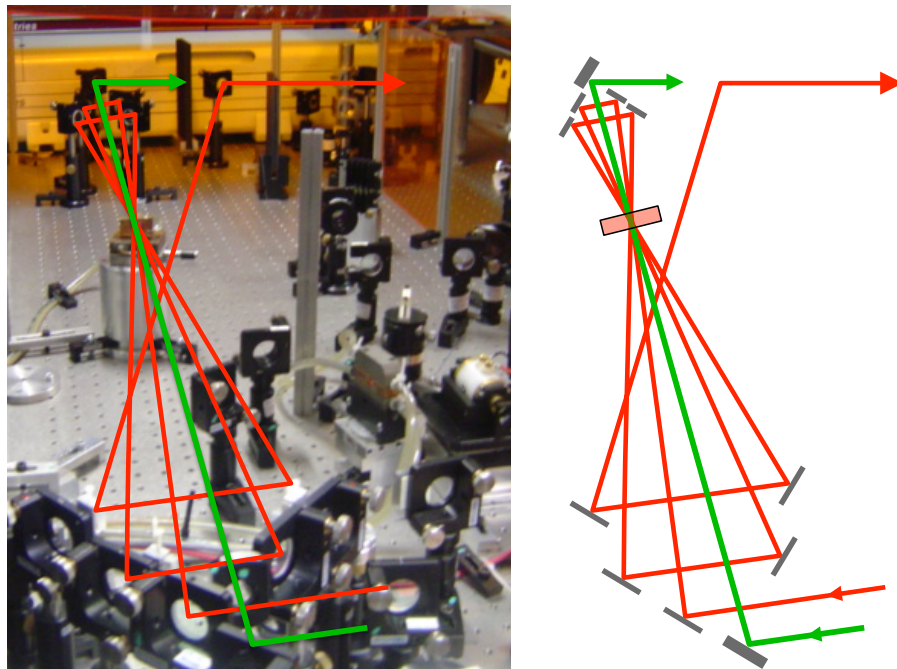
Figure 2.42.: Multipass amplifier, a scheme (right) and a photo (left).

The general scheme of the amplifier is presented in Fig. (2.42). From the scheme and the explanation above, it is intuitive that the distance between the mirrors and the crystal (half the round trip from one amplification step to the next) should be equal to twice the focal of the thermal lens. If it was an oscillator, this would represent a stability near to zero. In reality, the ideal situation is given when the distance between mirrors is ~ 1.7 times the focal length. This will allow the beam to be bigger near the mirrors and avoid the damage due to high fluency in the amplifier mirrors. Also the ideal beam in this situation is going to be nearly collimated with a small divergence. Please note that the rest of the pump is not reused in the amplification crystal.

For this amplifier, the pump laser is a Nd:YLF laser@527nm with an energy of $15\,mJ$ at 1 kHz repetition rate. In the crystal, the pump has a diameter of approximately 1 mm. The calculated thermal lens in this case is 0.9 m. We assembled the device using this values and obtained the

characteristic amplification values listed in Tab. (2.3). The energy per pulse at the output of the amplifier is 3.5 mJ.

Amplification stage	Energy per pulse (mJ)	Amplification
Entry of the amplifier	0.95	1
First stage	1.5	1.58
Second stage	2.2	1.47
Third stage	2.85	1.30
Fourth stage	3.5	1.23

Table 2.3.: Amplification and output energy at every amplification stage.

We can clearly see the effect that saturation has on the amplification coefficient, the fifth passage resulted in no gain. However the saturation can also be seen in the spectrum of the output laser. In reality, we registered that the multipass amplifier increases the spectral bandwidth between 10% and 20%, the output spectrum is between 1.3 nm and 1.7 nm, our best result was 1.1 nm, with $3.5\,{}^{mJ}\!/_{pulse}$.

CPA laser output

After the multipass amplifier, we have a holographic grating compressor that has been described above. Due to the compressor overall efficiency, the output of the amplification chain is $1.7\,{}^{mJ}\!/_{pulse}$, the spectrum is not cut by the compressor and remains the same spectrum that we have at the output of the multipass amplifier. The spectrum is characteristically centered at 803 nm however it is possible to change the spectral profile by 5 nm without significant change in the output energy or spectral width. The spectral bandwidth of the output pulse is between 1.1 and 1.7 nm.

2.6. Conclusion

We have first discussed OPCPA in a degenerated and in a non-degenerated configuration, we concluded that in a standard non-collinear wave mixing the spectral gain that could be obtained using a non-degenerated configuration was spectrally wider than in a degenerated configuration.

We discussed a seed pulse with an angular chirp and obtained the conditions that enable an enlargement of the spectral gain bandwidth by introducing an angularly chirped seed. In our configuration, we had two degrees of freedom, the angular chirp and the non-collinear angle. We used a derivation of the phase-matching condition in order to obtain two equations that, if combined, gave the conditions to obtain a large spectral gain bandwidth. We combined this with previous work to deduce a configuration that would enable at the same time, a wide spectral pump and a large spectral bandwidth of the amplified signal. We then confirmed numerically that angularly chirping the seed pulse can enlarge the gain bandwidth. We did a sweep of the angular chirp and of the non-collinear angle.

We found that in this case the degenerated configuration gives the widest spectral bandwidth. We calculated that the spectral gain is going to have a FWHM of 405 nm, between 645 and 1050 nm (centered at 850 nm) for a angular chirp of $\sim 2E - 4^{rad}/_{nm}$ in a collinear configuration.

We presented two mode-lock Ti:Sapphire laser oscillators. The first oscillator we describe in detail, has a spectral bandwidth FWHM of 96 nm, it emits between 750 and 900 nm, the pulse Fourier limited by 12 fs The ML laser in which we base our simulations is presented in detail. It has 150 nm spectral bandwidth, in which the dispersion control is assured not only by a traditional set of prisms but also by a ensemble of chirped mirrors, we present the details on the dispersion and spectral phase accumulated on a round-trip of the cavity (the dispersion of the prism set is positive). This enables the oscillator to be smaller and therefore more stable. We discussed the astigatism in the cavity, there are three components that create astigmatism in the cavity, one is the crystal and the other two are the concave mirrors of the sub-cavity. The crystal not only contributes to the astigmatism due to the simple transmission (the effective path in the tangential and sagittal planes is different) but also due to the astigmatic lenses that exist in the crystal (thermal and kerr lens). Both elements have to balance each other, in other words the folding of the mirrors of the sub-cavity has to compensate effects in the crystal. There is a formula to find the folding angle that compensates the path that is made inside the crystal, which gives an angle of 8.07º, we also used a simple simulation to find which angle would allow us to compensate the astigmatism of the output beam, and found that 7.2º would be the best value, experimentally we make a sweep of the folding angle to find the best angle to obtain an anastigmatic beam at the output of the cavity, we find that this angle is $\sim 7.5°$.

The second oscillator that we have presented is a sub-6 fs oscillator (4.8 fs Fourier limited), with a larger spectral bandwidth. We describe this oscillator summarily, it has a smaller crystal, 1.9 mm instead of the 4.5 mm that we had in the first oscillator and we use doubled chirped mirrors to compensate the dispersion accumulated by the pulse, in a cavity round trip, the Ti:Sapphire crystal, the two BaF2 plates, the two CaF2 wedges and the dispersion introduced by the air, the wedges are assembled in a translation stage with a motor that allows us to finely tune the dispersion inside the cavity. The SPM effect in this case is such that the output spectrum can go from 650 nm to 1125 nm while the output coupler has a flat transmission from 605 nm to 925 nm, in other words there is a part of the spectrum which half-life time in the cavity is smaller than the half-life time of the central part of the spectrum, which is only made possible due to the strong SPM inside the crystal that creates frequency components at each round-trip (Fig. 2.31).

We have presented several models to simulate the first femtosecond Ti:Sapphire laser oscillator. It has been known that the sub-cavity configuration is critical to the ML operation, what we tried to do is to find which are the distances within the sub-cavity that allow a good ML operation. In reality the thermal lens is hard to estimate if it is not measured experimentally and the models in which it is based are not perfect. We used two models to simulate this effect, as well as analyzing the cavity without any thermal lens. Finally, in one last model, we adapted the pump size at every point in the cavity in a CW configuration. We did this by scanning the effect that the pump size would have on

the spot size of the laser inside the Ti:Sapphire crystal (via the thermal lens). We memorized the spot size and the pump size that were closest to each other (in a CW configuration) and took this sizes to be the actual spot sizes of the CW and pump laser. The results may be seen in Fig. (2.24), we conclude that for this specific cavity the beam size can only be compatible with the pump size (within 50% difference) if the thermal lens is small, which means a pump size smaller than $\sim 53 \mu m$ (effective radius, $\sim 40 \mu m$). We used this value to make the calculations with a simple thermal lens and with a thermal lens in which the difference between the size of the pump and of the resonant beam. The way in which we analyzed the ML operation consisted not only in a study of the spot sizes in the middle of the gain medium, but also in an analyzes of parameters that evaluate the ability of the cavity to ML. The traditional way to analyze the ML operation has to do with calculating the mode size in a CW configuration and then introducing a small Kerr lens that enables us to evaluate what is the tendency to ML that a certain cavity configuration possesses. If the beam size inside the crystal decreases, it is an indication that the cavity is in a good configuration to enable ML. This is simply due to the fact that the ML process depends on the beam size, because we have an increase in gain when the beam is smaller. This is what is evaluated by Eq. (2.33). In order to go further, we have to evaluate the beam size in a ML configuration. It is important to notice that the switch to a ML configuration is a nonlinear process and so it is possible that the evaluation of a infinitesimal Kerr lens does not represent the entire process in which the beam intensity increases six orders of magnitude.

We explored several models in order to obtain the spot sizes of the beam in a ML configuration. The actual increase in laser power from a CW to a ML configuration is not known to us, the authors in [25] concluded that in their model the beam size is stable after 200 round trips for a 50 fs pulse, however for a 5 fs pulse the authors concluded that not even 100 round trips would make the beam size completely stable. We have 12 fs pulses, and so we do not know how the intensity increases.

In the first model we devised, we started by inputting into the cavity configuration a Kerr lens that had the actual power of the resonant beam inside the cavity (we estimated the duration of the beam inside the cavity considering the chirp introduced by the crystal and the spectral bandwidth). This is not to say that the Kerr lens was estimated, it only means that the power inside the crystal was estimated, but the Kerr lens also depends on the spot size which is what we want to know. However the actual power inside the cavity is only attained after the stabilization of the ML process. This model actually produces a spot size that is coherent with itself, and with the observed characteristics of the cavity (not with the sub-cavity dimensions because these were not measured with sufficient accuracy). However this model seems to find zones where the ML is not possible and where the differential ML parameter that we had discussed above does find appropriate ML parameters. And so even if the model is self-consistent, it might eliminate points where ML is possible but it was not obtained because of the calculation method. However for all thermal lens considered, we can clearly see the point where ML is optimal. With this model, the two stability zones that are found in a CW configuration divide themselves in into four zones.

The third quadrant stability zone (low L_1 bigger Z) gives the most interesting results concerning the ML parameter. In reality we obtain that it is in the edge of this zone that ML operation is more favorable[7], however comparing this zone with the zones obtained by the differential ML parameter we see that they do not coincide. This is simply due to the fact that the soft aperture ideal sub-cavity configuration that can be seen in Figs. (2.11), (2.16) and 2.19 is not stable when we introduced a Kerr lens. These results give us the perception that, with an increase in the intracavity power the crystal, the position that gives the operational ideal point changes. The distance between the sub-cavity mirrors also changes less depending on the thermal lens in play.

The second model we proposed was based on the first one, however whenever the ML operation seamed to be unobtainable the algorithm decrease the mode size to see if it would find a stable mode (we tried to use trials with bigger modes but no new operational sub-cavity configurations were obtained). This model obtained stability where the first model failed, we see configurations where the CW is possible and the ML operation is possible using this second model but not the first one. These operational points are situated in zones where the spot size is smaller, more specifically between the two stability zones that were created in the previous model by including the Kerr lens. The importance of having a ML operation on a point where the spot size is small is given by the increase in SPM that is obtained with this smaller spot size. This increase in SPM will mean a wider spectral bandwidth.

For a cavity where no thermal lens existed, we also tried to linearly increase the power inside the cavity in 20 steps, up to the power that is actually measured, we obtained a result similar to the first model. However in this model we found that introducing a gradual Kerr lens eliminates many points where ML could otherwise be obtained. This does not mean that the model is false, it simply means that this calculation method does not allow some sub-cavity configurations to be stable. Adjusting the pump and beam sizes, we calculated the spot sizes. From these spot sizes, we calculated the differential ML parameter. This gave us the impression that having a bigger thermal lens would be a favorable for a ML operation.

So far, we had considered that the intracavity power was the same for every distance between sub-cavity mirrors and crystal positions. We changed this, in our fourth model by increasing the pump power in 200 steps, evaluating at every step if the cavity was still stable. If this was not the case, we would memorize the last stable spot size. In this calculation the four zones that had been created by the introduction ad hoc of the thermal lens were recompressed into the previous two stability zones. We remark, that in this calculation, we obtained two zones where the sub-cavity configuration is good for ML; we can see these regions that are signaled by a "X" and a "Y" in Fig. 2.26. The region that is best suited for ML is the "Y" region, we could perceived this region ability for ML in the models that had an infinitesimal Kerr lens, but not so marked as in this one. This result is important because, in the previous models, we considered the laser power to be the same for every region and

---

[7]This was not the case in [106] simply because the thermal lens was considerably bigger and the folding of the stability zones was considerably higher.

this is simply not the case in an actual laser oscillator, and it also proves definitely that the use of the ML parameter as defined by Eq. (2.33) does not represent the totality of the ML process.

Afterwards, we studied a fifth model where the intracavity power increased exponentially. We used 10 points one order of magnitude apart from each other, up until the actual intracavity power, however at each increase in power we applied the second algorithm, searching at each energy increase a stable ML configuration. The results from this calculation are very similar to the sixth and final successful algorithm that was presented next, that consisted not in using the algorithm of Fig. (2.14) until it converges but only one time, we tested this algorithm. In reality these results confirm that the division of the two stability zones into four actually happens, the edge of the stability zone with the biggest distance between the mirrors and the smallest L_1 position is the preferential point for ML operation. Also these last algorithms seem to indicate that the stability zone where it is possible to have ML is larger than what had been previously calculated. They also seem to indicate that the existence of a strong thermal lens (if the beam mode allows) benefits ML operation or at least decreases the beam size at this point.

The second oscillator we presented has a smaller subcavity (concave mirrors with a smaller focal length) which creates a smaller spot size at the center of the crystal. The stability zones in this case are bended in such a way that the two stability zones are superimposed. In the meeting between the two stability zones, on the edge of the second stability zone we find the ideal point to have the laser in ML. At the ideal ML position the focal for the first oscillator is approximately $50\,mm$ ($35\,\mu m$ spot size), for the second oscillator, the beam size is smaller than $10\mu m$, in consequence the thermal lens is one order of magnitude smaller on the order of the *mm*. This enabled us to work in a region that is stable and at the same time with a spectral bandwidth bigger than an octave. We also verify that the point in which the cavity operates in ML the pump and beam size are similar at the central of the crystal, no other configuration of the sub-cavity as the same two characteristics. In the first cavity that was presented, the final model gives presents two points that where ML operation is feasible, one of them is coincident with the literature (see for instance [87, 112, 137]) on the other the pump and beam sizes do not match (compare Fig. (2.24) c) and the bottom graph of Fig. (2.28)), we envision that in future works an engineering parameter to define the ideal ML position would not only have into account the decrease in mode size due to the increase in power (which the ML parameter already does) but also the match between the pump and beam size inside the crystal.

In the end of this chapter, we have presented in great detail a Ti:Sapphire CPA laser chain that issues $1.7mJ$ per pulse, with a spectral bandwidth that can be as short as $1.1\,nm\,@\,802\,nm$. The design of this amplification chain includes two prisms inside the regenerative amplifier cavity that select the spectral bandwidth to be amplified. Saturation is important in this CPA chain and increases the amplified spectral bandwidth. In reality, the amplified spectral bandwidth of the regenerative amplifier is the superposition between the inputted spectrum and the spectrum of the regenerative amplifier when this is working in a free running mode. After this regenerative amplifier, the CPA chain had a 4-pass amplifier, the dispersion control was done using holographic gratings.

Part II.

Ultrashort pulses diagnostics

3. Introduction to autocorrelations and third order cross-correlations

Correlations and autocorrelations have been among the easiest diagnostics to implement in ultrafast sciences. This chapter, despite being done with ultrafast laser pulses in mind, may have applications in other areas of science. We present here a quick review on what is known about autocorrelations. We will use some of the features exposed here in Chap. (4) to reconstruct the intensity profile of ultrafast pulses.

In the second part of this chapter (Sec. (3.2)) we deal with third order cross-correlations (TOCC). We discuss the features of third order cross-correlators and third order cross-correlations. We present the mathematical proof that the TOCC plus IA completely defines the intensity profile, a result that, to the best of our knowledge, has never been published. We also give some results on a retrieval method that uses the TOCC and IA to obtain the pulse profile, where the results obtained sustain the mathematical proof referred above.

3.1. Autocorrelations

We treat the following autocorrelations:

1. Electric-field autocorrelation;

2. Intensity autocorrelation (IA);

3. Second order interferometric autocorrelation (IAC);

4. Second harmonic autocorrelation (SHAC)

5. Third order interferometric autocorrelation (TOIAC)

We present the main characteristics of these correlations, how to obtain them experimentally and the main problems of the experimental implementation will be discussed. Many of these problems have been approached by several authors, for a comprehensive presentation see [50].

The first characteristic of autocorrelations is that they are always symmetric and real, and so the Fourier transforms of these quantities are also symmetric and real. The Wiener–Khinchin theorem

(Eq. (3.1)) states that the autocorrelation and the squared modulus of the Fourier transform are Fourier pairs. And so knowing the Fourier modulus and knowing the autocorrelation are equivalent statements.

$$\int f(t)f^*(t-\tau) = |F(\omega)|^2 \tag{3.1}$$

Retrieving the electric field from the electric-field-autocorrelation or the intensity from intensity autocorrelation is a phase retrieval problem that is unsolvable on its own. In other words, there are more than one electric field that will have the same intensity autocorrelation and electric field autocorrelation. This topic has been treated successfully by J. H. Seldin and J. R. Fienup [143, 144] and it was has been proved that in a uni-dimensional case, the phase retrieval problem does not present a single solution. And so in principle assuming nothing else we cannot know a function using only its uni-dimensional autocorrelation.

When assuming a complex electric field there aren't any restrictions on the value of the electric field itself. But we can say that the intensity is a real and positive function limited in time and integrable. In order to be clear, when a function is defined by its Fourier modulus it means that there is only one solution for the phase of the Fourier transform that satisfies the existence of that Fourier modulus and other constraints that might exist in the frequency or time space. The probability for having a non unique solution for an autocorrelation of a given two dimensional function is dependent on the function itself, specially if the function dependence on one dimension is dependent or independent of the other dimension.

Correlations and autocorrelations are done in a correlator, which is a Michelson [145] or a Mach-Zehnder interferometer [146]. An autocorrelator uses a wavefront divider interferometer. This allows us to have two virtual identical sources, shifted in time by a certain delay, one arm of the interferometer sweeps the delay, while the other stays still. This allow us to obtain the time difference between the pulses.

Despite lacking the consistency of a 2D measurements like FROG (Frequency Resolved Optical Gating) [35], triple autocorrelations [147], SPIDER (Spectral Phase Interferometry for Direct Electric-field Reconstruction) [37, 38] or D-scan [39], autocorrelations provide information about the pulse profile, and we will see in this thesis that some of these measurements provide full pulse reconstruction or high contrast measurements. This measurements are easy to make, at the very least are initial measurements that the scientific community employs daily in every ultrafast laboratory.

Femtosecond autocorrelators are devices that must be designed according to a specific spectral bandwidth, they are normally designed for pulses with a small spatial beam divergency, and in an autocorrelator the intensity in both arms of the interferometer is balanced. A single path autocorrelator as we see in Fig. (3.1) is not a good autocorrelator. The multiple reflections in the beam splitter will create several parallel beams with different delays and so it is possible to observe several

autocorrelations. However it will be impossible to have the same quantity of material crossed by both beams. One solution for this problem is to have a second beam splitter on one of the paths (at 45°), but this will unbalance the intensity due to reflections in a second beam splitter.
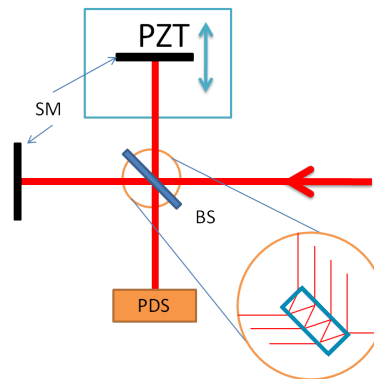
Figure 3.1.: Single-pass interferometer: SM-silver mirrors; PZT-piezoelectric; BS-Beamsplitter; PDS-photo-detecting system.

The solution would be to put it in a Brewster angle but then the paths wouldn't be the same, this details have unmitigated importance when the pulses are shorter than 15fs@800nm. The solution for this is to have a double pass interferometer where the coating on the BS is putted symmetrically on each incidence point (see Fig. (3.2)).
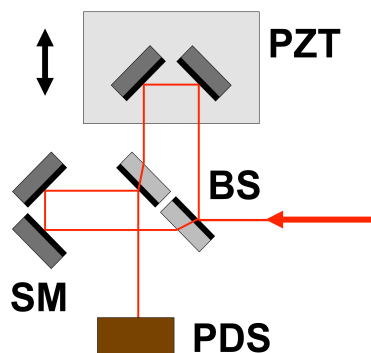
Figure 3.2.: Double path interferometer: the multiple reflections in the beam splitter are of no concern. Both beams pass through the same path and the coatings are reversed.

3.1.1. Electric field autocorrelation

The electric field autocorrelation is a well known entity which is equivalent to spectral power, the two quantities being related by a Fourier transform:

$$AC_E(\tau) = \int E(t)\overline{E}(t-\tau)dt$$

$$S(\omega) = \mathscr{F}\{AC_E(\tau)\} = |\widetilde{E}(\omega)|^2$$

(3.2)

The power spectrum can also be measured directly with a spectrometer. The autocorrelation can be taken using a correlator with a linear absorber. The quantity that arrives in the detector is:

$$DAC_E(\tau) = \iint |E(t,x) + E^*(t-\tau,x)|^2 dt dx = 2 \iint |E(t,x)|^2 + \mathbb{R}\left\{\iint E(t,x)\overline{E}(t-\tau,x)|^2 dt dx\right\}$$

(3.3)

Both arms have to be balanced. Spatial defects and wavefront defects will jeopardize the contrast. For ultrafast pulses it is sometimes more practical to measure the spectral intensity profile than the electric field autocorrelation.

3.1.2. Intensity autocorrelation

This autocorrelation is obtained using a nonlinear effect at the end of a wavefront divider interferometer (see Fig. (3.3)).
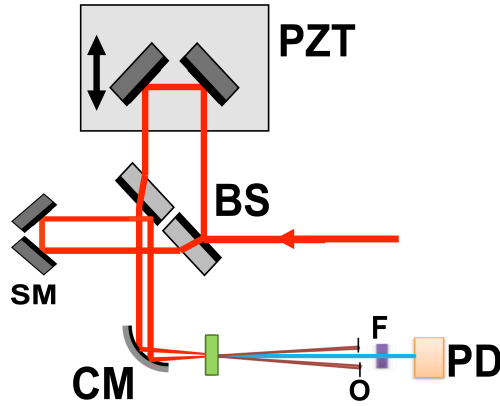
Figure 3.3.: Intensity autocorrelator: these beams are combined in a nonlinear crystal (SHC) and the contrast can be good due to the fact that we eliminate the original beams and their second harmonics. Because the wave-mixing is non-collinear, the originated second harmonic electric field will be proportional to $SH(t,\tau) = E(t)E(t-\tau)$. The photodiode reads its intensity, a convex mirror focus both beams in the crystal.

However to obtain a background free intensity autocorrelation the beams have to be non-collinear. In this case there is no interference between beams (in reality the beam interference figure is averaged over many fringes). Intensity autocorrelation is defined as follows in Eq. (3.4):

$$IA(\tau) = \int I(t)I(t-\tau)dt. \tag{3.4}$$

This autocorrelation is not sufficient to retrieve the intensity, however it is sufficient to retrieve the variance, because both variances are related by

$$\sigma(IAC(\tau)) = \sqrt{2}\sigma(I(t)). \tag{3.5}$$

Using the Hilbert transforms there were attempts to define the intensity from the autocorrelation [148], but these attempts fail for most pulses. Intensity is an integrable, real and positive, the intensity of a pulse is constrained in time, and therefore the intensity is not completely unrestrained.

Let us analyze some of this restrains using a certain Fourier intensity phase. The Fourier transform of the IA is $|\tilde{I}(\omega)|^2$, the intensity is given by:

$$I(t) = \int |I(\omega)| \exp(i\phi(\omega))e^{-i\omega t}d\omega \tag{3.6}$$

Considering that the intensity spectral phase (do not mix this intensity spectral phase with the field spectral phase, that are independent) is odd in order to give an intensity that is real (see Eq. (3.6)) however, the odd Fourier intensity phase does not assure that the intensity is always positive. Even phases are only possible in particular cases where:

$$\int\limits_0^\infty |\tilde{I}(\omega)| \cos(\omega t) \sin(\phi_{even}(\omega))d\omega = 0 \tag{3.7}$$

For an arbitrary $|\tilde{I}(\omega)|$ this is true when $\phi_{even}(\omega) = 0$. Therefore the constant component of the phase is zero. A linear phase in the Fourier domain will mean a delay in time and so a linear phase is always possible because the time origin is arbitrary, but it can also be disregarded if we chose the time origin.

If the phase is zero, the intensity will always be positive, real and symmetric. J. Peatross and A. Rundquist [149] have developed an algorithm in order to retrieve the intensity from its autocorrelation. They use the fact that the intensity has to be real and positive in addition with the condition $I(t_0) < 0$ then $I(t_0) = 0$.

The algorithm is explained in Fig. (3.4): the intensity is retrieved from an intensity autocorrelation using a Gerchberg-Saxton algorithm, which is equivalent to the retrieval of the spectral phase of the intensity. The initial phase guess starts with a odd phase, and a modulus of the intensity Fourier transform, the initial guess can be randomly generated. Then, for any point where the intensity is

negative, we impose the condition $I(t_0) = 0$. A new Fourier transform of the intensity is performed. We memorize the phase in the Fourier domain and replace the absolute value for the absolute intensity Fourier transform obtained by the intensity autocorrelation. The convergency of the error is presented in Fig. (3.6).
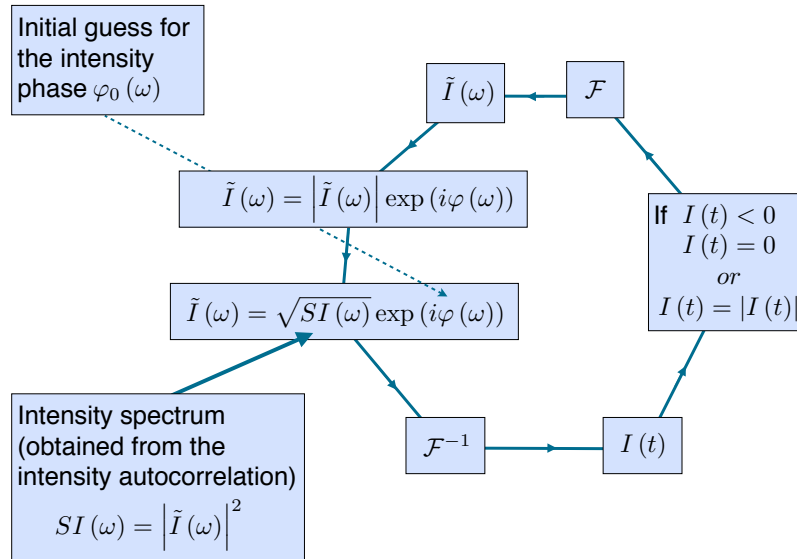
Figure 3.4.: Gerchberg–Saxton algorithm applied to the intensity autocorrelation.

We could have used any phase as an initial phase, however this is going to result in a complex intensity in the time domain, and then the condition will have to be changed to $I(t_0) = |I(t_0)|$. In this case the convergency will be slower.
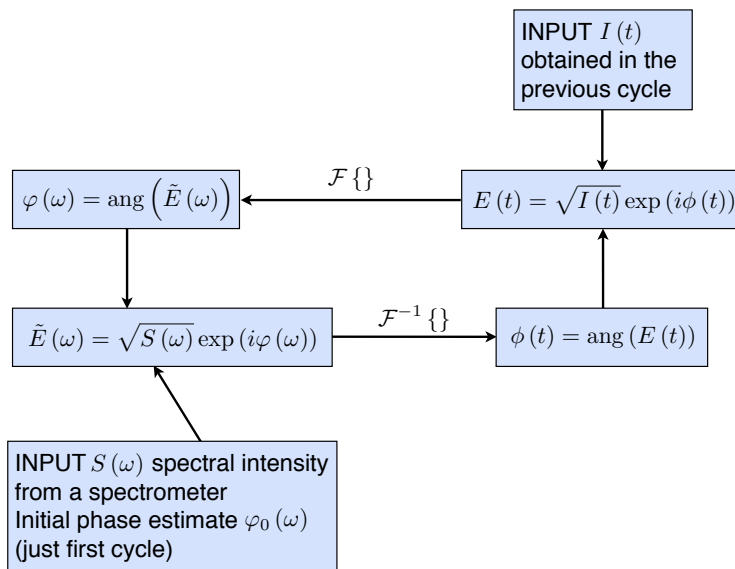
Figure 3.5.: Second cycle for the deconvolution of the pulse.

After using this algorithm, we observe that the obtained phase is not unique. We realize this by using different initial guesses for the phase, that result in different end result for the phase even if convergency is reached. In resume, it is not possible to define the phase from its modulus with such a week condition. A second Gerchberg-Saxton cycle was designed (Fig. (3.5)) to obtain the complete definition of the electric field in spectrum and time, this cycle inputs are the intensity profile and the spectral intensity; in other words, the two amplitude modulus of the Fourier pair in the direct and Fourier space.
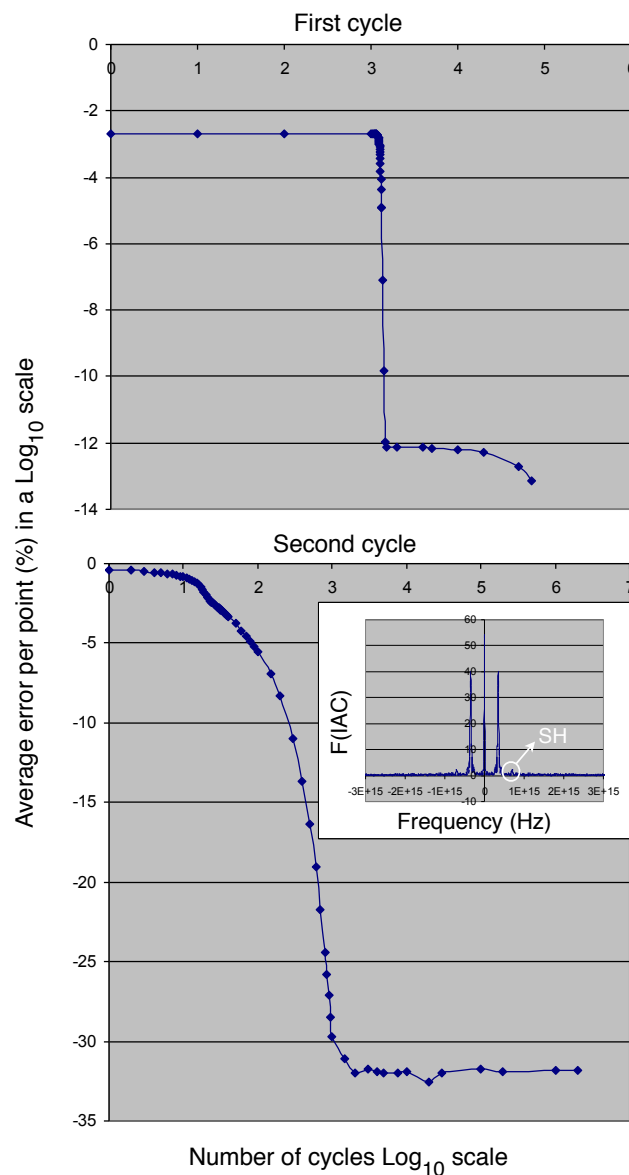
Figure 3.6.: Convergency of the cycles given above in Figs. (3.4) and (3.5). The small graph in the left bottom is the Fourier transform of IAC (interferometric second order autocorrelation) trace in this measurement, an excess in linear absorption made the S/N ratio of the second harmonic module approach 1. The pulse had a FWHM of about 26 fs in time and 80 nm of spectral FWHM.

The algorithm goes forward and backwards between the Fourier and direct space until it finds a stable solution where the phase of the electric field is consistent with both modulus. This second algorithm is explained in Fig. (3.5) and the convergency graphics in Fig. (3.6).

We use the intensity retrieved in the previous cycle (Fig. (3.4)) and from the experimentally measured spectrum. This has given approximated results in some cases, and it is used as a first algorithm before FROG [34].

3.1.3. Interferometric second order autocorrelation

This autocorrelation is a correlation obtained by a second order nonlinear effect. The correlator is similar to the one in Fig. (3.3) but the beams are perfectly aligned when they arrive to the detector (Fig. (3.7)).
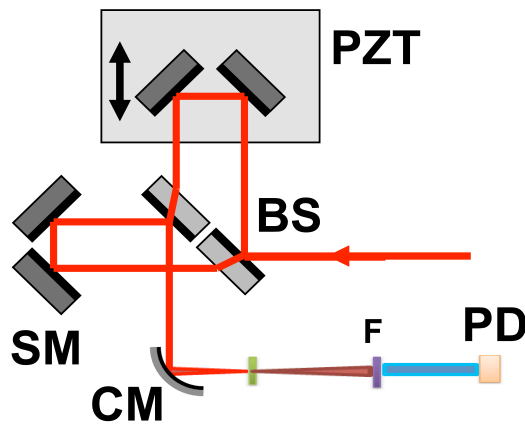
Figure 3.7.: An interferometric autocorrelator: the fields will be aligned so the second harmonic field will be given by the sum of both electric fields that add up coherently (at least when the delay between them is zero). It is important to observe that slight misalignments (or a beam splitter that is not perfectly plane) will give us a distorted wavefront, and this will result in a contrast that is smaller than 1 to 8.

In this case the electric field that arrives in the crystal is the algebraic sum of the electric fields as in a field autocorrelation. However the field sum is squared twice, one because of the second harmonic and the other one because we measure the intensity of the second harmonic.

$$IAC(\tau) = \int |E(t) + E(t - \tau)|^4 dt \tag{3.8}$$

This equation is divided in four terms

$$IAC(\tau) = 2DC + 4IAC(\tau) + 8X(\tau) + 2SHAC(\tau), \tag{3.9}$$

where:

$$DC = \int I^2(t)dt \tag{3.10}$$

$$IAC(\tau) = \int I(t)I(t-\tau)dt \tag{3.11}$$

$$X(\tau) = \int \frac{I(t)+I(t-\tau)}{2}\Re\left\{E(t)\overline{E}(t-\tau)\right\}dt \tag{3.12}$$

$$X(\tau) = \frac{X_1(\tau)+X_1(-\tau)}{2} \tag{3.13}$$

$$X_1(\tau) = \int I(t)\Re\left\{E(t)\overline{E}(t-\tau)\right\}dt \tag{3.14}$$

$$X(\tau) = \frac{\Re\left\{X_{11}(\tau)+X_{11}(-\tau)\right\}}{2} \tag{3.15}$$

$$X_{11}(\tau) = \int I(t)E(t)\overline{E}(t-\tau)dt \tag{3.16}$$

$$SHAC(\tau) = \int \Re\left\{E^2(t)\overline{E}^2(t-\tau)\right\}dt \tag{3.17}$$

Please note that: $DC = IAC(0) = X(0) = SHAC(0) = \int I^2(t)dt$.

Observing this, we may evaluate the importance that every part of the equation is going to have. Note that the origin value in time is the average value in the Fourier domain and vice-versa. The SHAC has a smaller S/N ratio than the other parts of IAC, because it has the smallest amplitude. This several parts will then be distinguishable in the Fourier domain. The contrast will be 1 over 8. A characteristic IAC and its Fourier transform can be viewed in Fig. (4.1). The Fourier characteristics of IAC and SHAC will be discussed in Chap. 4. The Fourier transform of $X(\tau)$, the crossed term, may be given by:

$$\tilde{X}(\omega) = \frac{1}{4}\left[\left[\tilde{I}(\omega)\otimes\tilde{E}(\omega)\right]\overline{\tilde{E}}(-\omega)+SS+CC\right] \tag{3.18}$$

SS is the centric-symmetric term. This term is actually very similar to the field autocorrelation and is centered at the same frequency. Note that $X(\tau) = X(-\tau)$.

This autocorrelation, together with the spectrum, is sufficient to reconstruct the pulse's electric field in both magnitude and phase. The proof is given by Naganuma et al. [150]. In Chapter 4 we analyze the attempts done in order to deconvolve the electric field from this measurement.

3.1.4. Second harmonic autocorrelation

SH autocorrelation is the field autocorrelation of the second harmonic and can be measured by doing the linear autocorrelation of the second harmonic so we may simply put a second harmonic crystal before the autocorrelator. The autocorrelation is given by:

$$SHAC(\tau) = \int E^2(t)\overline{E}^2(t-\tau) \tag{3.19}$$

This autocorrelation carrier frequency is approximately twice the carrier frequency of the main pulse, its Fourier transform can be given by:

$$\mathscr{F}\{SHAC(\tau)\} = |\tilde{E}(\omega) \otimes \tilde{E}(\omega)|^2 \tag{3.20}$$

A second harmonic autocorrelator is presented in Fig. (3.8):
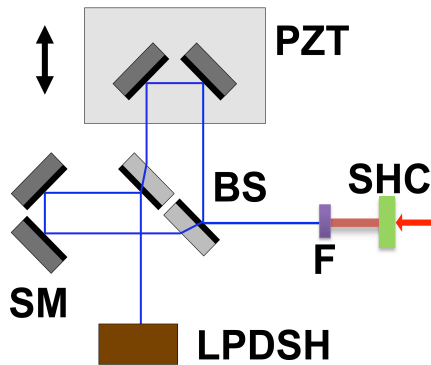
Figure 3.8.: A second harmonic autocorrelator: SHC - second harmonic crystal; F - spectral filter; BS - beam splitter; PZT - piezoelectric; SM - silver mirrors; LPDSH - linear photo-detector at the second harmonic wavelength.

Despite never being actually measured independently, we could measure the second harmonic spectrum using such a system, or we could simply measure the second harmonic spectrum using a proper spectrometer, this later proposal has a bigger S/N ratio.

3.1.5. Third order interferometric autocorrelation

This correlation is rarely used, however it is rather interesting. A third order nonlinear effect is necessary in order to obtain this autocorrelation, that can be given by a three photon absorption or a third harmonic generation. If we use three photon absorption in a photodiode for a 800 nm Ti:Sapphire laser with 100 nm bandwidth the required absorption of the photodiode should be centered at 266 nm, with a minimum flat gain spectral bandwidth of 33 nm. We tried to do this with a AlGaN photodiode - the Genicom GUVB-T11GD, that had an announced spectral bandwidth between 200 and 300 nm, however we did not observe a third order autocorrelation but rather something similar to a field autocorrelation, this is probably due to the fact that the linear absorption vastly surpasses the nonlinear absorption in the photodiode. This has been used to confirm IAC diagnostics where no other diagnostic had been implemented. The expression is given by:

$$TOIAC(\tau) = \int |E(t) + E(t - \tau)|^6 dt \tag{3.21}$$

This correlation contrast is 1 to 32. Let us decompose this in its Fourier components:

$$TOIAC(\tau) = 2DC + 18XIAC(\tau) + 30X1(\tau) + 12X2(\tau) + 2THAC(\tau), \tag{3.22}$$

where:

$$DC = \int I^3(t) dt \tag{3.23}$$

$$XIAC(\tau) = \int \frac{I(t) + I(t - \tau)}{2} I(t)I(t - \tau) dt \tag{3.24}$$

$$X1(\tau) = \int \frac{I^2(t) + I^2(t - \tau) + 3I(t)I(t - \tau)}{5} \mathbb{R} \left\{ E(t)\overline{E}(t - \tau) \right\} dt \tag{3.25}$$

$$X2(\tau) = \int \frac{I(t) + I(t - \tau)}{2} \mathbb{R} \left\{ E^2(t)\overline{E}^2(t - \tau) \right\} dt \tag{3.26}$$

$$THAC(\tau) = \int \mathbb{R} \left\{ E^3(t)\overline{E}^3(t - \tau) \right\} dt \tag{3.27}$$

This autocorrelation in addition to the spectrum completely define the electric field. It is intuitive that $XIAC(\tau) + X2(\tau)$ are the equivalent of $IA(\tau) + SHAC(\tau)$.

3.2. Design of a third-order cross-correlator and analysis of third-order crosscorrelations

Traditionally, third-order cross correlators have been used to obtain high contrast measurements of the laser pulse temporal profile, [40–44]. We should not confuse third-order cross correlations (TOCC), also called third-order correlations, with triple autocorrelations [151–154]. The later are seldom used because of the practical issues regarding the implementation of two delay lines in a single device [152–154]. Probably due to these limitations, they have never been implemented for high contrast measurements. However they provide measurements that completely define the pulse shape [147], unlike third-order correlators. On both devices the signal is read at the third harmonic wavelength. For example, for a Ti:Sapphire laser with a fundamental wavelength at 800 nm, the signal is read at 266 nm.

The advent of high intensity laser pulses brought up the need to analyze the pulse with a dynamic range of several orders of magnitude. The importance of this measurements is made clear by Marc Nantel et al. [53]. In short, if pre-pulses and/or amplified spontaneous emission (ASE) are present in the background of laser emission, their previous interaction with targets can modify them and the interaction of the main pulse might not be with the intended target.

The most common, but not only case where this is illustrated is in solid target interaction. In aluminum thin film targets, plasmas can be created for pulse intensities of $10^{12} \, W cm^{-2}$. Intensities of $10^{19} \, W cm^{-2}$ can be achieved with 100 TW lasers and so background cleaning of more than 7 orders of magnitude is necessary if we want the main pulse to interact with the thin film itself an not with a plasma created by the background of the pulse. This presents two problems: the measurement of the radiation in the background and the increase of the pulse contrast. In this work we will mostly deal with the first problem.

The measurement presented here is not conceived to simply analyze the pulse shape in a linear scale or within a few fs of the pulse maximum. It is conceived in order to analyze the pulse within a $\pm 500 \, ps$ time scale in a logarithmic scale. For longer time scales we may use a streak camera [53] or an oscilloscope.

The competing device to make high contrast measurements is the OPA correlator [155–159]. However OPA correlators have only been seldom used and third-order cross correlators at the third harmonic wavelength have been dominant in the scientific and technical communities until now. The principle of these two measurements are similar: two chained second order nonlinear processes, where the first nonlinear process is the same for both devices (the SH of part of the pulse). In the case of the OPA correlator the second nonlinear process is DFG between the SH and the fundamental pulse.

In a TOCC the second nonlinear process is the SFG of the second harmonic and the fundamental

signal and not the third-harmonic of the fundamental pulse. The SH field is normally shorter and sharper than the fundamental pulse. It is assumed that the SH is given by the square of the field. This means that the contrast will be improved by a factor of two on a logarithmic scale. For simple Gaussian shaped pulses the duration of the SH will be $\sqrt{2}$ shorter than the fundamental pulse itself. This SH field is used to scan the fundamental pulse.

It is important to notice that we assume that all these processes occur in a low depletion regime, which is equivalent to state that:

➤ the second harmonic intensity is proportional to the square of the intensity of the fundamental pulses (the proportionality constant is not relevant here):

$$I_{SH} \propto I_{\omega}^2 \qquad (3.28)$$

➤ The intensity of the signal before averaging over the time response of the detector is given by:

$$I_{sig} \propto I_{SH}(t)I(t-\tau) \qquad (3.29)$$

It is imperative to make sure that there is no saturation in the detectors or in the nonlinear processes, otherwise the two previous equations would not apply.

Both devices (TOCC and OPA correlator) allow a temporal analysis of the laser pulse intensity with at least 12 orders of magnitude. But in order to have this dynamic range the detectors on the device should have a dynamic range ratio of three orders of magnitude before saturation.

The SFG in a TOCC device is sometimes inefficient (for low pulse intensities). Also it is considered harder to measure a signal in the UV range then an IR one [159]. The OPA correlator was designed to solve this problem. DFG can achieve a high gain of the seed (10^6), which makes the signal easier to read. Another fact that helps the reading of the signal is that this beam is found in the near infrared part of the spectrum. However for most lasers where the high contrast measurement is needed the low efficiency of the process is not a problem because of the high energy in the laser pulses. In fact, we don't want the process to be too efficient in order to avoid saturation.

Also, in order to have a dynamic range in the detectors of 10^3, the background noise has to be clean. This is much easier with a measurement in the UV because there is no other beam in the device at that wavelength, (the signal is spectrally isolated). In a OPA correlator the signal is read at 800 nm as is the fluorescence ring and the fundamental pulse. In order to compensate for this effect the noncollinear OPA wave mixing is greatly increased [157], which creates a group velocity mismatch that has to be compensated for.

A second-order intensity autocorrelator with an high contrast of 8 orders of magnitude has been reported [54] (note that time direction is ambiguous in an IA and so post- and pre-pulses are in-

distinguishable). Not only the second order autocorrelator does not benefit from the normalization factor that we will discuss below, but also the background noise is larger than in a third-order cross-correlator. Like in the case of the OPA, we will not be able to spectrally isolate the signal. The signal is created at 400 nm and the second harmonic of each beam is also created at 400 nm.

Supercontinuum based correlations have also been reported [60]. With this design it was possible to obtain contrast ratios of 10^8 in a sweeping system and 10^6 in a single shot system.
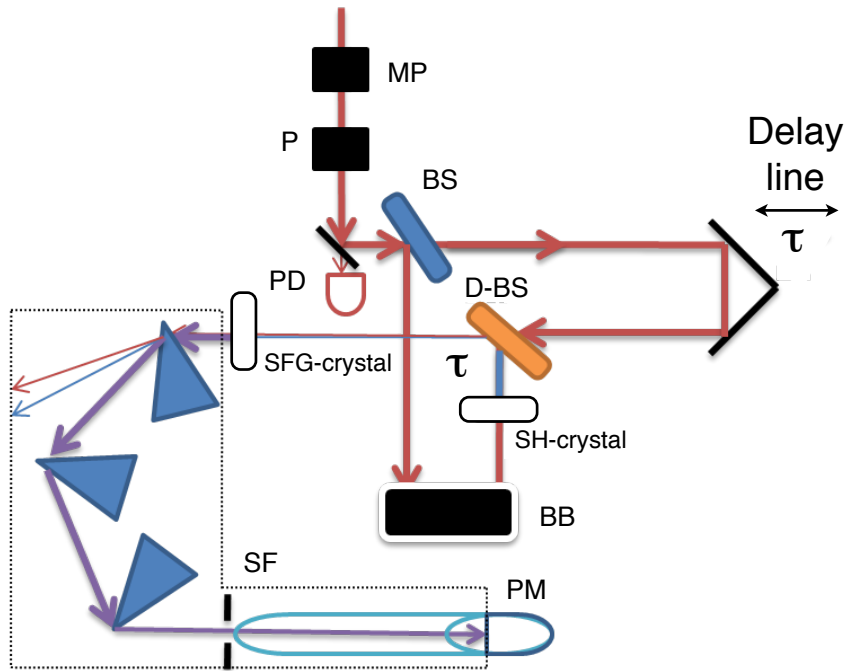
Figure 3.9.: Third-order cross correlator. MP - Adjustable polarizer; P - fixed polarizer; PD - photodiode inputted behind a mirror; BS - beam-splitter; D-BS - Dichroic beam-splitter; BB - Elevator system that rotate the polarization; SF - spectral filter with a set of prisms and a slit; PM - photomultiplier.

Let's discuss the possibility of having noise radiation at 266 nm ($\lambda/3$) in the device. The most intuitive way to get radiation at the third-harmonic wavelength, would be the appearance of THG in the materials where the beam is passing through. However this is highly unlikely due to the absence of phase-matching conditions. In reality THG is only possible if the interaction medium is nonuniform in the focal volume [160–162]. In other words only in materials where the interface plays an important role is it possible to have direct THG [163]. Direct creation of THG is only possible in cases where the dispersion obeys non normal conditions, like in photonic crystal fibers [164, 165]. The impossibility of having THG in bulk materials is well exposed by Rajesh Sreedharanpillai in [166]. In conclusion, we may say that in general it is not possible to have radiation at 266 nm that is not derived from the cascaded process of SHG+SFG.

A simple scheme of a TOCC is given in Fig. (3.9). The seed (fundamental wavelength) pulse used

in the SFG is delayed in relation to the second harmonic, the resulting signal is proportional to the amplitude overlap of the delayed fields and averaged over the time response of the photomultiplier. The signal seen at the UV detector (photomultiplier) is given by:

$$S_{PM} \propto \int I^2(t)I(t-\tau)dt \qquad (3.30)$$

However, we note that this signal dynamic range is only the dynamic range given by the photomultiplier (usually 3 or 4 orders of magnitude). We will have to use the fact that the signal in the photomultiplier varies with the cube of the intensity of the input pulse. This creates an additional degree of freedom with which to control the signal. We measure the quantity of IR that gets into the device with a photodiode, and we will normalize the photomultiplied signal using the photodiode signal. The correlation signal is then given by the following formula:

$$S_{3\omega} = \frac{S_{PM}}{S_{PD}^3}, \qquad (3.31)$$

or in other terms:

$$S_{3\omega}(\tau) \propto \frac{\int I^2(t)I(t-\tau)dt}{[\int I(t)dt]^3}. \qquad (3.32)$$

From Eq. (3.32) we see that the possible contrast dynamics of the signal is no longer given by the contrast of the photomultiplier (PM) but by the sum of the PM contrast plus three times the contrast of the photodiode. In order to achieve this we have to use the adjustable polarizer shown in Fig. (3.9). For zero delay between the pulses (maximum signal), the polarizer is rotated so that the signal in the PM is maximized and the intensity read by the photodiode (PD) is minimized. The PM signal near, but not, in saturation and the PD signal should be near the noise level. This is normally achieved by placing a neutral density filter before the PD.

When we obstruct the beam path after the photodiode the intensity read in the photomultiplier should be near its threshold of detection, at this point the polarizer is rotated until the PD is near saturation. If this does not happen, the density filter in front of the PD is adjusted and we uncover the beam path readjusting the high voltage (HV) applied to the PM. Then the correlation is done by sweeping the delay between the pulses. As this delay increases the adjustable polarizer rotates increasing the intensity, that gets into the device, not allowing the PM to reach saturation.

Like any other Michelson interferometer type device, the TOCC has the possibility of creating post pulses ("ghost pulses") that in reality do not exist in the input pulse. It is obviously important to avoid this measurement error. In order to do this several artifacts are implemented. In some devices where the polarizer creates pre/post pulses, the polarizer can be replaced by a periscope polarization rotator (for the adjustable polarizer) and by a Brewster polarizer for the fixed polarizer.

The wave mixing crystals are BBO type I, 100 μm thick (1 ps round trip time) wedged at 1°, in such a way that a pre-pulse created by multiple reflections in the crystal will be deviated from the main pulse. For other configurations see [42], pp. 10.

3.2.1. Beam splitter

In some designs it is not possible to choose the fraction of radiation that the beam splitter (BS) reflects [158]. However if we can choose the BS transmission we can optimize the two three wave mixing (TWM) processes.

Let's assume an intensity $I(t)$ entering the device the reflected part is $RI(t)$ and the transmitted part is $(1-R)I(t-\tau)$. The second harmonic intensity will depend on the square of the reflected part, $R^2 I^2(t)$ consequently the SFG signal will be proportional to $R^2(1-R)I(t-\tau)I^2(t)$, which is proportional to $R^2(1-R)$. We can maximize $R^2(1-R)$ as a function of R, which gives $R = 2/3$. In other words the beam used for SHG should have $2/3$ of the energy of the entry pulse and the fundamental pulse should have $1/3$ of the energy. Despite this value some authors prefer to have more intensity going into the SH arm of the device, such as 9:1 [42], rather than the 2:1 that the above calculation gives us.

3.2.2. Evaluation of the parametric approximation

We evaluate the domain where Eqs. (3.28) and (3.29) are valid. Mainly we are interested in the dependence of the output signal on the input seed intensity. The SHG and SFG processes are studied in Chap. 1 where we describe TWM processes in detail.

Here we ignore the complex propagation effects inside the crystal. We can do this because the objective of the diagnostic is not to give the temporal shape of the pulse. In other words the spectral phase introduced by the propagation inside the crystal will (for a fs pulse) have no effect on the temporal profile beyond the first few picoseconds. Phase modulation will create background radiation [167] unlike the smooth phase introduced by the BBO crystals. As seen above, the creation of radiation at 266 nm by other sources other than SHG+SFG can be discarded.

When we consider the analysis of OPA made in Sec. (1.4) we find that a factor that can compromise the validity of Eqs. (3.28) and (3.29) is saturation. Intuitively we may say that saturation is more easily achieved in SHG than in the SFG process. There is a larger amount of energy in the SHG process (due to the beam splitter that we have seen above) and so the nonlinear conversion efficiency should be greater. However, in some cases the two beams are focused on the SFG crystal and not on the SH crystal.

Independently of phase-matching conditions, an important quantity to retain is the nonlinear length (see Sec. (1.2)). As seen in Sec. (1.4), when the pulse propagates a distance of several nonlinear

lengths, the input beams can be depleted. In a first approach, we should make sure that the length of the crystal is smaller then the nonlinear length. If the crystal length equals the nonlinear length, the pulse intensity will be given by (see Sec. (1.2) of Chapter 1):

$$I_F(0) = n^3 \varepsilon_0 c \left(\frac{\lambda}{4\pi d_{eff} L_{CR}^{SH}} \right)^2 \simeq 6E22 \, W cm^{-2} \tag{3.33}$$

Not only is this 11 orders of magnitude above damage threshold [70], but it would also requires focusing of a 100 TW in a μm size spot. From the above calculation and from the fact that both crystals are BBO type I we safely say that the SFG crystal length is smaller then the nonlinear length. We resume this up by saying that:

$$L_{CR} \ll L_{NL} \tag{3.34}$$

In a plane wave approximation the SH intensity after propagation through the crystal is given by[1]:

$$I_{SH} = I_F(0)\eta_- sn^2 \left[\frac{L_{cr} 4\pi d_{eff}}{\lambda} \sqrt{\frac{\eta_+ I_F(0)}{\varepsilon_0 n^3 c}} \left| \frac{\eta_-}{\eta_+} \right| \right] \tag{3.35}$$

Eq. (3.35) is obtained by the same calculations presented in Sec. 1.4 in the OPA case. The two auxiliary values η_+, η_- are given by the following expressions:

$$\begin{aligned} \eta_- &= 1 + \frac{S^2}{8} - \sqrt{\left(\frac{S}{2}\right)^2 + \left(\frac{S^2}{8}\right)^2} \\ \eta_+ &= 1 + \frac{S^2}{8} + \sqrt{\left(\frac{S}{2}\right)^2 + \left(\frac{S^2}{8}\right)^2} \end{aligned} \tag{3.36}$$

where S is a measurement of the phase mismatch given by:

$$S = \Delta k L_{NL} \tag{3.37}$$

The dependence of the two auxiliary parameters on the phase mismatch is depicted in Fig. (3.10). The Jacobi sin elliptical function that we see in Eq. (3.35) can be expanded in a Taylor series. The second Taylor term is given by:

$$-I_F^4(0) \left[\frac{\eta_+ + \eta_-}{6} \right]^2 \left[\frac{1}{\varepsilon_0 n^3 c} \left(\frac{L_{cr} 4\pi d_{eff}}{\lambda} \right)^2 \right]^3 \tag{3.38}$$

---

[1] sn is the Jacobi sinus elliptical function, see Sec.(1.4) of Chap.(1) for more details.

Please note that this second term has a dependence in $I_F^4(0)$, so its relative magnitude will determine the validity of Eq. (3.28). We can put this in the form:

$$I_F(0) \ll \frac{3\varepsilon_0 n^3 c}{2(8+S^2)^2} \left(\frac{\lambda}{L_{cr}\pi d_{eff}}\right)^2 \qquad (3.39)$$
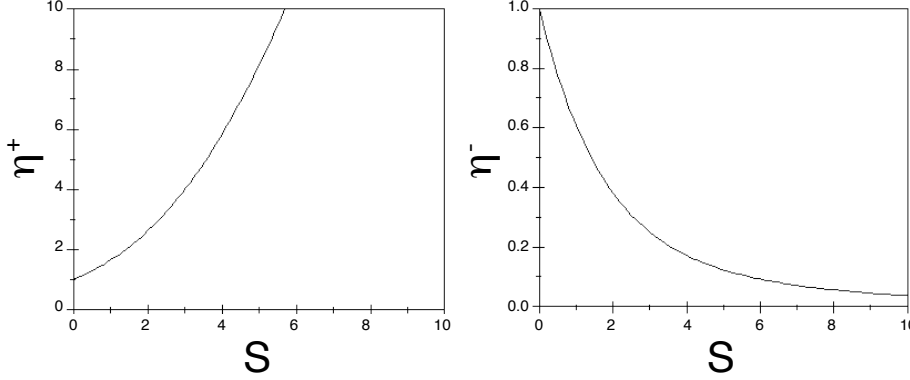
Figure 3.10.: Variation of the auxiliary parameters η_- and η_+ with phase-mismatch.

Comparing Eq. (3.39) with Eq. (3.33), we see that Eq. (3.39) is obeyed for every value of phase mismatch. The phase mismatch will only matter in the cases where the $\Delta k \gg L_{NL}^{-1}$. A similar analysis with a similar result can be made for the SFG. In both cases cases we can say that for BBO crystal thickness of less then 100 μm Eqs. (3.28) and (3.29) are fully valid.

In the rest of this section we analyze the dependence of the signal magnitude with the initial electric field intensity. There are three main features that the TOCC diagnoses:

➤ the pedestal around the main pulse, which is coherent with the pulse itself and is temporally extended due to imperfect compression, phase modulation and spectral modulations;

➤ spontaneous emission in the amplifier stages and its subsequent amplification. This ASE (amplified spontaneous emission) is going to constitute the background of the pulse intensity profile and can have several nanoseconds in duration;

➤ pre- and post-pulses that are due to imperfect extinction in regenerative amplifiers or multiple reflection in optical components will give rise to peaks in the intensity profile, that are essentially replicas of the main pulse but with smaller amplitudes.

It is more appropriate to use additional devices (other than the TOCC) in order to evaluate the first feature. The last two features are discussed in the following sections.

3.2.3. Pre- and post-pulses in a third-order correlation trace

One of the most important features that can be retrieved from a TOCC trace is the existence of pre/post pulses. In order to analyze of these features we will approximate them to delta Dirac functions. In fact if we look at the TOCC trace, the pre- and post-pulses seem like Dirac functions above a flat background that is normally due to ASE.

In the next two sections we will not consider the expression in Eq. (3.32). We re-normalize this measurement to its value at zero delay (this is how measurements appear and there is no loss of generality in doing so). Our signal is defined by Eq. (3.40).

$$S(\tau) = \frac{\int I^2(t)I(t-\tau)dt}{\int I^3(t)dt} \tag{3.40}$$

The TOCC signal of a single Dirac function is a Dirac function centered at zero delay (Eq. (3.41), Fig. (3.11)).

$$I(t) = A\delta(t) \Rightarrow S(\tau) = \delta(\tau) \tag{3.41}$$
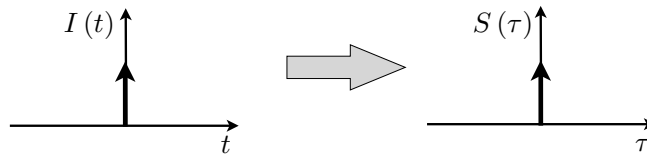
Figure 3.11.: TOCC of a Dirac function.

With two Dirac functions we obtain Eq. (3.42) and Fig. (3.12):

$$I(t) = A\delta(t) + B\delta(t-\tau_1) \Rightarrow S(\tau) = \delta(\tau) + A^2B\delta(\tau-\tau_1) + AB^2\delta(t+\tau_1) \tag{3.42}$$
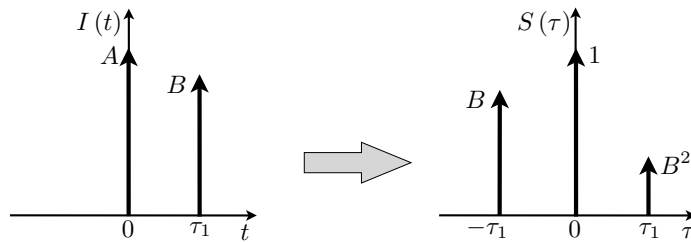
Figure 3.12.: TOCC of two Dirac functions.

We clearly see the creation of two new Dirac functions, one at τ_1 with the largest amplitude. For example a post-pulse with an intensity 10^{-3} times the intensity of the main pulse will create two features in the TOCC trace, one at 10^{-3} (centered at τ_1) and the other at 10^{-6} (centered at $-\tau_1$) of the maximum.

We have to take into consideration that the second feature might be under the background noise even if the first feature is not. In other words one might be able to see the feature with a magnitude of 10^{-3} (at τ_1) but not the other feature.

We assume that the measurement is normalized by $A^3 + B^3 = 1$. In most cases the signal at the zero delay is given by the main pulse itself, $A^3 = 1$. This is true for beams with a very high contrast, but not for beams with a low contrast.

For example, if a feature in a TOCC trace appears to represent a pulse with a magnitude of 1/2 the magnitude of the main pulse, this will not actually represent a secondary pulse with half the intensity of the main pulse. For low contrast measurements we have to solve two coupled equations and consider the contrast given at $+\tau_1$ and at $-\tau_1$:

$$(B/A)^3 + 1 = B/A S^{-1}(\tau_1) \tag{3.43}$$

$$(A/B)^3 + 1 = A/B S^{-1}(-\tau_1) \tag{3.44}$$

For instance, if the amplitude of both features (at $-\tau_1$ and at τ_1) is half the maximum magnitude of the feature at zero delay ($S(\tau_1) = 1/2$ and $S(-\tau_1) = 1/2$), then the intensity profile will simply consist of two pulses with the same intensity. However if one feature has magnitude of 0.5 and the other 0.3, then the secondary pulse will have an intensity of 61.8% of the main pulse. If the contrast is high enough the reading of TOCC traces is straightforward.

For an intensity profile composed of three delta functions we obtain Eq. (3.45) and Fig. (3.13).

$$\begin{aligned}
I(t) &= A\delta(t) + B\delta(t - \tau_1) + C\delta(t - \tau_2) \Rightarrow \\
S(\tau) &= \delta(\tau) + A^2 B\delta(\tau - \tau_1) + A^2 C\delta(\tau - \tau_2) \\
&\quad + AB^2\delta(\tau + \tau_1) + AC^2\delta(\tau + \tau_2) + \\
&\quad + B^2 C\delta(\tau - \tau_2 + \tau_1) + BC^2\delta(\tau - \tau_1 + \tau_2)
\end{aligned} \tag{3.45}$$

In practice the interactions between the secondary pulses are weak and sometimes are covered by the background noise. This simplifies the noise detection greatly.
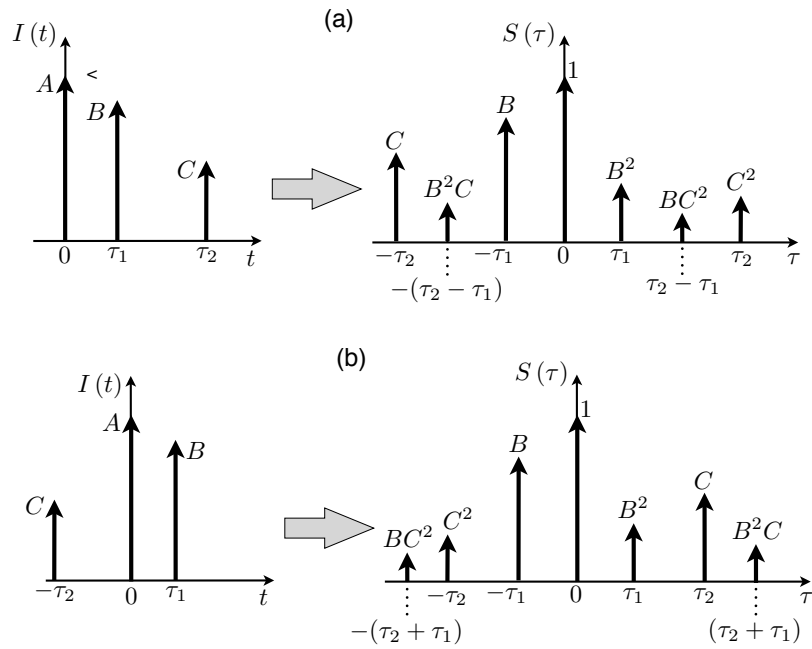
Figure 3.13.: TOCC traces of three pulses. (a) Both pulses are pre- or post pulses. (b) One pulse is a pre-pulse and the other is a post pulse.

Let us now apply the theory developed above in a concrete experimental measurement by taking into consideration the measurement taken at LOA (Fig. (3.14)):
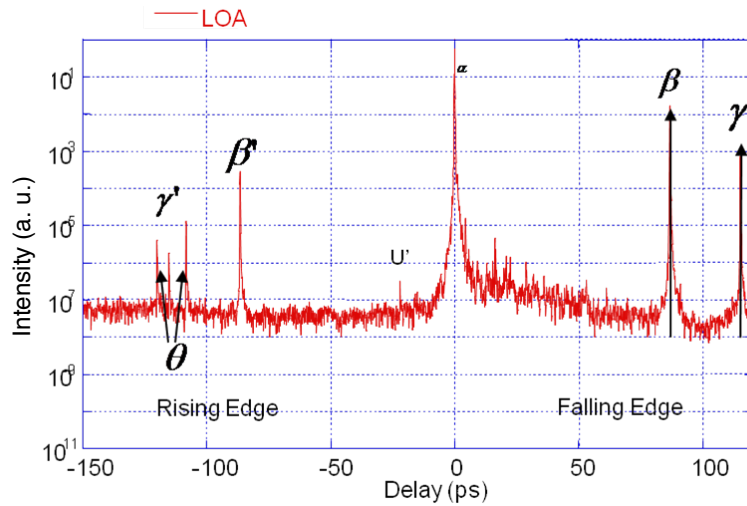
Figure 3.14.: TOCC trace done at LOA, *salle verte*.

Please observe that the features γ and β have a mirror image that is labeled γ' and β'. Both features occur at the same distance from the zero delay. Also, in a logarithmic scale we can perfectly see that features on the left side have half the magnitude of those on the right side.

3. Introduction to autocorrelations and third order cross-correlations

The post-pulse β is situated at 80 ps and its magnitude is 10^2 smaller then that of the main pulse. This post pulse also presents a secondary feature (β') at -80 ps at the 10^{-4} level. The post pulse γ is situated 120 ps from the main pulse at 10^{-3} of the main pulse. As expected, the corresponding secondary feature to appear at 10^{-6} of the main pulse and appears at -120 ps.

The peak designated by U' is actually a cross term between the secondary pulses β and γ. In other words, it's the measurement of γ made by β, $A_\beta^2 A_\gamma$. The other cross term, $A_\beta A_\gamma^2$, is smaller than the background noise. We calculate that this feature has a magnitude of 10^8.

The θ features appear to be two pre pulses situated at 110 ps and 130 ps with a magnitude of 10^{-5} and $10^{-5.2}$; their secondary features are below the background radiation: we expect them at 10^{-10} and 10^{-11}.

To resume Fig. (3.14), there are four secondary peaks visible, two pre-pulses and two post-pulses at levels $10^{-5.2}$, 10^{-5}, 10^{-3} and 10^{-2}.

Lets now analyze the equations for the general case of a train of N delta pulses. In this regard let's consider the pulse with the intensity A_0 to be the biggest one, in a high contrast field.

$$I(t) = \sum_{i=0}^{N} A_i \delta(t - \tau_i) \Rightarrow S(\tau) = \frac{\sum_{i,j=0}^{N} A_i^2 A_j \delta(t - (\tau_i - \tau_j))}{\sum_{i,j=0}^{N} A_i^2 A_j} \tag{3.46}$$

This signal is constituted by the following features (weak secondary pulses approximation) that should be analyzed from the most intense to the least intense:

➤ $S(0) = 1$, due to normalization;

➤ $A_0^2 A_i$ terms centered at $-\tau_i$ that determines the main feature of the secondary pulse i. If the amplitude of the TOCC feature is $1/c$ of the zero delay value then the secondary pulse is $1/c$ of the main pulse;

➤ $A_0 A_i^2$ terms centered at τ_i that determines the secondary feature of the secondary pulse i, if the TOCC feature is $1/c^2$ of the zero delay value then the secondary pulse is $1/c$ of the main pulse;

➤ If the contrast allows, the two last features have to appear and if they do not the trace has to be reinterpreted;

➤ $A_j^2 A_i$ terms centered at $\tau_j - \tau_i$. As long as the background noise allows, the pulses will correlate with each other. We need to account all these features, and verify that the features that appear are real pre-pulses and not correlations between secondary pulses.

3.2.4. ASE type background radiation

The ASE radiation appears as background noise in the TOCC trace. We assume several intensity profiles with different background radiation and try to find out their effect on the TOCC trace. We then give some specific examples.

The TOCC trace of a Gaussian pulse is a Gaussian profile[2] with a duration $\sqrt{3/2} \sim 1.22$ bigger than the initial pulse.

$$I(t) = A \exp - [t/\tau_0]^2 \Rightarrow S(\tau) = \exp - \frac{2}{3} [\tau/\tau_0]^2 \tag{3.47}$$
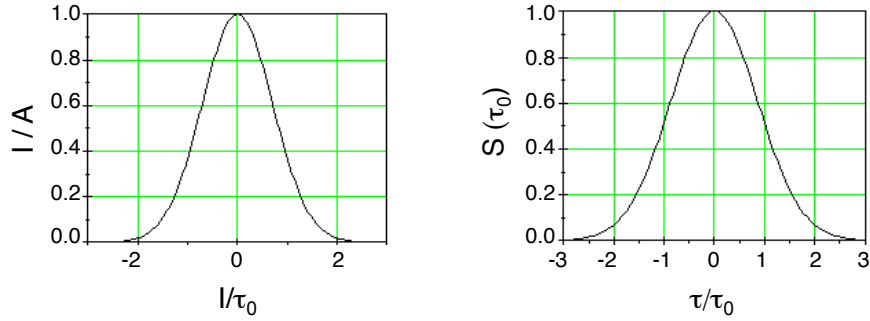
Figure 3.15.: Gaussian intensity profile and its TOCC profile.

We consider the same Gaussian profile but with a white noise background with amplitude n in relation to the maximum intensity amplitude, given in Eq. (3.48). Let us also consider that the PM averages over a certain window T. This time window is related to the response time of the detection, that is related to the PM response time (of the order of some hundreds of ps), and to the electronic amplifiers response time. In this case the TOCC signal is given by Eq. (3.49) below.

$$I(t) = A \left[\exp - [t/\tau_0]^2 + n \right] \tag{3.48}$$

$$S(\tau) = \frac{\exp - \frac{2}{3} [\tau/\tau_0]^2 + \sqrt{6} n . \exp - \frac{1}{2} [\tau/\tau_0]^2 + n \sqrt{\frac{3}{2}} + 3\sqrt{3} n^2 + \sqrt{3} n^3 (\frac{T}{\tau_0})}{1 + n \left[\sqrt{6} + \sqrt{\frac{3}{2}} \right] + 3\sqrt{3} n^2 + \sqrt{3} n^3 (\frac{T}{\tau_0})} \tag{3.49}$$

The term $\exp - \frac{2}{3} [\tau/\tau_0]^2$ represents the TOCC of the Gaussian pulse itself. The term $\sqrt{6} n . \exp - \frac{1}{2} [\tau/\tau_0]^2$ is the crossed Gaussian term that can also be represented as an intensity autocorrelation times the noise level; $n \sqrt{\frac{3}{2}}$ is the background line that gives us the ASE level.

---

[2]Please note that a Gaussian profile on a logarithmic scale seems like a quadratic function.

3. Introduction to autocorrelations and third order cross-correlations

In this case of a Gaussian pulse we see that a direct reading of the base flat line would be 1.22 times the actual ASE.

In Eq. (3.49) the noise term that varies as a n^2 function can be discarded. The importance of the term in n^3 however will be determined by the ratio between the integration time and the pulse duration, $\frac{T}{\tau_0}$. If the order of magnitude of the integration time is $10^{-10}s$ and the pulse duration $10^{-14}s$ this term would only be important if the ASE would be of the order of 10^{-4} of the pulse peak power. If this happens, the direct reading of a TOCC trace overestimates the ASE level.

Following the measurements done by A. Jullien [167] for several systems without temporal filtering, the ASE background noise is measured at a maximum of 10^{-5} of the peak pulse. In this case this term would only be important if the integration time is of the order of $10^{-4}s$, which is not realistic. In a realistic scenario we could have $n \sim 10^{-5}$ and $T \sim 10^{-5}s$. If this is the case the background measurement from the TOCC trace would be overestimated by approximately $\sim 14\%$ due to the $\sqrt{3}n^3(\frac{T}{\tau_0})$ term; the order of magnitude of the ASE level would remain the same though.

In Figs. (3.16), (3.17) and (3.18) we present the TOCC traces described by Eq. (3.49), calculated for several background noises and integration times. The red line represents the main pulse TOCC[3], the green line represents the cross Gaussian component, the blue line the flat noise line, and the pink line represents the $n^3\frac{T}{\tau_0}$ terms.
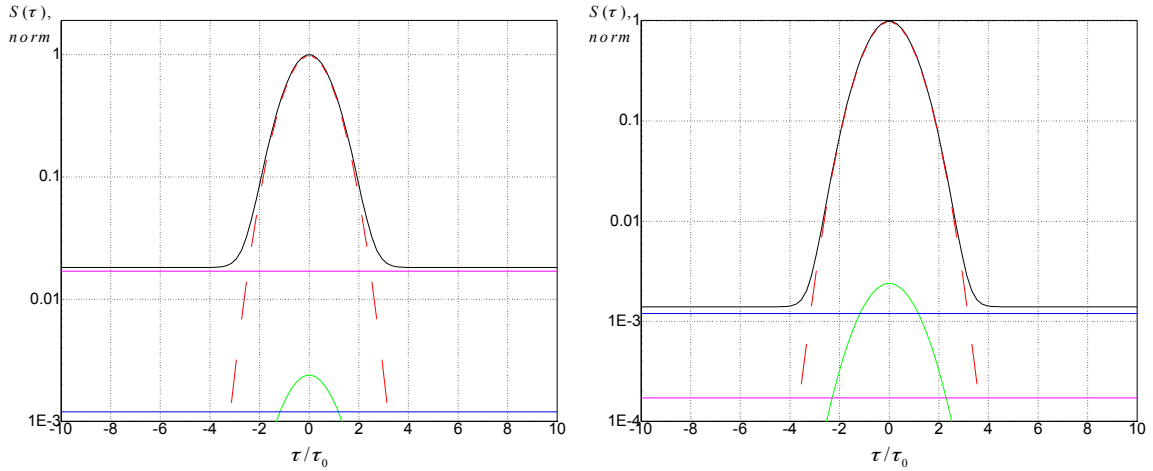
Figure 3.16.: TOCC profile in logarithmic scale for a noise level of $n = 1e^{-4}$, (right) $\frac{T}{\tau_0} = 10^7$, considering $\tau_0 = 10$ fs, $T = 0.1\,\mu$s and (left) $\frac{T}{\tau_0} = 10^5$ considering $\tau_0 = 10$ fs, $T = 1$ ns.

From Fig. (3.16) we see that for long values of the integration time (right plot) the ASE can be overestimated by the TOCC trace; the value of the contrast is of the order of 10^{-3}. We also see that the cross term (green line) is not important.

[3]All traces have been normalized as represented in Eq. (3.49).

118

Fig. (3.17) demonstrates that for contrast values of 10^{-4} the term in n^3 is not important. We also see that the crossed term (green line) is not important.
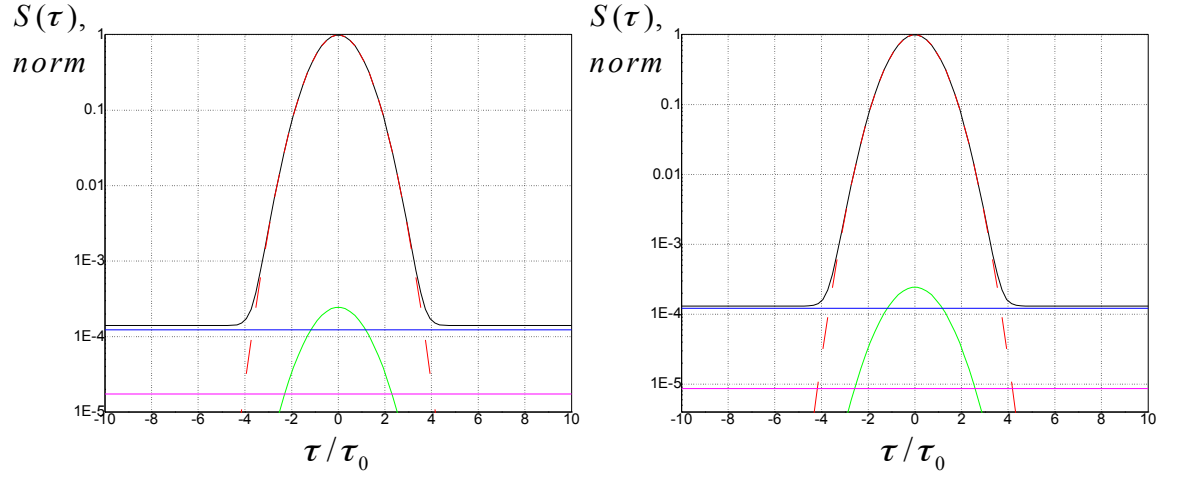
Figure 3.17.: TOCC profile in logarithmic scale for a noise level of $n = 1e^{-4}$, (right) $\frac{T}{\tau_0} = 10^7$, considering $\tau_0 = 10$ fs, $T = 0.1\,\mu$s and (left) $\frac{T}{\tau_0} = 10^5$ considering $\tau_0 = 10$ fs, $T = 1$ ns.

In Fig. (3.18) we see that the important terms are simply the main pulse correlation (red line) and the term $\sqrt{\frac{3}{2}}n$. The other terms are too small to be taken in consideration. The factor $\sqrt{\frac{3}{2}}$ is going to change with the intensity profile's ansatz in general. For a flat base line noise and a normalized intensity profile[4] $I_p(t)$ this factor is $\frac{\int I_p^2(t)dt}{\int I_p^3(t)dt}$.
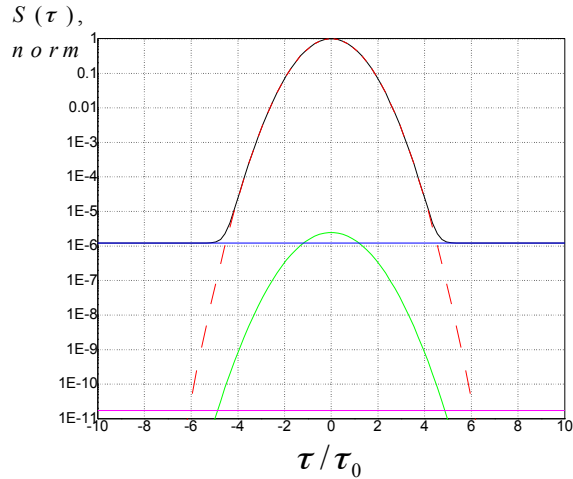
Figure 3.18.: TOCC profile in logarithmic scale for a noise level of $n = 1e^{-6}$, $\frac{T}{\tau_0} = 10^7$, considering that $\tau_0 = 10$ fs, $T = 0.1\,\mu$s.

We now study an intensity profile composed of two Gaussian functions, one representing the main

---

[4] $I(t) = I(0)\left[I_p(t) + n\right], I_p(0) = 1.$

119

pulse and the other representing a large feature with a low amplitude b and a characteristic duration τ_1. The intensity profile is given by:

$$I(t) = A \left[\exp - [t/\tau_0]^2 + b \exp - [t/\tau_1]^2 \right] \tag{3.50}$$

The TOCC is given by:

$$S(\tau) = \frac{\left[\begin{array}{l} \exp - \frac{2}{3} [\tau/\tau_0]^2 + \frac{\tau_2}{\tau_0} b \sqrt{3} \left(\exp - \left[(\tau/\tau_1)^2 \left(1 - (\tau_2/\tau_1)^2 \right) \right] + 2 \exp - \left[(\tau/\tau_0)^2 \left(1 - (\tau_2/\tau_0)^2 \right) \right] \right) + \\ + \frac{\tau_3}{\tau_0} b^2 \sqrt{3} \left(2 \exp - \left[(\tau/\tau_1)^2 \left(1 - (\tau_3/\tau_1)^2 \right) \right] + \exp - \left[(\tau/\tau_0)^2 \left(1 - (\tau_3/\tau_0)^2 \right) \right] \right) + \frac{\tau_1}{\tau_0} b^3 \exp - \frac{2}{3} [\tau/\tau_1]^2 \end{array} \right]}{1 + 3\sqrt{3} b \frac{\tau_2}{\tau_0} + 3\sqrt{3} b^3 \frac{\tau_3}{\tau_0} + b^3 \frac{\tau_1}{\tau_0}} \tag{3.51}$$

We can simplify this equation because $\tau_1 \gg \tau_0$, for which we obtain Eq. (3.54)

$$\tau_2^{-2} = 2\tau_0^{-2} + \tau_1^{-2} \ if \ \tau_1 \gg \tau_0 \Rightarrow \tau_2 = \frac{\tau_0}{\sqrt{2}} \tag{3.52}$$

$$\tau_3^{-2} = \tau_0^{-2} + 2\tau_1^{-2} \ if \ \tau_1 \gg \tau_0 \Rightarrow \tau_3 = \tau_0 \tag{3.53}$$

$$S(\tau) = \frac{\left[\begin{array}{l} \exp - \frac{2}{3} [\tau/\tau_0]^2 + \frac{\tau_1}{\tau_0} b^3 \exp - \frac{2}{3} [\tau/\tau_1]^2 + \\ + b \sqrt{\frac{3}{2}} \left(\exp - \left[(\tau/\tau_1)^2 \right] + 2 \exp - \left[\frac{1}{2} (\tau/\tau_0)^2 \right] \right) \end{array} \right]}{1 + 3\sqrt{\frac{3}{2}} b + 3\sqrt{3} b^3 + b^3 \frac{\tau_1}{\tau_0}} \tag{3.54}$$
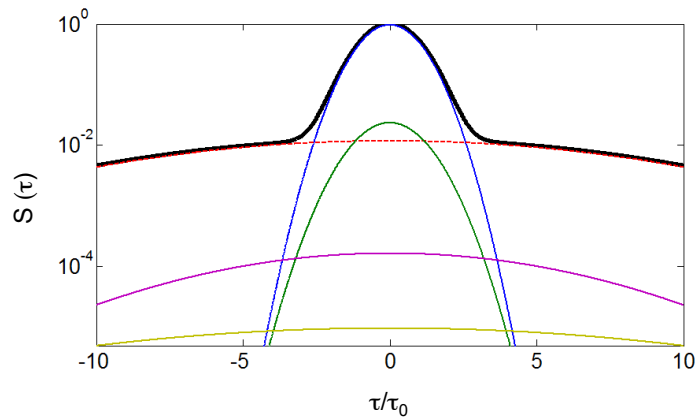
Figure 3.19.: Logarithmic TOCC trace and its components. (black line) TOCC trace as given by Eq. (3.51); blue, red, green, violet, yellow, are the first, second, third, fourth, and fifth terms of the sum in the numerator in Eq. (3.51).

Using Eq. (3.51) with $\tau_1 = 10\tau_0$ and $b = 10^{-2}$, we obtain the result shown in Fig. (3.19). As expected, only the first two terms in Eq. (3.51) are dominant in the TOCC trace.

3.2.5. Defining the pulse with a third-order cross correlation plus an intensity autocorrelation

We tried to retrieve as much information as possible from the TOCC trace. It is not possible to retrieve phase information from this trace alone and the device is not made to analyze the pulse in detail. However, we discovered that the TOCC trace and the intensity autocorrelation together completely define the intensity profile. The proof presented here is inspired in an article by Naganuma et al. [47]. In this work Naganuma et al. prove that the ensemble of power spectrum, SH power spectrum and intensity autocorrelation completely define the pulse shape. We mimic Naganuma et al. to prove that the TOCC and the intensity autocorrelation completely define the pulse shape.

Before presenting this demonstration, we will first try to correlate the IA trace with the TOCC trace. What we obtain experimentally are measurements proportional to $IA(\tau) = \int I(t)I(t-\tau)dt$ and to $TOCC(\tau) = \int I^2(t)I(t-\tau)dt$ and not the electric field intensity correlations themselves. We need to normalize one at the other's cost. This is best done by recalling the Fourier transform of each trace.

$$\mathscr{F}\{IA(\tau)\} = \left|\widetilde{I}(\omega)\right|^2$$
$$\mathscr{F}\{TOCC(\tau)\} = \widetilde{I}(\omega)\int \widetilde{I}(\Omega)\overline{\widetilde{I}(\Omega-\omega)}d\Omega \tag{3.55}$$

Let us also remember that the intensity is real and so the zero value of its Fourier transform also has to be real, even if in general the Fourier transform of the intensity is not. From this knowledge and from Eq. (3.55) we deduce Eq. (3.56) which relates both measurements. The retrieval of the intensity profile has to obey:

$$\mathscr{F}\{TOCC(\tau)\}(0) = \sqrt{\mathscr{F}\{IA(\tau)\}(0)}\int \mathscr{F}\{IA(\tau)\}d\Omega \tag{3.56}$$

Consider that the intensity is confined to a certain temporal window. In other words let us consider that the pulse is constrained in time between $-T$ and $+T$. Let us also consider that the intensity profile can be decomposed in its Taylor components, which can be done as precisely as we want [5]. The intensity can then be described as a Taylor series around $-T$:

$$I(t) = \sum_{j=1} \frac{I_j^-}{j!}(T+t)^j \tag{3.57}$$

---

[5]Note that the Taylor's theorem allows us to do this.

3. Introduction to autocorrelations and third order cross-correlations

and $+T$:

$$I(t) = \sum_{j=1} \frac{I_j^+}{j!}(T-t)^j \tag{3.58}$$

It is easy to intuit that it is possible to choose a time window where $I_0^+ = I_0^- = 0$. In other words can assume that the intensity in the extremes of the domain are zero.

The coefficients I_j^- are j^{th} order derivative of the functions at $t = -T$, $\left.\frac{\partial I(t)}{\partial t}\right|_{t=-T}$ and I_j^+ are $(-1)^j \left.\frac{\partial I(t)}{\partial t}\right|_{t=T}$. There is surely a mathematical relation between I_j^+ and I_j^- but we will not consider it.

The IA can be expressed as a function of the Taylor expanded intensity given above [6]:

$$IA(\tau) = \int I(t)I(t-\tau)dt$$
$$IA(\tau) = \sum_{j,k} \frac{I_j^+ I_k^-}{j!k!} \int_{-T+\tau}^{T} (T-t)^j(T+t-\tau)^k dt \tag{3.59}$$
$$IA(\tau) = \sum_{j,k} \frac{I_j^+ I_k^-}{j!k!}(2T-\tau)^{j+k+1}\int_0^1 (1-y)^j y^k dy$$

The integral $\int_0^1 (1-y)^j y^k dy$ [7] is a beta function $B(j+1,k+1)$:

$$\int_0^1 (1-y)^j y^k dy = \frac{j!k!}{(j+k+1)!} \tag{3.60}$$

So the intensity autocorrelation becomes:

$$IA(\tau) = \sum_{j,k} \frac{I_j^+ I_k^-}{(j+k+1)!}(2T-\tau)^{j+k+1} \tag{3.61}$$

We can compare this expression with an expansion of the intensiometric autocorrelation.

$$IA(\tau) = \sum_{m} \frac{A_{m+1}^+}{(m+1)!}(2T-\tau)^{m+1} \tag{3.62}$$

Recall that if the first nonzero pair of Taylor coefficients is j,k then the intensity autocorrelation will have its first nonzero term at $j+k+1$. From Eqs. (3.61) and (3.65) we obtain the relation between the intensity Taylor coefficients and the IA Taylor coefficients:

---

[6] $y = \frac{t+T-\tau}{2T-\tau}$.
[7] $y = \frac{t+T-\tau}{2T-\tau}$.

$$A_{m+1}^+ = \sum_{j<m} I_j^+ I_{m-j}^- \tag{3.63}$$

We find similar relations between the Taylor expansion of the intensity profile and the TOCC signal in the PM:

$$
\begin{aligned}
TOCC(\tau) &= \int I^2(t) I(t-\tau) dt \\
TOCC(\tau) &= \sum_{j,k,l} \frac{I_j^+ I_k^+ I_l^-}{j!k!l!} \int_{-T+\tau}^{T} (T-t)^{j+k} (T+t-\tau)^l dt \\
TOCC(\tau) &= \sum_{j,k,l} \frac{I_j^+ I_k^+ I_l^-}{j!k!} (2T-\tau)^{j+k+l+1} \int_0^1 (1-y)^{j+k} y^l dy \\
TOCC(\tau) &= \sum_{j,k,l} I_j^+ I_k^+ I_l^- \frac{(j+k)!}{j!k!} \frac{(2T-\tau)^{j+k+l+1}}{(j+k+l+1)!}
\end{aligned}
\tag{3.64}
$$

Similarly we can rewrite the TOCC signal as a Taylor expansion:

$$TOCC(\tau) = \sum_m \frac{B_{m+1}^+}{(m+1)!} (2T-\tau)^{m+1} \tag{3.65}$$

Where we have identified the coefficients B_{m+1}^+ with the Taylor expansion coefficients:

$$B_{m+1}^+ = \sum_{j,k\,(j+k<m)} \binom{j+k}{j} I_j^+ I_k^+ I_{m-k-j}^- \tag{3.66}$$

Eqs. (3.66) and (3.63) define the relations between the Taylor expanded intensity profile, and the Taylor expanded intensity autocorrelation and third-order cross correlation. If the intensity profile is univocally defined by IA and TOCC then the Taylor coefficients B_{m+1}^+ and A_{m+1}^+ have to univocally define I_j^+ or I_j^-. Here we prove they define both, not by inverting the sum operations in Eqs. (3.66) and (3.63) but by proving they can be inverted.

The first four orders of the Eq. (3.63) are:

$$
\begin{aligned}
A_1^+ &= I_0^+ I_0^- \\
A_2^+ &= I_1^+ I_0^- + I_0^+ I_1^- \\
A_3^+ &= I_2^+ I_0^- + I_1^+ I_1^- + I_0^+ I_2^- \\
A_4^+ &= I_3^+ I_0^- + I_2^+ I_1^- + I_1^+ I_2^- + I_0^+ I_3^-
\end{aligned}
\tag{3.67}
$$

In general the A_n^+ term can be decomposed in terms up to the $n-1$ order, that we designate as a_n^+,

and two terms subsequent terms:

$$A_{n+1}^+ = I_n^+ I_0^- + I_0^+ I_n^- + a_n^+ \tag{3.68}$$

The first four orders of Eq. (3.66) are:

$$
\begin{aligned}
B_1^+ &= I_0^+ I_0^+ I_0^- \\
B_2^+ &= 2I_1^+ I_0^+ I_0^- + I_0^+ I_0^+ I_1^- \\
B_3^+ &= 2I_2^+ I_0^+ I_0^- + I_0^+ I_0^+ I_2^- + I_1^+ I_1^+ I_0^- + 2I_0^+ I_1^+ I_1^- \\
B_4^+ &= 2I_3^+ I_0^+ I_0^- + I_0^+ I_0^+ I_3^- + 4I_2^+ I_1^+ I_0^- + 2I_0^+ I_2^+ I_1^- + 2I_1^+ I_0^+ I_2^-
\end{aligned}
\tag{3.69}
$$

We can also say that the A_n^+ coefficients can be decomposed in terms up to the $n-1$ order, b_m^+ :

$$B_{m+1}^+ = 2I_m^+ I_0^+ I_0^- + I_0^+ I_0^+ I_m^- + b_m^+ \tag{3.70}$$

We define the first Taylor coefficient of the intensity profile as:

$$I_0^+ = \frac{B_1^+}{A_1^+} \tag{3.71}$$

And:

$$I_0^+ = \frac{\left(A_1^+\right)^2}{B_1^+} \tag{3.72}$$

This can be used as initial condition in a mathematical induction proof. Now we have to prove that if all the coefficients up to the $(m-1, n-1)^{th}$ order are known, then the $(m,n)^{th}$ order term can also be known. For this purpose we use Eqs. (3.68) and (3.70) and reorganize them:

$$
\begin{bmatrix} B_{m+1}^+ \\ A_{n+1}^+ \end{bmatrix} = \begin{bmatrix} 2I_0^+ I_0^- & I_0^+ I_0^+ \\ I_0^- & I_0^+ \end{bmatrix} \begin{bmatrix} I_m^+ \\ I_n^- \end{bmatrix} + \begin{bmatrix} b_m^+ \\ a_n^+ \end{bmatrix}
\tag{3.73}
$$

From Eq. (3.78) we see that if the determinant of the multiplying matrix is different from zero then the system is always solvable:

$$
det \begin{bmatrix} 2I_0^+ I_0^- & I_0^+ I_0^+ \\ I_0^- & I_0^+ \end{bmatrix} = I_0^+ I_0^+ I_0^- = B_1^+
\tag{3.74}
$$

If the coefficient of the third-order cross-correlation B_1^+ is nonzero then the demonstration is done, since we proved by mathematical induction that if the coefficients B_n^+ and A_n^+ are known then the coefficients I_n^- and I_n^+ can be deduced. This demonstrates that if B_1^+ is nonzero then the intensity

autocorrelation plus the TOCC completely define the pulse intensity profile. However we saw above that we can choose a temporal window where the intensity at the extremes is zero. In this case, $I_0^+ = I_0^- = B_1^+ = 0$.

We have then to revisit the proof considering that the first nonzero coefficients are I_p^+ and I_q^-. In this case the first nonzero measured coefficients are A_{M+1}^+ and B_{N+1}^+, where $M = p+q$ and $N = 2p+q$.

$$B_{N+1}^+ = \begin{pmatrix} 2p \\ p \end{pmatrix} (I_p^+)^2 I_q^-$$
$$A_{M+1}^+ = I_p^+ I_q^-$$

(3.75)

Inverting the relations, if the first nonzero Taylor coefficients of the measured IA and TOCC are A_{M+1}^+ and B_{N+1}^+, then the first nonzero intensity Taylor coefficients have $p = N - M$ and $q = 2M - N$. From Eqs. (3.66) and (3.63) we can deduce the intensity Taylor coefficients as:

$$I_{p=N-M}^+ = \frac{[(N-M)!]^2}{[2(N-M)]!} \frac{B_{N+1}}{A_{M+1}}$$
$$I_{q=2M-N}^+ = \frac{[2(N-M)]!}{[(N-M)!]^2} \frac{(A_{M+1})^2}{B_{N+1}}$$

(3.76)

With Eq. (3.76) we prove that the firsts nonzero coefficients I_p^+ and I_q^- are defined. Now we have to prove that if I_{r-1}^+ and I_{s-1}^- are known then I_r^+ and I_s^- are also known. For this effect we rewrite Eqs. (3.66) and (3.63) as follows:

$$A_{m+1} = I_r^+ I_q^- + I_p^+ I_s^- + \alpha_m$$
$$B_{n+1} = 2 \begin{pmatrix} r+p \\ p \end{pmatrix} I_r^+ I_p^+ I_q^- + \begin{pmatrix} 2p \\ p \end{pmatrix} (I_p^+)^2 I_s^- + \beta_n$$

(3.77)

As done in Eq. (3.78) we can rewrite this as:

$$\begin{bmatrix} B_m^+ \\ A_n^+ \end{bmatrix} = \begin{bmatrix} 2 \begin{pmatrix} r+p \\ p \end{pmatrix} I_p^+ I_q^- & \begin{pmatrix} 2p \\ p \end{pmatrix} (I_p^+)^2 \\ I_q^- & I_p^+ \end{bmatrix} \begin{bmatrix} I_r^+ \\ I_s^- \end{bmatrix} + \begin{bmatrix} b_m^+ \\ a_n^+ \end{bmatrix}$$

(3.78)

Similarly the determinant of the matrix in Eq. (3.78) is nonzero:

$$det \begin{bmatrix} 2 \begin{pmatrix} r+p \\ p \end{pmatrix} I_p^+ I_q^- & \begin{pmatrix} 2p \\ p \end{pmatrix} (I_p^+)^2 \\ I_q^- & I_p^+ \end{bmatrix} = \left[2 \frac{(r+p)! \, p!}{(2p)! \, r!} - 1 \right] B_{N+1}^+ > 0, \ r > p$$

(3.79)

If $r = p$ the determinant is B_{N+1}^+. However per definition $r > p$, and so the value of the determinant

is always larger. Given that B_{N+1}^+ is by definition larger than zero Eq. (3.78) is always reversible.

We have therefore proven that a particular pair of intensity autocorrelation and third-order correlation corresponds one and only one intensity profile.

The retrieval of the intensity profile using this method is not practical due to numerical errors (Naganuma et al. said the same thing about their demonstration [150]), but the validity of the demonstration is not jeopardized by this fact.

Note that the TOCC signal given by $TOCC(\tau) = \int I^2(t)I(t-\tau)dt$ is analogous to the signal obtained with nonlinear Kerr effect in a third-order autocorrelation function as described by Major et al. [168] and also to the polarization gating and self-diffraction correlations studied by Kabelka et al. [169], and so this proof also extends to these cases.

3.2.6. Preliminary study on retrieval algorithms and intensity reconstruction using TOCC and IA

If we find the adequate algorithm we could find the intensity profile from the two quantities, like we can obtain from other measurements like FROG, SPIDER or D-scan. However there are specific contexts in which the combination of TOCC and IA might be unique. First the measurements are independent of the spectral shape and so in order to obtain the intensity profile in cases where the spectral shape is not well defined or cannot be measured with sufficient accuracy. Second and most importantly, both measurements can be taken with a dynamic contrast of several orders of magnitude (8 and 12 orders of magnitude respectively for IA and TOCC) [40, 54] . Because of this it is reasonable to assume that both measurements combined also contain enough information to reconstruct the intensity with a similar accuracy. This might be particularly interesting to retrieve the pedestal of the pulse that is many times due to imperfections in the pulse compression and that without nonlinear filtering can be 10^{-3} within a window of hundreds of femtoseconds [170, 171].

We present a preliminary retrieval of the intensity profile using TOCC and IA that uses the elitist genetic algorithm presented in Chap. (4). We remark that due to the first expression in Eq. (3.55) we can define a trial intensity temporal profile ($I_T(t)$) from the intensity autocorrelation ($IA(\tau)$) and a certain phase ($\Phi_T(\Omega)$), that is the phase of the Fourier transform of the intensity profile:

$$I_T(t) = \mathscr{F}^{-1}\left\{\sqrt{\mathscr{F}\left\{IA(\tau)\right\}}\exp i\left\{\Phi_T(\Omega)\right\}\right\} \tag{3.80}$$

As in Chap. (4) we know the magnitude of the Fourier transform but not the phase, we can transform this in a minimization problem in which $\Phi_T(\Omega)$ is the minimization argument. We need to minimize the difference between a target TOCC ($TOCC(\tau)$) and a trial TOCC ($TOCC_T(\tau)$) obtained using the trial intensity profile given by Eq. (3.80) (N is the number of points used to describe the TOCC):

$$\delta = \frac{1}{N} \sqrt{\sum_{i=1}^{N} (TOCC_T(\tau_i) - TOCC(\tau_i))^2} \tag{3.81}$$

In order to solve this minimization problem we used the algorithm presented in Fig. (4.29), with a mutation adaptation that is given in Fig. (4.40). In our algorithm we use a random number generator and describe the phase point by point. Please note that due to the fact that the intensity is real the phase is an odd function, and if the intensity profile is even than the phase is zero.

However, note that we are trying to obtain the intensity profile with a dynamic contrast of several orders of magnitude (preferably 8 orders of magnitude) because of this we also need to define the intensity spectral phase with the same precision ($1 - 10^8$ preferably). In the algorithm above we start with a random number generator and a point-by-point description of the phase, this creates imprecisions in the phase that might be hard to overcome. Due to this fact we design a second algorithm that applies a smooth function (3 point smooth function) to the spectral phase when the error given by the genetic algorithm seams to have converged. It is not guaranteed that this function creates a spectral profile with a smaller error.

A third algorithm was tested in these preliminary reconstructions attempts. We noticed that the phase of the Fourier transform of the TOCC and the phase of the Fourier transform of the intensity are similar. Because of this we searched for a phase that proportional to the phase of $\mathscr{F}\{TOCC(\tau)\}$ and that minimized the error given in Eq. (3.81). This gave an approximate result which served as an initial guess for the genetic algorithm.

Let's summarize this three algorithms:

1. Elitist genetic algorithm, using a point-by-point phase description and an adaptable magnitude mutation;

2. Consecutive smooth functions applied to an initial guess until we find a solution that minimizes the error with a smooth function;

3. Phase proportional to the phase of $\mathscr{F}\{TOCC(\tau)\}$.

In the cases that we have studied not all the algorithms gave satisfiable results, we claim to have preliminary results and not an algorithm that can retrieve the pulse intensity with several order of dynamics. However as we will present bellow these algorithms reproduce the pulse intensity with a dynamic of at least 10^4 in all tested cases.

In order to test the algorithm we generated several trial cases. We designed these cases, having in mind possible cases that we might find in an experiment. The first case was constituted by a main pulse (Gaussian pulse with 25 fs FWHM) and a background pedestal with a Gaussian profile that had a 10^{-3} magnitude near the main pulse and reached 10^{-6} magnitude in a time window of 2 ps.

We applied the first algorithm until it converged and then the second algorithm obtaining the result presented in Fig. (3.20) as retrieval A, we observe using this algorithm we could reconstruct the pulse with a until a contrast level of 10^{-6}, however the transition between the two Gaussian curves is not completely reproduced.
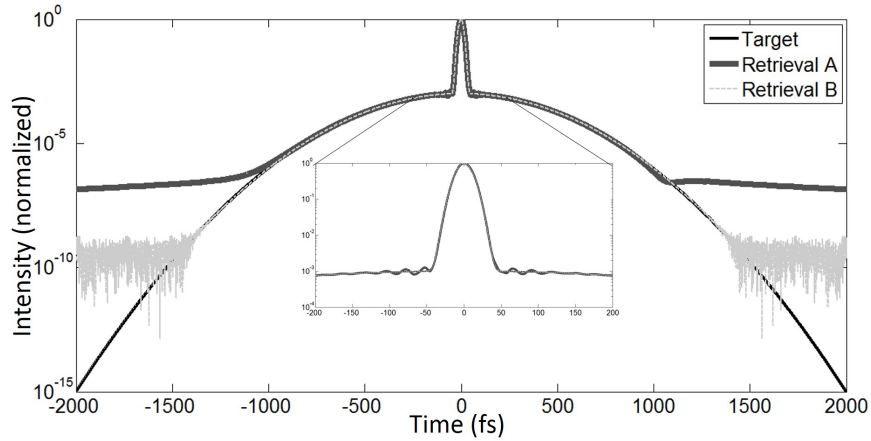
Figure 3.20.: Reconstruction of the first trial function (Gaussian pulse with a Gaussian background), the targeted intensity (black), the retrieved using the first and second methods (A, thick grey) and the retrieved using the third method (B, thin traced).

We then used the the third retrieval method which gave us a perfect reconstruction up to a level of 10^{-10}. In this case the phase of $\mathscr{F}\{TOCC(\tau)\}$ is also the phase that we want to retrieve, which means that 10^{-10} is the best possible result in this case, due to numerical errors (it is due to the noise induced by the FFT and IFFT through leakage [172], it varies from function to function).
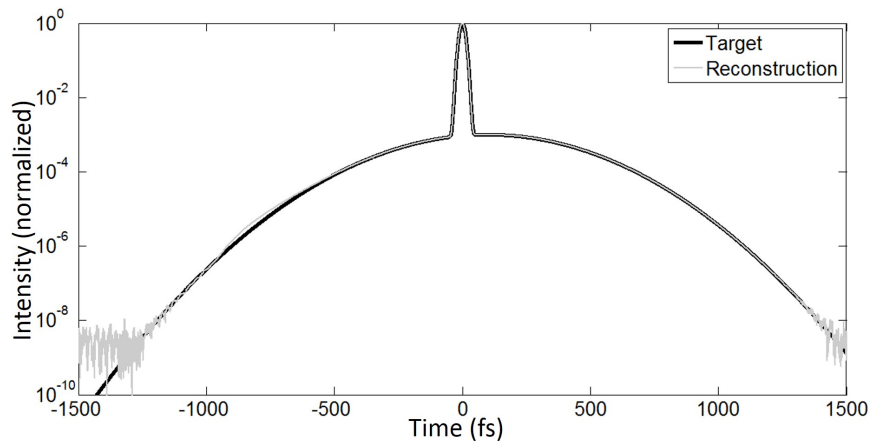
Figure 3.21.: Reconstruction of the second trial function (Gaussian pulse with an unsymmetrical Gaussian background), the targeted intensity (black), and the retrived one (grey). The results were obtained using the third and then the second algorithm.

The last case we used is an ideal situation because the pulse is symmetric, which means that the phase we are looking for is simply zero. We have to beware that in reality the pedestal and the main pulse will not be symmetrical and the TOCC will not give us a symmetrical shape. Due to this we choose an asymmetrical function for our second trial. We use same Gaussian main pulse and pedestal, but this time the pedestal will be deplaced from the main pulse by 100 fs. We reconstruct an unsymmetrical background which we can try to retrieve. For this case the best retrieval algorithm was to fist apply the third algorithm and then to apply the first algorithm, the result is given in Fig. (3.21). We can clearly see that apart from a small difference between -500 fs and -800 fs the pulse is reconstructed with a contrast of 9 orders of magnitude.

For our third trial case we use an experimental spectrum (5.9 Fourier limited) taken from a Femtolasers Rainbow oscillator. We first used the spectral shape without introducing any spectral phase, we obtain the pulse intensity as well as correspondents IA and TOCC. From these we try to reconstruct the pulse. The results are given in Fig. (3.22). As in the first case we used the first and second algorithm obtaining the result A and we used the third algorithm obtaining B.
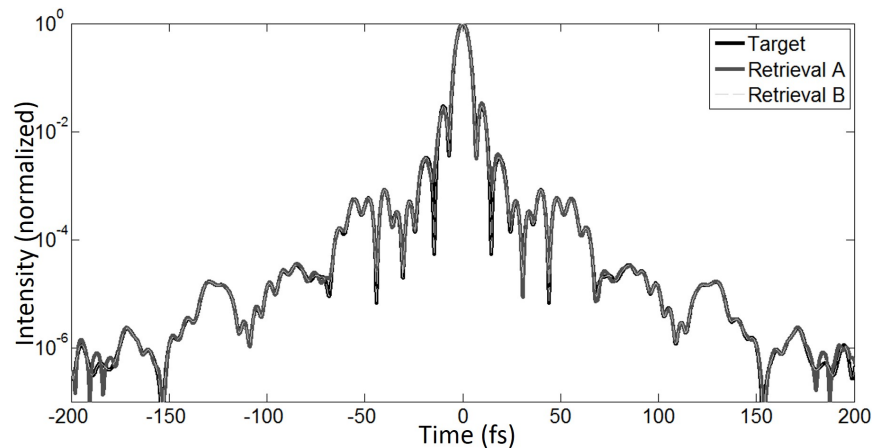
Figure 3.22.: Reconstruction of the third trial function, obtained using an experimental spectrum, the targeted intensity (black), the retrieved using the first and second methods (A, thick grey) and the retrieved using the third method (B, thin traced).

As in the first case this is a symmetrical intensity profile, which correct phase is a flat zero and so the second algorithm reproduces the profile perfectly. We can see in Fig. (3.22) that the first retrieval attempt can reconstruct the pulse with a contrast of 10^{-6}.

One of the things the algorithm should be able to reconstruct is the residual phase after compression (which normally causes the pedestal). In order to test the proposed algorithms we inputted a spectral phase with $\frac{\partial^5 \phi}{\partial \omega^5} = 5000 \, fs^5$, from the IA and TOCC we reconstruct the intensity. The results are given in Fig. (3.23), the retrieval A line is obtained using the first and second algorithm and the retrieval B line is obtained using the third and then second algorithm. In the first case we can reproduce the

pulse with a contrast of 10^{-5}, in the second case we can reproduce the intensity, but not the high frequency variations of the intensity.
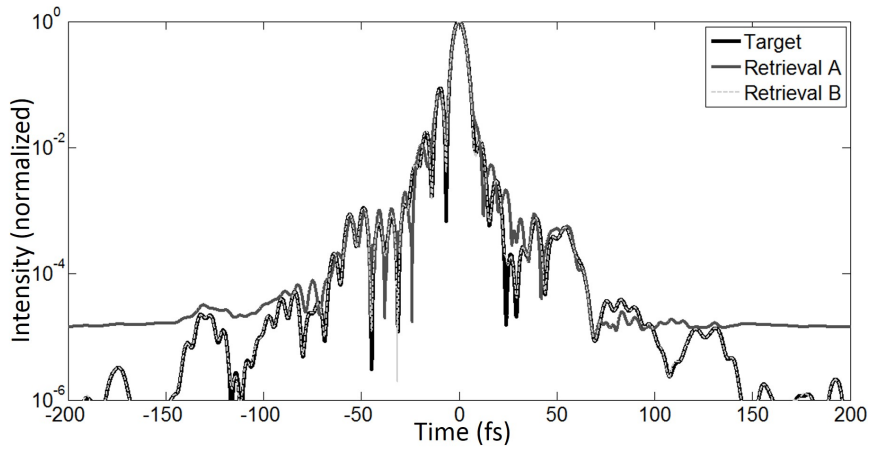
Figure 3.23.: Reconstruction of the fourth trial function, obtained using an experimental spectrum spectral phase with $\frac{\partial^5 \phi}{\partial \omega^5} = 5000 fs^5$, the targeted intensity (black), the retrieved using the first and second methods (A, thick grey) and the retrieved using the third method (B, thin traced).

As it can be observed, with the trial functions above, the algorithms we proposed were able to reconstruct the intensity profile with a contrast of 10^5.
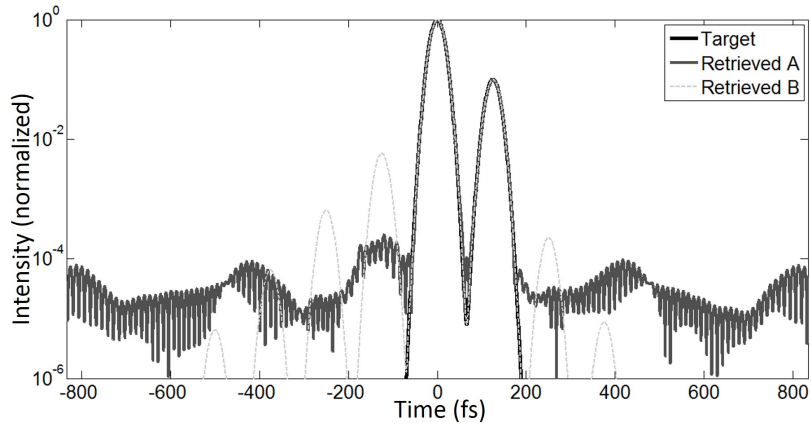
Figure 3.24.: Reconstruction of the fifth trial function, obtained using a Gaussian main pulse and a replica, the targeted intensity (black), the retrieved using the first method a smooth function and then the first method again (A, thick grey) and the retrieved using the third method (B, thin traced).

The last test case we used, is used to simulate what would happen with a post pulse. We used a main pulse with a 25 fs FWHM (Gaussian pulse) with a replica situated 100 fs from the first pulse, the results are given in Fig. (3.24). The best result in this case is given by using the first algorithm until it converges, and then a smooth function, afterwards we use the first algorithm again, we present this

in Fig. (3.24) as "Retrieved B". We also present the result obtained using the third retrieval method, we then tried to apply the first retrieval method to this result without obtaining a better result.

With this method we obtain a retrieved pulse that fits the targeted pulse with a dynamic range of four orders of magnitude. Please note that in the other cases a combination of the third retrieval method plus the first retrieval method achieved a smaller error, however in this last case the first and second retrieval methods worked better. We were nevertheless able to retrieve the pulse shape with a contrast of at least 10^4 in every case.

Even if there is work to do on what kind of algorithm we can use to retrieve the pulse, we can say that these simulations support the analytical proof given previously. The pulse intensity can be determined using a TOCC and a IA.

3.3. Conclusions

We make a quick summary of the properties of autocorrelations and autocorrelators. We discuss the application of a Gerchberg-Saxton algorithm to the intensity autocorrelation, and studied its convergency which is obtained after 10^3 cycles, this algorithm is sometimes used as a prelude to FROG reconstruction.

Afterwards we describe TOCC and the instruments that allow us to make a high contrast measurement of a laser temporal profile. In this measurement we measure a SFG signal with a PM and the intensity at the entrance of the correlator with a PD. We show that the high contrast of this measurement comes from using the full dynamics of the PM plus three times the dynamics of the PD. The ideal BS to be used is also discussed and it should have an intensity division of $2/3; 1/3$.

We then discuss the validity of the TOCC measurement to make high contrast measurements. We find that there are no optical reasons why the measures would be valid.

A series of trial functions is then used in order to better evaluate the TOCC trace. A series of pulse replicas is studied using a series of Dirac deltas and we conclude that each replica (with a high enough contrast) creates at least two features at symmetrical positions from the zero delay position, one with the intensity of the replica and the second one with the square of that intensity. It is possible to have crossed terms between several replicas if the contrast of the measurement and the ASE background allow it.

We then analyze several measurements where background noise was also input in order to study its effect on the TOCC trace. We conclude that for a high contrast pulse the background noise seen in the measurement is approximately $\frac{\int I_p^2(t)dt}{\int I_p^3(t)dt}$ higher than the actual background noise of the pulse, for a Gaussian this is approximately 1.22 (note that the order of magnitude is the same).

Afterward we presented a mathematical proof that the IA and the TOCC traces completely define the

intensity profile. Due to the fact that these measurements can be obtained with a higher contrast then most measurements. We then presented preliminary retrieval algorithms with which we retrieved the pulse intensity profile, the retrieved intensity profile was limited to a contrast of 10^{-4}, due to the reconstruction algorithm further work is needed to obtain the ideal retrieval algorithm and then apply it any experimental data. We conjecture that in the future this concept might be used to deconvolve complex background noise or the pedestal of a pulse intensity profile. This is supported by the fact that IA [54] and TOCC [40–44] have been obtained been obtained with a dynamic range of 8 and 12 orders of magnitude.

4. Spectral phase reconstruction via spectral intensity and interferometric autocorrelations using optimization algorithms

In this chapter we explore the potential of simple ultrafast measurements that have been available for some decades [46, 173], namely, interferometric autocorrelations (IAC), and direct spectral intensity measurements, (interferometric autocorrelations are also called second order interferometric auto-correlations, fringe resolved second-order autocorrelations, and fringe resolved second-harmonic autocorrelations). These diagnostics are not only easy to obtain but they also have known properties [47, 174] that we will explore in detail.

Ultrafast pulses are spectrally wide, and so the typical resolution of modern compact spectrometers is enough to measure the spectrum of these pulses. In other words, the Nyquist-Shannon sampling theorem [175] is easily obeyed in the spectral domain. In the time domain, interferometric auto-correlations imply a well balanced and aligned Michelson (or Mach-Zehnder) interferometer, with a sweeping arm, a nonlinear detector, and sufficient energy in order to make use of this detector.

In 1989, Naganuma et al. [47, 150] proved that interferometric second-order autocorrelations and field autocorrelations (which give us the spectrum alone) completely define the electric field. However, the retrieval method presented in [47], had convergence problems. The algorithm would only converge for a small number of cases and could not actually be used for pulse retrieval in a general case (a summary of this method is given in Sec. (4.4)).

In 2001, Chung and Wiener [48] used pairs of pulses, both symmetric and asymmetric, with a difference in FWHM duration of about 10% between pulses and pulse durations varying from 20 to 40 fs FWHM. They used pairs of pulses with the same spectral profiles and intensity autocorrelations, and observed the differences obtained in the IAC trace. Note that the variance of the intensity autocorrelations, $\Delta(IA)$, is inherently connected with the intensity variance, $\Delta(I)$, by $\Delta(IA) = \sqrt{2}\Delta(I)$ (see Section (3.1.2) of Chapter 3) and so it should be possible to determine the temporal variance of these pulses from the IAC trace.

Apart from confirming numerically that the IA and spectrum are not sufficient for pulse retrieval

(which was already known from other previous studies – see Chap. 3 and [148, 149]), Chung and Wiener, also compared the interferometric autocorrelations of the pulse pairs, detecting just slight differences between them. In conclusion, it seemed that despite the fact that interferometric autocorrelations combined with spectral intensity measurements completely defined the pulse, the sensitivity of these measurements to different spectral phases was insufficient to make it a viable pulse diagnostic. This issue was solved in 2002 by Hirayama et al. [49], who showed that by using a simple frequency filter it is possible to do measurements that are sensitive to slight changes in the pulse spectral phase (or intensity profile). This method is called MOSAIC (spectrally modified interferometric autocorrelation) and is presented in section (4.2) below.

In Chapter 3 we already exposed some features of IACs. In the first section of this chapter we will approach some more features of IAC traces in an attempt to identify all the information that can be extracted from this diagnostic alone.

4.1. Interferometric autocorrelations and correlators

In Chap. 3, we saw that interferometric autocorrelations are obtained with a nonlinear detector after a wavefront division interferometer. Right before the nonlinear detector the total field consists of two electric fields superimposed, given by $E(t) + E(t - \tau)$, where $E(t)$ is the electric field of one arm after passing through the beam splitter, a nonlinear vector is going to measure the square of the intensity that arrives at the detector.

Typically there are two kinds of second order nonlinear detectors:

➤ A SH nonlinear crystal, phase-matched for SH generation, plus a filter to block the fundamental frequency of the pulse, with a linear detector (photodiode, or a photomultiplier), to measure the SH signal. This involves a $\chi^{(2)}$ process within the nonlinear medium. This is the most classic detector and is used by several authors [146, 149, 150, 176]. A good discussion on the limits of this detector is given in [174][1].

➤ A two photon absorption photodiode (TPA), which must have a bandgap wider than the higher frequency in the fundamental beam, a high purity and high crystal quality, in order not to compromise the band structure (if the photodiode has too many impurities, defects in the band structure appear, which could result in linear absorption). This is effectively a third order nonlinear process. This detector works well for few cycle laser pulses [177] and is now commonly used [178].

---

[1]In this article, K. Yamane et al. used sub-10-fs FHWM pulses with a Gaussian spectral shape. Gaussian shapes have the smallest time-bandwidth product $\Delta\omega\Delta t$. However this is not indicative of the necessary spectral window to measure the pulse because the wings of the spectrum cannot be discarded (the intensity decreases with $\exp\left(-\left[\frac{\omega - \omega_0}{\Delta\omega}\right]^2\right)$). Our pulses may have a larger $\Delta\omega$ but the spectral window that needs to be covered by the detector is not larger.

In the second case, it is necessary to remove the glass window and resin that typically cover the sensitive surface of the photodiode in order for the beam not to be modified by these materials (which are dispersive). Also, to a smaller extent, the photodiode window/glass may have a partial reflection that can affect the S/N signal in the TPA process.

In both cases the resulting electric signal is usually submitted to some kind of amplification. Also, the detection system and the amplifier have to be such that an average is done over the pulses (for which the repetition rate is characteristically tens of MHz for oscillators and kHz for single-stage amplification lasers). This means that a low-pass filter is needed, and the cutoff frequency must be lower than the pulse repetition rate. However this filter must also be able to resolve the interferometric fringes of the second-harmonic electric field. Apart from these considerations, the detection time should be fast enough to detect possible slow thermal variations in the pulse profile. Therefore the cutoff frequency f_c is determined by:

$$\frac{4v_p}{\lambda_0} < f_c < f_{rep} \tag{4.1}$$

Where v_p is the velocity of the translation stage, λ_0 is the central wavelength fundamental beam, and f_{rep} is the repetition rate of the laser. In both types of detection, the IAC trace is given by the following expression:

$$IAC(\tau) = \int |E(t) + E(t-\tau)|^4 dt. \tag{4.2}$$

Note that the integration time is given by the inverse of the cutoff frequency, $1/f_c$.

In Chap. 3 we showed that IAC traces have a 1 to 8 contrast and can be decomposed in several Fourier terms (Eq. (4.6)). Before discussing those terms we should first discuss the nature of the nonlinearity, in particular the spectral acceptance of the detector which has to suit to the large spectral bandwidth of the ultrafast pulse.

For a second-harmonic detector the phase matching conditions are of utmost importance. In an ideal situation the conversion efficiency should be the same for the entire spectrum. However this is not the case and we need to address it. When calculating the phase matching, the phase-mismatch vector Δk is always multiplied by the path in the crystal, $\Delta k.z_{crystal}$, and so it is possible to decrease importance of the phase matching by decreasing the crystal width. Not only, can we choose an appropriate crystal in order to have the smallest possible Δk, but we may also reduce the beam path using the thinnest possible crystal. For a sub 30 fs pulse a BBO crystal would have to be thinner than 20 μm, a sub 10 fs pulse would have to be measured with a 10 μm crystal and a sub 7 fs pulse would have to be measured with a 5 μm crystal in order to have a sufficiently flat conversion efficiency.

Saturation must be avoided both in the TWM process ($z \ll L_{NL}$) and in the signal amplifier. For the

second-harmonic, in order to know if saturation has been reached, it is useful to use the nonlinear length equation that is given in the introduction and repeated here:

$$L_{NL}^{SH} = \frac{\lambda_1 n_1}{2\pi\chi} \sqrt{\frac{\varepsilon_0 n_0 c}{I_1(0)}}.$$
(4.3)

Using this we see that saturation of the SH process is not a problem. For instance, attaining saturation, in a 5 μm thin crystal would mean breaking the BBO damage threshold.

In two photon absorption it is necessary to avoid linear absorption, in order to measure the IAC trace and improve the signal-to-noise ratio of the MOSAIC trace. In some cases this can be done by using optical high-pass wavelength filters, (this will unavoidably change the pulse temporal shape due to dispersion and the spectral cutoff). Nevertheless, linear absorption does not affect the MOSAIC measurement described in the next section, and so it does not affect pulse reconstruction. However, the presence of linear absorption will diminish the signal intensity and the S/N ratio of our measurement. Linear absorption can be avoided using a photodiode adequate to the laser spectral shape, that must obey the following equations:

$$\frac{\lambda_{max}^B}{2} < \lambda_{max}^{PD} < \lambda_{min}^B$$
(4.4)

$$\lambda_{min}^{PD} < \frac{\lambda_{min}^B}{2}$$
(4.5)

where λ_{min}^{PD} and λ_{max}^{PD} are minimum and the maximum wavelengths that the photodiode absorbs and λ_{min}^B and λ_{max}^B are the minimum and maximum wavelengths of the laser.

The Fourier terms of the interferometric autocorrelation are given by:

$$IAC(\tau) = 2DC + 4IA(\tau) + 8X(\tau) + 2SHAC(\tau)$$
(4.6)

This expression is also obtained in Chap. (3). Each one of the terms on the right-hand side has the same weight (the same integral). Given this: the DC component has half the weight of the intensity autocorrelation $IA(\tau)$ (in Fourier space the DC component is a single point at zero frequency). The cross component, $X(\tau)$, at the pulse central frequency has twice the weight, and the second-harmonic autocorrelation ($SHAC(\tau)$) has the same weight as the DC component.

In the following figures we will try to show the main characteristics of the IAC in time and frequency. Figs. (4.1) (a), (b) and (d) correspond to a Gaussian pulse[2], the IAC is represented in Fig. (4.1) (a),

---

[2]The spectral Gaussian shape of the "Gaussian pulse" presented in Fig. (4.1) is centered at 950 nm with a Fourier limited pulse duration of 7.58 fs FWHM.

Fig. (4.1) (b) is the Fourier transform of the IAC. In Fig. (4.1) b), five distinct zones are visible. DC is the Fourier transform of the DC component, which is only a Dirac term at zero frequency. The IA term is the Fourier transform of the intensity autocorrelation which is centered at zero frequency. The X term is the Fourier transform of the crossed terms (centered at the central frequency) and the SH term is the Fourier transform of the second harmonic autocorrelation (centered at twice the central frequency).
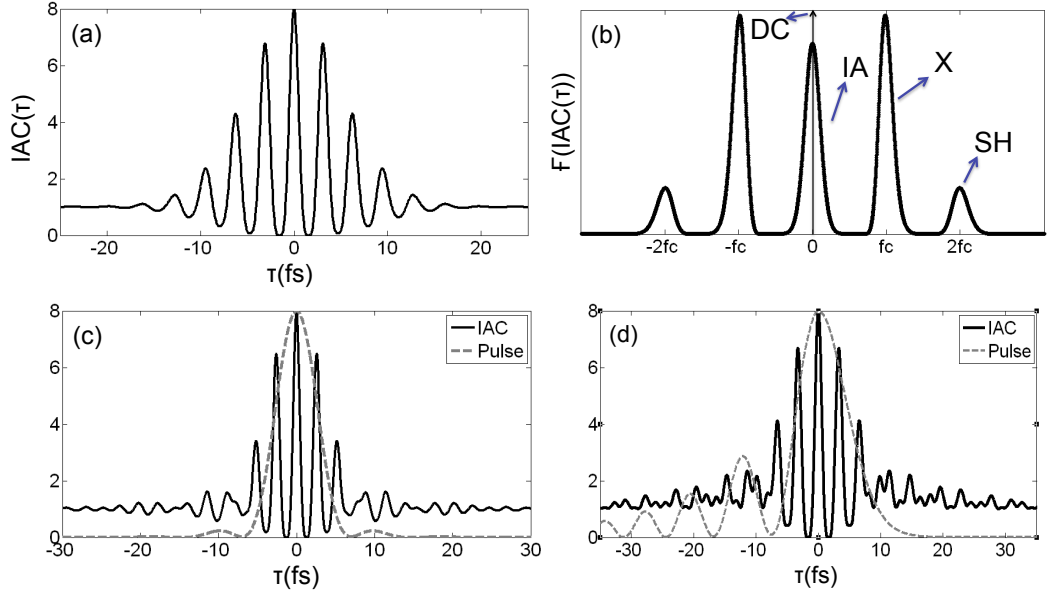
Figure 4.1.: (a) Autocorrelation of a Fourier limited Gaussian pulse. (b) The Fourier transform of (a) showing the DC component, the IA term, the crossed term X, and the SH term. (c) Fourier limited IAC using a experimental spectral shape. (d) Intensity of a chirped Gaussian pulse with post-pulses and its IAC.

In this chapter whenever we refer to a second, third or forth order chirp we are referring to the components of the second $\left(\frac{\partial^2 \phi(\omega)}{\partial \omega^2} \Big|_{\omega=\omega_0} \right)$, third $\left(\frac{\partial^3 \phi(\omega)}{\partial \omega^3} \Big|_{\omega=\omega_0} \right)$ and fourth $\left(\frac{\partial^4 \phi(\omega)}{\partial \omega^4} \Big|_{\omega=\omega_0} \right)$ order derivatives of the spectral phase at the central frequency.

The spectral phase is defined by:

$$\phi(\omega) = \sum_n^N \frac{1}{n!} \frac{\partial^n \phi(\omega)}{\partial \omega^n} \Big|_{\omega=\omega_0} (\omega - \omega_0)^n \tag{4.7}$$

Figs. (4.1) (c) and (d) correspond to beams with pre- and post-pulses. In (a) we use a Gaussian spectral shape and an unchirped beam to calculate the IAC. However it is possible to have pre-pulses and post-pulses by two means: an unchirped pulse with a non smooth spectral shape or by introducing a spectral phase. Fig. (4.1) (c) shows the intensity profile and the IAC of a Fourier transformed pulse with a pre-pulse and a post-pulse, (the spectral shape used is an experimental spectral profile, from

the output of a Femtolasers Rainbow laser oscillator [145]). Fig. (4.1) (d) corresponds to a chirped Gaussian pulse with a series of post pulses. By comparing (c) and (d) it's easy to deduce that the wings on the side of the central autocorrelation profile are due to pre and/or post pulses. However, from the IAC alone we cannot know if the reason behind this is a non smooth spectral shape or a chirped pulse.

In the following pages we will analyze the influence of the spectral phase on a pulse and on its IAC trace. A quadratic phase or a pure linear chirp increases the pulse FWHM, as shown in the introduction Sec. (D.1). For highly chirped pulses (quadratic phase) the pulse profile in time mimics the spectral profile, as shown in Fig. (4.2). Almost all the experimental spectral profiles referred in this chapter are given by Fig. (4.2).
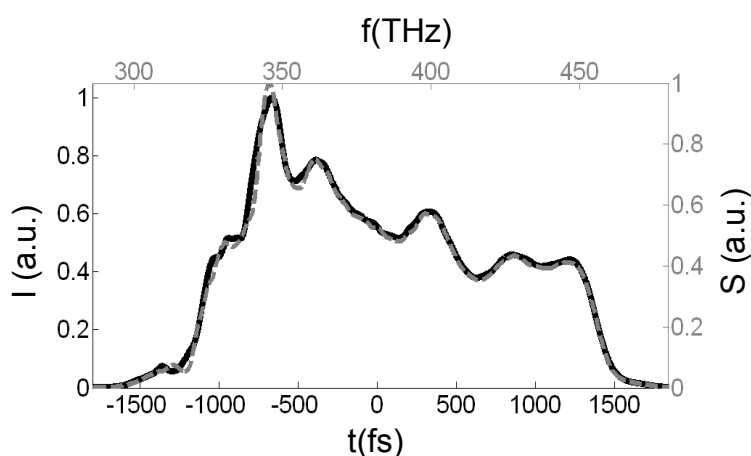
Figure 4.2.: Highly quadratically chirped pulse in time (black continuous line) and spectrum (traced gray line).

In the case of highly chirped pulses the frequencies are widely distributed and the profile of the IAC is going to be dominated by the intensity autocorrelation as shown in Fig. (4.3). In the wings of the IAC trace there is no dominant interference between the pulses because the frequency that makes up the signal in these wings is too different. Third-order chirp will create several pre and/or post pulses; the FWHM duration of the pulses will also increase. The effect that the pre- and post-pulses have on the IAC traces is seen in Fig. (4.1) (d).

More examples are given in Fig. (4.4) with several pulses with cubic chirp and its correspondent IAC traces. Fig. (4.4) also shows fields with a cubic spectral phase (more precisely with the pre and post pulses) that present wings on their corresponding IAC traces. Nevertheless in practice the differences observed between the traces in Fig. (4.4) mean that the diagnostic is almost insensitive to this phase.

The traces in blue are presented with a duration of 20.0/10.0 fs because the the pre-pulse maximum value is more than half of the pulses maximum value which means that counting only the main pulse we would have 10 fs FWHM but counting with the pre-pulse we would have 20 fs FWHM.
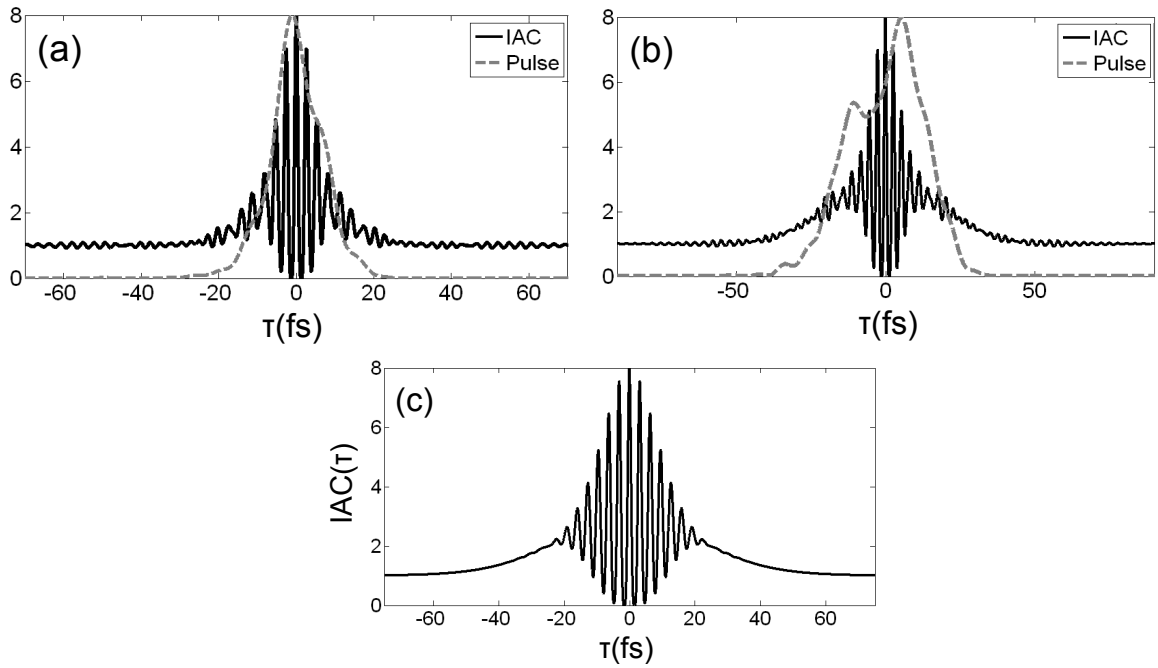
Figure 4.3.: IAC traces of pulses with a quadratic spectral phase. (a)-(b) correspond to pulses with an experimental spectrum and a Fourier limit duration of 5.98 fs. (a) 13.8 fs FWHM pulse duration and 27 fs^2 of second order chirp. (b) 30.4 fs FWHM pulse duration with a chirp of 50 fs^2. (c) pulse with a Gaussian spectral shape, 31 fs FWHM with a chirp of 90 fs^2, the pulses Fourier limited duration is 7.8 fs.

With a fourth order chirp the pulse duration increases and a pedestal is created. This dispersion creates a pulse background containing frequencies in the extremes of the spectrum.
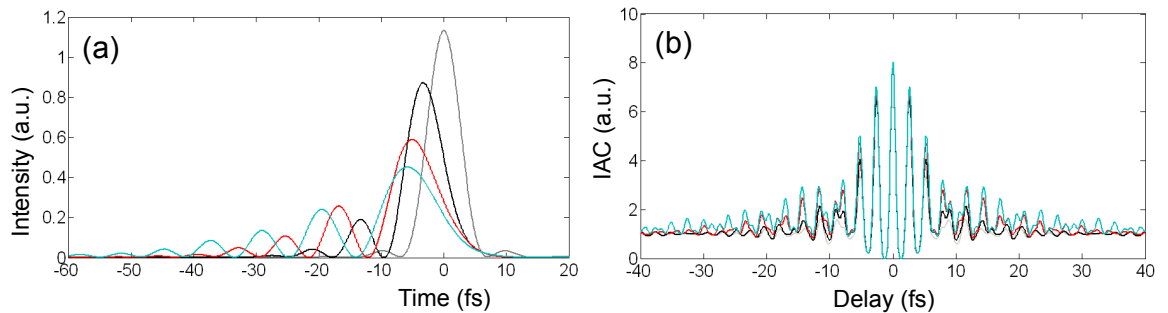
Figure 4.4.: (a) Temporal intensity of pulses with an experimental spectrum and increasing cubic phases. The FWHM pulse durations are: 5.98 (gray), 6.2 (black), 8.6 (red), and 20.0/10.0 fs (blue) (see text for further details). with corresponding (b) corresponding IAC traces. The corresponding third order chirp values are: 0, 75, 300, and 450 fs^3

In Fig. (4.5) we see the effect of the fourth order spectral phase on the wings of the IAC trace. It is possible to see that as this spectral phase increases the pulse interference at the wings of the IAC

trace also increases.
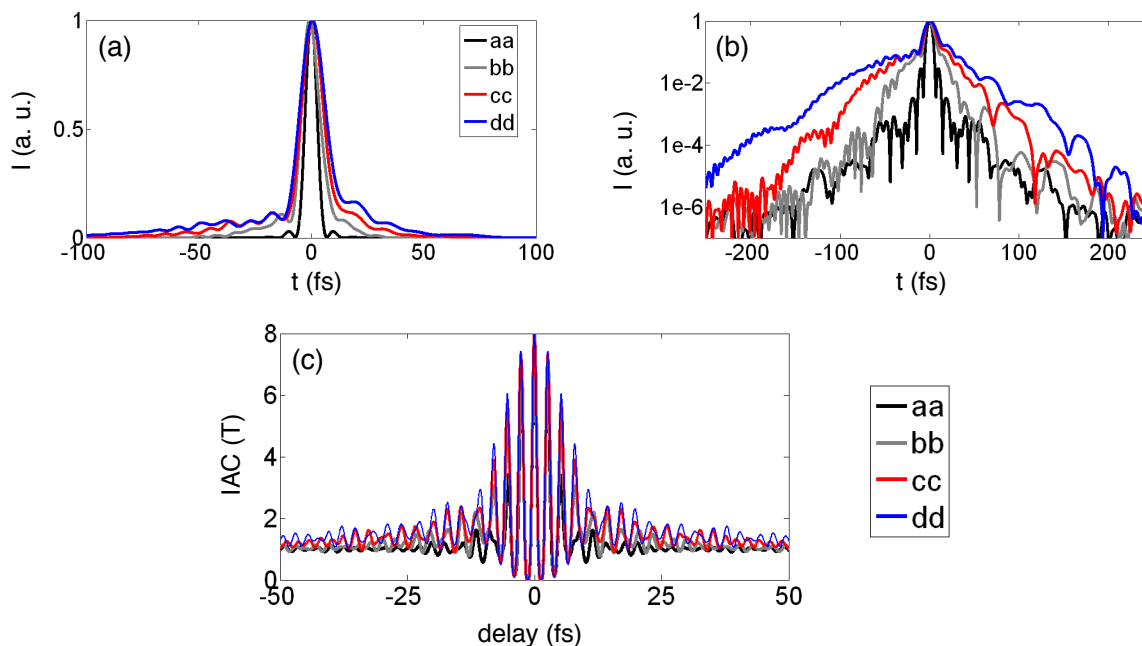
Figure 4.5.: Pulses with fourth order chirp. aa to dd represent pulses with 5.98 fs, 9.46 fs, 11.28 fs 13.40 fs, fourth order chirp values of $0\,fs^4$, $1800\,fs^4$, $3600\,fs^4$, $5400\,fs^4$. Intensity profile on (a) a linear and (b) a logarithmic scale. (c) The corresponding IAC traces.

4.2. Spectrally modified autocorrelations, MOSAIC

IAC traces have been used for pulse measurement since Diels et al. introduced them in 1978 [173]. In 1989, K. Naganuma et al. [47] proved that IAC together with the spectral intensity completely defines the pulse shape. Naganuma et al. also proved that it is possible to determine the pulse direction, and the signal of the spectral phase [150]. More specifically we need the intensity autocorrelation and the second harmonic autocorrelation both of which can be retrieved from the IAC trace, see Fig. (4.1) b).

In 2001 Chen et al. [48] showed that IAC has little sensitivity to changes in the pulse profile. In 2002 Toshiyuki Hirayama and Mansoor Sheik-Bahae [49] created a diagnostic that has a much bigger sensitivity to the spectral phase but it is built with an IAC trace, the MOSAIC.

MOSAIC is a measurement that uses an interferometric autocorrelation, and puts it through a digital, or analogue frequency filter. In fact this filter is designed to obtain maximum sensitivity to the chirp or to the spectral phase.

In Fig. (4.6), we see that the crossed IAC term is similar to the spectral intensity shape itself. So it's quite obvious that this term will be affected just slightly by the spectral phase. This term can simply be ignored, since it is not required to completely define the pulse.
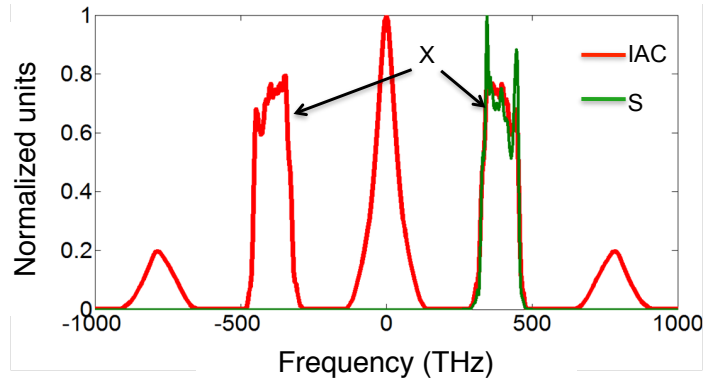
Figure 4.6.: IAC Fourier transform with the superimposed spectral intensity, S. The crossed term, X, is similar to the spectral intensity itself.

The use of frequency filters in autocorrelations was first proposed by Sheik-Bahae in 1997 [179], and it was first applied to IAC traces by the same team in 2002 [49]. An auxiliary quantity, independent of the crossed term, was defined by:

$$MOSAIC_n(\tau) = 4IA(\tau) + 2nSHAC(\tau) \tag{4.8}$$

We have to define n (Eq. (4.8)) in order for the measurement to be highly sensitive to changes in the spectral phase. It is obvious that this occurs is given when both terms (IA and SH) have the same weight, i.e., for $n = 2$.

In practice this will mean applying a spectral filter to the IAC trace: between $\left[-\frac{3}{2}f_c, \frac{3}{2}f_c\right]$ with weight 1, to $\left[\frac{3}{2}f_c, \frac{5}{2}f_c\right]$ and $\left[-\frac{5}{2}f_c, -\frac{3}{2}f_c\right]$ with weight 0, and to $\left[\frac{5}{2}f_c, \frac{7}{2}f_c\right]$ and $\left[-\frac{7}{2}f_c, -\frac{5}{2}f_c\right]$ with weight 2, where f_c is the carrier frequency of the electric field. The MOSAIC trace in time is then given by:

$$MOSAIC(\tau) = 2\left[IA(\tau) + SHAC(\tau)\right] \tag{4.9}$$

Compared to IAC the MOSAIC trace is more sensitive to spectral phase changes. As shown in the following examples, Fig. (4.7), shows the IAC and MOSAIC traces of several pulses with an increasing linear chirp. Clearly the IAC traces present a much smaller sensitivity to the pulse shape than the MOSAIC trace.

Let us now study systematically the effect that several terms of a Taylor expanded spectral phase have on the MOSAIC trace.

Fig. (4.8) below shows a comparison between IAC and MOSAIC traces of linearly chirped pulses. We see that the base line of the MOSAIC traces clearly moves upward as the chirp increases.
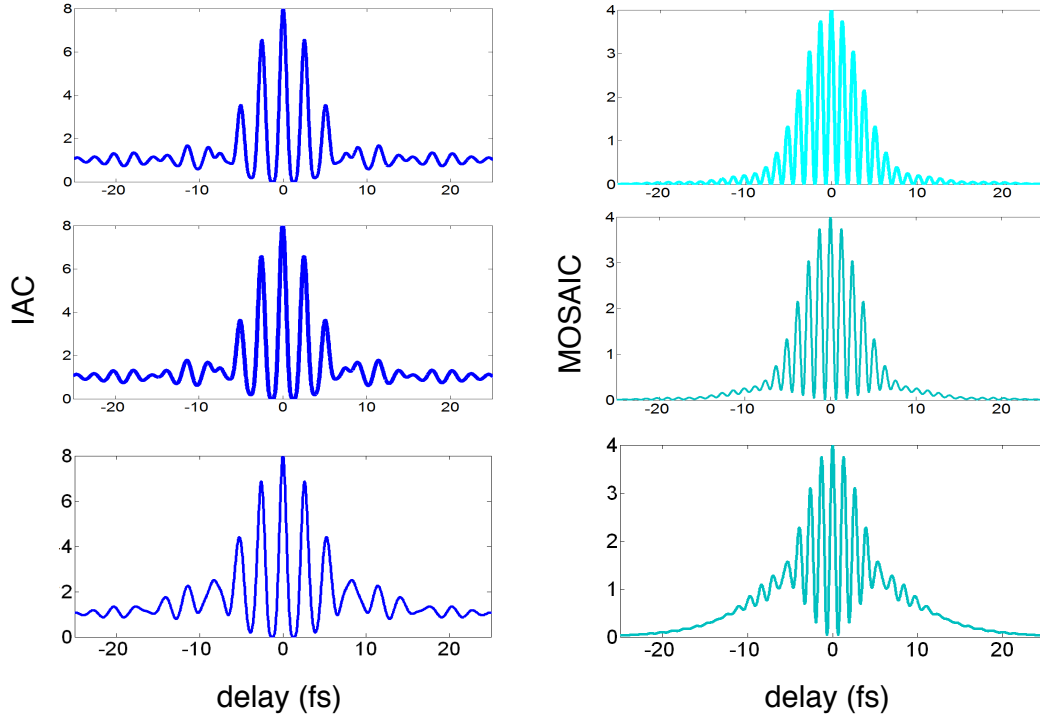
Figure 4.7.: Comparison of IAC (a), (c) and (e) and MOSAIC (b), (d) and (f) traces. The pulses' FWHM are: 5.98 fs (Fourier limit), 6.16 fs, and 8.05 fs (chirp values of $0\,fs^2$, $7.2\,fs^2$, and $20\,fs^2$).

In Fig. (4.8) the base line of the MOSAIC traces, changes with an increase in quadratic chirp. Considering an electric field given by $E(t) = A(t)\exp(i\phi(\omega))$ the MOSAIC baseline is given by the difference [49]:

$$MOS_{base}(\tau) = IA(\tau) - \sqrt{(IA_{\cos}(\tau))^2 + (IA_{\sin}(\tau))^2} \qquad (4.10)$$

Where,

$$IA_{\cos}(\tau) = \int I(t)I(t-\tau)\cos(2\Delta\phi(t,\tau))dt$$
$$IA_{\sin}(\tau) = \int I(t)I(t-\tau)\sin(2\Delta\phi(t,\tau))dt \qquad (4.11)$$

In practice this difference is hard to calculate (due to sampling demands), but in order to evaluate the sensibility of this feature of the MOSAIC trace we design an equivalent feature in the Fourier domain. Applying a Fourier transform to both terms in Eq. (4.10) we get:

$$FMOS_{base}(\omega) = |\widetilde{I}(\omega)|^2 - |\widetilde{SH}(\omega)||\widetilde{SH}(-\omega)| \qquad (4.12)$$

Where the following identities were used:

$$\mathscr{F}\{IA_{\cos}(\tau)\} = \frac{\left|\widetilde{SH}(\omega-2\omega_0)\right|^2 + \left|\widetilde{SH}(2\omega_0-\omega)\right|^2}{2}$$
$$\mathscr{F}\{IA_{\sin}(\tau)\} = \frac{\left|\widetilde{SH}(\omega-2\omega_0)\right|^2 - \left|\widetilde{SH}(2\omega_0-\omega)\right|^2}{2i}$$

(4.13)

$FMOS_{base}(\omega)$ can be integrated in the frequency domain. Here we calculate $\int FMOS(\omega)d\omega$ using ω in THz and normalizing $|\widetilde{I}(\omega)|^2$ to 1. This quantity is not exactly representative of the peak of the baseline but is representative of the baseline integral variation (in order to see the peak of the baseline dependence on the temporal chirp see [49], here we concern ourselves with spectral chirp).
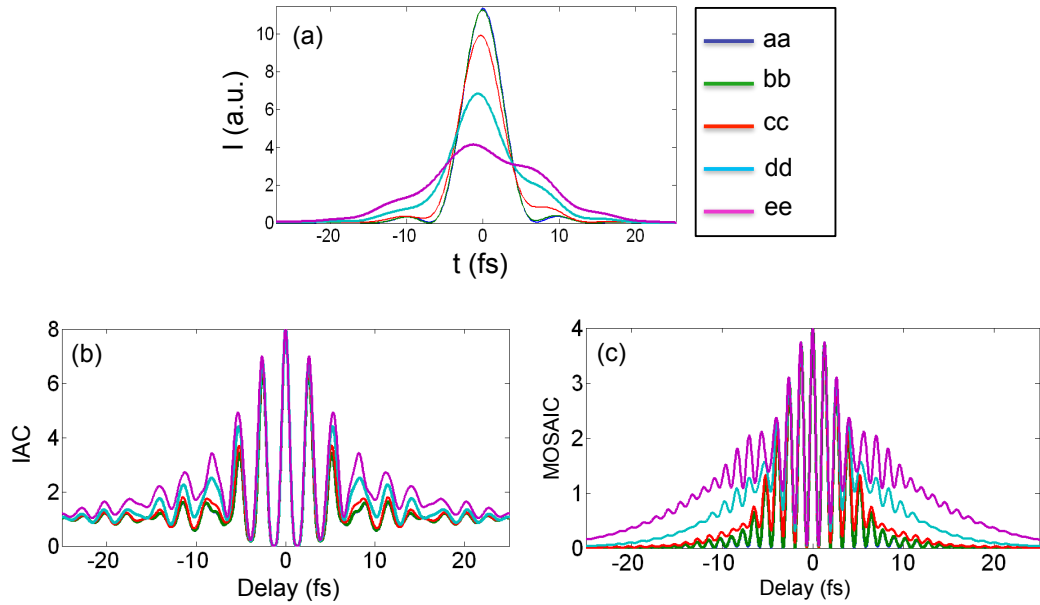
Figure 4.8.: (a) intensity profile, (b) IAC traces and (c) MOSAIC traces of linearly chirped pulses. The curves aa to ee relate to pulses with increasing FWHM: 5.98 fs, 5.99 fs, 6.34 fs, 8.05 fs, 16.04 fs, with quadratic dispersions of $0\,fs^2$, $2\,fs^2$, $10\,fs^2$, $20\,fs^2$, and $30\,fs^2$, respectively .
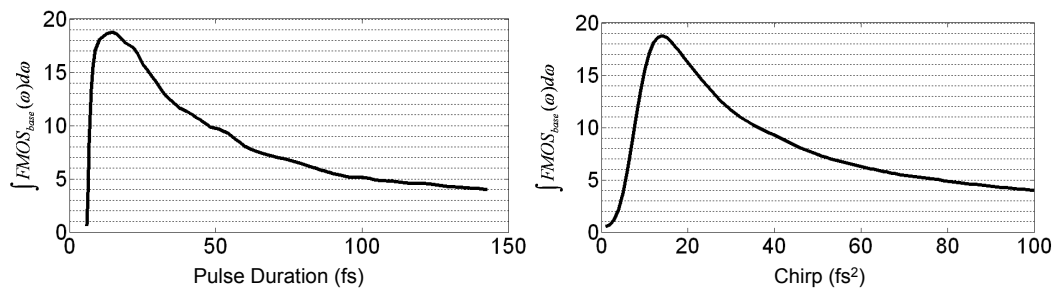
Figure 4.9.: Variation of $\int FMOS(\omega)d\omega$ as a function of pulse duration (right) and of second-order dispersion (left).

For a quadratically chirped pulse, the dependence of $\int FMOS(\omega)d\omega$ on the chirp and pulse duration

is shown in Fig. (4.9). We see a sharp variation when the chirp is small so the MOSAIC trace has a high precision for slightly chirped pulses but the precision decreases for pulses that have a large time-bandwidth product.
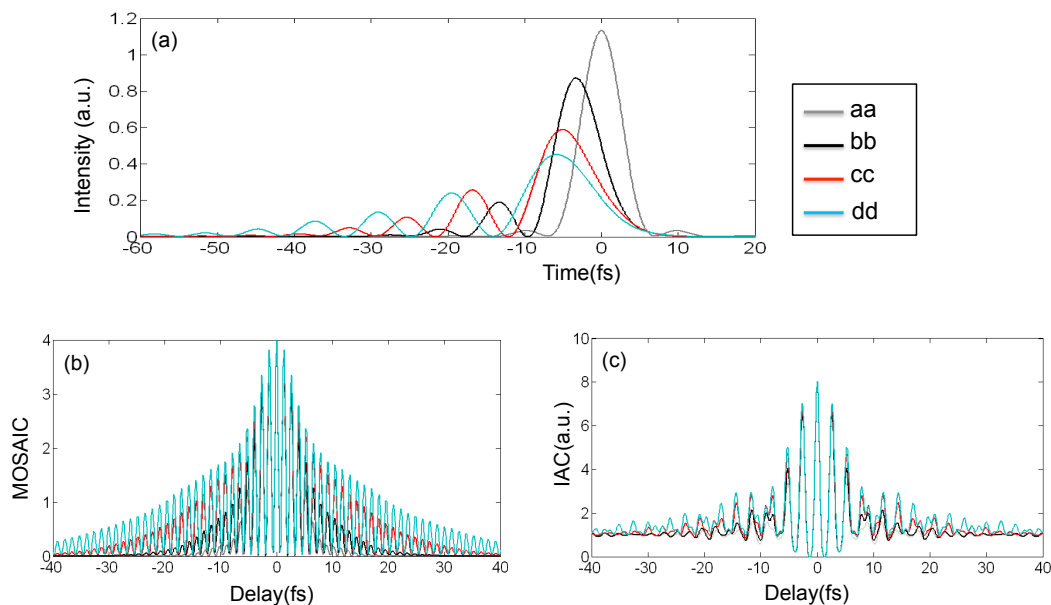
Figure 4.10.: (a) intensity profiles, (b) MOSAIC traces and (c) IAC traces of cubically chirped pulses. FWHM pulse duration from aa to dd: 6.0, 6.2, 8.6 and 20.0/10.0 fs (cubic chirp values of 0, 75, 300, and 450 fs^3).
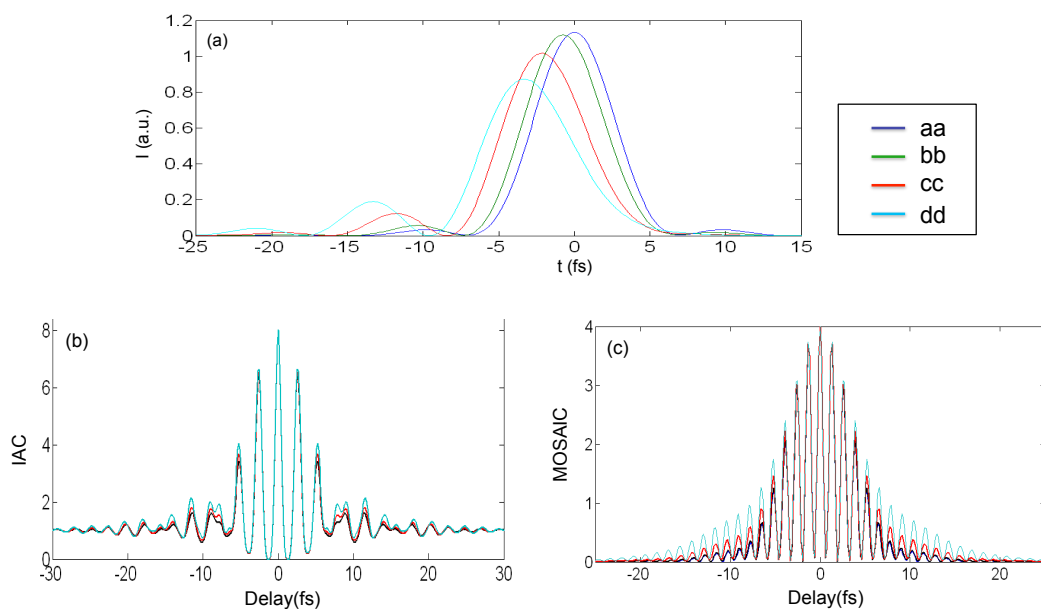
Figure 4.11.: (a) intensity profile, (c) MOSAIC traces and (b) IAC traces of pulses with a slight cubic phase. FWHM pulse duration from aa to dd: 5.98 fs, 6.01 fs, 6.30 fs, and 6.82 fs (cubic chirp values of 0, 30, 90, and 150 fs^3).

We now proceed to studying variations in the MOSAIC profile in the presence of a cubic phase. It was already shown that in IAC the third order chirp results in temporal wings in the trace. The result of a cubic phase in the MOSAIC trace is shown in Fig. (4.10) and Fig. (4.11). They show the sensitivity of MOSAIC to a cubic spectral phase.

From these figures we see that the MOSAIC trace suffers a widening due to third order dispersion, however, the baseline is not affected by it. Also, the trace widens more on the base than on the center of the MOSAIC trace. The maximum value of $\int FMOS(\omega)d\omega$ for a cubically chirped pulse is 0.6 which is small when compared to the value of 20 as in the case of second order dispersion (see Fig. (4.9)).

We now analyze the influence of fourth order dispersion on the MOSAIC trace. We already saw that fourth order dispersion creates a background on the pulses temporal profile. Also, the fourth order term of a Taylor expansion is not orthogonal with the second order term so a similarity between the features of MOSAIC traces of pulses with second and fourth order dispersion might be expected.

As in the case of second order dispersion, fourth order dispersion creates a characteristic baseline in the MOSAIC trace as shown in Fig. (4.12).
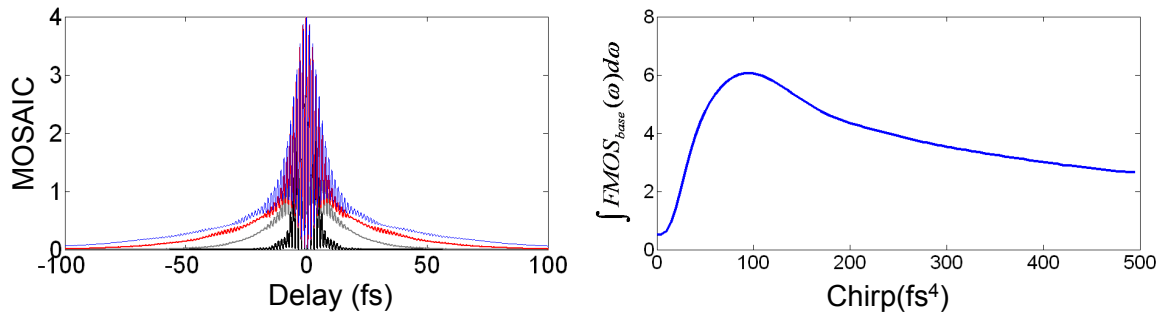
Figure 4.12.: (left) MOSAIC traces for pulses given in Fig. (4.5). (right) base line integral of the MOSAIC trace in the Fourier domain as a function of fourth order dispersion.

The MOSAIC trace is not affected by an intensity unbalance in the autocorrelator despite being affected by an unbalance in the beam path. Also, the trace is not affected by the linear absorption that can take place in the detector, but it is affected by the S/N ratio at the SH frequency.

Below we give a list of equivalent expressions for the MOSAIC trace:

$$MOSAIC(\tau) = IA(\tau) + SHAC(\tau) \tag{4.14}$$

$$MOSAIC(\tau) = \int I(t)I(t-\tau)\left[1 + \cos(2\omega_0\tau + 2\Delta\phi(t,\tau))\right])dt \tag{4.15}$$

4. Spectral phase reconstruction via spectral intensity and interferometric autocorrelations

$$MOSAIC(\tau) = \int I(t)I(t-\tau)\cos^2(\omega_0\tau + \Delta\phi(t,\tau))dt \qquad (4.16)$$

$$MOSAIC(\tau) = IA(\tau) + |SHIA(\tau)|\cos(2\omega_0\tau + \Delta\Phi(\tau))dt \qquad (4.17)$$

where

$$SHIA(\tau) = \int I(t)I(t-\tau)\exp(2i\Delta\phi(t,\tau))dt \qquad (4.18)$$

$$\Delta\Phi(\tau) = \arctan(\Im\{SHIA(\tau)\}/\Re\{SHIA(\tau)\}) \qquad (4.19)$$

The baseline is given by Eq. (4.10) or by the equivalent expression:

$$MOS_{base}(\tau) = IA(\tau) - |SHIA(\tau)| \qquad (4.20)$$

which is zero for an unchirped pulse since $\Delta\phi(t,\tau) = 0$ and $SHIA(\tau) = IA(\tau)$. The baseline increases for even order dispersion, while for odd terms it is almost unaffected. The odd dispersions terms affect the envelope of the MOSAIC diagnostic, by increasing its wings. The envelope of the MOSAIC trace is given by:

$$MOS_{env} = IA(\tau) + \sqrt{(IA_{\cos}(\tau))^2 + (IA_{\sin}(\tau))^2}$$
$$MOS_{env}(\tau) = IA(\tau) + |SHIA(\tau)| \qquad . \qquad (4.21)$$

In the case of an unchirped pulse this is simply the IA trace. As in the IA trace, the MOSAIC envelope is mostly affect by the variance of the pulse. There have been attempts based on using these two features of the MOSAIC (the envelope and the baseline) to reconstruct the pulse [180], but these gives only an approximation to the pulse shape.

In [181] Daniel A. Bender et al. give a slight different version of the MOSAIC envelope traces that allows to distinguish between of temporal and spectral dispersion. In this diagnostic the crossed term is not used; however in [182] Avnish Kumar Sharma et al. used the crossed terms in a diagnostic that is sensitive to the asymmetry/symmetry of the pulse.

To summarize, we have presented a diagnostic derived from IAC and a frequency filter called MOSAIC. This measurement's features are highly sensitive to spectral phase variations. The spectral dispersion's even order terms affect the baseline and odd order terms widen the wings of the diagnostic.

4.3. Retrieving the IA and the SHAC from the IAC: practical approach

In order to obtain the second harmonic autocorrelation and the intensity autocorrelation from the IAC, we need to process this measurement. It is necessary to determine the DC component, the wave central frequency and the autocorrelation time scale. Knowing the DC component will guarantee that the IA Fourier transform is well measured. The central frequency and the IAC's time/frequency scale allow us to identify and isolate the SHAC and the IA components.

The DC component can be determined directly from the IAC trace in time simply by subtracting an average of IAC values for large delays. Alternatively, the DC correction can be calculated by interpolating the IA Fourier transform without the IA value for zero frequency which is the method that we used.

The 1 to 8 contrast in the IAC trace is a measurement of the diagnostic quality. This contrast is sometimes hindered by defects in the pulse wave front due to the autocorrelator optics (beam splitter mainly). Phase distortions do not allow for perfect constructive/destructive interference, which will affect the IAC's contrast. In order to measure the contrast the DC component should be discarded.

The central frequency of oscillation is important, not only to help us determine the zones where a frequency filter is required but also to determine the time and frequency scale. We note that in the IAC Fourier transform (see Fig. (4.1) (b)) there are two distinct zones that can help us determine the central frequency, one centered at the central frequency, $X(\tau)$, and the other centered at twice that frequency, $SHAC(\tau)$.
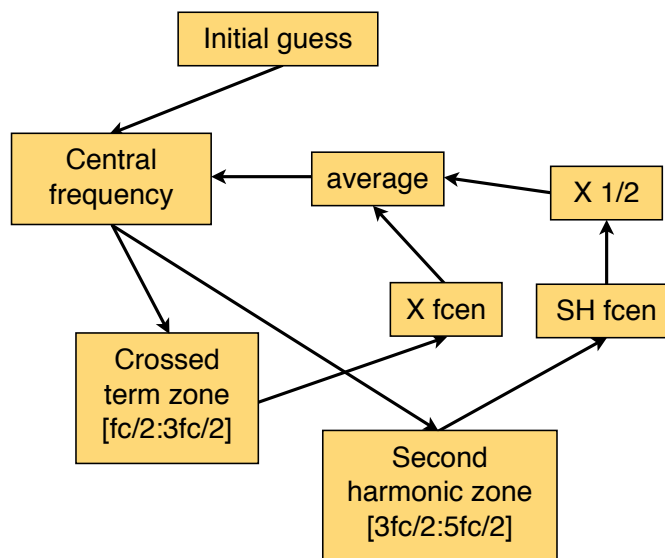
Figure 4.13.: Schematic of the cycle used to obtain the central frequency.

4. Spectral phase reconstruction via spectral intensity and interferometric autocorrelations

The central frequency can be determined by finding the average central frequency within these two zones. This procedure is described in Fig. (4.13).

Convergence usually occurs within 10 iterations. Once we know the central frequency given by IAC we calibrate it using the spectrum's central frequency. The initial guess for the central frequency, may be based on upon the observation of the Fourier transform of the IAC trace and inputing a value manually or by designing an algorithm that detects the maximum of the Fourier transform of the IAC trace that is far from zero frequency, which is normally within the cross term Fourier transform.

We used an algorithm that detects the three zones where the IAC Fourier transform is higher than 1/5 of the maximum (the DC component has already been eliminated) and then we calculate the center of the second zone.

An important question is whether the central frequency given by the autocorrelation and obtained by Fig. (4.13) is the same central frequency given by the spectral shape of the field. After some failed attempts to prove this analytically we opted to do simulations using an experimental spectral shape.

From this we calculated IAC traces using different spectral phases, and then used the algorithm in Fig. (4.13) to obtain the central frequency.
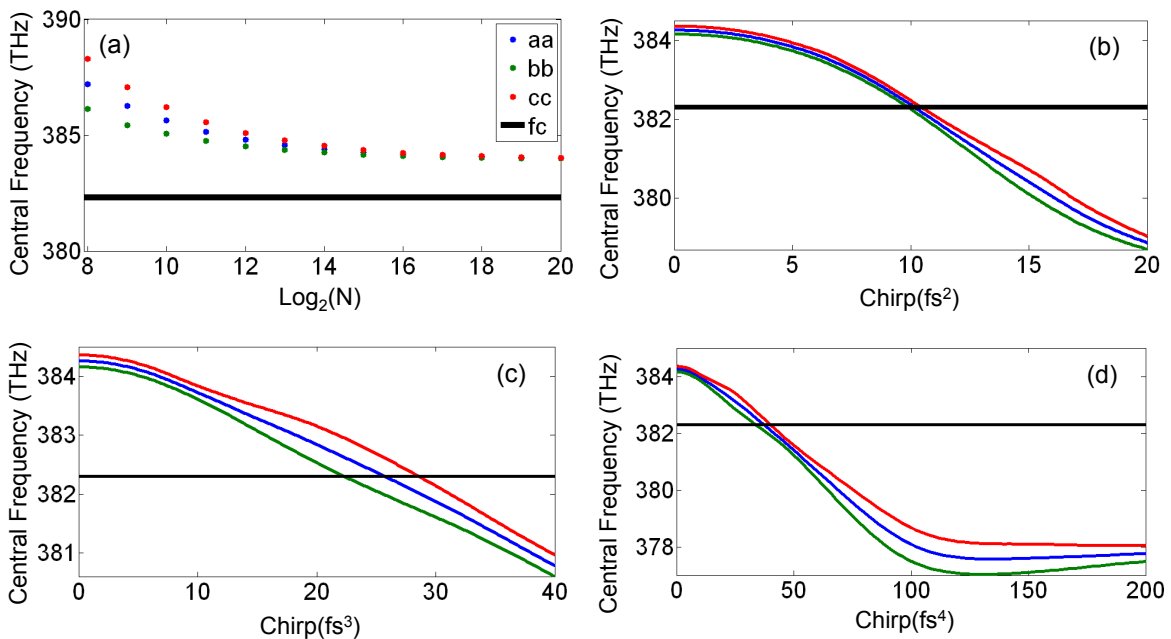
Figure 4.14.: Central frequency obtained with Fig. (4.13). (black line-fc) spectrum central frequency. (green line-bb) central frequency of the crossed term, (red line-cc) second harmonic autocorrelation central frequency over two, (blue line-aa) average of the two. Variations of: (a) number of points used in the spectral shape, (b) second order dispersion, (c) third order dispersion, (d) fourth order dispersion. The values of chirp given in this picture are the a_n values as found in Eq. 4.29.

The results are given in Fig. (4.14) and even in the worst case the maximum deviation to the spectral central frequency does not exceed 1.5%.

Knowing the central frequency f_c, a super-Gaussian frequency filter (8th order or more) is then used to isolate the IA Fourier transform, Eq. (4.22), and the second harmonic autocorrelation Fourier transform, Eq. (4.23). We opted for a super Gaussian filter to avoid apodization issues.

$$\mathscr{F}\{IA(\tau)\} = \mathscr{F}\{IAC(\tau)\} \exp-\left[\frac{2f}{f_c}\right]^8 \tag{4.22}$$

$$\mathscr{F}\{IA(\tau)\} = \mathscr{F}\{IAC(\tau)\} \exp-\left[\frac{2(f-2f_c)}{f_c}\right]^8 \tag{4.23}$$

4.3.1. Other ways to retrieve the intensity autocorrelation and the second harmonic autocorrelation

The methods presented above to determine the IA and the SHAC require a IAC trace. If no IAC measurements are possible, another method can be used to obtain MOSAIC traces and completely define the pulse shape. However, this method requires two independent measurements, one of the IA and another of the SHAC.

There are autocorrelators that directly give the intensity autocorrelation. These autocorrelators are considered easier to operate than second order interferometric autocorrelators.

The second harmonic autocorrelation is the Fourier transform of the second harmonic spectrum. It is possible to measure this spectrum using an appropriate spectrometer and a SH obtained with a thin crystal (in order to have sufficient spectral bandwidth). This measurement would allow for a better S/N ratio.

In order to obtain the MOSAIC trace, the normalization in Eq. (4.24), is needed:

$$IA(0) = SHAC(0) \tag{4.24}$$

This normalization has been suggested for the case when both measurements are retrieved in the same IAC trace [180], but in the presented experimental cases this was not necessary.

From an IA trace and the SH spectrum, it is possible to generate a MOSAIC trace by combining them in a single function in the Fourier space and doing an inverse Fourier transform.

4.4. Iterative reconstruction of pulse phase, using a Gerchberg-Saxton like algorithm (IRIS)

In this section we describe an algorithm that was first presented by K. Naganuma et al. [47] that was the first proposed algorithm for pulse reconstruction from the three one-dimensional quantities given above, namely the spectral intensity, IA and SHAC. It is based on the Gerchberg-Saxton algorithms [183] described in Chapter 3 and used for pulse reconstruction attempts using simply the IA.

The general scheme is given in Fig. (4.15). The algorithm starts with a certain guess phase (random or flat) and the measured spectral shape. It has been reported by some authors that this algorithm does not converge properly [34]. Nevertheless we tried it ourselves.

We used an experimental IAC trace and fed it into the algorithm. This trace was of an experimentally measured slightly chirped pulse, (Fourier transform limit of 5.98 fs, actual duration around 7.5 fs). We found that even after 1000 interaction the results did not converge.
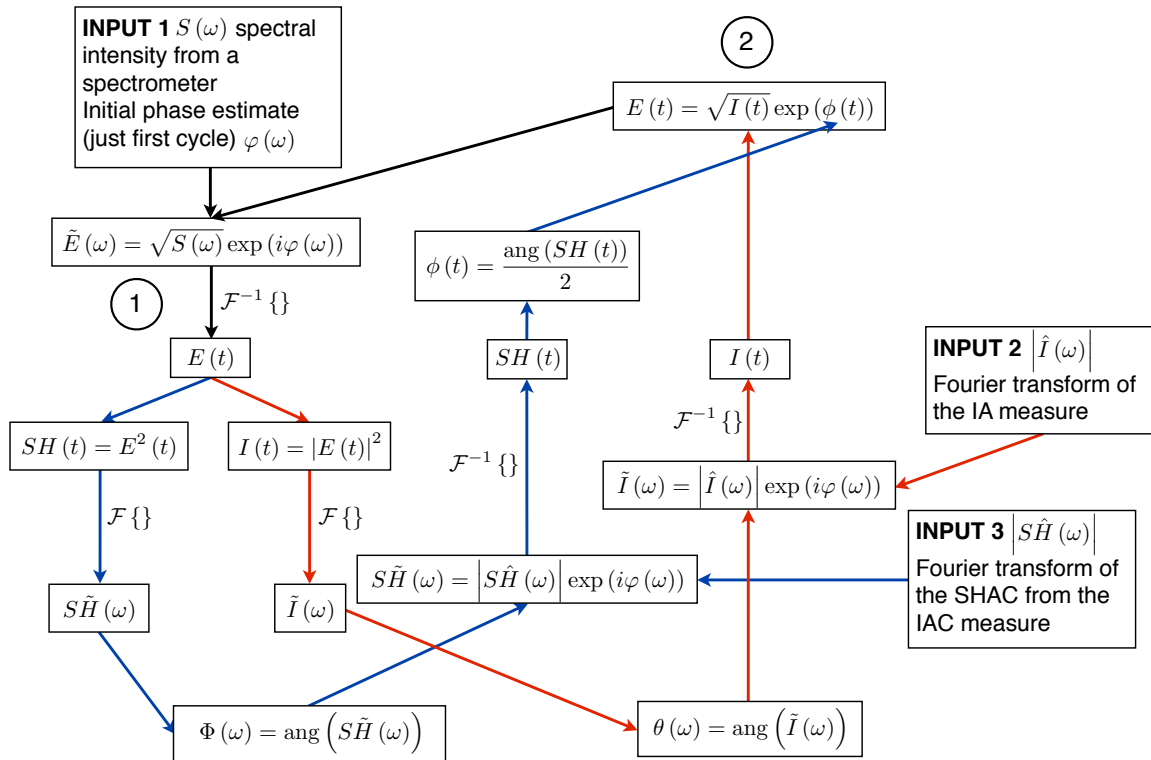
Figure 4.15.: IRIS retrieval method.

The error[3] seems to have a random evolution, and it does not decrease. In fact it actually increases, with the number of cycles. The FWHM duration of the pulse is random. In order to understand

---

[3]The error measurement is obtained by summing the magnitude errors before replacement. We sum the differences of all

why the algorithm does not converge we look at the results after 1000 loops presented in Fig. (4.17). These results show a very peculiar problem. We see the appearance of a peak in the spectrum at the pulses' central frequency. Note that the pulse is sampled around the central frequency in order to reduce the number of points needed, and so the peak at the central frequency is actually a DC component that the algorithm artificially produces.
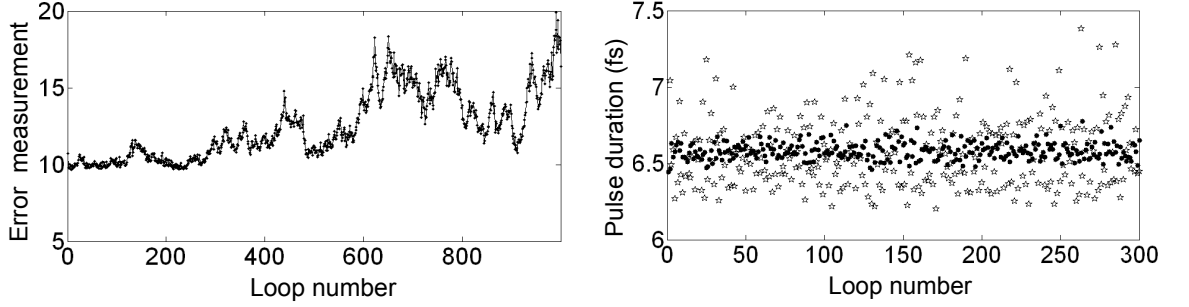
Figure 4.16.: Convergence of the IRIS algorithm, (left) error measurement as a function of the number of cycles. (right) pulse duration in each cycle, (black points) FWHM of the pulse at stage "2" in Fig. (4.15); (hollow stars) pulse duration at stage "1" in Fig. (4.15).
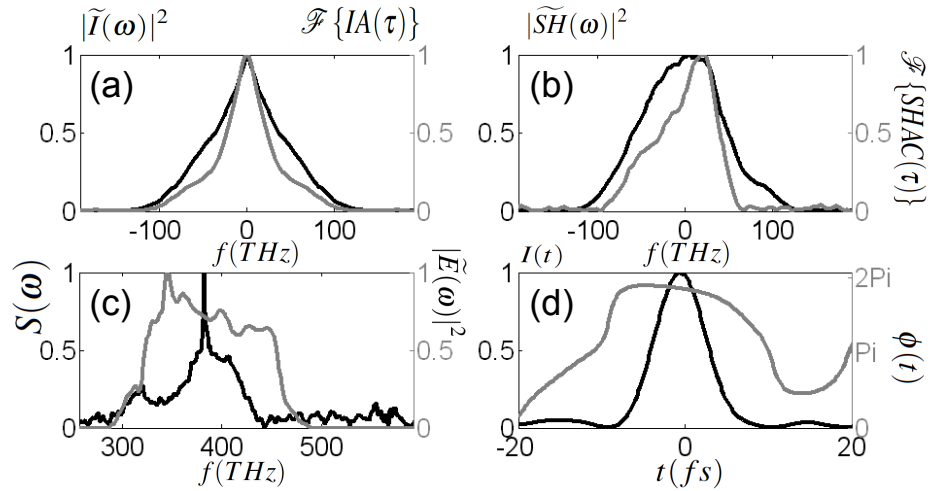
Figure 4.17.: IRIS results after 1000 loops, (a) (gray) IA Fourier transform as fed into the algorithm (black) intensity Fourier transform magnitude obtained. (b) (gray) SH spectrum as fed into the algorithm; (black) SH spectrum obtained. In (c) (gray) electric field spectrum as fed into the algorithm; (black) the spectrum obtained. (d) (gray) the phase of the electric field in time; (black) intensity profile.

the points and normalize them with the input norm.

$$error = \frac{\sum\left(|\tilde{I}(\omega)| - \mathscr{F}\{IA(\tau)\}\right)^2}{\sum(\mathscr{F}\{IA(\tau)\})^2} + \frac{\sum\left(|\widetilde{SH}(\omega)| - \mathscr{F}\{SHAC(\tau)\}\right)^2}{\sum(\mathscr{F}\{SHAC(\tau)\})^2} + \frac{\sum\left(|\tilde{E}(\omega)| - S(\omega)\right)^2}{\sum(S(\omega))^2}. \tag{4.25}$$

4. Spectral phase reconstruction via spectral intensity and interferometric autocorrelations

We speculated that this peak could be due to imperfection in the measurements, namely a possible background noise in time which would correspond to a peak in frequency space. More specifically the contrast of the measurement used was not 1 to 8 but 1 to 7.4.

We can also speculate that the DC component appears because the IRIS procedures obligates the intensity to be real and positive, $I(t) = |E(t)|^2$ and so any noise in time will add up to a DC component.
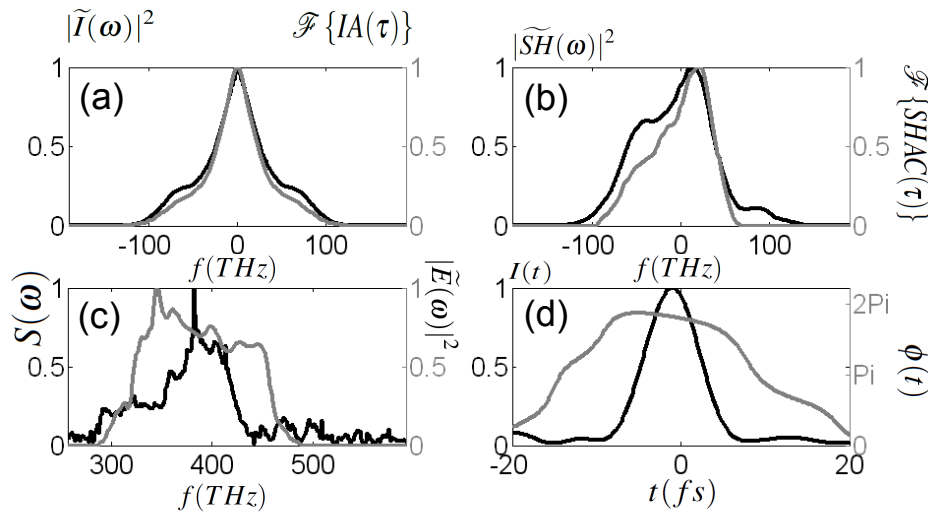
Figure 4.18.: Effect of eliminating the background noise (these plots correspond to those given in Fig. (4.17)).

In order to solve this problem we eliminated the background of the measurement, in the hope that the background was actually noise rather than signal, and ran the algorithm again. We also cleaned the background at each turn of the algorithm. The result is given in Fig. (4.18), where we see no significant improvements by this background cleaning. The corresponding convergence cycle is given in Fig. (4.19).
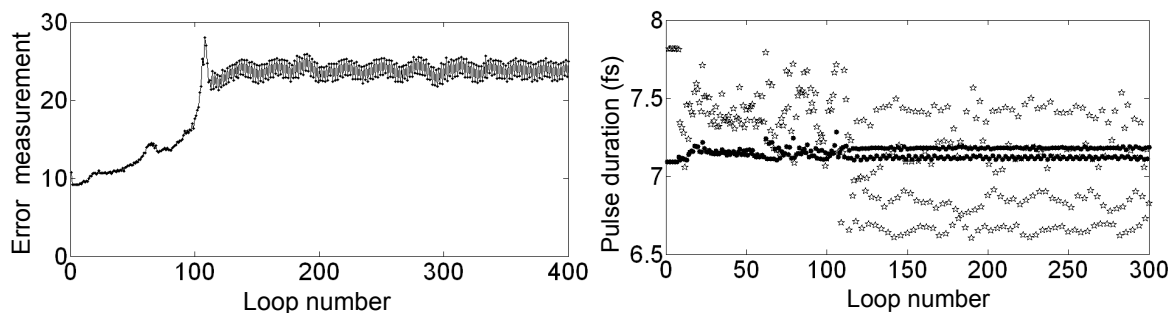
Figure 4.19.: Convergence of the IRIS algorithm, when one eliminates the background noise (these plots correspond to those given in Fig. (4.16)).

The error increases in the first 120 loops (see Fig. (4.19)) after this point it stabilizes between 2 levels, this behavior does not change in the first 1000 loops. We can clearly see that the results obtained with this algorithm do not minimize the error, instead the error demonstrates a quasi oscillatory behavior. However, the pulse duration behaves randomly.

We then tried to use two theoretical results, just to test the feasibility of the algorithm in ideal conditions:

1. A pulse chirped with a 40 fs^2 linear chirp to a FWHM duration of 24.2 fs (the spectrum has a Fourier limit of 5.98 fs and can be seen in Fig. (4.2));

2. A Fourier limited pulse with the same spectrum. The IRIS initial phase guess is flat; in other words we used the initial condition the algorithm was suppose to provide.

The evolution of error/pulse duration for the first case is given in Figs. (4.20) and (4.21). For the second case the error is shown in Fig. (4.22) and the results after 1000 loops are given in Fig. (4.23).
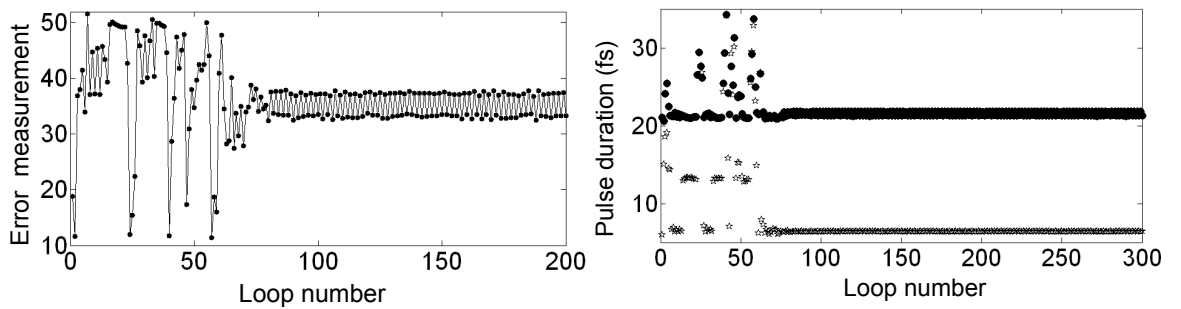
Figure 4.20.: Convergence of the IRIS algorithm for case (1) (these plots correspond to those given in Fig. (4.16)).
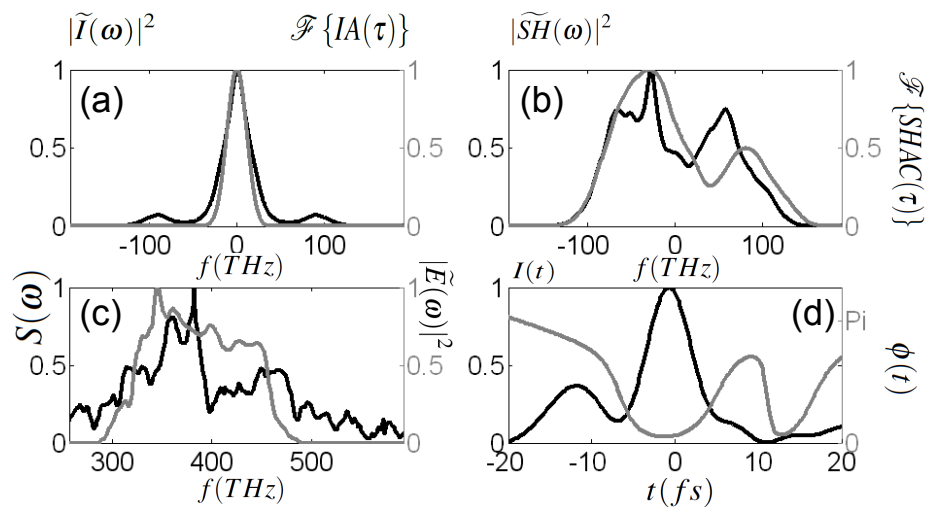
Figure 4.21.: Results after 1000 loops for case (1) (these plots correspond to those given in Fig. (4.17)).

4. Spectral phase reconstruction via spectral intensity and interferometric autocorrelations

In case (1) (see Fig. (4.20)) the behavior observed between the 80th loop and the 200th does not change in the first 1000 loops. We see an erratic behavior until the 80th loop. In some of the initial loops the agreement is better than in the initial guess or in the stable region.

Fig. (4.20) also shows that the pulse duration stabilizes after 80 loops. The pulse duration measured after the spectrum correction (point 1 of Fig. (4.15)) is the Fourier limited duration of the pulse. The pulse duration measured after correcting the intensity Fourier magnitude (point 2 of Fig. (4.15)) is the one related to the intensity autocorrelation FWHM. We did not obtain a stable region where the pulse duration in points 1 and 2 of Fig. (4.15) is the same.

Fig. (4.21) presents the results after 1000 loops, in (c) we can observe a persistence of the DC component despite its magnitude decrease. We can conclude that this feature is not related to experimental errors but rather to the algorithm itself.
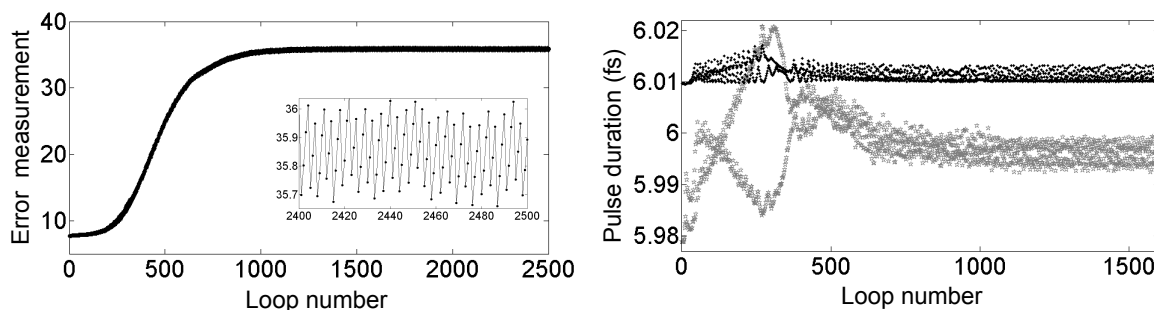
Figure 4.22.: Convergence of the IRIS algorithm for case (2) (these plots correspond to those given in Fig. (4.16)).

In case (2) (see Fig. (4.22)) the results are similar. The error increases in the first 500 loops and then a stable zone is found. Even in this case where the initial values are the correct ones the algorithm is not able to maintain it. In Fig. (4.23) (c) we still observe a DC peak even if it is a slight one. Fig. (4.23) (a) and (b) show a good agreement between the power spectrum of the intensity and of the SH. However Fig. (4.23) (c) shows that an agreement with the power spectrum of the field itself is not achieved.

To conclude this section about the IRIS algorithm, we point out that in this algorithm the error does not always converge, and even in the cases where it does, it is not to one single value. Rather the error converged to an oscillation within certain limits. Regardless of the convergence the IRIS algorithm does not find a minimum value for the error (for the tested cases).

To the best of our knowledge, IRIS fails to give the correct solution and it should not be envisioned to retrieve the pulse profile in any case. The FWHM obtained using IRIS follows the FWHM of the measurements, the Fourier transform of the spectral shape and the intensity autocorrelation. This happens regardless of the pulse shape, as shown in Fig. (4.20). Also, all the results have a DC peak in frequency space, probably due to noise. Case (2) results were tested until 10^6 loops without any

observed change in behavior. We conclude that, to the best of our knowledge, no convergence can be obtained with the IRIS algorithm for the relevant cases in our work.
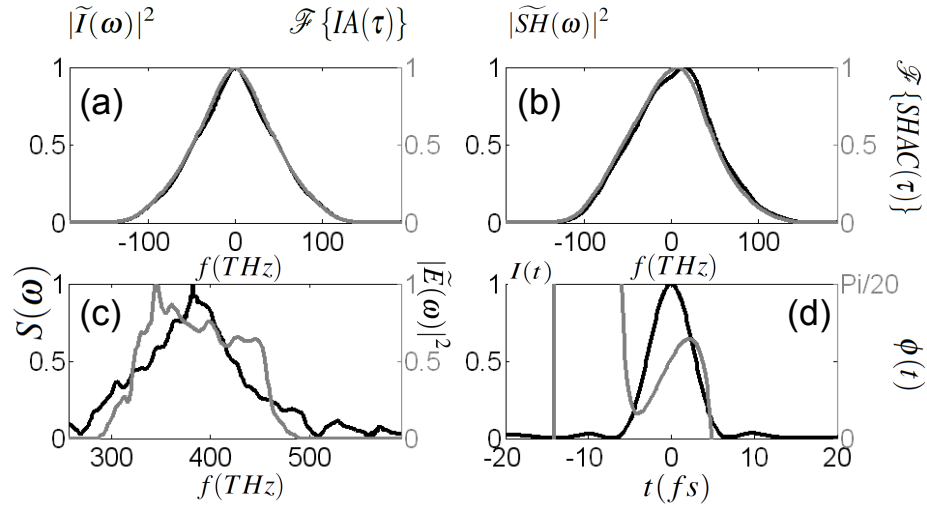
Figure 4.23.: Results after 1000 loops for case (2) (these plots correspond to those given in Fig. (4.17)).

4.4.1. Phase retrieval algorithms based in the Gerchberg-Saxton algorithm

We tested another Gerchberg-Saxton like approach in order to search for a field that obeys the three constraints: spectrum, intensity autocorrelation and second harmonic spectrum.
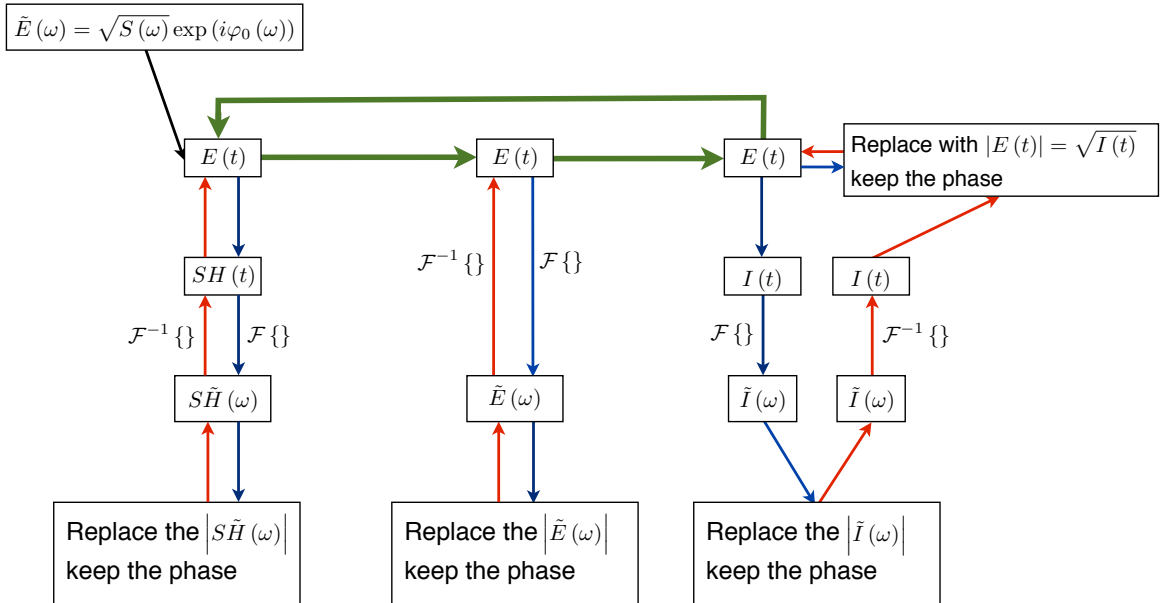
Figure 4.24.: Alternative Gerchberg-Saxton algorithm for spectral phase retrieval. Subroutines are given by the blue/red arrows. The green arrows explicit the behavior of the main routine.

4. Spectral phase reconstruction via spectral intensity and interferometric autocorrelations

We can simply use a scheme like the one given in Fig. (4.24) in order to obtain the better possible approximation. This algorithm, to the best of our knowledge, has never been tried, and is based in the fact that the final solution has to fit the three quantities referred above. Like any Gerchberg-Saxton approach we cannot be sure that the results will converge or that the best solution will be obtained. We simply tried these algorithms because they are fast when compared with the error minimization algorithms presented in the following sections.

The algorithm starts with the measured spectral shape and a random phase (any other initial phase is possible). Afterwards the algorithm uses three sub-routines and in each one the electric field is given. From this electric field we calculate one of the following three quantities: the Fourier shape of the electric field, the second harmonic Fourier transform or the intensity Fourier transform. The modulus of these quantities is replaced by the measurements and the phase is kept. The cycle is then repeated.

The algorithm in Fig. (4.24) is cyclical and there is no objective reason why it should converge to an electric field that obeys all three constraints. The results are given in Figs. (4.25) and (4.26). We used the spectral shape given in Fig. (4.2) (Fourier limited duration of 5.98 fs FWHM) and obtained two chirped pulses, one with 7.0 fs and the other with 10.0 fs. The output fields shown in Figs. (4.25) and (4.26) are obtained after each cycle, before replacing the SH power spectrum. In this output point the obtained electric field has the correct temporal variance, because the last replacement was the magnitude of the intensity Fourier transform.
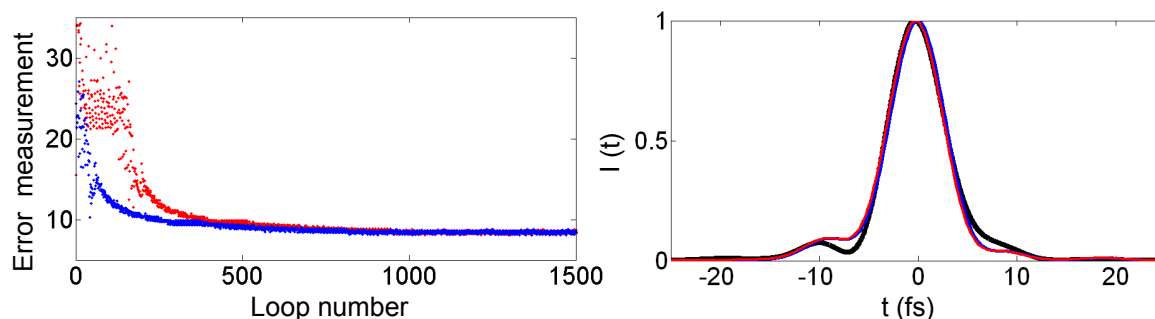
Figure 4.25.: (left) Error (error for an initial random phase is 219%, and for a flat phase is 16%) (red) flat initial phase, (blue) random initial phase. (right) Intensity results after 1500 cycles, (black line) pulse intensity profile, (blue and red) solutions obtained by this method, the blue and red lines are almost superimposed.

In Fig. (4.25) the solutions converge to the same point but the pulse is not reconstructed. The reconstructed pulses have the correct variance, but the FWHM duration is 6.7 fs for the reconstructed pulse while the actual pulse is 7.0 fs long.

In Fig. (4.26) the solutions converge to a zone, however the pulse is not reconstructed. The reconstructed pulses have the correct variance, however the reconstructed FWHM duration is 8.9 fs and

the actual duration is 10 fs.

The algorithm converges after 50-100 loops (fast convergence) as we see in Figs. (4.25) and (4.26). We observe that the results obtained by this algorithm for chirped pulses present a smaller error than for the Fourier limited pulse (this was not the case in IRIS). Note that we used two different initial conditions but obtained very similar results. This means that the initial guess for the spectral phase, does not interfere with the intensity profile obtained by this algorithm.
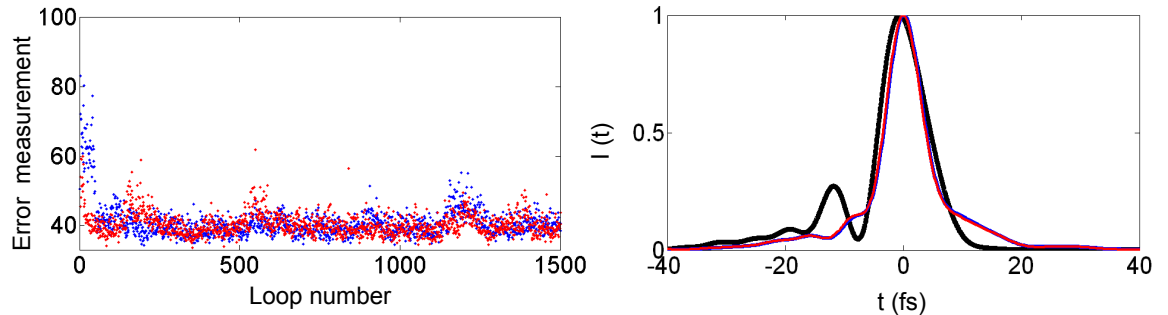
Figure 4.26.: (left) Error (the error for a random phase is 216%, for flat phase is 55%) (red) flat initial phase, (blue) random initial condition. (right) Intensity profile results after 1500 cycles, (black) actual pulse, (blue and red) the solutions obtained by this method, the blue and red lines are almost superimposed.

Despite this, it simply does not give us the correct pulse reconstruction. However, because the algorithm is very fast, it could be used to obtain an initial guess for other algorithms.

4.5. Phase retrieval as a minimization problem

Based on the work by K. Naganuma [47], we know it is only necessary to obtain the right spectral phase that obeys and connects the three conditions that define the pulse shape: spectral intensity $S(\omega)$, the modulus of the Fourier transform of the intensity $\widetilde{I}(\omega)$, and the modulus of the Fourier transform of the second harmonic, $\widetilde{SH}(\omega)$.

It is possible that the spectral phase that exactly matches the three quantities is not found, this could be due to a number of factors, including experimental imprecision or discretization issues. However this should not be discouraging. After all this is an attempt to match three quantities taken by at least two independent measurements.

The pulse and the IAC trace discretization have to obey the sampling theorem in the frequency and time domain. The number of points needed to obey these conditions increase quadratically with pulse chirp, more specifically with the time-bandwidth product. In other words we need to obey the sampling theorem for the spectral intensity of the pulse and for its phase. If isolated points and/or

fluctuations in the spectral phase are obtained, this probably means that the data does not obey the sampling theorem.

We can assume that the spectral intensity is measured precisely. This is justified by practical reasons: the spectral intensity measurement is much easier to perform than the interferometric autocorrelation measurement, and the spectrum its not subject to so many experimental errors, provided that the spectrometer is properly calibrated.

For a given spectral intensity, a trial intensity Fourier modulus can be calculated from:

$$FI_{trial}(\omega) = \left| \mathscr{F} \left\{ \left| \mathscr{F}^{-1} \left\{ \sqrt{S(\omega)} \exp(i\phi_{trial}(\omega)) \right\} \right|^2 \right\} \right|. \tag{4.26}$$

A trial power spectrum of the second harmonic can be given by:

$$FSH_{trial}(\omega) = \left| \mathscr{F} \left\{ \mathscr{F}^{-1} \left\{ \sqrt{S(\omega)} \exp(i\phi_{trial}(\omega)) \right\}^2 \right\} \right|. \tag{4.27}$$

Using Eqs. (4.26) and (4.27) we can define an error to be minimized between these two trial functions or their squares:

$$\varepsilon = \int \left[\left(FI_{trial}(\omega) - \sqrt{\mathscr{F}\{IA(\tau)\}} \right)^2 + \left(FSH_{trial}(\omega) - \sqrt{\mathscr{F}\{SHAC(\tau_i)\}} \right)^2 \right] d\omega. \tag{4.28}$$

4.5.1. Basis function for the spectral phase

We consider several ways to describe the trial phase. In the study of ultrafast pulses it is usual to describe the spectral phase of the pulses using a Taylor series expansion around the central frequency ω_0:

$$\phi(\omega) = \phi_0 + a_1(\omega - \omega_0) + a_2(\omega - \omega_0)^2 + a_3(\omega - \omega_0)^3 + ... \tag{4.29}$$

Where, $\phi_0 = \phi(\omega_0) =$ constant and the a_n coefficients are related to the derivatives of $\phi(\omega)$ at ω_0 by:

$$a_n = \frac{1}{n!} \frac{d^n \phi(\omega)}{d\omega^n} \bigg|_{\omega = \omega_0}. \tag{4.30}$$

If the trial phase is defined in this base, the constant term usually has no importance (except in the case of few cycle laser pulses where it can play a major role), and the linear term simply means a bulk temporal shift in the pulse. An expansion up to the term, $a_{n+1}(\omega - \omega_0)^{n+1}$ means we have a minimization problem with n dimensions.

However we can expand the phase in several other bases. Chebyshev polynomials have been a quite useful base for spectral methods [184, 185] . These are given by:

$$\delta = \omega - \omega_0,$$
$$b_n = \frac{\pi}{2} \left\{ \left(\delta - \sqrt{\delta^2 - 1} \right)^n + \left(\delta + \sqrt{\delta^2 - 1} \right)^n \right\}. \tag{4.31}$$

Legendre polynomials are orthogonal and also constitute another possible base. The same can be said about a Fourier series base[4]. A base expanded in sin and cos functions is important for a step-down approach because the expansion coefficients are not so interdependent, which simplifies the problem of phase retrieval[5].

We also include in this study a configuration where each point in the array used to represent the phase is variable. We simply consider the spectral phase point by point. This point per point is a discretization based base and gives the minimum error but is the one that is more slowly convergent.

4.5.2. Two function minimization

In every minimization problem where two quantities have to be adjusted, there is a question about the weight of the two quantities, namely which one is more important and how their combination can be optimized.

In our minimization problem we consider that the spectral intensity is given and that the adjustments are preformed on the modulus of the Fourier transform of the intensity profile and on the the Fourier transform of the second harmonic profile.

Given this it is possible to define an error measurement with a weighted error (w is the weight):

$$\varepsilon = (1 - w) \sum_i \left(|\widetilde{I}(\omega_i)| - \mathscr{F}\{IA(\tau_i)\} \right)^2 + w \sum_i \left(|\widetilde{SH}(\omega_i)| - \mathscr{F}\{SHAC(\tau_i)\} \right)^2. \tag{4.33}$$

We should choose the weight in such a way that the algorithm adjusts to the function that is the least adjusted. More exactly, w tends to 1 if the SH error is much larger than the IA error and tends to 0 if the error related to the intensity profile is dominant. A function that obeys these two conditions is:

---

[4]For every polynomial base $P(\omega)$ we may use the spectral log10 FWHM, $\Delta_{log_{10}}\omega$ as a reference to normalize the frequency, this gives us a physically significant result:

$$\phi(\omega) = \sum_j^N a_j P\left(\frac{\omega - \omega_0}{\Delta_{log_{10}}\omega} \right) \tag{4.32}$$

in the case of a point per point approach or when using a Taylor expansion this is not important.

[5]It is important to say that even if a base is orthogonal, this does not mean that it is orthogonal in this problem.

$$w = \frac{\sum_i \left(|\widetilde{SH}(\omega_i)| - \mathscr{F}\{SHAC(\tau_i)\} \right)^2}{\sum_i \left(|\widetilde{I}(\omega_i)| - \mathscr{F}\{IA(\tau_i)\} \right)^2 + \sum_i \left(|\widetilde{SH}(\omega_i)| - \mathscr{F}\{SHAC(\tau_i)\} \right)^2}, \tag{4.34}$$

which results in the solution:

$$\varepsilon = \frac{\left(\sum_i \left(|\widetilde{I}(\omega_i)| - \mathscr{F}\{IA(\tau_i)\} \right)^2 \right)^2 + \left(\sum_i \left(|\widetilde{SH}(\omega_i)| - \mathscr{F}\{SHAC(\tau_i)\} \right)^2 \right)^2}{\sum_i \left(|\widetilde{I}(\omega_i)| - \mathscr{F}\{IA(\tau_i)\} \right)^2 + \sum_i \left(|\widetilde{SH}(\omega_i)| - \mathscr{F}\{SHAC(\tau_i)\} \right)^2}. \tag{4.35}$$

This equation can be used to balance the fit between both measurements. This is quite important in cases where a local minimum appears and one of the functions has been completely reproduced but not the other.

4.6. Using *fminsearch*

After unsuccessfully trying out Gerchberg-Saxon type algorithms, we have tried to obtain the spectral phase using a different minimization approach.In this section we present a study based on a very simple algorithm that is included in the Matlab base code, *fminsearch*. It is based on a very simple minimum search algorithm that uses a simplex mirror method. We hoped that this algorithm could facilitate the use of more complex algorithms that would be inherently more difficult to implement.

In fact we may look at the spectral phase retrieval as a minimization/optimization problem.

Once the spectral intensity $S(\omega)$ is known, as well as the two other functions (the modulus of the Fourier transform of the intensity, $FI(\omega) = |\mathscr{F}[I(t)]|$, and the second harmonic Fourier modulus, $FSH(\omega) = |\mathscr{F}[SH(t)]|$), we can always determine trial functions obtained using the spectral intensity $S(\omega)$ and the trial spectral phases $\phi(\omega)$. In this case, the algorithm will minimize the following functional:

$$\delta^2\{\phi(\omega)\} = \left[\begin{array}{l} \int \left(\left| \mathscr{F}\left\{ \left| \mathscr{F}^{-1}\left\{ \sqrt{S(\omega)}\exp(i\phi(\omega)) \right\} \right|^2 \right\} \right|^2 - FI(\omega)^2 \right)^2 d\omega + \\ + \int \left(\left| \mathscr{F}\left\{ \mathscr{F}^{-1}\left\{ \sqrt{S(\omega)}\exp(i\phi(\omega)) \right\}^2 \right\} \right|^2 - FSH(\omega)^2 \right)^2 d\omega \end{array} \right] \tag{4.36}$$

In numerical calculations, the integral is replaced with a sum.

We simply input this functional into the Matlab code (*fminsearch*) and the above mentioned minimum

search algorithm tries to find its minimum.

The algorithm uses a Nelder-Mead simplex method [186, 187] that is a non-gradient non-stochastic search method with a series of simplex reflections (a simplex is the equivalent of an equilateral triangle in N dimensions). It is known to be an adaptable and strictly convergent algorithm [188] that does not distinguish between local and global minima.

Since the algorithm is already part of Matlab base code, we have to use it directly and cannot make any changes to its code. However an artifice can be made: an amplified version of the phase is used as the search parameter so that the algorithm is able to explore a wider range of trial phases. This lets the algorithm converge faster to some minimizing phase.

The Matlab function has some optimization parameters by default, namely the termination tolerance, the maximum number of functions evaluated and the maximum number of iterations allowed. Using a point per point base approach, we chose a 0.01% precision as the target to halt the algorithm. The maximum number of functions to be evaluated is 3×10^9 and the maximum number of iterations is 3×10^4. This last parameter is the limiting parameter for almost all trial cases.

In order to test the algorithm we used a test pulse with a spectral phase affected by second, third and fourth order dispersion terms that chirp the pulse from a 5.98 fs (Fourier limited) to 9.0 fs FWHM, and also creates pre-pulses.

We used two decompositions for the spectral phase: a point-by-point approach in which all points can vary, and a type I Chebyshev polynomial in which the coefficients of the polynomial varied. We used to initial guesses, zero and a random number approach in each case (the Chebyshev series are considered up to the 20th order).

The amplification referred above consists simply on not feeding our search space directly into the spectral phase but multiplying the search space (either the discrete points or the sum of the Chebyshev polynomials) by an amplification factor, "*amp*". In a point-by-point approach we obtain:

$$\phi = [1,...,N] \times amp \tag{4.37}$$

in which the algorithm object space is a N dimensional space where each phase point represents a variable on the simplex method. The amplification factor allows the algorithm to search a wider range of spectral phases.

We tried this point-by-point approach, with a flat phase initial condition and with a random initial phase. For each initial condition two trials are presented. For the flat phase initial condition the results are completely reproducible, which means that this is not a random algorithm. For these, point-by-point trials no convergence was obtained before the maximum number of evaluated functions was reached, which indicates that by increasing the number of functions that can be evaluated we might

get better results. The results are shown in Fig. (4.27).

Actually, for a point-by-point approach, the algorithm converged to a precision of 0.01%. This is not to say that it did not converge to a error of 0.01%, it means that the changes in the error did not converge within a tolerance of 0.01% of itself, or within 4 significant digits.

The measurement error is simply the sum of the error for each measurement (without a weight function). The error reduction function presented in Fig. (4.27) is given by:

$$Error_{red} = \frac{Max\{\Delta\} - \Delta}{T},$$
(4.38)

where Δ is the measured error for several amplification factors and T is the algorithm running time. It is basically a measurement of the efficacy of the algorithm per unit of time.
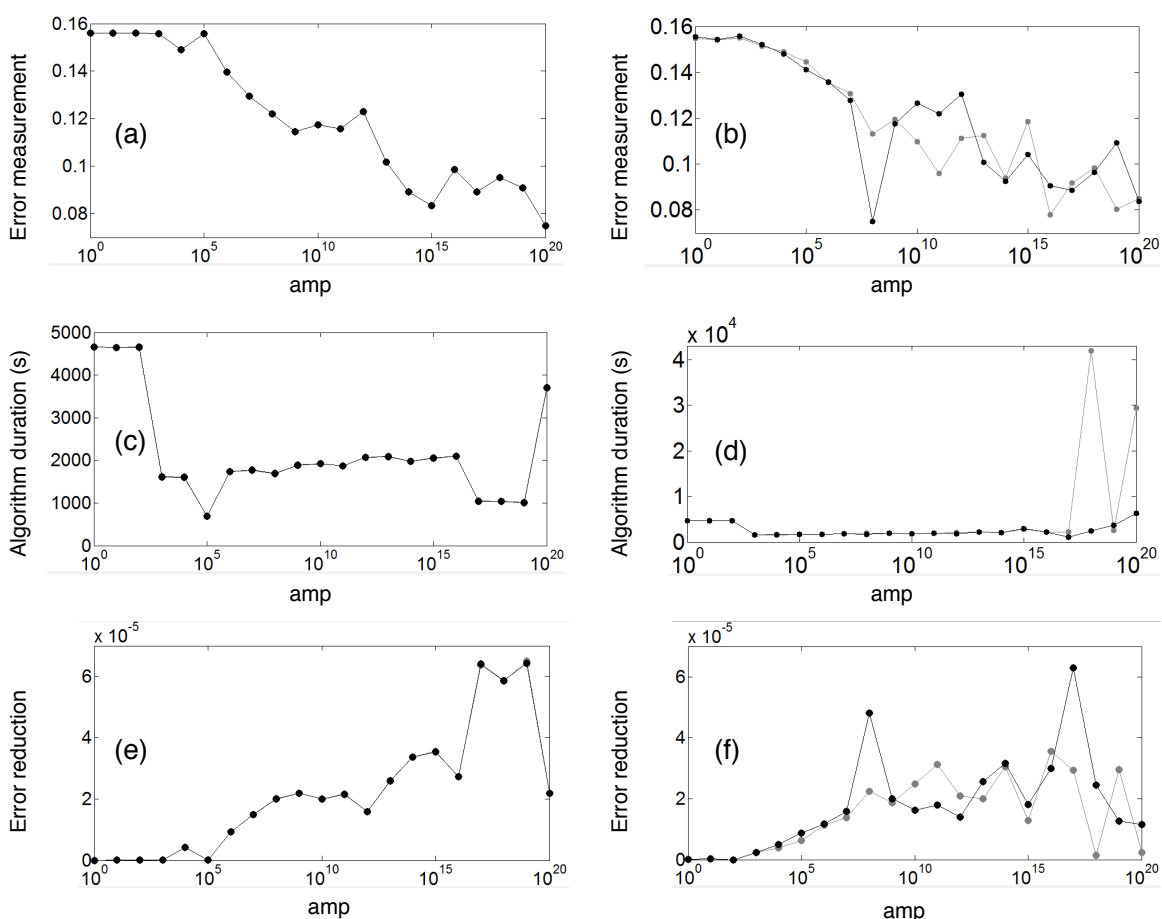
Figure 4.27.: *fminsearch* results. (a), (b) and (c) are the results for a flat phase initial condition; (d), (e) and (f) are the results for a random initial phase condition, the two lines in each figure represent two different trials with different random initial spectral phases.

From Fig. (4.27) it is clear that the amplification factor has a considerable influence on the results. We see that starting from the same initial conditions the search is reproducible. Also the error reduction function is maximized for an amplification factor $amp = 10^{19}$. The inclusion of the *amp* factor into the algorithm makes no significant difference from $amp = 1$ to $amp = 1E3$. For higher amp values the error decreases. The algorithm ran with an amplification factor of 10^{19} for several days but did not converge.

For a random initial phase we obtained different results. For large values of amplification factor the execution time needed to get similar results can double. From a random initial phase the results are not entirely reproduced but it decreases; however these results suggest that the maximum reduction can be obtained with amplification levels between 10^{15} and 10^{17}.
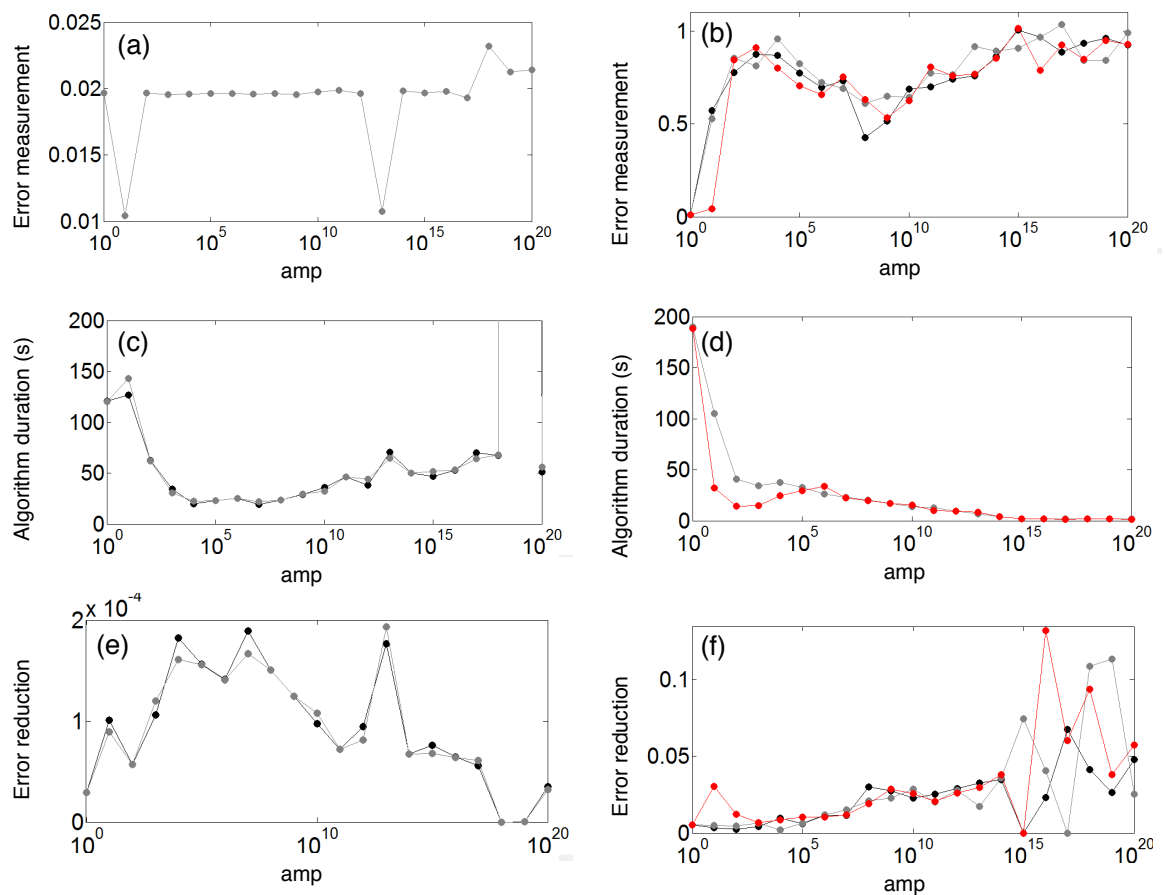
Figure 4.28.: *fminsearch* convergency results using a Chebyshev polynomial base. (left) Flat phase initial condition; (right) Random initial conditions.

We also tried to use a spectral phase described by Chebyshev polynomials, where we considered the polynomial expansion up to the 20th order. In this case the coefficients of each polynomial term are the minimizing argument. As in the previous case we also used two initial conditions: a first one where all the polynomial coefficients were zero and a second one where the coefficients were

random. We used type I Chebyshev polynomials (that are orthonormal with the weight function $\frac{1}{\sqrt{1-f^2}}$).

The error reduction factor is not important in this case because the maximum error is obtained for large values of *amp*. From the error values given in Figs. (4.28) and (4.27) we can deduce that the error is smaller using a point-by-point base instead of Chebyshev polynomials. We also see that the amplification factors that were useful in a point-by-point approach do not present a clear advantage when using a Chebyshev polynomial base. Actually, in Fig. (4.28), with a flat initial condition and an amplification factor of 10^{19}, the algorithm finds a minimum, we repeated this calculation several times to confirm this fact. This means that using Eq. (4.36) as a quantity to be minimized and Chebyshev polynomials we can obtain local minima. However using a discretization base approach we do not see any local minima.

4.7. Genetic algorithms

Genetic algorithms are a group of optimization algorithms, whose original design is normally attributed to Nils Aall Barricelli. Barricelli, a biogeneticist, worked on the early computers in Princeton in the early 1950's [189, 190], in numerically testing the theory of evolution. Other works by the same group on evolutionary algorithms simulated natural systems, from genetic systems to intelligence [191].

In 1957, George Box[192] used a simple genetic algorithm to optimize industrial productivity.

Throughout the later decades these algorithms have been used to optimize a variety of complex problems, from economics to nuclear physics, car production and mirror design for solar energy harvesting. They have been known for their high versatility in solving complex problems [193].

Genetic algorithms are known to avoid local minima, and for finding several optimal solutions when the underlining problem is prone to have several optimal solutions [194]. Genetic algorithms always converge, but the convergence time can be quite high (genetic algorithms normally present an asymptotic convergence [195] and are stochastic in nature). No definite result is guaranteed to be obtained. As in most optimization algorithms used for complex problem solving, in genetic algorithms a compromise between the time it takes to achieve a convergent set of solutions and the precision obtained with the algorithm must be reached. This is a quite intuitive idea and highly dependent on the problem at hand.

Genetic algorithms, as their name alludes to, are based on the breeding and selection of solutions according to their fitness to survival. In a genetic algorithm we start with a certain set of breeding specimens. We then evaluate the fitness of these solutions to obey the problem's constraints. Using this information, a certain population is selected to breed new solutions. When a mutation genetic algorithm is used, the new solutions are simply slightly modified versions of the initial solutions.

In the case where sexual reproduction is simulated, a combination between different solutions can be performed by a linear combination of the parents' genetic code, or more commonly in discrete problems combining different parts of genetic code of two or more parents.

Most genetic algorithm optimization is employed in discrete problems. In this case the object space is constituted not of real numbers but of sequences of discrete numbers, letters, nucleotides (A G C T), etc..., normally with a limited number of options. In this case, the mutation rate reflects the probability that each base has of being changed. The combination of sequences is done by combining parts of two parent sequences in a final sequence. In a discrete case there is no sense in doing a linear combination of the bases.
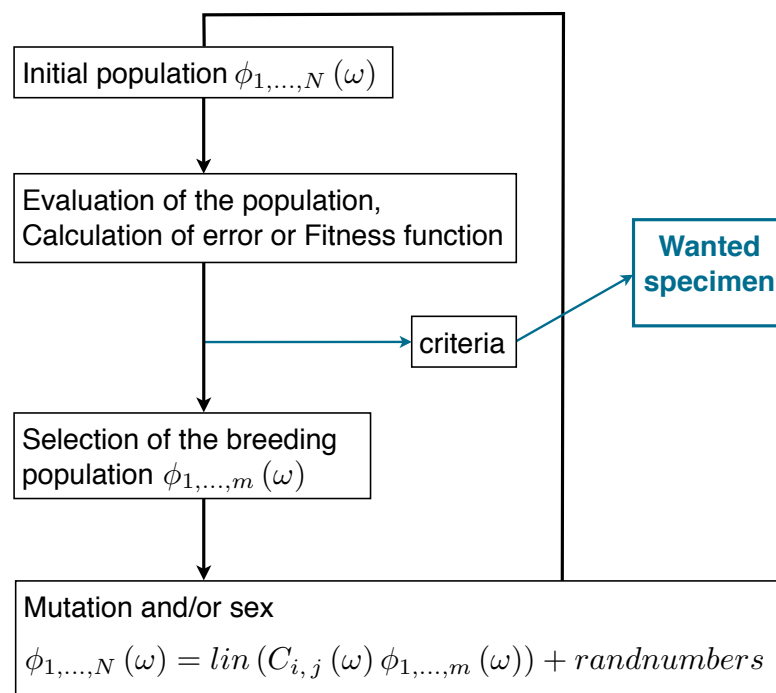
Figure 4.29.: Simple view of a genetic algorithm.

In our case we are solving a continuous problem and so a mutation is not replacing one base pair by another, and we do not determine the percentage of base pairs that should be mutated but rather we obtain neighbor solutions using a small random discrepancy from the parent solution. Also in a continuous problem it is not so clear what sex, or combination of genes really means. Combination can be a linear sum of parent genes or a combination of parts of two parent solutions in a single gene sequence. For instance we could take the quadratic phase coefficient from one parent and the cubic phase of another parent.

For some set of problems the ideal population size can be determined. For linear problems the population size as determined in [196] can be used. Our problem is not linear, but it is generally accepted that the cardinal of the population is a function of the number of degrees of freedom in the

system [197]. More accurately it is proportional to the square root of the number of variables that are used as optimization arguments.

In a genetic algorithm the parent population of the following generation is determined using the best set of solutions. This is done not by simply choosing the best parents but by enhancing the possibility that the solutions with the least error may be chosen for parents. The solution is chosen when the algorithm finds a specimen with an error lower than a given criterion.

The mutation rate within a continuous problem is not related to the number of bases that are changed. Rather, it is the amplitude of the random number that can be used in the algorithm or a mutation amplitude. If the random number generator is given by *rand*, and takes values from -1 to 1, the mutation is going to be:

$$new\_solution = old\_solution + mutation\_mag*rand.$$

4.7.1. Simplified genetic algorithms applied to phase reconstruction

We used a simplified highly elitist version of a genetic algorithm. In fact we used the algorithm in such a way that the square root of the number of individuals in a generation were chosen to be the parents of the next generation, and we chose only the best solutions.

Other approaches to this problem using a genetic algorithm have been made. Chen et al. [198] used a population split genetic algorithm with combination and mutation for phase retrieval of an experimental 25 fs pulse and theoretically generated 50 fs pulses. Kyung-Han Hong et al used a direct comparison with the IAC trace [199] with sub-10-fs pulses.

Genetic algorithms and gradient optimization were used by Yang et al. [200] to improve the computation time. These studies used a Taylor base phase description. Here we have also studied this possibility.

In a point-by-point base we used a mutation where we added to the previous phase a random set of numbers. However we discovered that the best set of random numbers is not one for which the density is a flat profile but rather a Gaussian one. In order to do this we used a flat density random number generator from Matlab, multiplied it by a certain mutation amplitude and sums it up 20 times. This has shown to work better than a simple flat density random mutation. In fact this mutation works better than a polynomial base mutation.

We are not sure of the reasons why a random number generator with a Gaussian distribution works better than a generator with a flat number distribution. It might simply be because it decreases the mutation rate of the algorithm, concentrating solutions around the known parents but at the same time allowing for a a wide range of solutions.

Fig. (4.30) shows that this algorithm completely reproduces the spectral shape for low-chirped pulses. In order to prove this we used a Gaussian pulse stretched to 9 fs using a quadratic spectral phase and Gaussian spectrum with a Fourier limited duration of 7 fs FWHM. In Fig. (4.30) we show that the Fourier transform of the intensity and the second harmonic spectrum are completely reconstructed. We opted for this pictures because it directly compares what is input into the algorithm and comes out.
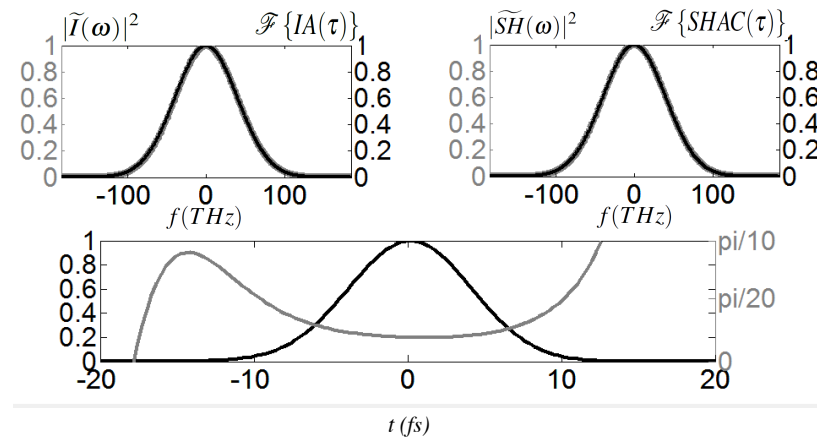
Figure 4.30.: Deconvolution of a Gaussian pulse quadratically stretched from 7 fs to 9 fs. On top (left) magnitude of the Fourier transform of the pulse intensity, (right) Fourier transform of the second harmonic (grey as obtained by the algorithm and back as inputed initially in the algorithm), (below) retrieved pulse intensity in black and its temporal phase in grey.
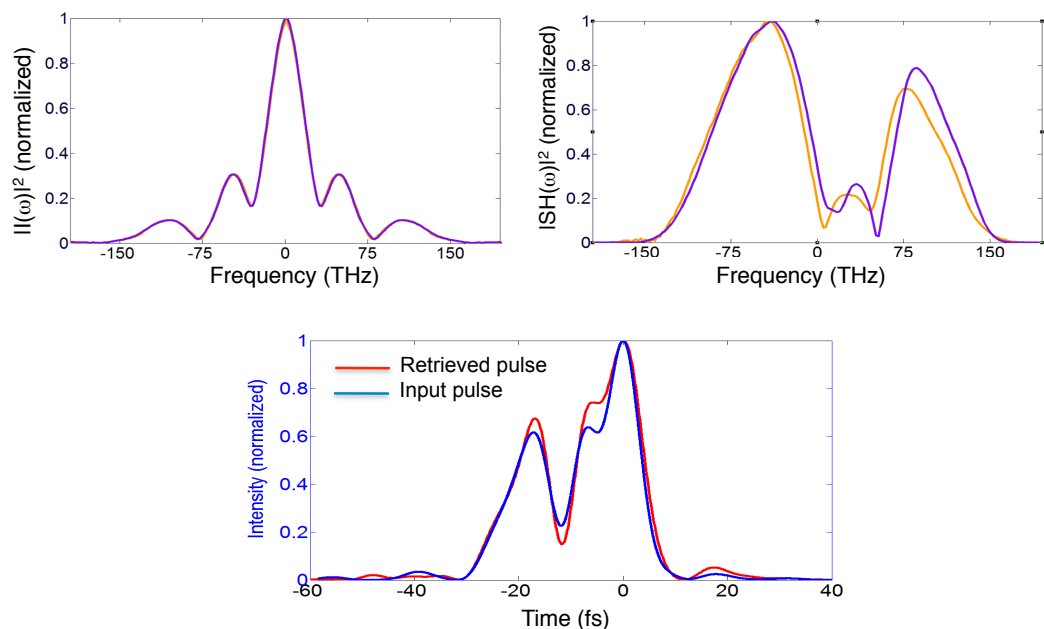
Figure 4.31.: Reconstruction of a structured pulse. On top (left) $F\{IA(\tau)\}$ and (right) $F\{SHA(\tau)\}$ retrieved traces in blue; input data in orange. Bottom: retrieved and input intensity profiles.

4. Spectral phase reconstruction via spectral intensity and interferometric autocorrelations

However, as we have seen in Sec. (4.2) these measurements are not so sensitive for highly chirped pulses. In this case, it would be admissible that the algorithm would have some difficulty retrieving the spectral phase. In order to test this we used a highly chirped pulse with an experimental spectral shape (Fourier limited by 5.98 fs) and a fourth order Taylor phase which results in a FWHM duration of 42 fs in two major pulses, the largest of them with 24 fs.

The results are shown in Fig. (4.31). Having proved that the algorithm retrieves complex pulses in theory, the next step is to use this algorithm with known experimental data.

We used a pulse emitted by a Femtolasers Rainbow oscillator that is slightly stretched in time. The results obtained are shown in Fig. (4.32). The retrieved measurement of IAC and MOSAIC is shown in Figs. (4.33) and (4.34) respectively.
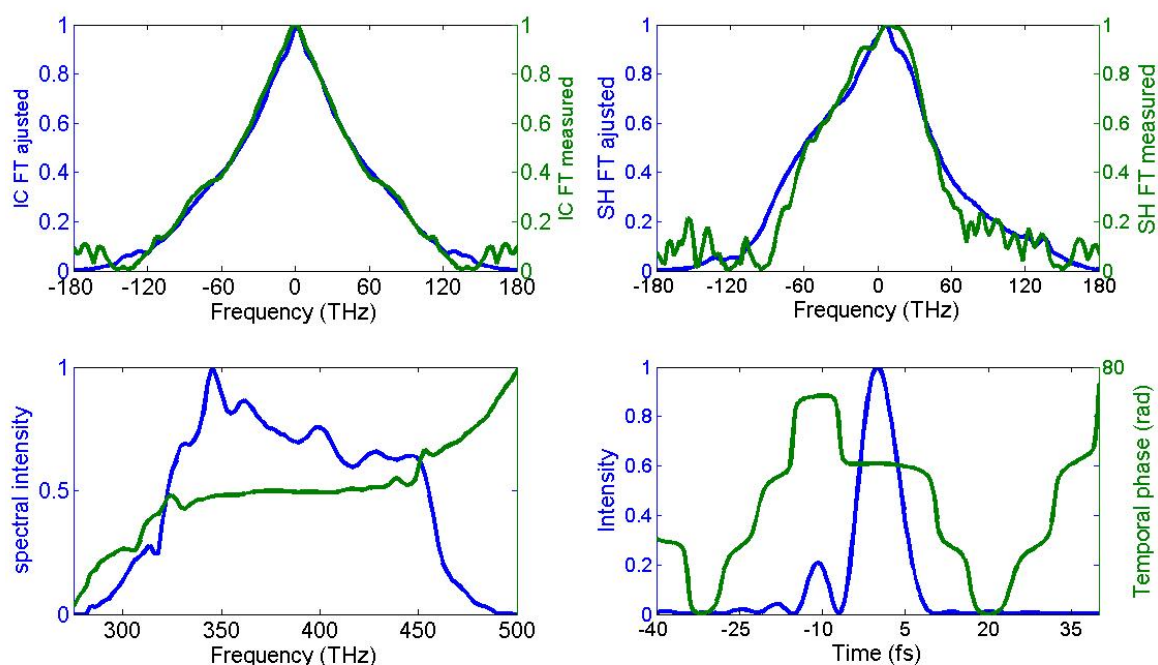
Figure 4.32.: (Top left) Fourier transform of the IAC and (above right) Fourier transform of the second harmonic, experimental data (green) and reconstructed (blue). (Bottom) reconstructed pulse, in the spectral (left) and time (right) domains, in phase (green) and intensity (blue).

In Fig. (4.32) we see that the background white noise affects the SH spectrum more than it affects the Fourier transform of the intensity autocorrelation. This is rather intuitive simply because the second harmonic spectrum has a magnitude of 1/4 of the intensity autocorrelation, as we can see in Fig. (4.6).

From Fig. (4.32) it is also possible to see that the background noise is not retrieved but that the main features of the measurements are well fitted by the algorithm.
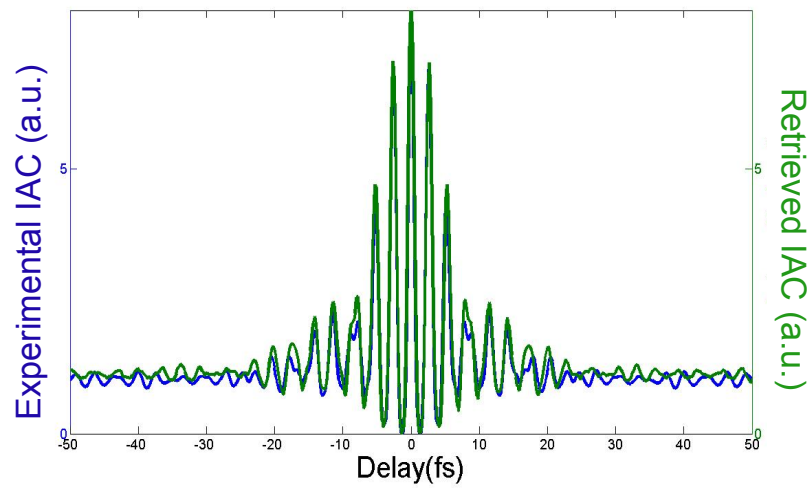
Figure 4.33.: Experimental (blue curve) and retrieved (green curve) IAC traces.
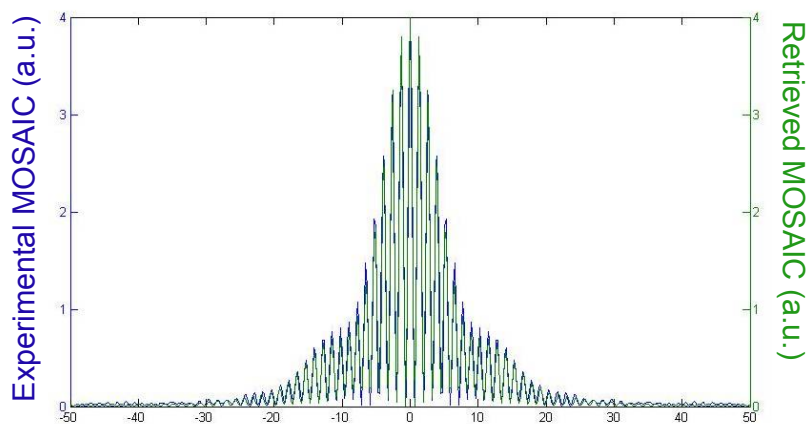
Figure 4.34.: Experimental (blue curve) and retrieved (green) MOSAIC traces.

In order to test the robustness of this algorithm to fluctuations/errors in the retrieval we repeated the algorithm obtaining the several results given in Table (4.1).

Trial	Duration
1	7,613 fs
2	7,625 fs
3	7,622 fs
4	7,618 fs
5	7,617 fs
6	7,616 fs

Table 4.1.: Pulse duration obtained after several reconstruction trials with different initial phases, the average duration is 7.619±0.004 fs.

It is easy to see that the algorithm is resilient to the initial phase conditions, and that the errors associated with the measurement are not due to the reconstruction method itself but to errors that might be presented in the measurement or the data processing. In fact the time scale error can be larger than the subsequent fluctuations due to the algorithm. We can compare Table (4.1) with the results given in Fig. (4.14). The noise in Fig. (4.32) shows that the experimental error is also larger than the precision due to imperfections of the algorithm. We have to remember that the signal-to.noise ratio of the the initial traces is not the signal-to-noise ratio of the measurement but its square root, divided by one in the case of the IA, and by four for the SH spectral shape.

We also tried to retrieve the pulse shape using a Taylor polynomial as a base to describe the spectral phase. A Taylor expansion up to the 250th order was used. The results are shown in Fig. (4.35) and Table (4.2). It is quite clear that the Taylor expansion only reconstructs part of the pulse shape, but not the entire pulse shape that is reconstructed with a point-by-point approach.
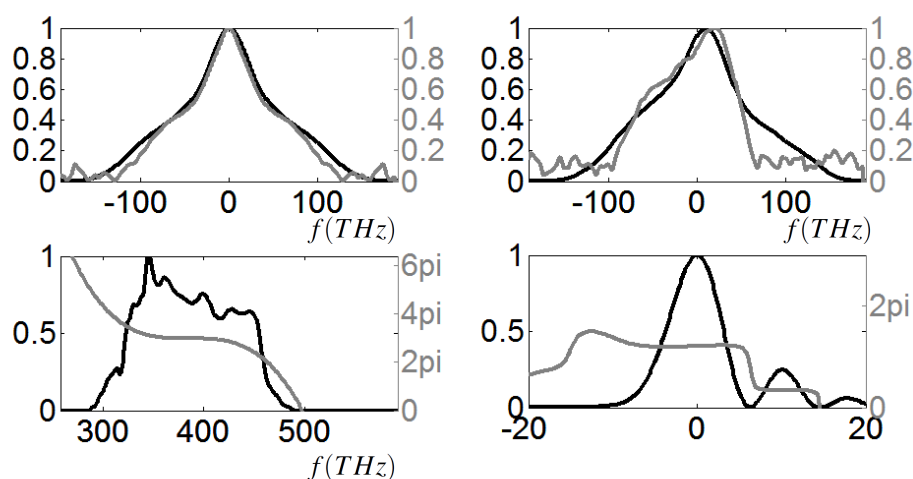
Figure 4.35.: Deconvolution using a Taylor-decomposed spectral phase. (above, left) Fourier transform of the IAC, (above, right) Fourier transform of the second harmonic, with the experimental data in grey and the reconstructed pulse in black. (Below) the reconstructed pulse phase (grey) and intensity (black) in spectrum (left) and in time (right).

Please note that we used the same experimental data than for the results in Fig. (4.32); this fact allows us to test the algorithm in a real situation, and we see that this base does not allow for error reduction below a certain point. Had the Taylor base algorithm been tested using a spectral phase initially built upon a polynomial base, it would be expected that the algorithm would be able to completely reconstruct the pulse, as it was done by Kyung Han Hong et al. in 2007 [199].

In Table (4.2) we see that an increase in the order of the Taylor polynomial does not change the results significantly, it is clear that the values overlap for 3 and 30 coefficients. We may also see that the algorithm is reproducible, and at least has a precision larger than the experimental error seen in Sec. (4.3). We did trials with initial random Taylor coefficients and with a flat phase. We also

tried a Taylor polynomial with an expansion that went up to the 250th order (flat phase as an initial guess for the spectral phase). The calculation was very slow for this case and the algorithm did not fully converge. We obtained a pulse duration of 6.936 fs, a duration slightly larger than the duration obtained for Taylor polynomials with 3 and 30 coefficients.

Duration (fs)	
(3rd order polynomial)	
6.940	6.934
6.930	6.931
6.933	6.932
6.917	
6.931 ±0.008	

Duration (fs)	
(30th order polynonial)	
6.934	6.926
6.932	6.930
6.931	6.929
6.924	6.923
6.929	
6.929 ±0.004	

Table 4.2.: Pulse duration results obtained after several trials of the algorithm using a Taylor expansion as the basis for the phase, with (left) a third order polynomial and (right) a 30 order Taylor expansion.

The time it takes for the third order Taylor expansion to run is on the order of some seconds. The Taylor expansion up to the 30th order takes around one hour to run. We see that using the Taylor base a small order expansion should be chosen, as the running time does not provide any further precision. In fact, if a low order Taylor expansion is not sufficient, it is better to use a point-by-point base.
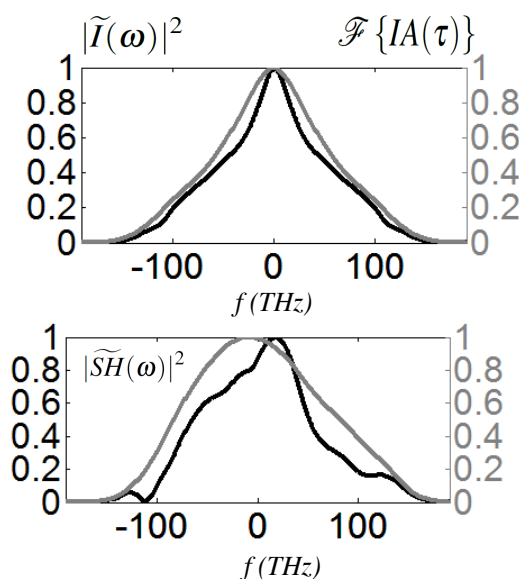
Figure 4.36.: Retrieval results with a bad calibration on the spectral shape. (top) Fourier transform of the IAC and (below) Fourier transform of the second harmonic, with the experimental data in black and the reconstructed pulse in grey.

One question that remains is the sensitivity of the algorithm to experimental errors made when measuring the spectral shape. These errors normally arise if the calibration of the spectral shape

is not made. We tried to retrieve the pulse shape with a faulty spectral shape, and the reconstruction failed. This shows that the algorithm is sensitive to errors and it also indicates that even if the three quantities used for pulse reconstruction can define a pulse, not all combinations of three curves taken as the referred quantities define a pulse profile. A further trial was made in which the background noise on the temporal measurements was cleaned using a super Gaussian filter. However a good agreement was not obtained. The results are shown in Fig. (4.36).

More complex pulses can also be retrieved using this method. We used it to obtain the phase of pulses after soliton compression in a nonlinear photonic crystal fiber (PCF). PCF's are known to have outputs that can have at the same time a complex phase and a spectral bandwidth that extends over one octave. The results are shown in Figs. (4.37), (4.38) and (4.39).
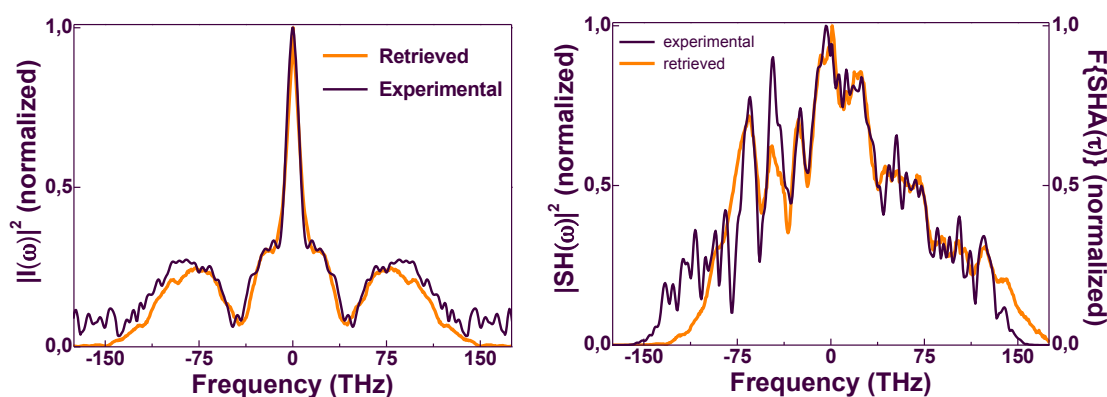
Figure 4.37.: (right) Intensity spectrum and (left) SH spectrum, obtained experimentally (in black) and retrieved by the genetic algorithm (orange).
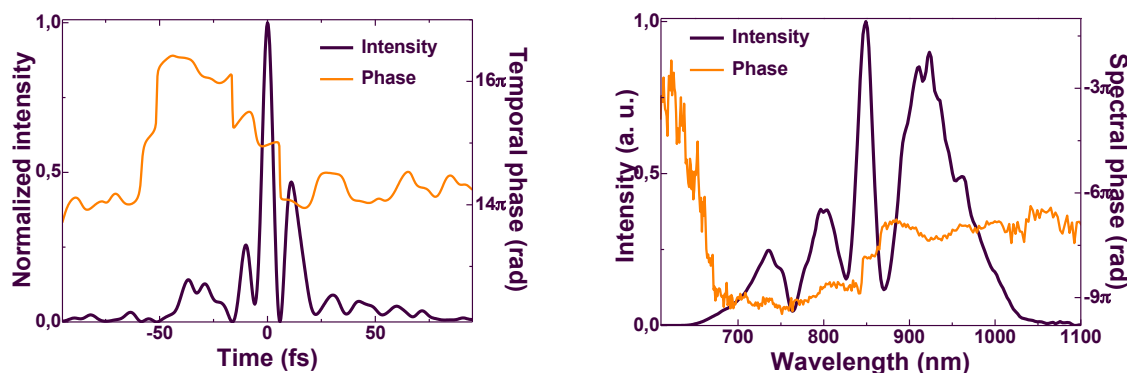
Figure 4.38.: Results obtained for the spectral shape (right) and temporal profile (left).

Figs. (4.37), (4.38), (4.39) show that the algorithm can reconstruct the spectral phase and consequently the pulse shape even for results obtained in complex experimental conditions, in which pulses have sub-two cycle durations and a complicated spectral phase [176, 201].
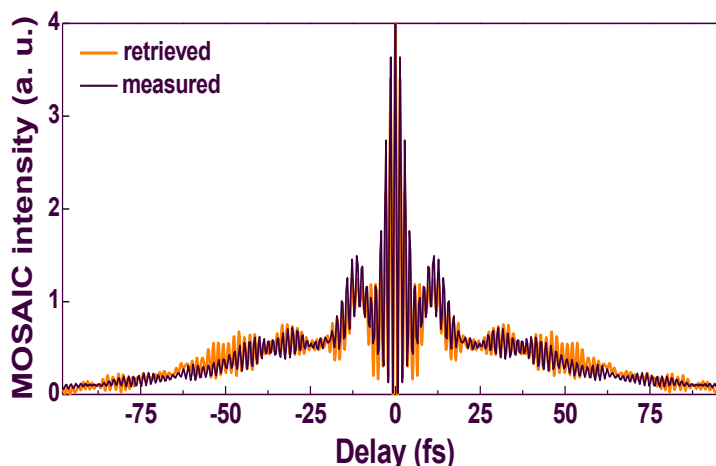
Figure 4.39.: Retrieved MOSAIC trace (orange), and experimental measurement (black).

4.7.2. Using an adaptive mutation magnitude

A difficult parameter to optimize is the magnitude of the mutation[6]. Using an intelligent mutation magnitude has already been studied, however, after the equations presented by Thomas Back and Martin Schutz in [202] failed to give better results than a non adaptive mutation, we used a very simple approach which significantly decreased the calculation time and improved the agreement between the obtained and the retrieved Fourier transforms of IA and SHAC. In reality in the approach presented in [202] the mutation rate dropped too fast.

The algorithm behaves as follows: first it adjusts the test pulse to the main features of the measurements and then starts to produce finer adjustments to the details of the IA and SHAC. This behavior is observed regardless of the initial phase or the base used to represent the pulse. Given this, the procedure that we will subsequently describe is intuitive.

At first we adapted the mutation magnitude manually. Initial a high value for the magnitude of the mutation is used (higher than 2π rad for a point-by-point approach). When the algorithm does not find better solutions, it stops, and the magnitude of the mutation is manually decreased to smaller values until a good agreement is reached, normally ending up with a mutation magnitude of 10^{-4} rad. This procedure however requires manual intervention to an algorithm that may run for a few hours, and so it's unpractical.

---

[6]The phase is altered by using the following algorithm:
for (1:20): $\Delta\phi = \Delta\phi + mutation\,mag * rand$ and $\phi_{new} = \phi_{old} + \Delta\phi$.
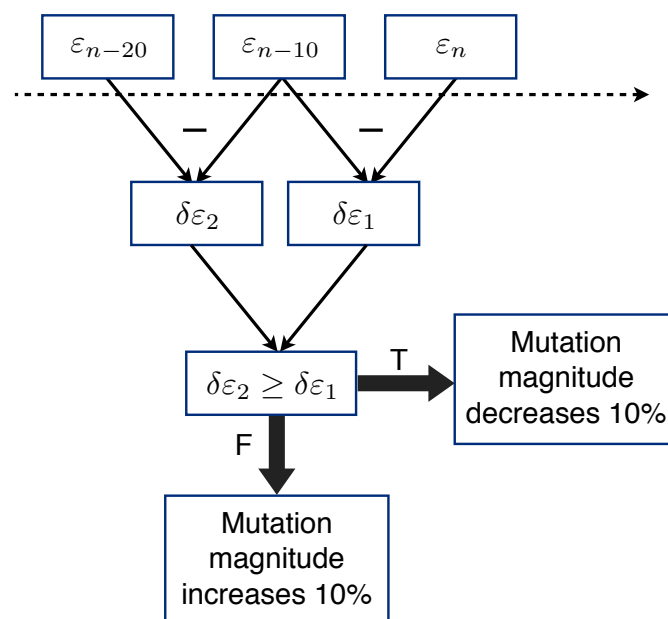
Figure 4.40.: Scheme showing the adaptive mutation.

In order to improve the algorithm's performance, an adaptive subroutine was devised in which the mutation magnitude changed with the error variation. This is exemplified in Fig. (4.40), and works the following way:

➤ consider the algorithm is at its nth generation;

➤ The error difference achieved between n-20 and the n-10 generation is calculated, as well as the decrease in error in the last 10 steps.

  • If in the last 10 steps the algorithm worked worst than in the previous 10, the mutation magnitude decreases.

  • If on the contrary the algorithm has achieved a better error reduction in the last 10 steps than in the previous 10, the mutation magnitude increases.

  • If no better solution is found, the mutation magnitude decreases, because the algorithm is near a minimum.

Despite being simple, this subroutine allows a larger search space and faster convergence at the same time. In practice, the adaptation algorithm tends to decrease the value of the mutation magnitude, and so initially a large mutation magnitude should be used (more than 2π for a point-by-point base).

In reality, the adaptation could be improved if the mutation rate would be a function of the error evolution. The results presented in Subsection (4.7.1) were all obtained using this adaptive reconstruction.

4.7.3. Mutation and combination in algorithms applied to phase reconstruction

Chen et al. have reported that by introducing combination/sex into the algorithm the calculation time increases, allowing for a better phase reconstruction [198]. We note that they used a Taylor expansion in order to describe the phase.

We tried the same approach with a point-by-point model and discovered that despite converging with minimal error this method had to be computed for several days (in a laptop computer Intel Core i7-3630QM CPU @ 2.4 GHz) before it actually gave a satisfactory result. We used the spectral shape given in Fig. (4.2) and stretched it from 5.98 to 14.40 fs, using a second order chirp of $27.9\,fs^2$, a cubic chirp of $1.05\,fs^3$ and fourth order chirp of $0.134\ fs^4$.

The algorithm with linear combination of parent solutions was run for several days. In Fig. (4.41) the results obtained after 1 and 2 days are presented. The algorithm hits its lowest error after computing for several days, and we see that this is a valid algorithm for spectral phase reconstruction, even though of little practical use due to its the extensively long computation time.
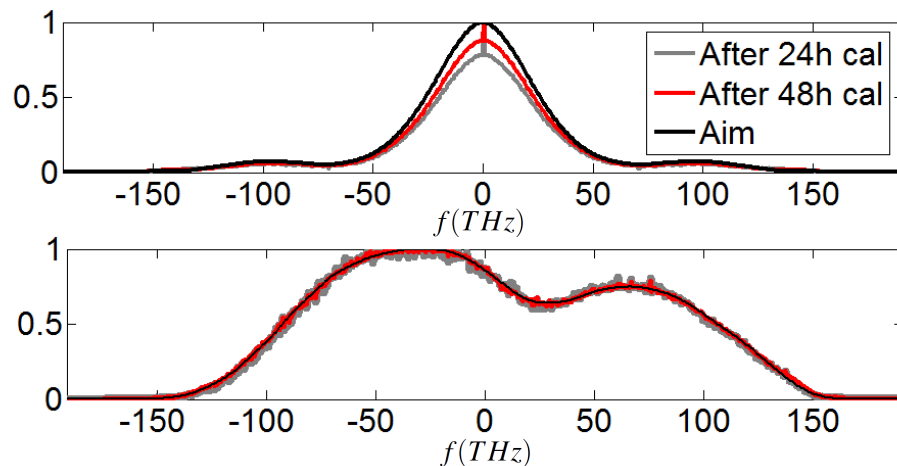
Figure 4.41.: Results for genetic algorithm with combination. (above) Intensity spectrum, (below) SH spectral shape. The aim of the algorithm in black, grey line after 24 hours of calculation and red line after 48 hours.

4.8. Particle swarm optimization (PSO)

Particle swarm optimization (PSO) is a method based on the harmonic movement of coupled oscillators and on the behavior of animal swarms. It is a stochastic method, just like the genetic algorithm, and it was invented in 1995 by James Kennedy and Russell Eberhart [203]. It has been extensively compared with genetic algorithms [204].

4. Spectral phase reconstruction via spectral intensity and interferometric autocorrelations

In this problem we consider an ensemble of particles in $\mathbb{R}^M$ space and give each particle a certain velocity. This velocity is going to be coupled to the others particles' best positions, like an oscillator would be coupled to its equilibrium position. In this algorithm each particle knows its best previous position and we also keep track of the best position of the entire population, so it basically works as a discrete damped harmonic movement of coupled oscillators in the object phase space with the already found minimizing points acting as attractors.

In practice we start with a certain random number of positions and velocities for the phase, in phase space:

$$\begin{aligned} \phi_{1,\dots,N}^r \\ \phi_{1,\dots,N}^v \end{aligned} \tag{4.39}$$

The first step consists in evaluating $\delta^2\{\phi_{1,\dots,N}^r\}$ (the error function of each particle) and obtain which of the particles $\phi_{1,\dots,N}^r$ minimizes the error function. This will serve as an attractor. We also memorize for each particle the historical particle position that minimized the error. In other words, in the first loop we store the error of each particle and consider that each particle is an attractor represented as $\phi_{L1,\dots,LN}$. In the second loop we compare the memorized errors of each particle and the error in the second loop. If the particle error is smaller than the memorized one, the particle attractor is replaced by the new position. In the subsequent loops the mechanism is repeated. We then use these attractors to change the velocity of the particles with a random number. The velocity is damped by a factor α, and the velocity changes are proportional to the distance between the particles and the attractors, like in a harmonic oscillation, as given by:

$$\begin{aligned} \phi_i^v = \alpha\phi_i^v - c_1 r_1(\phi_i^r - \phi_G^r) - c_2 r_2(\phi_i^r - \phi_{Li}^r) \\ \phi_i^r = \phi_i^r + \phi_i^v \end{aligned} \quad , with\ i = 1,\dots,N \tag{4.40}$$

In this expression ϕ_G^r is the phase that minimizes the error in the general set. The other attractor ϕ_{Li}^r, as discussed above, is the position that minimizes the error function. The coefficients r_1, r_2 are random sets of M positive numbers and c_1, c_2 are coupling constants, with ideal value 2 [205].

$$(\phi_i^r - \phi_G^r) \qquad\qquad c_1(\phi_i^r - \phi_G^r)$$
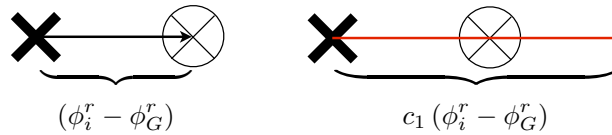
Figure 4.42.: 1D PSO. A particle position represented by the black cross and an attractor represented by the reticule. The red line represents the possible positions the particle can take in the next interaction due to the attractor.

In order to realize what the constants mean, we consider the existence of a particle ϕ_i^r represented in Fig. (4.42) by a black cross, and an attractor ϕ_G^r (shown as a circular shape with a cross). If the velocity, and other attractors are discarded, the positions that the particle can assume are represented

by the red line in the picture, or analytically by $c_1(\phi_i^r - \phi_G^r)$. If $c_1 = 2$, this reduces to an harmonic oscillator: the oscillation occurs between this point and a symmetric point on the other side of the attractor, which can be considered the equilibrium point. The random numbers r_1 and r_2 can be considered as an integration over a random time. Then we evaluate ϕ^r again. If any minimum is obtained, it replaces either the local or the global minimum, and it will serve as the attractor for the next iteration. We reapply Eq. (4.40) and the evaluation of the subsequent positions until convergence is achieved.

4.8.1. Particle swarm optimization applied to phase reconstruction

There are several versions of the particle swarm optimization method [206, 207], and an international journal is actually dedicated to them [52].

In PSO, it is usual to use subgroups of particles using the best position in the subgroup as another attractor. This third coupling delays the algorithm convergence, for the case of population split genetic algorithms. This would force us to use a third term $-c_3 r_3(\phi_i^r - \phi_{SG}^r)$ in Eq. (4.40). We tried this approach, where the fact of having 3 references (attractors) should delay convergence and enable the algorithm to find a real global minimum. However we find this 3 attractor algorithm incapable to find better solutions than the 2 attractor algorithm.

With 3 attractors, the algorithm is slower for the same set of parameters (coupling and damping constant), and there is a narrower set of parameters for which the algorithm converges. However, the results do not improve. We found the 2 attractor algorithm better suited for this problem.

Having adequate α, c_1, c_2 coefficients is crucial for a good performance [205]. Ultimately the distance between the particles is what makes this algorithm viable. If there is no distance between the particles the algorithm cannot evolve, no matter the solution found. Also, if the particles are not coupled ($c_1, c_2 \sim 0$) there is no guarantee that the algorithm is going to converge to the optimal solutions found in previous iterations. If the α coefficient is larger than one, convergence will never occur; if it is too small, the algorithm will not explore sufficient phase space. For some problems it is known that the ideal value for the dampening constant is 0.77 [205]. However we cannot be sure that this is the case for our system.

We explored the coupling coefficients from 0 to 2 in steps of 0.1 and the undamping coefficient, α from 0 to 1. The results are rather confusing and are shown in Tables (4.3) and (4.4). It is important to realize that the algorithm is stochastic, and so different runs do not give the same results. In order to test this algorithm we used a test pulse that had been stretched from $5.98\,fs$ Fourier limited (the spectral shape given in Fig. (4.2)), to $14.40\,fs$, using a quadratic chirp of $27.9\,fs^2$, a cubic chirp of $1.05\,fs^3$, and quartic chirp of $0.134\,fs^4$. From these data we constructed a pulse and obtained a IAC trace. We then used the PSO algorithm instead of the genetic algorithm to reconstruct the pulse's spectral phase.

4. Spectral phase reconstruction via spectral intensity and interferometric autocorrelations

$\alpha \backslash c_1 = c_2$	0	0,1	0,2	0,3	0,4	0,5	0,6	0,7	0,8	0,9	1
0	245,92	234,96	219,34	219,76	205,66	191,94	219,33	167,81	209,20	180,33	235,30
0,05	252,42	219,75	211,32	212,79	199,47	194,09	178,99	173,14	182,07	162,38	169,86
0,1	248,84	214,50	212,35	220,67	181,69	178,67	167,15	183,97	170,68	127,95	159,34
0,15	255,99	210,14	217,23	199,20	210,32	179,79	202,03	133,63	175,68	164,14	213,34
0,2	250,74	220,79	215,18	201,62	203,49	183,16	150,83	170,56	164,50	160,17	156,49
0,25	247,54	214,33	206,69	191,78	182,57	184,82	170,51	164,32	155,14	130,84	106,15
0,3	266,07	215,86	199,95	214,37	187,30	189,51	179,30	185,30	168,02	136,20	114,65
0,35	260,98	208,86	203,99	184,24	201,42	173,20	153,88	138,85	142,28	101,31	166,93
0,4	266,11	208,99	189,85	183,54	181,65	163,43	156,12	151,58	127,93	107,58	192,69
0,45	300,27	211,61	190,47	178,98	173,01	145,12	153,23	164,08	140,40	101,24	124,37
0,5	255,94	201,20	187,05	200,47	157,65	138,49	165,89	136,69	128,36	77,42	192,69
0,5	282,42	214,78	211,76	183,56	200,11	186,42	156,22	165,16	150,75	171,26	148,77
0,55	256,44	226,85	196,34	195,48	172,98	147,17	164,89	152,27	144,90	135,10	181,97
0,6	255,10	212,96	186,44	169,00	164,89	157,21	167,32	140,71	134,31	121,11	136,23
0,65	270,27	218,90	182,76	196,01	126,67	160,72	165,36	123,47	176,14	127,14	112,08
0,7	242,17	209,29	185,37	162,75	143,29	139,05	139,31	149,29	120,20	117,38	92,85
0,75	270,39	194,79	151,40	148,29	125,17	125,55	106,09	87,85	94,45	120,73	110,81
0,8	243,88	160,99	155,44	135,03	131,14	117,22	129,25	107,29	89,25	84,87	89,22
0,85	250,62	161,28	117,73	114,53	118,15	90,88	115,28	140,22	45,71	37,64	88,66
0,9	229,16	128,19	106,15	100,70	58,23	42,24	87,21	70,25	105,56	96,30	142,24
0.95	224,29	123,83	58,00	43,07	65,30	45,09	109,65	154,45	180,00	184,05	205,36
1	220,41	193,41	195,60	173,13	183,63	193,06	183,92	211,44	221,24	218,56	196,80

$\alpha \backslash c_1 = c_2$	1,1	1,2	1,3	1,4	1,5	1,6	1,7	1,8	1,9	2
0	200,88	192,90	193,57	174,20	188,31	198,36	234,58	189,06	227,41	225,71
0,05	193,07	176,52	191,70	197,05	193,29	178,01	164,66	153,16	139,55	186,85
0,1	197,95	182,58	162,22	180,49	177,60	171,06	163,38	160,64	156,79	204,78
0,15	194,05	178,33	159,50	187,64	176,23	179,76	125,50	151,81	115,26	189,12
0,2	194,33	194,67	183,86	180,00	182,01	177,31	125,80	159,25	125,90	164,54
0,25	171,52	193,56	189,37	168,32	135,95	127,05	125,71	127,32	95,06	178,22
0,3	168,42	170,49	168,81	156,77	170,14	162,71	131,78	136,34	121,26	113,57
0,35	155,90	154,04	163,99	165,49	135,53	139,51	116,79	111,65	76,52	159,17
0,4	150,86	142,17	134,55	121,82	157,58	131,65	115,77	102,44	96,76	144,09
0,45	178,05	166,42	162,71	140,15	156,50	128,24	99,64	43,54	116,75	150,74
0,5	129,78	154,81	159,00	113,17	122,89	96,49	111,99	98,31	77,02	179,40
0,5	147,26	143,38	139,71	114,67	116,50	127,24	61,99	25,34	205,68	172,92
0,55	160,78	129,28	131,25	132,47	119,27	105,10	72,33	63,57	176,20	193,37
0,6	123,82	108,33	118,15	126,19	100,20	76,03	24,62	171,29	163,62	194,67
0,65	115,06	114,25	123,33	103,08	91,63	30,72	79,91	125,43	139,36	190,73
0,7	120,46	90,26	127,57	74,10	75,62	93,14	97,54	190,57	195,09	203,65
0,75	101,32	112,56	50,50	29,23	34,23	207,22	190,45	183,32	195,09	209,80
0,8	53,77	96,20	79,00							
0,85										
0,9										
0.95										
1										

Table 4.3.: Error results obtained by performing a sweep over the parameters associated to the PSO. The coupling parameters c1 and c2 varied from 0 to 2 and the undamping factor α varied from 0 to 1.

$\alpha \backslash c_1 = c_2$	0	0,1	0,2	0,3	0,4	0,5	0,6	0,7	0,8	0,9	1
0	3	3	5	5	5	24	4	67	7	21	4
0,05	7	28	24	22	30	31	34	75	61	265	55
0,1	8	15	11	35	31	33	34	80	61	207	88
0,15	8	28	32	39	38	35	35	96	72	152	40
0,2	8	39	38	32	34	43	41	74	105	149	111
0,25	11	24	35	34	36	39	56	144	125	177	586
0,3	13	40	43	40	42	45	52	283	109	231	246
0,35	14	51	37	44	44	76	170	251	108	208	151
0,4	14	36	39	52	64	83	429	102	176	457	119
0,45	16	49	48	53	79	64	148	140	181	284	268
0,5	21	42	54	54	99	248	102	169	267	819	151
0,5	19	46	57	49	50	53	56	97	67	166	76
0,55	24	52	67	56	60	69	68	70	223	146	102
0,6	22	70	68	87	71	75	80	86	318	146	162
0,65	24	84	71	75	82	93	185	113	120	138	154
0,7	34	89	114	94	131	160	119	166	174	229	295
0,75	39	95	113	116	131	459	190	207	300	293	354
0,8	51	124	145	152	197	222	249	321	430	466	599
0,85	79	177	198	426	261	414	419	566	850	1037	873
0,9	93	282	350	446	734	865	387	342	1260	376	1008
0.95	212	646	999	963	184	1025	1025	560	1025	1025	1025
1	1025	1025	1025	1025	44	1025	1025	1025	1025	1025	1025

$\alpha \backslash c_1 = c_2$	1,1	1,2	1,3	1,4	1,5	1,6	1,7	1,8	1,9	2
0	24	32	40	91	57	9	3	11	3	3
0,05	37	37	39	42	64	61	138	278	312	57
0,1	31	36	45	41	48	116	93	143	254	42
0,15	37	45	52	43	120	59	82	135	313	35
0,2	43	56	49	61	215	71	138	119	329	260
0,25	55	58	72	158	107	119	164	356	303	103
0,3	67	102	95	127	93	79	127	216	385	329
0,35	100	58	62	229	130	121	159	235	615	166
0,4	61	614	164	127	113	193	249	438	467	211
0,45	111	74	137	189	249	170	290	903	369	382
0,5	86	230	145	140	338	341	501	349	711	233
0,5	131	156	105	161	232	284	399	1810	78	264
0,55	112	179	137	167	309	272	645	1161	147	196
0,6	132	156	170	200	417	522	1536	147	255	322
0,65	184	211	350	168	450	1036	1465	550	501	150
0,7	241	353	466	251	1607	1134	1456	343	364	326
0,75	465	501	767	1762	5263	283	165	399	410	633
0,8	715	907	3167							
0,85										
0,9										
0.95										
1										

Table 4.4.: Number of iterations until convergence is obtained as a function of the PSO parameters. The coupling parameters c_1 and c_2 varied from 0 to 2 and the undamping factor α varied from 0 to 1.

4. Spectral phase reconstruction via spectral intensity and interferometric autocorrelations

In Tables (4.3) and (4.4) there are some absent values. These are seen in situations where the value of α falls between 0.85 and 1 and the values of the coupling constants lie between 1.6 and 2. In these cases the algorithm does not converge within a 24 hour calculation. The values in red correspond to cases where convergence was achieved within a reasonable time frame.

Convergence is achieved if either the coupling constant or the undamping factor is low. The best results however are given for low values of the coupling constant and an undamping factor close to one (but not one) or for small undamping factor and a high coupling coefficient. This is either $\{\alpha = 0.9 - 0.95\} \wedge \{c1 = c2 = 0.3 - 0.5\}$ or $\{\alpha = 0.5 - 0.6\} \wedge \{c1 = c2 = 1.7 - 1.8\}$.

Note that we also repeated the results of the simulations for $\alpha = 0.5$. We see that these results are different in the two runs, which confirms the stochastic nature of the algorithm.

The PSO results given in Tables (4.3) and (4.4) present a large error between the expected results and what is actually obtained via this method. The results obtained with c1=c2=1.7, $\alpha = 0.6$ are given in Fig. (4.43).
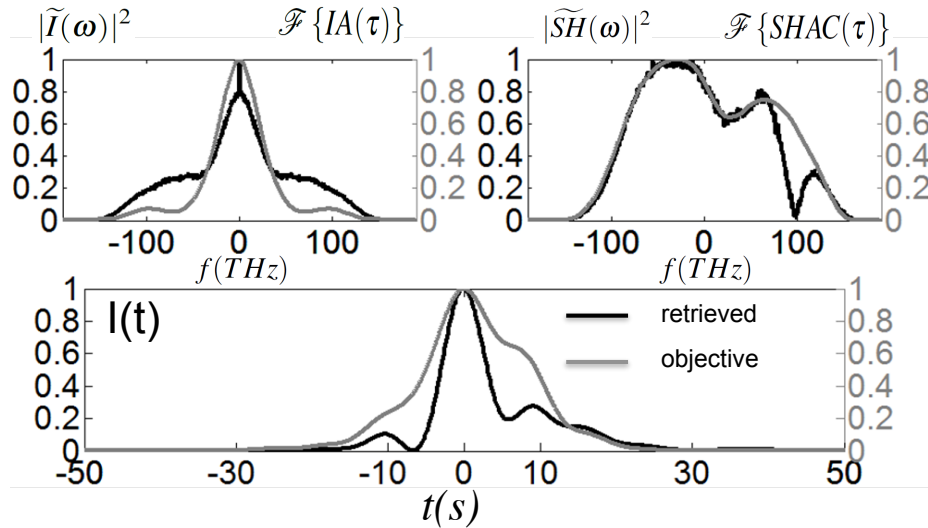
Figure 4.43.: Results obtained using c1=c2=1.7, $\alpha = 0.6$. On top (left) intensity spectrum, (right) SH spectrum, on the bottom the intensity profile, the actual results (black) and the desired curve (gray).

We see that despite sweeping through the algorithm parameters, the PSO algorithm does not reconstruct the spectral phase in one run.

To summarize, this algorithm can give some results using the appropriate working parameters but we must point out that it gets stuck because the velocity and distance between the particles goes to zero and it stops evolving. In order to have a good solution for our problem we need a better, more reliable version of the PSO algorithm, namely the repulsive particle swarm algorithm discussed in the next subsection.

4.8.2. Repulsive particle swarm optimization (RPSO)

This method is used in cases where PSO provides fast convergence but gets stuck at some point that might not even be a minimum or an optimal solution. Repulsive particle swarm optimization (RPSO) was invented by Jacques Riget and Jakob S. Vesterstrøm in 2002 [206].

The RPSO algorithm makes use of a repulsive force to make the particles move away from each other in $\mathbb{R}^{\mathbb{M}}$ space. The procedure is actually the same as in PSO, but a small random repulsive force is applied to the particles and in consequence the convergence rate decreases. In this case Eq. (4.40) changes to

$$\phi_i^v = \beta r_3 + \alpha \phi_i^v - c_1 r_1 (\phi_i^r - \phi_G^r) - c_2 r_2 (\phi_i^r - \phi_{Li}^r)$$
$$\phi_i^r = \phi_i^r + \phi_i^v \qquad\qquad ,i = 1,...,N , \qquad (4.41)$$

where we simply add a random array, βr_3, to each particle velocity, this perturbs the ensemble of the particles which slip away from one another and allows the algorithm to search in other zones of the phase space. The factor β is controlled in order to allow convergence, and so β must be a function of the cycle number or the error.

We can also maintain the PSO algorithm until convergence and then apply the repulsive force repeating the PSO algorithm subsequently.

4.8.3. RPSO applied to phase reconstruction

In our attempts to apply this algorithm to the phase reconstruction problem we used two approaches. In the first approach the velocity is determined by Eq. (4.41). Here we did not find a β that achieved convergence and a small error at the same time; either the convergence time was too long and the results too disperse, or the convergency time was too small and the results gave a large error.

Instead of the traditional RPSO algorithm, we used a modified version, namely a simple PSO algorithm, as in Subsection (4.8.1), with a undamping constant of 0.6 and a coupling value of 1.7. When the algorithm converged we reseted the initial velocity randomly, effectively giving a kick to the swarm. We repeated the PSO until it converged, and then nudged it again. The perturbation was reduced at every interaction, until convergence was achieved. Technically, the velocity was being reinitialized to $\phi_v = \frac{2\pi rand}{N}$, where N is the number of times we ran the simple PSO algorithm.

With this algorithm we tried to retrieve the spectral phase. As in the previous subsection we used a pulse that had been stretched from $5.98\,fs$ Fourier limited (the spectral shape given in Fig. (4.2)), to $14.40\,fs$, using a quadratic chirp of $27.9\,fs^2$, a cubic chirp of $1.05\,fs^3$, and quartic chirp of $0.134\,fs^4$. From these data we constructed a pulse and obtained a IAC trace. We then used the RPSO algorithm instead of the genetic algorithm used in the previous section.

The results can be seen in Fig. (4.44). These were obtained using the parameters given above of $c_1 = c_2 = 1.7$ and $\alpha = 0.6$. It was not possible to reproduce the results using $c_1 = c_2 = 0.2$ and $\alpha = 0.8$ within the same time frame, which means that the parameters (coupling and undamping) are critical in a RPSO approach. Moreover it means that even if in the PSO simulations we had two parameter zones where the results were similar $\{\alpha = 0.9 - 0.95\} \wedge \{c_1 = c_2 = 0.3 - 0.5\}$ or $\{\alpha = 0.5 - 0.6\} \wedge \{c_1 = c_2 = 1.7 - 1.8\}$.

In a RPSO simulation we obtained better results using this second zone, probably because in a PSO algorithm this zone tends to converge a faster than the first one.
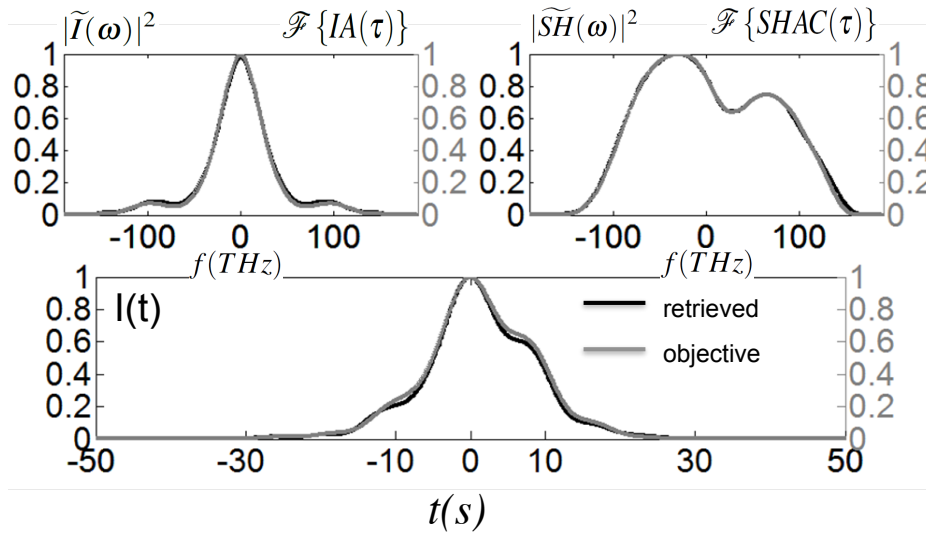
Figure 4.44.: Results with c1=c2=1.7, $\alpha = 0.6$. On top (left) intensity spectrum, (right) SH spectrum, on the bottom the intensity profile, the actual results (black) and the desired curve (gray).

To conclude this section, we have studied a method for spectral phase reconstruction, using an advanced version of a particle swarm optimization, and proved that obtaining the spectral phase using an intensity autocorrelation, the spectral profile and the second harmonic spectrum is possible if an appropriate minimization method is found, either a repulsive particle swarm optimization or a genetic algorithm.

4.9. Conclusion

In this chapter we proved that spectral phase reconstruction based on the well known measurements of interferometric autocorrelation and power spectrum is possible. We analyzed several theoretical and experimental measurements and in all of them we were able to reconstruct the spectral phase using minimization algorithms, the power spectrum, and the Fourier transforms of IA and SHAC. From this study, we believe, that it is possible to reconstruct the phase of any ultrafast pulse using

a MOSAIC trace and the spectral intensity profile as long as the Nyquist theorem in frequency and time is obeyed.

In detail, this chapter has reviewed the known facts about the interferometric autocorrelation traces, IAC. We describe the Fourier transform of the IAC in three parts: one centered at 0 frequency (the intensity autocorrelation) other centered at the EM central frequency and a third centered at twice that frequency (the SH spectrum). This ensemble completely defines the EM field temporal profile, as long as the EM field is contained within a finite time frame, and has finite energy. However, the carrier envelope phase cannot be measured by this method, and there is an ambiguity in the signal of the spectral phase, that translates in an ambiguity in the time direction, this ambiguity however can be easily surpassed by taking two measurements of pulses with a known spectral phase difference between them [150].

MOSAIC traces that are highly sensible to the pulse chirp were presented, which means that using this measurement (or its Fourier transform) precise measurements of the pulse profile can be made.

We then tried several approaches to reconstruct the spectral phase. First we used a Gerchberg-Saxton type algorithm, invented by K. Naganuma et al., and at least in the cases we studied no spectral phase reconstruction was possible: the algorithm did not converge the results are completely random, and we were not able to improve these results even with background cleaning.

Then we devised another method based on a Gerchberg-Saxton algorithm. This algorithm behaved better than the algorithm presented previously. It either converged or presented a loose convergence. However, full phase reconstruction was not possible: the final error was still too large, the variance of the pulse was correct but not its intensity profile.

We then used a minimization approach, where the spectral phase was the minimization argument and the factor to be minimized was the error between the experimental and the retrieved traces, as given by Eq. (4.28). We used the spectral shape to calculate the electric field because it is easier and also because it is also easier to measure the pulse spectrum of the field than its IAC trace. After calculating the electric field using the spectrum and a trial spectral phase $\widetilde{E}(\omega) = \sqrt{S(\omega)} \exp\left[i\phi(\omega)\right]$, we calculated the intensity spectrum $\left|\widetilde{I}(\omega)\right|^2 = \left|\mathscr{F}\left\{\left|\mathscr{F}^{-1}\left\{\widetilde{E}(\omega)\right\}\right|^2\right\}\right|^2$ and the SH spectrum $\left|\widetilde{SH}(\omega)\right|^2 = \left|\mathscr{F}\left\{\left(\mathscr{F}^{-1}\left\{\widetilde{E}(\omega)\right\}\right)^2\right\}\right|^2$. In summary, the method assumes that the spectral shape is correct, the algorithm's argument is the spectral phase and the factor to be minimized is the error in the other two measurements, given by Eq. (4.28).

In theory it would be possible to assume a correct SH spectrum $SSH(\omega) = \left|\widetilde{SH}(\omega)\right|^2$ instead of assuming a correct field spectrum. The minimizing argument would be the second harmonic spectral phase and the electric field would be redefined by a complex expression[7]. The error would be

---

[7]$\widetilde{E}(\omega) = \mathscr{F}\left\{\sqrt{\mathscr{F}^{-1}\left\{\sqrt{SSH(\omega)} \exp\left[i\phi_{SH}(\omega)\right]\right\}}\right\}.$

redefined using the two other quantities. This would not be convenient because calculations would be harder, and because the SH spectrum obtained from IAC has the smallest S/N ratio of the two measurements (field spectrum and SH spectrum). If the SH spectrum was measured directly the S/N ratio might improve. Also a direct measurement enables us to correct deviations of the SH from $E^2(t)$ shape due to imperfect phase matching.

Having redefined our problem as an error minimization problem we tried several algorithms to solve it. First we tried a minimization algorithm included in Matlab base code (*fminsearch*) this algorithm proved able to decrease the error, even if it did not provide full spectral phase reconstruction. In this algorithm we used an amplification factor in order to increase the searched space. For a point-by-point base, the amplification factor enables the algorithm to achieve a better agreement (smaller error), however in the cases studied this algorithm did not converge to a minimum. In fact the algorithm ran for several days without finding a minimum, which means that the algorithm is too slow to solve our problem this way. We tried the same minimization algorithm but instead of describing the phase point-by-point we used a base built upon type I Chebyshev polynomials. In this case the algorithm was able to find a minimum, however this was a local minimum where the spectral phase had not been reconstructed. In summary, *fminsearch* is not able to reconstruct the spectral phase. Local minima may exist when we use Chebyshev polynomials to describe the spectral phase. We cannot say that local minima do not exist when we describe the spectral phase point per point. However, we can say we have not found any.

We finally presented an algorithm that successfully finds a spectral phase that adjusts the three independent measurements. This algorithm is based in a simple elitist genetic algorithm with an adaptive mutation. At first the spectral phase is constructed with a Taylor polynomial and afterwards with a point-by-point base.

We successfully reconstructed electric fields using theoretically generated and experimental data. Note that the S/N of the measurement is not actually the S/N ratio of the resulting electric field because we use the square root of the data in order to implement the algorithm, so the minimizing factor of our S/N is $\frac{\sqrt{\delta}}{2}$, with δ is the data S/N ratio.

The experimental data used for spectral phase reconstruction were:

➤ Pulses issued from a few cycle femtosecond oscillator;

➤ 4.9 fs pulses generated by soliton effect compression in a photonic crystal fiber [176, 201].

We also researched the possibility of using sex in the genetic algorithm to obtain a bigger degree of precision in the reconstruction. We were able to reproduce the spectral phase as we had done with the simple genetic algorithm. However the time demands of this upgrade did not result in any (observed) increase in precision.

Having found an algorithm that completely reconstructed the spectral phase, we tried to find another

algorithm that would do the same. We found that a repulsive particle swarm optimization algorithm with a high undamping factor and a low coupling constant was also able to reconstruct the pulse's spectral phase.

The measurements discussed here (IAC and power spectrum, IA, SH power spectrum) are routinely taken as preliminary measurements in ultrafast laboratories around the world, as they are easy to obtain and are applied where other measurements are hard to perform. It is our hope that this work may enhance the usefulness of these measurements by providing an accurate way to obtain the pulse temporal profile.

5. Single shot correlations based in a sagittal focal line configuration for use in Ti:Sapphire based lasers

5.1. Overview

We have seen in Chap. 3 that in pulsed laser systems it is possible to use correlations in order to obtain some information on the shape and duration of the laser intensity.

When using quasi-continuous lasers the stability preformed by this lasers assures repetitive pulse shapes. In this case a sweeping correlator is reliable and there is no need to analyze pulse to pulse variations. However at low repetition rates and/or high energy lasers, thermal effects can make the pulses non-reproducible. In this case a sweeping correlator is not a viable option. Even if there are no changes pulse to pulse at a low repetition rate, the time it takes to measure the pulse makes it unpractical to use a sweeping diagnostic. In a sweep correlator, each point is measured using a different pulse. So if there are significant changes from pulse to pulse, it is no longer useful to use this method. It is important to design a system where a correlation can be done in single shot, with a unique pulse.

This chapter proposes a Single Shot Intensity Autocorrelator (SSIA) and a Single Shot third order intensity Cross-Correlator (SSCC). The wave mixing is done in a BBO crystal with a type I phase matching. As exposed in Sec. (3.2), a third order cross correlator implies two wave mixing process second harmonic generation and SFG between the second harmonic and the fundamental beam creating radiation centered at 266 nm, the third harmonic wavelength. We design the device for use with a Ti:Sapphire laser with a central wavelength at 800 nm, and a bandwidth that can go up to 200 nm.

This chapter main objectives are to present a delay line based on the superposition of two sagittal focal lines, to discuss ways to enhance the contrast of single shot cross-correlators using phase-matching conditions and to present the main experimental results of a intensity autocorrelator based on this approach.

5.2. Overview of past work

Single shot measurements have been used for some decades. Tilted front diagnostics were proposed and used by J. Janszky et al. [55] and are the most widely used systems. These diagnostics are useful not only to analyze temporal characteristics with intensity autocorrelations [56] but also to study spectral characteristics [169]. Other tilted front diagnostics were done to analyzed UV pulses, like multi-photon correlators [208] and transient grating correlators [209] (equivalent to a third order correlator).

Finally tilted front diagnostics which contain a Fresnel biprism to obtain mirrorless systems have been developed: first and second order interferometric autocorrelations with spatial resolution [210], pulse spatial chirp diagnostics [211] and third order cross correlations [57]. Summing up, tilted front systems have been the dominant method used for single shot pulsed laser diagnostics since 1977. Some diagnostics are commercially available like the intensity autocorrelators by Coherent, Inc. [51] and Minioptic Technology, Inc. [52].

Some other single shot configurations have been designed. For example GRENOUILLE [212] is a single shot FROG [34] design and SPIDER [37, 38], has also been design for use in a single shot configuration [213]. F. Théberge et al. [214] developed a system to obtain information in a single shot 3D profile of the pulse shape two photon absorption signal in a dye dispersive medium. A system to fully characterize the electric field of a ultrashort pulse called STRIPED FISH has been studied by Pablo Gabolde in his PhD thesis [215].

For single shot or quasi single shot high contrast diagnostics, several configurations have been considered because we are interested in analyzing the intensity profile in a logarithmic scale over a long time window, not the pulse shape in a linear scale near to the peak. This implies a different configuration. Single shot third order cross correlations were first tried by Collier et al. [57]. The contrast in these experiments was limited to 1 to 7.1 (estimation done using the graphics presented in the paper). A high contrast single shot supercontinuum correlator was reported by Filip et al. [60] with a contrast given by the CCD camera of 10^6 over a 7 ps window.

High contrast third order cross correlators have been developed in several works: Dorrer et al. [61, 62] used a pulse replicator and obtained 10^6 contrast for a 1053 nm (Nd:Glass) pulse with 8-ps pulse duration, this configuration overcomes the normal detector contrast efficiency by replicating the SH pulse with smaller intensities for smaller delays, and thus obtaining a delay dependent intensity.

This enables the signal at zero delay to have a small gain and the signal at big delays to have a big gain. In other words, the contrast that can be obtained with the device is bigger than the contrast of the CCD cameras used in the measurement. The system had a time window of 250 ps. It is a discrete delay system and so it is perfect for systems where the pulse duration is bigger than the time difference between replicated pulses.

I. Jovanovic et al. [59] presented another single shot cross correlator with a delay line based in a grating and a step variable filter, the device had a 200 ps window and a dynamic range in excess of 10^5. A mix single shot - sweeping third order correlator has been developed by V.N. Ginzburg et al. [63], the single shot window had a 1 ps range and a 10^4 contrast, the entire system had 100 ps time window and a 10^8 contrast. Finally Gerrity [58] has developed a concept for a single shot cross correlation, with a 10^5 contrast ratio and a time window in excess of 50 ps.

Daniel Sütterlin et al [216] have published a coherent transition radiation diagnostic that also uses an off axis focal line, but for a different diagnostic (similar to a Martin-Puplett Interferometers), his work was done with toroidal mirrors, not with the spherical mirrors that we are considering.

5.3. Delay line

We will compare the two delay line configurations, the standard tilted front configuration and our own proposal based on the sagittal focal line of a spherical mirror. We will compare the values obtained with each system.

5.3.1. Tilted front configuration

Single shot intensity correlators normally use two tilted fronts that are overlap and mix in a nonlinear crystal. This two wave-fronts have an angle between them, this will result in a path difference between the beams for each point of the crystal, the time window is proportional to the spatial size of the beam in the crystal.
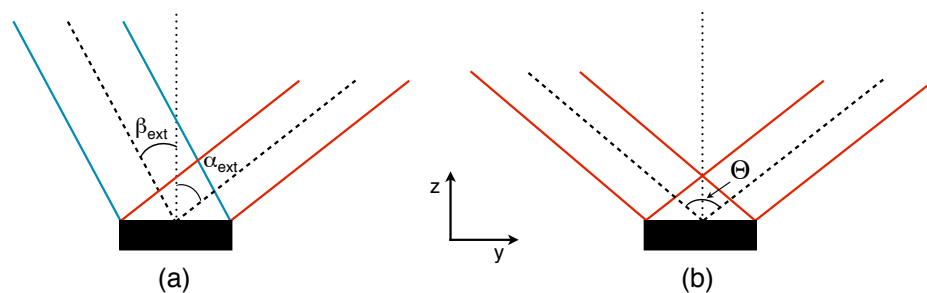
Figure 5.1.: Tilted correlator scheme, the black rectangle represents the crystal; (a) single-shot-TOCC (b) single-shot IA.

Tilted front intensity autocorrelator basic scheme is presented in Fig. (5.1) (b) and the TOCC tilted front version in Fig. (5.1) (a). For the intensity autocorrelator, in order for the output beam to be perpendicularly to the crystal, the input beams have to be in a perfect symmetrical configuration.

In a third order cross correlator this is not the case and the beam configuration is quite different. The

beam at the fundamental wavelength and the one at the second harmonic have to obey the condition $k_\omega \sin(\alpha_{int}) = k_{2\omega} \sin(\beta_{int})$ in order to guarantee that the third beam exits the crystal perpendicularly to the crystal itself. The fact that the beam exits perpendicularly to the crystal is important to guarantee that the image of the wave-mixing in the crystal is not affected by spatial/beam pointing distortions.

Notice that because the phase-matching angles are the same for every delay (for every y position) the shape of the signal obtained in this configuration is dependent on the spatial and temporal shape of the pulse, not on phase-matching conditions. However the magnitude of the SH/SFG signal generated in the mixing crystal is going to be affected by the phase-matching between beams.

In fact, the angle between the beams in a tilted front configuration does not change more than the divergence of the beams. This is does not happen in our proposal, we use a sagittal focal line and where there is a considerable angular variation of the $\vec{k}$ vector between the two beams that arrive at the SH/SFG crystal.

Notice that, in this traditional configuration, the spatial profile of the pulse is critical to the reliability of the measurement. In fact, the single shot TOCC signal is given by Eq. (5.1) and the IA single shot is given by Eq. (5.2). This equation is such that the spatial and temporal details of the pulse are intertwined in the resulting signal, $\alpha_{ext}, \beta_{ext}$ and Θ_{ext} are the angles outside the crystal, that are represented in Fig. (5.1) , α_{int}, β_{int} and Θ_{int} are the angles inside the crystal that can be found from the first ones using Snell-Descartes' law.

$$
\begin{aligned}
SSCC(x,y) &= \int \int I_\omega\left(x,y,t-\tau_\omega(y,z')\right) I_{2\omega}\left(y,t+\tau_{2\omega}(y,z)\right) dt dz' \\
\tau_\omega(y) &= \tfrac{y\sin(\alpha_{ext})+z'\cos(\alpha_{int})}{c} \\
\tau_{2\omega}(y) &= \tfrac{y\sin(\beta_{ext})+z'\cos(\beta_{int})}{c}
\end{aligned}
\tag{5.1}
$$

$$
\begin{aligned}
SSIA(x,y) &= \int \int I_\omega\left(x,y,t-\tau_\omega(y,z)\right) I_\omega\left(y,t\right) dt dz' \\
\tau_\omega(y,z) &= 2\tfrac{y\sin\left(\frac{\Theta_{ext}}{2}\right)+z'\cos\left(\frac{\Theta_{int}}{2}\right)}{c}
\end{aligned}
\tag{5.2}
$$

Please note that the intensity dependency on the $y-axis$ is not the intensity profile as given at the entrance of the correlator[1]. Considering the axis that is perpendicular to the propagation before the crystal is the $y'-axis$, the relation between the the intensity in the two axis is given by the expression $I(y')dy' = I(y)dy$. This applied to the intensity autocorrelation and the third order cross correlation becomes[2]:

$$
\begin{aligned}
I(y) &= I(y')\cos\left(\tfrac{\Theta_{ext}}{2}\right) \\
I_\omega(y) &= I_\omega(y')\cos(\alpha_{ext}) \\
I_{2\omega}(y) &= I_{2\omega}(y')\cos(\beta_{ext})
\end{aligned}
\tag{5.3}
$$

---

[1] We use $\{x,y,z\}$ as the original propagation axis before the device, and $\{x',y',z'\}$ are used as the propagation axis on the wave-mixing crystal.

[2] For the IA: $y = \frac{y'}{\cos\left(\frac{\Theta}{2}\right)}$.

In the case of the intensity autocorrelator, no further questions arise. However in third order cross-correlator, for $I_{2\omega}(y,t)$ to be proportional to $I_{\omega}^2(y,t)$, the beam has to be dilated (because the angles are different, the projection is also different), the SH beam has to be dilated by $\frac{\cos(\alpha_{ext})}{\cos(\beta_{ext})}$.

The temporal window for the intensity autocorrelator in this design is $\frac{2Y_{MAX}\sin\left(\frac{\Theta}{2}\right)}{c}$. For the temporal window of the SSCC, we have the expression: $Y_{MAX}\frac{\sin(\alpha_{ext})+\sin(\beta_{ext})}{c}$.

The temporal resolution might be limited by the wave mixing process. Let us consider that we image the crystal on a camera, it is reasonable to consider every point we see in the camera is an integration over the thickness of the crystal; we have expressed this in Eqs. (5.1) and (5.2) as an integration over z. If the delay between the beams does change in the $z-axis$, it is obvious that this change is going to limit to the temporal resolution of the measurement. Given this in the SSCC, the temporal resolution will be limited by the crystal thickness L_{cr}, more precisely by: $L_{cr}\frac{\cos(\beta_{int})-\cos(\alpha_{int})}{c}$. In the SSIA there is no given temporal resolution limit because in the $z-axis$ direction the path difference is always the same.

Let us treat the SH mixing in the SSIA scheme (see Fig. (5.1)). In order to find values for the temporal window allowed in this configuration some considerations have to be made. It is possible to envision that the angle Θ could be as close to 180º as possible, however this would not be practical, because there would be no phase-matching and the SH generated by each beam with itself would overshadow the SH generated by the mixing of the two beams.

We have to envision the maximum aperture angle Θ, where the phase-matching condition exits. In a type I phase-matching ($o + o \rightarrow e$) the crystal e-axis is in vertical plane as well as with the electric field of the second harmonic. In this configuration, the fundamental field inside the crystal is horizontal and within the o-axis. We could rotate the system and have the o-axis and the fundamental wave electric field on the vertical plane, in consequence the e-axis and the SH electric field is placed horizontally parallel to the front window of the crystal In the first option there is a certain liberty for micro adjustments by changing the crystal orientation, in the second case no micro-adjustments are possible. For a BBO crystal the maximum aperture angle Θ_{MAX} is given by:

$$\Theta_{MAX} = 2\arcsin\left(n_o(\omega)\sin\left(\arccos\left(\frac{n_e(2\omega)}{n_o(\omega)}\right)\right)\right) \tag{5.4}$$

Eq. (5.4) is obtained considering a type I phase-matching. The electric field oscillation at the fundamental wavelength is done in the plane formed by the two inputted beams, it is perpendicular to the crystal interface. The ordinary plane of the crystal, is exactly in this same plane. The polarization of the SH generated by the two beams is perpendicular to the other polarizations and is parallel to the extraordinary axis of the uniaxial crystal (see Fig. (5.2)).

Considering Eq. (5.4) and a central wavelength of 800 nm, we obtain maximum aperture angle of $\Theta_{MAX} \approx 66,3º$ (for 700 nm $\Theta_{MAX} \approx 63º$). For a crystal with a length of 50 mm, the time window is

176 ps, for a 25 mm crystal it would be 88 ps. In resume we obtain a delay per unit of length in the crystal of 3.5 *ps/mm*.
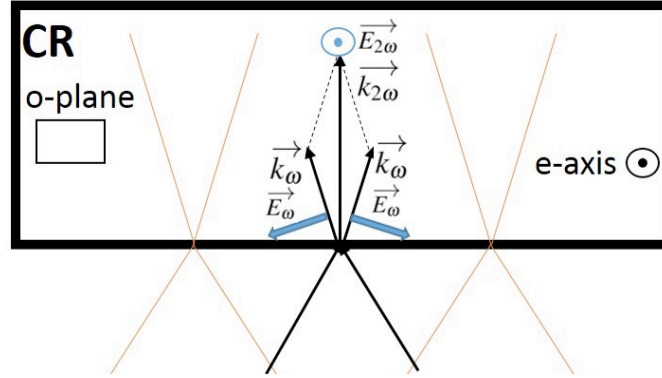
Figure 5.2.: Top view of the crystal The electric fields are represented in blue and the $\vec{k}$ vectors in black. The represented plane is the ordinary plane of the crystal and the e-axis is perpendicular to it. The polarization of the beams at the fundamental wavelength are within the plane. The polarization of the SH beam is perpendicular to it.

If we had considered that the phase-matching was not important, we could have opted for a quasi-parallel incidence ($\Theta = 180°$), in this case delay per unit of length in the crystal would be 6.7 *ps/mm*.

Let us now make the same considerations in order to obtain the maximal possible time window in the SSCC of Fig. (5.1). In this case the phase-matching conditions are given by:

$$3n_e(3\omega) = 2n_o(2\omega)\cos(\beta_{int}) + n_o(\omega)\cos(\alpha_{int})$$
$$n_o(\omega)\sin(\alpha_{int}) = 2n_o(2\omega)\sin(\beta_{int}) \tag{5.5}$$

Solving Eq. (5.5) we obtain $\alpha_{int} = 23.9°$ and $\beta_{int} = 11.5°$ or $\alpha_{ext} = 42.3°$ and $\beta_{ext} = 19.7°$. Considering these angles, we obtain a maximum delay of 3.3*ps/mm*, which is the equivalent of 86 ps for a 25 mm crystal and 167 ps for a 50 mm crystal. The resolution limit given by the nonlinear mixing is approximately 18 fs. Please compare this with a common high contrast third order cross correlator where the time window can reach up to 990 ps with a 70 fs resolution [42].

5.3.2. Sagittal astigmatic focal line as a delay line

Using this configuration, we achieve at the same time a delay line and an integration of the spatial profile in one direction ($x - axis$). This will originate a semi focused beam that will increase the efficiency of the nonlinear process.

The sagittal line of a curved mirror is parallel to the beam that enters this mirror (under the paraxial

approximation), the scheme is given in Fig. (5.3). We see that there is a time delay between A and B, this time delay is the basis of our configuration. In order to create an autocorrelator or a correlator, we superimpose two sagittal lines in a nonlinear crystal, the general scheme comprising the curved mirrors and the nonlinear crystal is given in Fig. (5.4).
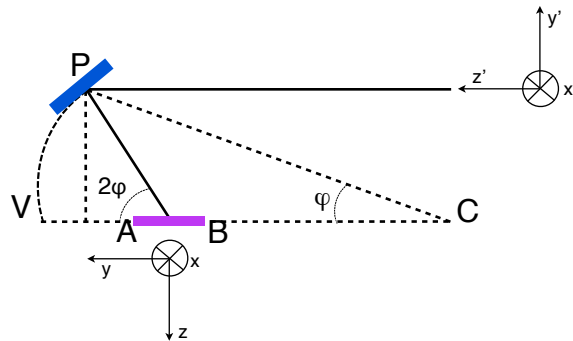
Figure 5.3.: Sagittal focus line (in magenta) from a spherical mirror with a curvature ray centered in C. The incidence angle φ and the A B points are the extremes of the sagittal line.
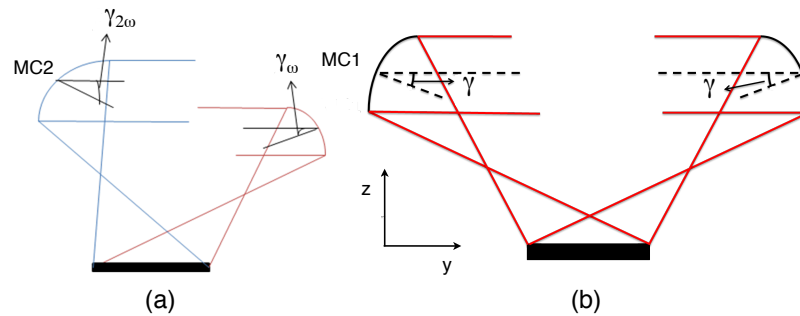
Figure 5.4.: Sagittal line correlator scheme, the black rectangle represents the crystal; (a) SSCC (b) SSIA.

This scheme allows for an integration in the $x-axis$ allowing the measurement to be taken independently of the beam profile in this direction, which reduces the influence of hot points in the nonlinear process. However the geometrical optics bijectivity between the two incident beams, the beams at the entry of the mirror and at the focal plane is not strait forward.

In an intensity autocorrelator we overlap two beams that arrive symmetrically to the nonlinear crystal Using geometrical optics considerations, we find the relations between the different beam profiles in the sagittal plane and at the entry of the lens. We do not make considerations about the propagation effects of these beams (this could be done using Fresnel propagation integral [217]). Given this, we associate the intensity in the original $y'-axis$ with the one in the $y-axis$ with the first three expressions in Eq. (5.6). We choose the origin of the $y'-axis$ in order for it to coincide with the central point (geometric center) of the beam profile, the incident angle of this point is γ_0. The last expression in Eq. (5.6) is the time delay at each point of the focal line in relation to the central point

5. Single shot correlations based in a sagittal focal line configuration

that of the beam profile.

$$\gamma = \arcsin\left(\sin\left(\gamma_0\right) + \tfrac{y'}{R}\right)$$
$$y = \tfrac{R}{2}\left(\tfrac{1}{\cos(\gamma)} - \tfrac{1}{\cos(\gamma_0)}\right)$$
$$I(y) = \tfrac{I(y')}{\tan(\gamma)}$$
$$\tau(\gamma) = R\left[\tfrac{1}{2}\left(\tfrac{1}{\cos(\gamma)} - \tfrac{1}{\cos(\gamma_0)}\right) + \cos\left(\gamma\right) - \cos\left(\gamma_0\right)\right]$$

(5.6)

Using Eq. (5.6) we obtain the delay in the focal plane for one mirror. We used a curvature radius of 2 m (1 m focal length) for the spherical mirror and obtained the graphics shown in Fig. (5.5).
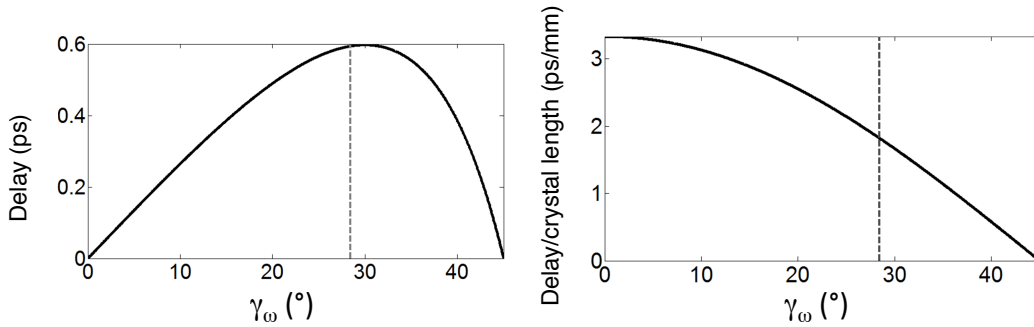
Figure 5.5.: Sagittal line delay as a function of the incidence angle. We consider a Super-Gaussian (order 10) beam profile at the entry of the mirror. The values represented are the FWHM of the delay considering a 1mm beam at the entry of the mirror (a), or the delay per unit of length on the focal plane (b). The traced line is the minimal angle where phase matching is achieved for a SH non collinear configuration ($\gamma_\omega = 28.4°$).

Where we represent the delay in the focal plane, we used a square function at the entry of the astigmatic spherical mirror. In Fig. (5.5) (a) we use a 1 mm beam width at the entry of the mirror and obtain the delay in ps. In Fig. (5.5) (b) we obtain the delay per distance in the focal plane (mm).

The maximum delay (τ_{max}) per unit of width on the incoming beam ($\frac{\partial \tau}{\partial y'}$) is achieved at 30° with 0.6 ps/mm on the mirror plane or $\frac{\partial \tau}{\partial y} = \frac{5}{3}$ ps/mm on the focal plane. However if we see this in the perspective of the crystal, the maximum delay per unit of distance ($\frac{\partial \tau}{\partial y}$) in the focal plane is obtained with an angle close to zero with a maximum delay per unit of length of $\frac{\partial \tau}{\partial y} = \frac{10}{3}$ ps/mm (twice the one obtained with 30° incidence angle). For a 50 mm beam the maximum delay is 30 ps (incidence angle of 30°) and the width of the beam in the crystal is 18 mm. In consequence for a 25 mm beam the delay is 15 ps for a crystal of 9 mm. The values are scalable as long as the width of the beam remains small compared with the focal length. Trying to equal the values of 30 or 15 ps for very small angles is not possible because the size of the beam profile at the entry of the curved mirror exceeds the focal length of the mirror.

For an intensity autocorrelator, the reasoning is strait forward. Both angles of incidence into the

mirror are the same. The maximum aperture angle (angle to the normal of the crystal at the incidence point) where null phase mismatching is possible is 33°, in other words if $\gamma_0 > 28.4°$ phase-matching is possible (for more details see previous section) so 30 degrees incidence angle is good for our device. This is true if we are restrained by the size of the beam in the curved mirror, in this case we will have a delay window of 60 ps for a 18 mm crystal and 50 mm diameter for both beams at the entry of the astigmatic mirrors.

However if we are restrained by the size of the crystal, we can use $\gamma_0 = 28.4°$. For a beam size of a 50 mm at the entry of the astigmatic mirror, the delay window is 59.4 ps and the crystal length is 16.3 mm. Because the angles are so similar, the distinction between both situations is not important. In resume for a SSIA we have $\frac{\partial \tau}{\partial y} = 3.64$ps/mm or $\frac{\partial \tau}{\partial y'} = 1.2$ps/mm for $\gamma_0 = 30°$ and for $\gamma_0 = 28.4°$ we have $\frac{\partial \tau}{\partial y} = {}^{10}/_{3}$ps/mm or $\frac{\partial \tau}{\partial y'} = 1.2$ps/mm

For a third order cross correlator, the beams arrive at the nonlinear crystal with different incident angles. We take this into consideration and obtain Eq. (5.7), γ_ω, $\gamma_{2\omega}$ are explained in Fig. (5.4) (a).

$$2 \sin \left(\frac{\pi}{2} - 2\gamma_{2\omega} \right) = \sin \left(\frac{\pi}{2} - 2\gamma_\omega \right) \tag{5.7}$$

This means that γ_ω varies between 0° and 45° while $\gamma_{2\omega}$ varies between 30° and 45°, this relation is expressed in Fig. (5.6). This angle difference means that we might have a significant change in beam size between the two beams. In order to adjust this, the SH beam size is refitted in such a way that both beams have the same size on the focal plane.

For every calculation, we considered a constant beam size of $1\,mm$ for the fundamental beam and $2\,m$ of curvature radius for the curved mirror. In order to refit the SH beam size, first we calculate the beam size of both beams at the focal point (considering that both have $1\,mm$ size); second the ratio of the beam sizes in the focal line is used to change the SH beam size at the entry of the mirror ($size_{SH} = ratio \times 1mm$), the beam ratio is given in Fig. (5.6). If we repeat this process, the SH beam size does not change more than 0.1%.
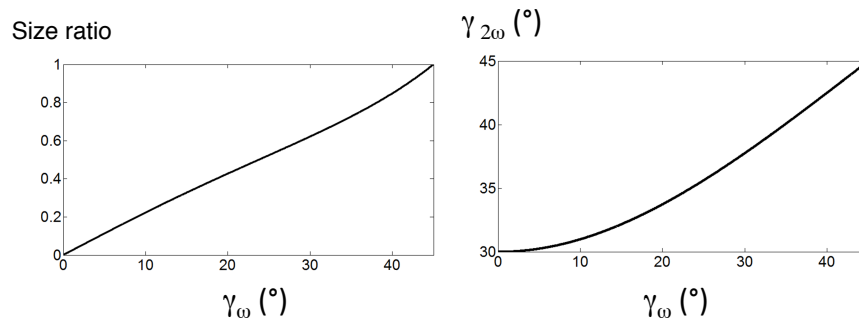
Figure 5.6.: (right) variation of the second harmonic beam angle as a function of the fundamental beam angle and (left) size ratio between the beams as a function of the fundamental beam angle.

The results are given in Figs. (5.6) and (5.7). The maximum delay is obtained for the values of $\gamma_\omega = 30°$, $\gamma_{2\omega} = 37.76°$ with a delay window of $0.9\,ps$ where $\frac{\partial \tau}{\partial y} = 2.5\,ps/mm$. The maximum $\frac{\partial \tau}{\partial y}$ is given for $\gamma_\omega = 0°$ with $5\,ps/mm$. The minimum γ angle where it possible to obtain a null phase-matching condition ($\gamma_\omega = 23.85°$) is smaller than the maximum delay angle ($\gamma_\omega = 30°$). This means that we may use $\gamma_\omega = 30°$, $\gamma_{2\omega} = 37.76°$ to design our cross correlator if we are restricted by the size of the beam at the entry of the astigmatic mirror. However if we are limited by the size of the beam at the crystal then the ideal angle is $\gamma_\omega = 23.85°$, $\gamma_{2\omega} = 35.17°$.
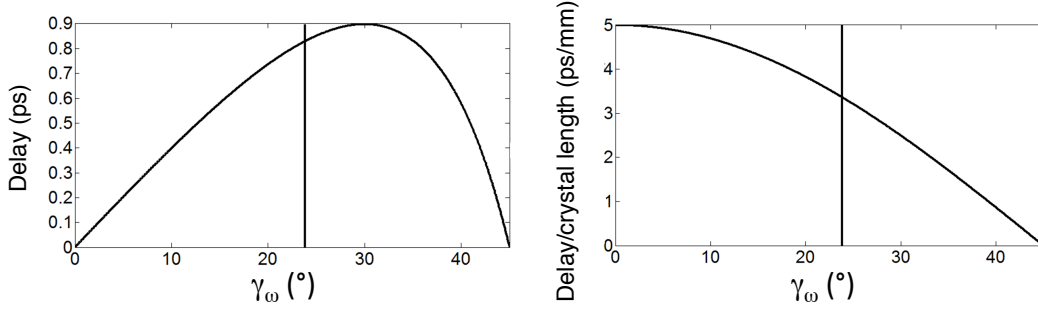
Figure 5.7.: Sagittal line delay as a function of the incidence angle γ_ω. FWHM of the delay for both beams (fundamental plus SH) considering the deformation of the profile due to astigmatism. (a) considering a 1mm beam at the entry of the mirror for the fundamental beam (b) delay per unit of length on the focal plane. The vertical lines are the minimal aperture angle where phase-matching is achieved.

For a mirror input beam with $50\,mm$ in diameter (fundamental wave) and $\gamma_\omega = 30°$, $\gamma_{2\omega} = 37.76°$, we obtain 44.9 ps in a 18 mm crystal Please note that due to a ratio of 0.62 between the two beams, the SH beam has to be $31\,mm$ in length. If the mirror incidence angles are $\gamma_\omega = 23.85°$, $\gamma_{2\omega} = 35.17°$, the 50 mm beam size (fundamental wave) will originate a maximum delay of $41.4\,ps$, the size of the beam in the crystal will be $12.3\,mm$. Please note that due to a ratio of 0.5, the SH beam size is $25\,mm$.

5.3.3. Delay configuration comparison

We compare the two configurations reported in the previous section with Tab. (5.1).

We consider two astigmatic configurations and compare them with the tilted configuration. Astigmatic configuration 1 is calculated maximizing the delay per unit of length in the beam at the entry of the curved mirror $\left(\max\left(\frac{\partial \tau}{\partial y'}\right)\right)$, which means we use the values $\gamma_0 = 30°$ for SSIA and $\gamma_\omega = 30°$, $\gamma_{2\omega} = 37.76°$ for SSCC. Astigmatic configuration 2 is calculated maximizing the delay per unit of length in the crystal, which means using $\gamma_0 = 28.4°$ for SSIA and $\gamma_\omega = 23.85°$, $\gamma_{2\omega} = 35.17°$ for SSCC.

In Tab. (5.1), we see that the tilted configuration is significantly better when we are restricted by the size of the mirror but not when we consider the crystal length as the limiting factor. When the size

of the crystal determines the maximum possible delay, the delay line using an astigmatic mirror can be better than a tilted configuration.

For a single shot IA this is self evident for both astigmatic configurations that the delay obtained using an astigmatic line is similar to the delay obtained using a tilted front. For a single shot TOCC, the astigmatic configuration can be better than the tilted configuration if we use the maximum possible aperture.

Delay	Tilted configuration	Astigmatic configuration 1	Astigmatic configuration 2
IA-CR=1 mm	3.5 ps	3.3 ps	3.65 ps
IA-CR=25 mm	88 ps	83.2 ps	90.9 ps
IA-M=1 mm	3.0 ps	1.2 ps	1.2 ps
IA-M=50 mm	147.5 ps	59.7 ps	59.4 ps
TOCC-CR=1 mm	3.3 ps	2.5 ps	3.4 ps
TOCC-CR=25 mm	82.5 ps	62.4 ps	85 ps
TOCC-M=1 mm	2.5 ps	0.90 ps	0.83 ps
TOCC-M=50 mm	127 ps	44.8 ps	41.4 ps

Table 5.1.: Delay obtained using the configurations presented above. Astigmatic configuration 1 is calculated for maximum $\frac{\partial \tau}{\partial y'}$ and astigmatic configuration 2 is calculated for maximum $\frac{\partial \tau}{\partial y}$. The value in front of CR is the width of the crystal, and the one in front of M is the length of the mirror.

5.4. Single shot intensity second order autocorrelator

In this section, a design of an intensity autocorrelator, a discussion on what to expect as signal and device parameters and some experimental results will be presented.

This intensity autocorrelator uses two astigmatic lines of a spherical mirror and overlaps them in a SH crystal as exposed in the previous chapter. As a result of the astigmatic configuration, we integrate the profile in the $x - axis$. The effect of the phase-matching conditions is discussed. The fact that both beams are astigmatic will result in a deformation of the intensity in the focal plane.

In this study we assume that the spatial and temporal aspects of the pulse are independent of each other. This assumption will allow us to independently evaluate:

➤ the effects of the astigmatism in the spatial profile.

➤ the phase-matching conditions between the beams.

These effects will be specific for every position in the SH crystal and constitute a gain coefficient that is superimposed to the temporal intensity autocorrelation. These effects deform the intensity autocorrelation profile and might increase or decrease the contrast of the measurement.

In the previous section, Eq. (5.1) represents the signal obtained using a tilted front configuration. In

that case, it is quite obvious how to dissociate the temporal and spatial features of a pulse. In our case, it is more complicated. First the $x-axis$ pulse shape is integrated, second the spatial profile in the $y-axis$ is not the same as the spatial profile in the $y'-axis$. We have to use $I(y')dy' = I(y)dy$ and the bijection between y' and y that is presented in Eq. (5.6). Doing this, we obtain $I(y) = \dfrac{I(y')}{\tan(\gamma(y'))}$. For each y coordinate, the delay is given in the last expression of Eq. (5.6).

As we said above, we dissociate the spatial and temporal dependencies of the signal obtaining a gain factor $G(y)$ that will change from point to point. This feature is represented by Eq. (5.8).

$$SSIA(x,y) = G(y) \int I(t - \tau_{SH}(y)) I(t) dt$$
$$G(y) = I(y_1)I(y_2)\Re^2 \left\{ \int \exp(i\Delta kz) dz \right\} \int I^2(x)dx$$

$$(5.8)$$

It is very important to obtain characteristic curves for the gain factor. The phase mismatch dependence $\left(\Re^2 \left\{ \int \exp(i\Delta kz) dz \right\}\right)$ is treated in the next subsection, here we will treat the impact of the product of the profile intensities on the focal line. The delay time $\tau_{SH}(y)$ is equal to twice the delay given in Eq. (5.6). Let us consider that the pulse to be analyzed has a tenth order Super-Gaussian spatial profile.
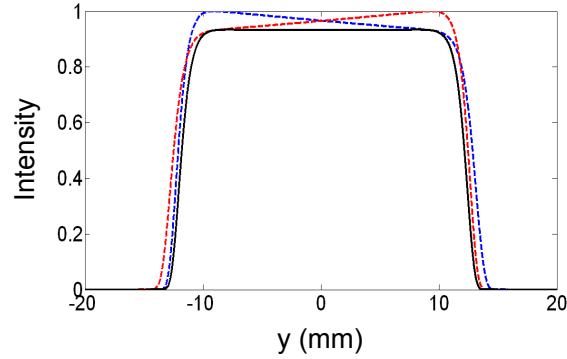
Figure 5.8.: Intensity of the profiles on the sagittal focal plane (red and blue lines), and multiplication of both profiles (black line). The entry beam has 75 mm width.

Fig. (5.8) shows the deformation suffered by the astigmatism of both superimposed beams and the correspondent multiplication of both intensities. This may be viewed as a gain factor for the intensity autocorrelation profile. We can clearly see that, despite the fact that astigmatism brings a deformation to the spatial profile of both beams, the multiplied effect is canceled out and the astigmatism effect on the intensity autocorrelation is null, in fact the gain line is nearly flat.

If the laser to be analyzed had another spatial profile, the result would be different, this is due to the coupling between the spatial and temporal profile of the pulses that is also found in tilted front correlators, however the effect is similar to the effect that is obtained in tilted front correlators and is not really the influence of the astigmatism. In Fig. (5.8), we use $\gamma_0 = 28.4°$, however if we use

$\gamma_0 = 30º$ the qualitative effect in the result does not change, in fact the result is so similar that we opted not to show it.
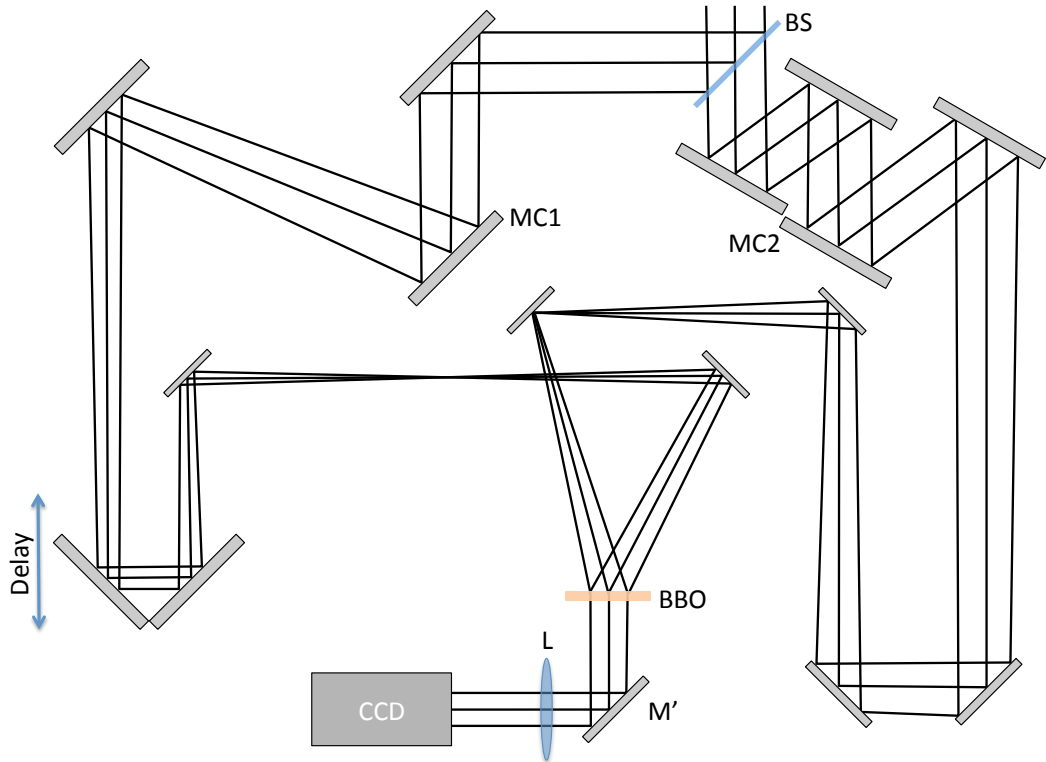
Figure 5.9.: Single shot intensity autocorrelator. We use two curved mirrors (MC1 and MC2) in order to have a delay line, a beam splitter (BS) is used to divide the beams and we measure the same path between the BS and the curved mirrors. A delay line is added in order to give a fine adjustment to the system, a BBO crystal to obtain the second harmonic signal, M' is high reflective for 400 nm, lens L to image formation and a camera to capture the signal

We design an autocorrelator based on this principle, that is presented in Fig. (5.9). In order to test this diagnostic tool we used a 10 Hz, 110 fs/0.5 TW laser also called vert laser at LOA. The beam spatial profile is a quasi top hat profile which makes it ideal to test the device. The infrared laser is spectrally centered at 810 nm.

In this device we used curved mirrors (MC1 and MC2) with a curvature radius of 2 m. The angles were adjusted with a fine tuning (($1/6$) degrees precision). The transport mirrors were dielectric high power mirrors. The BBO crystal is described in the following section, we used a 45º mirror M' that has high reflectivity at 400 nm, a +50 mm lens and a CCD Spiricon 12 bits camera. During the assembling two 1 mm BG39 blue filters were introduced in front of the camera. Characteristic results are shown below.

5.4.1. Phase matching conditions

It is conceivable that, due to the beams astigmatic distortions, the phase-matching conditions in the SH BBO crystal are not uniform. As referred above, we use geometrical optics considerations in order to propagate the pulse and guess the pulse intensity distribution and path duration. In here, we do the same to obtain the direction of the $\vec{k}$ momentum vectors and the incidence angles of each beam at each point in the crystal.

We consider a plane pulse wavefront at the entry of the curved mirrors and use Fig. (5.3) to find the non-collinear internal angle (inside the SH crystal) that is $\arcsin{(n\cos{(2\gamma)})}$. The angle $\gamma(y)$ changes from point to point in the focal plane, as exposed in Eq. (5.6). Considering this, we establish for each point a geometrical configuration of two beams at the fundamental wavelength: with two defined angles, with a refraction index characteristic of the ordinary plane and a null phase-matching parallel to the entry plane. With these conditions, we obtain the direction of the output beam, that never diverges more than 2.5° from the perpendicular to the crystal Finally with all these elements, we obtain the phase mismatch at every point of the crystal This phase mismatch effect was included in Eq. (5.8) in order to obtain the gain profiles that we present below.
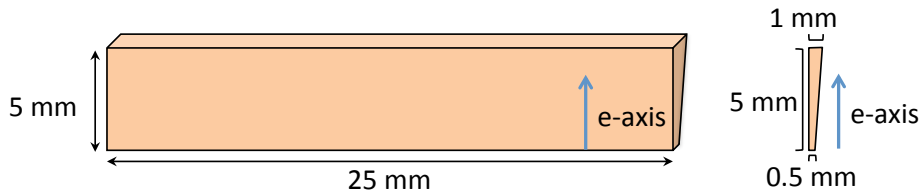
Figure 5.10.: Crystal used for TWM in the single shot autocorrelator.

In the previous section, we saw that the configuration with the biggest delay per length (length at the entry of the mirror) is given for an angle $\gamma_0 = 30°$ which is close to the minimum angle where phase-matching is possible ($\gamma_0 = 28.4°$). Because these angles are so close, the gain profile will be almost identical In order to profit from the maximum possible aperture, we use the crystal represented in Fig. (5.10) to have the SH beam. As we said above, in this configuration the two fundamental beams enter perpendicularly to the crystal, with an horizontal polarization that is within the ordinary plane of the crystal. The SH beam polarization is in the e-axis with the correspondent refraction index.

Notice that the crystal is wedged in order to have a fine adjustment of the crystal insertion. This can influence on the gain profile and the gain magnitude that is coupled to the intensity autocorrelation. If this gain factor was smaller on the center than on the edges of the profile, then it would be conceivable that the contrast enabled by the device would be bigger than the contrast range of the detectors.

However, from Fig. (5.11), it is quite obvious that the gain profile modulations are small and that the device should not be envisioned to obtain high contrast measurements. In the single spectral

linewidth calculation, for a very thick crystal (1 *mm*), we might obtain a contrast gain by a factor of two. However for a 50 nm bandwidth laser, it is clear that it is not possible to obtain a contrast gain with this system.
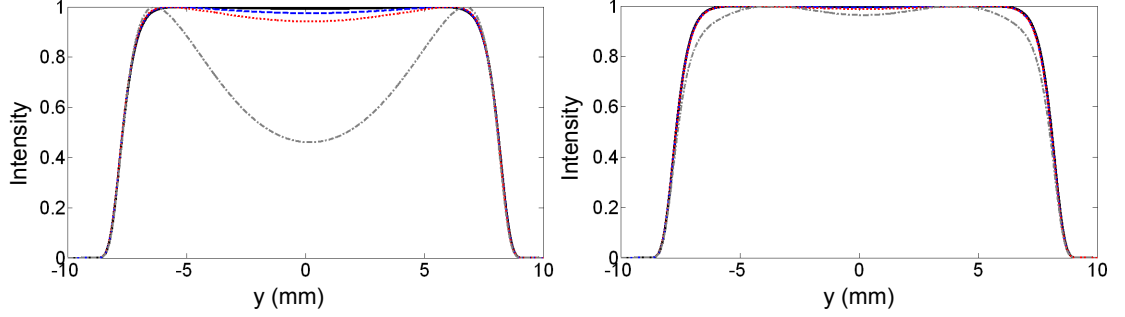
Figure 5.11.: Gain profile considering both the astigmatic deformation and phase-matching. (left) calculations done for a single linewidth spectral profile at 800 nm and (right) using a 50 nm bandwidth centered at 800 nm for different crystal thicknesses - 100μm (black), 200μm (blue), 300μm (red) and 1mm (gray). The considered incidence angle in the astigmatic mirror is 28.4°, the minimum incidence angle where phase-matching occurs.

The reasoning for the phase-matching effect on the gain profile presented above only applies to a single spectral linewidth pulse. In order to estimate the effect on a pulse with a certain spectral bandwidth, we sum the amplitude of the effect of each spectral component. However considering that the beam at one wavelength is going to interact with all other wavelengths we have to integrate it twice.

$$G(y) = \left| \int \int \sqrt{I(y_1, \lambda_1) I(y_2, \lambda_2)} \left[\int \exp\left(i\Delta k(\lambda_1, \lambda_2)z\right) dz \right] d\lambda_1 d\lambda_2 \right|^2 \tag{5.9}$$

With this estimation we obtain the gain profiles given in Fig. (5.11) (right).

5.4.2. Experimental results

We assembled the correlator described in the beginning of this section, the results captured by a CCD camera are reported here. We must be clear that between the BBO crystal and the camera we had a blue BG39 filter and an imaging lens. The lens is putted in a 2f-2f configuration, in order to image the crystal with a magnification of 1. However it is not guaranteed that the scale on the camera is exactly the same scale as in the crystal, in other words there may be some amplification between the crystal and the camera, that is not accounted here.

The characteristic results in the CDD camera may be viewed in Fig. (5.12). We can clearly see the structure of a main pulse that extends itself on the horizontal direction. It is also evident that the

201

intensity autocorrelation at zero delay is not centered at middle of the picture, this is intentionally done in order to show the main and secondary pulses in the same frame.

Figure 5.12.: The intensity autocorrelation evidencing the existence of a main and a secondary pulse.

Figure 5.13.: The camera captures obtained using different delays, with variation of delays between pictures of 10 mm. The gray scale is not the same in every picture.

The first test to our autocorrelator is to change the delay between the fields arriving at the crystal, this will help us calibrate the delay in the crystal, and explore the pulse shape beyond the maximum delay allowed by the crystal. In Fig. (5.13), we see consecutive pictures of the autocorrelation when varying the delay. From these pictures, we observe that the secondary pulse is 21.2 ps away from the main pulse, and the movement of the zero delay zone in the sagittal line.

We use the position of the maximum of the intensity autocorrelation, to obtain the relation between the delay and the position in the camera. The values obtained are represented in Fig. (5.14), we took several measurements for every delay and represented the averaged value plus the experimental error due to these measurements.

In Fig. (5.14) we observe the linear dependence between the position in the crystal and the delay line position. We convert the slope of this curve in order to obtain the variation of delay as a function of y, or $\frac{\partial \tau}{\partial y}$. In order to do this, we have to remember the relation between the delay screw reading (Δ) and the pulse time delay ($\Delta\tau$) that is approximately $\Delta\tau = 6.6(ps/mm) \times \Delta$.
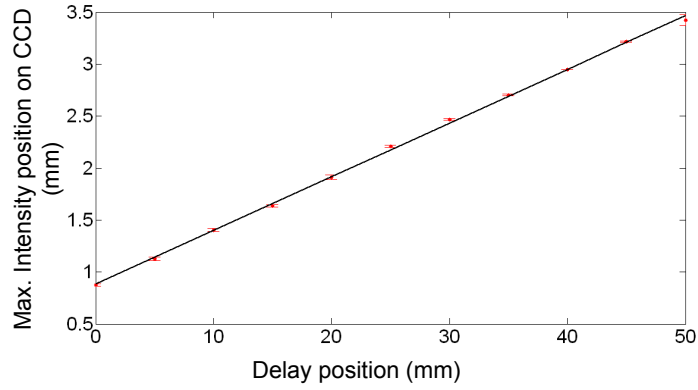
Figure 5.14.: Maximum of the intensity position on the CCD camera versus the delay in the micrometer screw thread, both expressed in mm.

The linear approximation given by Fig. (5.14) can be expressed by the relation $\Delta = 0.517y + 0.8836$, which means $\frac{\partial \tau}{\partial y} \simeq 3.45 ps/mm$. It is clear that this value is within the values of $3.6 ps/mm$ and $3.3 ps/mm$ given above. However we cannot compare both values directly, because we must account for a possible deviation due to a magnification factor between the crystal and the CCD scale.

We can determine the uncertainty from this calibration, the slope coefficient of Fig. (5.14) as an uncertainty of 10^{-3}, which gives an uncertainty of $\delta\left(\frac{\partial \tau}{\partial y}\right) = 7 \times 10^{-3} ps/mm$, which by it self gives an uncertainty of 0.2% for slope coefficient, the uncertainty of the duration measurements however will be given by: $\frac{\delta\tau}{\tau} = \sqrt{\left[\frac{\delta\left(\frac{\partial \tau}{\partial y}\right)}{\frac{\partial \tau}{\partial y}}\right]^2 + \left[\frac{\delta y}{y}\right]^2} = \sqrt{(0.2\%)^2 + \frac{1\mu m}{y(\mu m)}}$, where y is the length of the autocorrelation as measured on the camera (the camera can measure dimensions with 1 μm uncertainty). The length of the autocorrelations is of the order of the millimeter, which means that the uncertainty will

be of approximately 0.3 %. However for smaller durations we need to take into account the spatial mode (and propagation) of the pulse profile, which will be the determining factor of the shortest pulse that can be measured with this system.
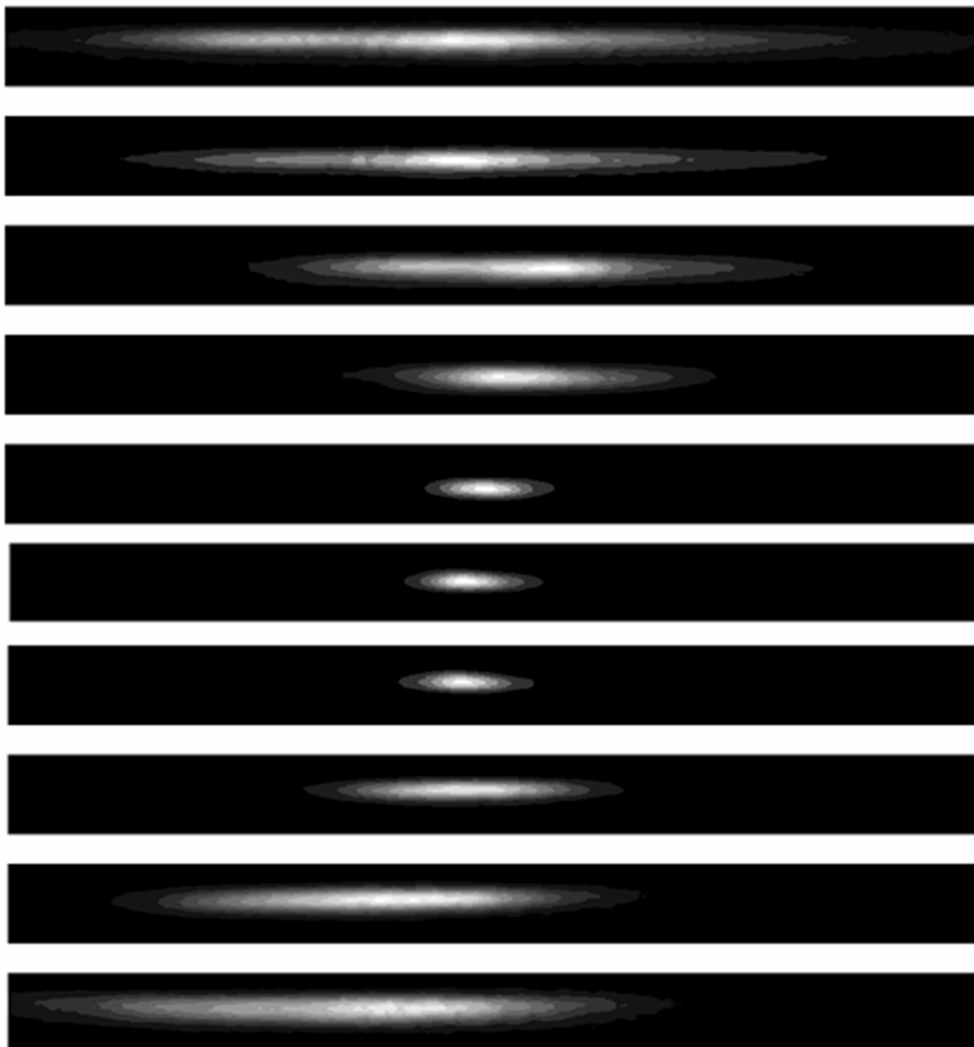
Figure 5.15.: The camera captures obtained using pulses with different durations. Between each frame we changed the position of the compressor grating by 1 cm.

Once we have established a time scale on our device, it is possible to estimate the pulse duration[3]. We used the grating compressor at the output of the CPA system in order to obtain a variable pulse duration. The results are given in Fig. (5.15) and Fig. (5.16). For every position of the compressor, we took several measurements, we present for each compressor position a sample of the obtained correlations and in Fig. (5.15) we present the average duration value in Fig. (5.16).

---

[3]In order to estimate the pulse FWHM duration (Δt) from the intensity autocorrelation we used the relation between the pulse variance and the IA variance proved in Chap. 3. In reality we used the FWHM intensity autocorrelation ($\Delta \tau$) and the relation $\Delta t = \frac{\Delta \tau}{\sqrt{2}}$.

The minimal pulse duration estimated by the quadratic fit is 331 fs, the measured value for the compressor position that minimizes the pulse duration is $273 \pm 74\,fs$, value that is taken with several measurements of the pulse duration without moving the compressor. In a single measurement, the minimum duration obtained was $180\,fs$. This means that the pulse to pulse fluctuations are bigger than the precision of this of the single shot intensity autocorrelator that is presented here.
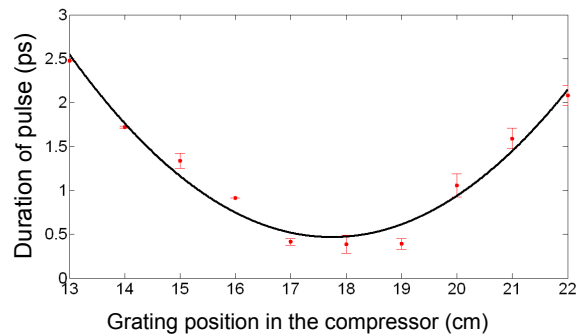
Figure 5.16.: Pulse duration guessed from the intensity autocorrelation versus the grating position in the compressor.

In Fig. (5.16), it is clear that the zero delay position is not the same for all pulses, this might mean that the system presented a high sensibility to angular deviations in the beam direction, that were not perfectly compensated. This slight changes appeared when the compressor granting is moved. Experimentally it is obvious that the biggest barrier to achieve a high contrast in a similar configuration might be defects in the crystal itself. We have to obtain a clean crystal, otherwise the fundamental beam or the residual SH of the beam itself can pass across the spectral and spatial filters and constitute a background noise captured by the camera.
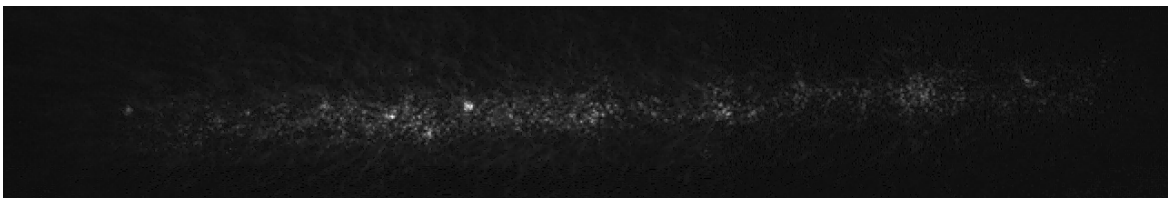
Figure 5.17.: Sagittal line profile photographed without the BG39 filter.

Fig. (5.17) is a photograph taken of the sagittal line without the BG39 filter. Comparing this with the pulse profile, we clearly saw that the hot points are due to imperfections in the crystal.

5.5. Single shot third order cross-correlator

In Sec. (3.2), the third order cross correlation is presented. Here we concentrate on the design of a single shot third order cross-correlator, we discuss the simulation results of the delay line and the effect of the phase-matching conditions, as we did in the previous section. In this device, the SH spatial profile can be controlled, as well as the phase-matching conditions on the SFG.

Similarly to what we obtained in the previous section, it is possible to obtain a gain profile that changes from point to point in the crystal line. This might lead to a cross-correlation contrast gain.

$$SSCC(y) = G(y) \int I_{2\omega}(t - \tau_{2\omega}(y)) I_\omega(t + \tau_\omega(y)) dt$$
$$G(y) = I_{2\omega}(y) I_\omega(y) \int \exp(i\Delta kz) dz$$

(5.10)

We assume that the pulse at the entry of the correlator has a Super-Gaussian profile. The $\vec{k}$ vectors for each wave vary from point to point according to Eq. (5.6), and the values of the delay for each beam $\tau_\omega(y)$ and $\tau_{2\omega}(y)$ may also be found in the last expression of Eq. (5.6).
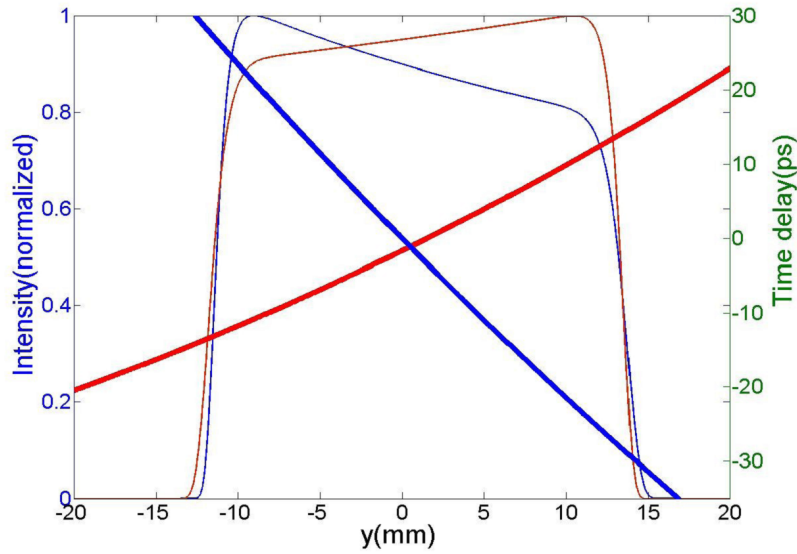
Figure 5.18.: Spatial profile in the SFG crystal with a 90 ps time window, the red curve representing the fundamental beam and the blue curve the second harmonic beam. The results are consistent with a 24 mm crystal $\gamma_\omega = 23.85°$, $\gamma_{2\omega} = 35.17°$. The thick lines represent the time delay and the thin lines the spatial intensity profile.

In this measurement, the SH is normally considered as a probe for the fundamental pulse. This is reasonable to assume because the SH has a bigger contrast than the fundamental pulse. In the next section, we analyze the effect of controlling the SH spatial profile, however here we analyze the astigmatic profile influence on the resulting gain profile.

We remember that the central incidence angles on the crystal are not equal, which is different from what we had seen in SSIA. This creates a non-flat gain profile, it creates a slight slope in the gain profile throughout the crystal.

Considering the delay line presented above and the phase-matching considerations presented below, we design a SSCC as given in Fig. (5.19). The system L1-L2 and SH crystal uses a high numerical aperture system in order to modulate the SH spatial profile. MC1 and MC2 are curved mirrors (R=2 m), used in an astigmatic configuration. M4 to M7 are folding mirrors. E1 and E2 are elevators, E1 is a crossed elevator with a beam splitter that rotates the polarization of the beam in order to have a type I phase-matching configuration on all wave mixing, E1 is an elevator with a delay line. The lenses L3 and L4 (NA=0.35) form a telescope that increases the size of the fundamental beam twice (see sub-Sec. (5.3.2) were the ratio between beam sizes is discussed).
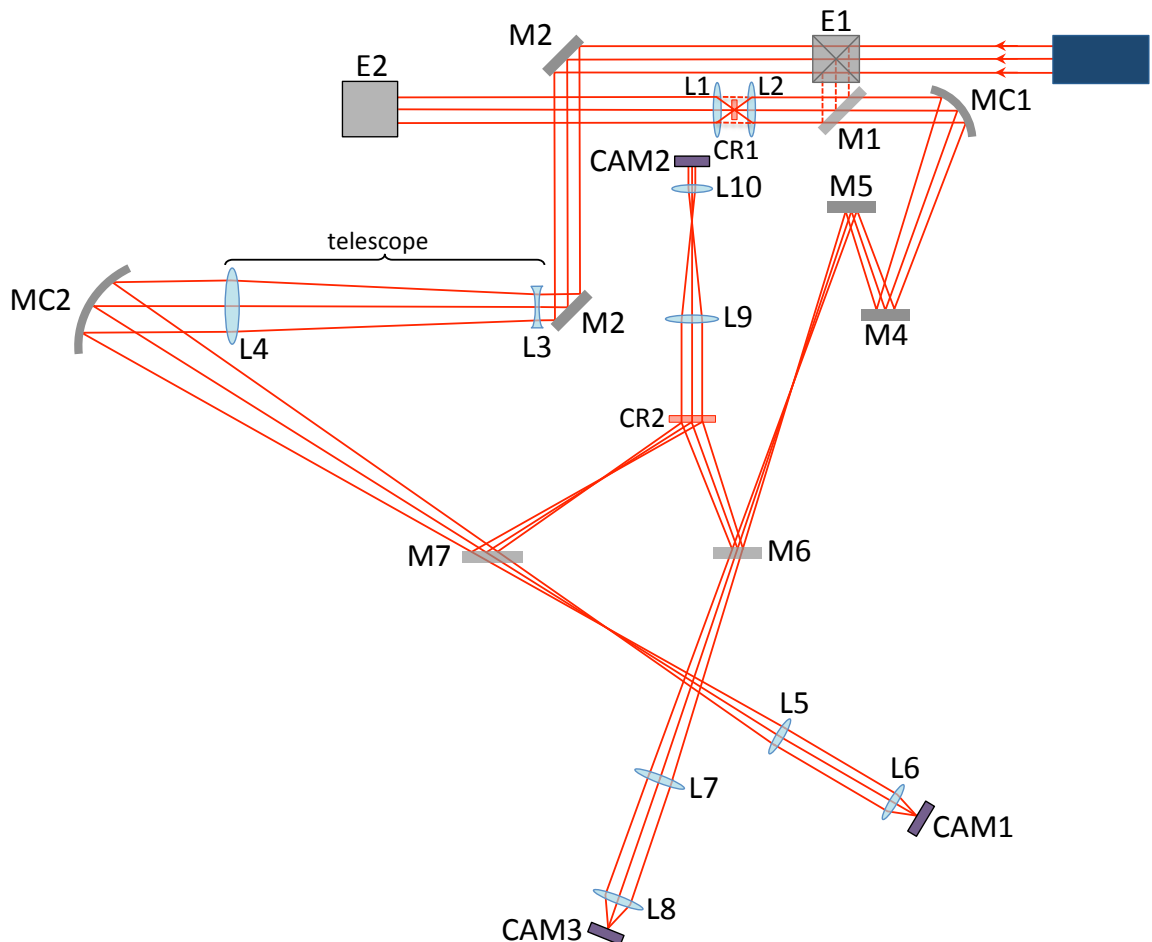
Figure 5.19.: Single shot cross-correlator based on a sagittal astigmatic line. M1-7 are plane mirrors, L1 and L2 are two cylindrical 0.35 NA lenses. L5-L10 are pairs of imaging 2f1-2f2 systems, L3-L4 is a telescope; E1 is a crossed elevator (descendent); E2 is an elevator (ascendent); MC1 and MC2 are curved mirrors. CR1 is the second harmonic crystal and CR2 the SFG crystal wedge crystal.

In this manner, the size of the astigmatic lines of both beams will coincide and therefore will be superimposed. We start with a beam that has 25 mm in diameter, that is used directly in the SH beam, the size of the fundamental beam will be 50 mm. CAM1 and CAM3 image the SH and the fundamental beam spatial profile. CAM2 records the SFG signal originated by the two beams. L5 to L10 are imaging lenses.

5.5.1. Second harmonic simulation in high aperture situation

The SH beam is obtained by focusing the fundamental beam with a high numerical aperture lens. This high aperture lens creates a wide angular $\vec{k}$ spectrum, each angular component is going to obey the phase-matching condition differently. Fig. (5.20) describes our problem where the wide angular beam is decomposed in its angular components with the electric field E included in the o-axis, and with the e-axis parallel to the crystal surface. The intensity spatial profile considered at the entry of the device is top hat (this approximation is valid for high energy lasers). The crystal used here is bigger than the crystal used in the TWM of the intensity correlator, described in the previous section. This is simply because we want to use a bigger $\Delta k.z$ and will enhance the importance of the phase-matching conditions. In consequence it will give us a spatial modulation on the SH after the crystal The wedge crystal will be used to adjust the beam path and, accordingly, to adjust the spatial modulation, and the gain magnitude.
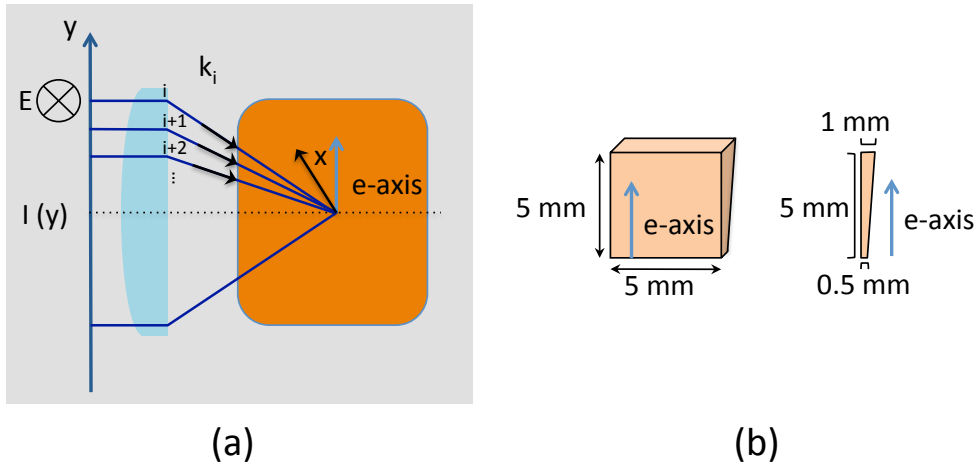
Figure 5.20.: (a) SH crystal with the e-axis scheme, the polarization of the electric field and $\overrightarrow{k_i}$ vectors that are used in the calculation, with the focal lens in blue and the crystal in orange; (b) schematics of the real crystal.

Please note that, in order to simulate the SH production in this scheme, we cannot simply make the SH of each angular component, without considering the influence of the other components. Normally,we have to make the convolution for each electric field component as we have seen in the introduction.

Let us first explain the procedure without using a wavelength decomposition. We only consider an electric field with a wavelength λ. Aside from the angular decomposition used in the simulations, we used an angle θ between the e-axis and the y-axis, this allows an exploration of several configurations which resulted in different intensity profile modulations.

In this case, we use an amplitude electric field decomposition, A_i (this amplitude is calculated using the square root of the intensity on the focus multiplied by the step used for the decomposition) with correspondent Δk_i, where $i = 1, ..., N$. In theory the resulting electric field that is obtained by the wave mixing of these waves is given by the sum seen in Eq. (5.14) (to see the used normalizations see Sec. (1.2)).

$$\frac{\partial B_h}{\partial z_h} = \sum_{i,j}^{N,N} A_i A_j e^{i\Delta k_{i,j} z_h} \tag{5.11}$$

However this would result in N^2 SH fields which would be complicated to integrate with each other. Each h field will be given in a different $\theta_{2\omega}$ direction and results in a number of superimposed electric fields with each other that can neither be summed strait forward nor can they be treated independently.

Before exposing the way to integrate all the B_h, let us find the B_h electric field that results from the interaction between two angular components of the electric field. Consider the electric fields A_i and A_j. In order to calculate the resulting h direction, using the null phase-matching condition parallel to the entry surface of the crystal $k_h^\parallel = k_i^\parallel + k_j^\parallel$, we use Eq. (5.12)[4], please note that θ_i, θ_j are the angles between k_i, k_j and the normal of the crystal, and $\theta_{2\omega}^h$ is the angle of the second harmonic to the normal of the crystal, $a, b, c, p,$ and yy are auxiliary variables.

$$p = \tfrac{1}{2} \left(n_o(\lambda) \sin(\theta_i) + n_o(\lambda) \sin(\theta_j) \right)$$

$$a = 1 - p^2 \left[n_o^{-2}(\lambda/2) + \cos^2(\theta) \left[n_e^{-2}(\lambda/2) - n_o^{-2}(\lambda/2) \right] \right]$$

$$b = \tfrac{\sin(2\theta)}{2} \left[n_e^{-2}(\lambda/2) - n_o^{-2}(\lambda/2) \right]$$

$$c = p^2 \left[n_o^{-2}(\lambda/2) + \sin^2(\theta) \left[n_e^{-2}(\lambda/2) - n_o^{-2}(\lambda/2) \right] \right]$$

$$yy = \tfrac{-b + \sqrt{b^2 + c}}{a}$$

$$\theta_{2\omega}^h = \tfrac{p}{|p|} \arctan(yy)$$

$$\tag{5.12}$$

This will allow us to calculate the angle from which the h component of the electric field will appear.

---

[4]Please note that all the angles used in the formulas are internal angles, inside the crystal - they can be converted into external angles using Snell-Descartes' law.

5. Single shot correlations based in a sagittal focal line configuration

With this, we can easily calculate the refraction index and the phase mismatch:

$$n_{2\omega} = \left[n_o^{-2}(\lambda/2) + \sin^2\left(\theta - \theta_{2\omega}\right) \left[n_e^{-2}(\lambda/2) - n_o^{-2}(\lambda/2) \right] \right]^{-\frac{1}{2}}$$
$$\Delta k_{i,j} = \frac{2\pi}{\lambda} \left[2n_{2\omega}\cos\left(\theta_{2\omega}\right) - n_o(\lambda)\cos\left(\theta_i\right) - n_o(\lambda)\cos\left(\theta_j\right) \right] \tag{5.13}$$

The solution of Eq. (5.14) results in a series of sinc functions. Please note that the distance propagated by the field h is not the thickness of the crystal L_{cr} but rather $\frac{L_{cr}}{\cos(\theta_h)}$.

Let us now consider that we apply this procedure to the electric fields $i = 1$ and to all $j = 1, .., N$. This creates a mesh of the SH electric field with a spectral distribution of $\theta_{2\omega}^h$, $h = \{(1,1), ..., (1,N)\}$. We interpolate this mesh with a reference mesh θ_r, and memorize the result (phase and amplitude).

We repeat the procedure with $h = \{(2,1), ..., (2,N)\}$, and again we interpolate the values obtained, we then sum the values obtained with $i = 1$ with the ones obtained with $i = 2$, we do this for all values of i until we obtain the SH electric field, summing the final electric fields.

The procedure above is valid to obtain the electric field of a single spectral component. In order for the above calculations to be valid for ultrashort pulsed lasers, we have to consider wide spectrum lasers and an integration for all spectral components. This will result in a sum over the different spectral components Eq. (5.14).

$$\frac{\partial B_h}{\partial z_h} = \sum_{i\omega,j\omega}^{N_\omega,N_\omega} \sum_{iy,jy}^{N_y,N_y} A_{iy,i\omega} A_{jy,j\omega} e^{i\Delta k_{iy,jy,i\omega,j\omega} z_h} \tag{5.14}$$

We have to apply the same procedure to all wavelengths and all the angular components. Let us first consider the interaction between the electric field at wavelength λ_i with the angle θ_i to the normal of the crystal, with the electric field at wavelength λ_j and with the angle θ_j to the normal of the crystal. As before a, b, c, p, and yy are auxiliary variables.

$$\lambda_{SH} = \frac{\lambda_i \lambda_j}{\lambda_i + \lambda_j}$$

$$p = \left(\frac{n_o(\lambda_i)\sin(\theta_i)}{\lambda_i} + \frac{n_o(\lambda_j)\sin(\theta_j)}{\lambda_j} \right) \lambda_{SH}$$

$$a = 1 - p^2 \left[n_o^{-2}(\lambda_{SH}) + \cos^2\left(\theta\right) \left[n_e^{-2}(\lambda_{SH}) - n_o^{-2}(\lambda_{SH}) \right] \right]$$

$$b = \frac{\sin(2\theta)}{2} \left[n_e^{-2}(\lambda_{SH}) - n_o^{-2}(\lambda_{SH}) \right] \tag{5.15}$$

$$c = p^2 \left[n_o^{-2}(\lambda_{SH}) + \sin^2\left(\theta\right) \left[n_e^{-2}(\lambda_{SH}) - n_o^{-2}(\lambda_{SH}) \right] \right]$$

$$yy = \frac{-b + \sqrt{b^2 + c}}{a}$$
$$\theta_{2\omega}^h = \frac{p}{|p|} \arctan\left(yy\right)$$

In this case, in order to be precise, we should apply the same sum procedure but instead of using a reference mesh only for the angular dispersion θ_r, we should use a reference mesh for both quantities (θ_r, λ_r). However we are interested in the angular (spatial) profile, not in the SH spectral profile, in this device the SH is used as a probe to the fundamental pulse, and so in the calculations presented here we simply sum the results for all spectral components.

Despite being as complete as possible, this simulations consider a low depletion calculation seen that we do not consider the feedback result from the fundamental field propagation. We estimate that the results are valid while the fundamental beam depletion is not important $z_h \ll L_{NL}$ (see the introduction). The dispersion suffered by the SH electric field is only partially simulated (as a part of the phase mismatch in Eq. (5.14)).
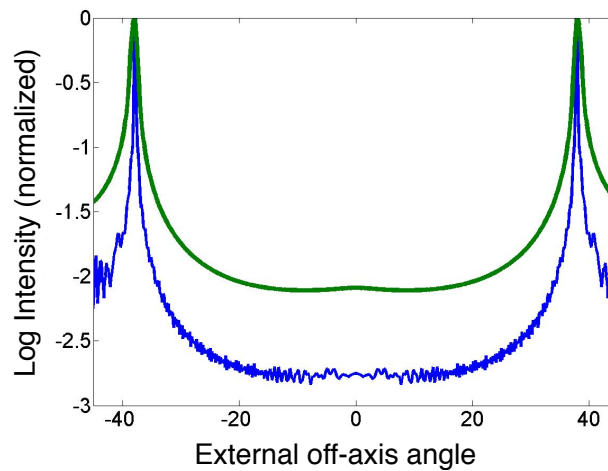
Figure 5.21.: SH angular profile on the sensitive phase matching direction, the entrance spatial profile is top hat. The blue line is the second harmonic efficiency if the beam is monochromatic and the green line is the sum over 50 nm flat spectrum centered at 800 nm.

The results of the simulations explained above are given in Fig. (5.21), we can see that it is possible to obtain spatial profile modulation with several orders of magnitude, however for an ultrashort pulse, this is limited to less than 2 orders of magnitude. They were obtained using a Super-Gaussian spatial profile and a lens with a numerical aperture of 0.35 and a crystal as described in Fig. (5.20).

5.5.2. Sum frequency generation and phase matching conditions

We used the SH obtained in the previous subsection and a fundamental pulse with a Super-Gaussian profile in order to evaluate a possible gain function of this device. We use the same reasoning applied in the intensity autocorrelation in order to evaluate the gain profile; the results are shown in Fig. (5.22).

The crystal used for the calculation is equal to the crystal presented in Fig. (5.10). For this calculation,

a 24 mm crystal was used with 90 ps time window and the largest possible aperture angle. This corresponds to $\gamma_\omega = 23.85°$, $\gamma_{2\omega} = 35.17°$.

The calculated gain profile is irregular. In the best possible scenario, we could get 3 orders of magnitude contrast increase in the configuration we have presented. Within the simulated crystal thicknesses, we found no significant differences.
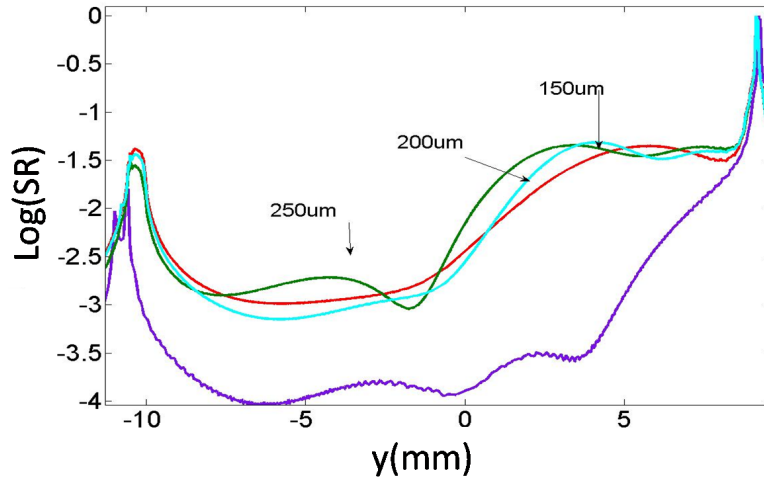
Figure 5.22.: Logarithmic gain profile as a function of the position in the crystal The red blue and green lines are different distributions considering different crystal thicknesses for a 50 nm pulse bandwidth centered at 800 nm. The purple line is obtained using a single linewidth spectrum at 800 nm.

5.6. Conclusions

We have presented a single shot correlator configuration that uses an astigmatic line in order to obtain a delay configuration. We used this principle to design and simulate a single shot intensity autocorrelator and a single shot cross correlator where the spatial profile of the beam is integrated in one direction.

We compared the astigmatic configuration with the standard tilted front configuration. Concerning the same crystal lengths, we concluded that the two configurations present a similar time window (the astigmatic configuration time window is 4% bigger for an intensity autocorrelator and is 3% bigger for a cross correlator). If our biggest restrain is the size of the beam at the entry of the device then the astigmatic configuration is not recommendable, the time window obtained will only be 36% (cross correlator) and 40% (intensity autocorrelator) of the time window obtained in a tilted front correlator.

We analyzed the influence of the astigmatism on intensity profile in the focal plane and on the phase-matching conditions. For an intensity autocorrelation, we concluded that this influence may be

discarded. For a cross correlator, we can have a modulation of the gain along the position in the crystal, this modulation may reach 3 orders of magnitude, this means that the contrast of the device can be bigger than the contrast granted by the detectors by 3 orders of magnitude. In order to achieve this contrast, the SH spatial profile is modulated. This is achieved because the SH is obtained with a 1mm crystal thick and a lens with a numerical aperture of 0.35.

We employed this new design on a new single shot intensity autocorrelator obtaining results that are coherent with the theory presented, we concluded that the main contrast limitations for this intensity autocorrelator were possible defects in the crystal surface. We calibrated the time frame, which resulted in $3.45\,^{ps}/_{mm}$, and obtained the IA of pulses with hundreds of fs pulse duration. The sensibility to the beam direction was also tested, and it is self-evident that the zero delay position changes with the beam direction at the entry of the device. The uncertainty that is due to calibration is approximately 0.2 %. We can also conclude that the shot to shot duration changes are bigger than the precision given by the device.

Please note that the solutions proposed here to increase the contrast of the measurements only regulate the phase-matching conditions. In order to achieve a high contrast solution, it would be possible to use gradient shading in order to increase the contrast [59].

6. Conclusion

We have tried to make each chapter as independent as possible and so, at the end of each chapter, we have drawn all the conclusions appropriate to that chapter. Here we will simply try to summarize the main features of this thesis and its main conclusions.

We start by studying the equations that rule TWM, in a quasi plane wave approximation. We solve the coupled TWM equations in the case of DFG and applied it to OPA. We make a quick introduction regarding some of the features involved in optical amplification, particularly optical parametric amplification.

In Chapter 2 we presented a study on optical amplification, describing the design and construction of an optical oscillator, a CPA chain with particular properties and a theoretical study of OPA. In this chapter presented two mode-lock Ti:Sapphire laser oscillators. The first oscillator, which we describe in detail was used at the beginning of the presented CPA laser chain, has a spectral bandwidth FWHM of 96 nm, it emits between 750 and 900 nm, the pulse Fourier limited by 12 fs The ML laser in which we base our simulations is presented in detail. It has 150 nm spectral bandwidth, in which the dispersion control is assured not only by a traditional set of prisms, which in this case are only 24.8 cm apart from each other and so have a net dispersion that is slightly positive, but also by a ensemble of chirped mirrors, we present the details on the dispersion and spectral phase accumulated on a round-trip of the cavity. This enables the oscillator to be smaller and therefore more stable. We discussed the astigmatism in the cavity, there are three components that create astigmatism in the cavity, one is the crystal and the other two are the concave mirrors of the sub-cavity. The crystal not only contributes to the astigmatism due to the simple transmission (the effective path in the tangential and sagittal planes is different) but also due to the astigmatic lenses that exist in the crystal (thermal and Kerr lens). Both elements have to balance each other, in other words the folding of the mirrors of the sub-cavity has to compensate effects in the crystal. There is a formula to find the folding angle that compensates the path that is made inside the crystal, this formula gives an angle of 8.07°, we also used a simple simulation to find which angle would allow us to compensate the astigmatism of the output beam, and found that 7.2° would be the best value, experimentally we make a sweep of the folding angle to find the best angle to obtain an anastigmatic beam at the output of the cavity, we find that this angle is of approximately 7.5°.

A regenerative amplifier was also design and built, this amplifier had a set of prism inside it's cavity. These prisms were tilted in the same direction (unlike a standard prism compressor) and had the

objective of serving as spectral filters. The rest of the CPA chain was constituted by a Öffner triplet stretcher, a multipass amplifier and a holographic-grating compressor. The CPA laser chain delivers $1.7\,mJ$ per pulse, with a spectral bandwidth that can be as short as $1.1\,nm@802\,nm$. Due to this design where two prisms were inserted inside the regenerative amplifier cavity we may select the spectral bandwidth to be amplified. The objective in this work was to be able to amplify a spectrum as short as possible in order to optimize and stabilize a subsequent OPA scheme, this OPA however was never stable.

We also developed several models to analyze the ML operation of the laser oscillator and to retrieve its spatial characteristics.

Our analysis of the ML operation consisted not only in analyzing the spot sizes in the middle of the gain medium, but also in introducing parameters to evaluate the ML configuration in this cavity. The traditional way to analyze the ML operation relies upon calculating the mode size in a CW configuration and then introducing a small Kerr lens that enables us to evaluate the tendency to ML that a certain cavity configuration possesses: if the beam size inside the crystal decreases, this is an indication that the cavity configuration should enable ML; however, when the laser goes from a CW configuration to a ML configuration the beam intensity increases by six orders of magnitude. This is a nonlinear process and so it is possible that the evaluation of an infinitesimal Kerr lens does not represent the entire process. The hard thing about calculating the ML parameter using the size of the beam in ML, as stated by Eq. (2.34), is to calculate the actual spot size in a ML configuration. In reality the beam size is going to depend on the Kerr lens and the Kerr lens will depend on the beam size. In order to evaluate this we first devised a recursive algorithm between the two quantities. For a laser with a small thermal lens, the consequence was a break up of the two stability zones that are observed in ML into four distinct zones. Of these four zones, the one where the crystal was closer to the back mirror and the sub-cavity mirrors were further apart is the most favorable zone to ML. More precisely, the ideal region for ML is on the edge of the zone where the crystal is farther apart from the back mirror and the sub-cavity mirrors are the closest to one another. We designed several more models to explain the ML operation, this were a mix of search models and of power increase models. We were able to deduce that for this configuration the four stability zones are maintained even when the size of the pump beam is swept from zero to $130\,\mu m$. However we found that there are several configurations where ML existed and was not predicted in the first two models. We have also found that pulses that are temporally larger are easier to ML because the region favorable to ML is larger.

We used several models for our thermal lens concluding that the thermal lens inside the cavity should not be smaller than 10 cm. We found that for our laser the CW mode was not compatible with a pump beam smaller than $40\,\mu m$. At first we used no thermal lens whatsoever. Secondly, we considered a thermal lens with a constant dioptric power. In our case the dioptric power of the thermal lens is not too large: the stability zones bend but the ideal operational point does not move because of it. We then used a thermal lens that considered the mismatch between the pump and cavity beam sizes. We

concluded still that for our values of thermal lens, inclusion of this thermal lens did not change the ideal sub-cavity configuration for ML. Nevertheless, both thermal lenses change the ideal distance between prisms slightly, because they change the stability zones.

The second oscillator that we have presented is a sub-6 fs oscillator (4.8 fs Fourier limited), with a larger spectral bandwidth. We describe this oscillator summarily, it has a smaller crystal, 1.9 mm instead of the 4.5 mm that we had in the first oscillator and we use doubled chirped mirrors to compensate the dispersion accumulated by the pulse, in a cavity round trip, the Ti:Sapphire crystal, the two BaF_2 plates, the two CaF_2 wedges and the dispersion introduced by the air, the wedges are assembled in a translation stage with a motor that allows us to finely tune the dispersion inside the cavity. The SPM effect in this case is such that the output spectrum can go from 650 nm to 1125 nm while the output coupler has a flat transmission from 605 nm to 925 nm, in other words there is a part of the spectrum which half-life time in the cavity is smaller than the half-life time of the central part of the spectrum, which is only made possible due to the strong SPM inside the crystal that creates frequency components at each round-trip (Fig. 2.31). This oscillator has a smaller sub-cavity (concave mirrors with a smaller focal length) which creates a smaller spot size at the center of the crystal. The stability zones in this case are bended in such a way that the two stability zones are superimposed. In the meeting between the two stability zones, on the edge of the second stability zone we find the ideal point to have the laser in ML. At the ideal ML position the focal for the first oscillator is approximately $50\,mm$ ($35\,\mu m$ spot size), for the second oscillator, the beam size is smaller than $10\mu m$, in consequence the thermal lens is one order of magnitude smaller on the order of the mm. This enabled us to work in a region that is stable and at the same time with a spectral bandwidth bigger than an octave. We also verify that the point in which the cavity operates in ML the pump and beam size are similar at the central of the crystal, no other configuration of the sub-cavity as the same two characteristics. In the first cavity that was presented, the final model gives presents two points that where ML operation is feasible, one of them is coincident with the literature (see for instance [87, 112, 137]) on the other the pump and beam sizes do not match (compare Fig. (2.24) c) and the bottom graph of Fig. (2.28)), we envision that in future works an engineering parameter to define the ideal ML position would not only have into account the decrease in mode size due to the increase in power (which the ML parameter already does) but also the match between the pump and beam size inside the crystal.

It is obvious to us that further work on these models must include a simulation of the gain, and the pulse temporal evolution inside the cavity.

In Chap. 2 presented several OPA configurations. We studied the difference between degenerate and non degenerate configurations, as well as the introduction of an angular chirp in the seed pulse. We obtained the conditions that enable an enlargement of the spectral gain bandwidth. In our configuration we had two degrees of freedom, the angular chirp and the non-collinear angle. We used a derivation of the phase-matching condition in order to obtain two conditions that gave the configuration that enlarges the spectral gain bandwidth. We combined this with our previous work to

deduce a configuration that would enable at the same time a wide spectral pump and a large spectral bandwidth of the amplified signal. We then numerically confirmed that chirping the seed pulse angularly can enlarge the gain bandwidth. We found that in this case the degenerate configuration gives the widest spectral bandwidths. We calculated that the gain will have a FWHM of 405 nm, between 645 and 1050 nm centered at 850 nm for a chirp of $\sim 2E - 4 \, rad/nm$, without the spatial chirp such a configuration would result in a gain with 150 nm bandwidth.

In Chapter 3 we discuss several properties of autocorrelations, introducing their main characteristics, also in this chapter we deal with third order cross correlations. We start by exposing the main characteristics of the measurement; afterwards we use trial functions to analyze the TOCC trace. For Dirac delta functions we conclude that each replica (with a high enough contrast) creates at least two features at symmetrical positions from the zero delay position, one with the intensity of the replica and a second one with the square of that intensity. With a series of background noises we conclude that the background noise in the measurement (when larger than the experimental limit) has the same order of magnitude as the pulse contrast, with its actual value slightly higher than the pulse contrast. For a Gaussian pulse the apparent contrast on the TOCC trace is $\sim 22\%$ higher than the true pulse contrast.

We end this chapter by proving that TOCC and IA completely define the pulse intensity profile. This property might be useful for measuring the pedestal of ultrafast pulses. We presented preliminary retrieval algorithms with which we retrieved the pulse intensity profile, in a worst case scenario, the retrieved intensity profile was limited to a contrast of 10^{-4} due to the reconstruction algorithm, further work is needed to obtain the ideal retrieval algorithm and then apply it any experimental data.

In Chapter 4 we research the potential of IAC traces to a very high extent. We start by clarifying known properties of IAC and MOSAIC traces. From here we conclude that even order spectral phase terms created a distinct feature on the baseline of MOSAIC traces and that odd terms enlarge the envelope of the MOSAIC traces. As it had already been reported [49], when compared to IAC traces, MOSAIC traces are more sensitive to the spectral phase.

We then used several algorithms in order to retrieve the pulse shape from the intensity autocorrelation, the SH autocorrelation and the field autocorrelation traces. It is well known that it is not possible to retrieve a pulse from a single autocorrelation, but in our case we retrieve it from three autocorrelations, not a single one (the proof that these three quantities completely determine the pulse profile is given by Naganuma et al. in [47]).

First we used two Gerchberg-Saxton type algorithms to attempt a pulse retrieval. These attempts failed: in the first attempt, no convergence was obtained, and in the second convergence was achieved but spectral phase retrieval was not achieved.

We then tried minimization algorithms. Since our retrieval problem is equivalent to a spectral phase retrieval, we assumed that the spectrum intensity is known exactly and try to guess the spectral phase

so that it fits the other two measurements, thereby reconstructing the pulse profile. Note that the minimization factor of our S/N is $\frac{\sqrt{\delta}}{2}$ where δ is the data S/N ratio.

A simplex minimization algorithm (namely the *fminsearch* algorithm in Matlab) failed to reconstruct the spectral phase. However, from this experience we learned that the base chosen to represent the pulse spectral phase is of the utmost importance. More specifically we learned that using a polynomial base (Chebyshev polynomials) could enable the existence of local minima in our problem. This is very important because if our problem has local minima we may encounter a minimum and wrongly take this minimum to be the best possible solution. With the same algorithm we also tried a spectral phase not described by any polynomial, where all points of the spectral phase were minimization arguments. With this approach no local minima were found. It is quite normal that no local minima exist in this base if we are obeying the sampling theorem in all spaces, for all measurements and fields.

We then devised a simple elitist genetic algorithm with an adaptive mutation and used it to reconstruct the spectral phase. This approach was successful and despite the stochastic nature of the algorithm, it gave consistent reproducible results independent of the initial guess used for the spectral phase. At first we used this algorithm to reconstruct IAC traces that we had computed. After successfully retrieving the pulse shape of these virtual measurements we applied this method to actual measurements. The results indicated that in these cases the reconstructions continued to be reproducible and successful. Using this method, we have reconstructed the spectral phase of actual few-cycle laser pulses with a FWHM duration of 5.9 fs and 4.9 fs. With these experimental measurements we used two bases for the spectral phase: a Taylor polynomial and a point-by-point base. The second base was able to reproduce the pulse with a larger precision than the first one. Using a Taylor polynomial we concluded that a low order polynomial should be used (third order). The gain in precision obtained by using a high order Taylor polynomial does not compensate the computer capacity required. We concluded that a third order Taylor polynomial can be used in a first approach but then, in order to have more precision, a point-by-point discretization should be used.

Finally we evaluated the PSO and RPSO algorithms as potential tools for spectral phase reconstruction. We found that a RPSO algorithm with a high undamping factor and a low coupling constant was able to reconstruct the pulse spectral phase as efficiently as the genetic algorithm.

As a final remark on this subject we must say that with these algorithms the measurement limitation is not on the retrieving algorithm itself but on the experimental measurement noise, specially on the measurement of the SH autocorrelation. In order to overcome this shortfall, another method to measure the SH autocorrelation should be envisioned. We propose that instead of retrieving the SH spectrum from the IAC trace, this measure should be done appropriately with an adequate spectrometer.

In Chapter 5 we presented a pulse delay configuration based upon the sagittal line of a spherical mirror. We used this principle to design and simulate a single shot intensity autocorrelator and a

single shot cross correlator. In this configuration the spatial profile of the beam is integrated in one direction.

We compared the astigmatic configuration with the standard, tilted front configuration. If we consider the same crystal for both cases we conclude that the astigmatic configuration presents a slightly bigger time window.

We analyzed the influence of astigmatism on the intensity profile in the focal plane and on the phase-matching conditions. For an intensity autocorrelation we concluded that this influence can be neglected. For a cross-correlator, the measured signal along the position in the crystal is not the cross correlation itself because it can be modulated by the astigmatism and the phase-matching conditions, and this modulation can affect the signal by up to 30 dB.

We employed this new design on a new single shot intensity autocorrelator testing this device with a 180 fs laser pulse. We concluded that the main contrast limitation for this intensity autocorrelator is given by the imperfections in the crystal surface. From the measurements it is clear that the shot to shot fluctuations in pulse duration are larger than the device's precision.

In sum we have studied analysis techniques that allow temporal measurements of ultrafast pulses using correlations. Optical amplification has been studied we assembled a CPA chain and studied the influence of angular chirp on OPCPA. We studied ultrafast pulse generation, by studying KLM Ti:Sapphire laser cavities, another part of ultrashort pulse generation consisted on a study of ultrashort pulses on PCF, this study was presented in detail elsewhere [81, 176], however the reconstruction results can be viewed in Chap. (4).

List of publications by the author

Conferences

P. Oliveira, F. Augé-Rochereau, and H. M. Crespo, "Complete determination of the temporal intensity profile of ultrashort pulses via the intensity autocorrelation and the third-order cross-correlation", ICONO/LAT 2013.

Helder Crespo, Miguel Miranda, Pedro Oliveira, Rosa Weigand, "Broadband 5.9 fs Ti:Sapphire laser characterized using the dispersion-scan technique", CLEO-IQEC 2013.

C. S. Gonçalves, A. S. Silva, M. Miranda, F. Silva, P. Oliveira, H. Crespo and D. S. Schmool, "Novel dual-color architecture for ultrafast spin dynamics measurements in the sub-10 fs regime", UMC 2013.

P. Oliveira, J. L. Silva, A. A. Amorim, and H. M. Crespo, "Spectral phase retrieval of sub-two-cycle pulses from modified interferometric autocorrelations and spectra using genetic algorithms", UFO 2009.

P. Oliveira, Moana Pittman, and F. Augé-Rochereax, "Third order single shot cross-correlator, contrast limitations and enhancements", UFO 2009.

P. Oliveira, Moana Pittman, and F. Augé-Rochereau, "Third order single shot cross-correlator, with enhancement of the contrast by spatial shaping of the second harmonic spatial profile", SSIULP 2009.

Miguel N. Miranda, Pedro B. Oliveira, L. M. Bernardo, Franz X. Kärtner, Helder M. Crespo "Space-time focusing of phase-stabilized nanojoule-level 2.5-cycle pulses to peak intensities $> 3 \times 10^{13}$ W/cm2 at 80 MHz" CLEO IQEC 2009.

Alexandra Amorim, Marco Tognetti, Pedro Oliveira, Luis Bernardo,Franz Kärtner, and Helder Crespo, "Experimental demonstration of sub-two-cycle soliton-effect pulse compression in a photonic crystal fiber", CLEO-IQEC 2009.

Articles

A. A. Amorim, M. V. Tognetti, P. Oliveira, J. L. Silva, L. M. Bernardo, F. X. Kärtner, and H. M. Crespo, "Sub-two-cycle pulses by soliton self-compression in highly-nonlinear photonic crystal fibers," Opt, Lett. 34, 3851-3853 (2009).

Pedro Oliveira, A. A. Amorim, J. L. Silva, and H. M. Crespo, "Spectral phase retrieval of sub-two-cycle pulses from interferometric autocorrelations and spectra", Appl. Physics B, Submitted.

Pedro Oliveira, Helder Crespo, "Variational approach to ultrafast propagation in nonlinear medium with second and third order nonlinearities", Phys. Rev. A, To be submitted.

Helder Crespo , Miguel Miranda, Pedro Oliveira, Rosa Weigand, "Broadband 5.9 fs Ti:sapphire laser characterized using the dispersion-scan technique", Appl. Physics B, To be submitted.

P. Oliveira, Miguel Macau, F. Augé-Rochereau, and H. M. Crespo, "Complete determination of the temporal intensity profile of ultrashort pulses via the intensity autocorrelation and the third-order cross-correlation", Laser Physics, To be submitted.

Bibliography

[1] J. Collier R. Clark C. B. Edwards S. Hancock P. Hatton S. Hawkes M. H. R. Hutchinson C. Hernandez-Gomez A. Kidd W. Lester D. Neely P. Norreys M. Notley D. Pepler M. Pitts C. Reason D. A. Rodkiss T. B. Winstone R. W. W. Wyatt C. N. Danson, R. Allott and B. Wyborn. Cpa design considerations for the vulcan petawatt upgrade. In *Int. Fusion Sci. Applicat. Conf. Proc.*, 1999.

[2] Erhard W. Gaul, Mikael Martinez, Joel Blakeney, Axel Jochmann, Martin Ringuette, Doug Hammond, Ted Borger, Ramiro Escamilla, Skylar Douglas, Watson Henderson, Gilliss Dyer, Alvin Erlandson, Rick Cross, John Caird, Christopher Ebbers, and Todd Ditmire. Demonstration of a 1.1 petawatt laser based on a hybrid optical parametric chirped pulse amplification/mixed nd:glass amplifier. *Appl. Opt.*, 49:1676–1681, 2010.

[3] Tae Jun Yu, Seong Ku Lee, Jae Hee Sung, Jin Woo Yoon, Tae Moon Jeong, and Jongmin Lee. Generation of high-contrast, 30 fs, 1.5 pw laser pulses from chirped-pulse amplification ti:sapphire laser. *Opt. Express*, 20(10):10807–10815, May 2012.

[4] Kun Zhao, Qi Zhang, Michael Chini, Yi Wu, Xiaowei Wang, and Zenghu Chang. Tailoring a 67 attosecond pulse through advantageous phase-mismatch. *Opt. Lett.*, 37(18):3891–3893, Sep 2012.

[5] Artem V Korzhimanov, A A Gonoskov, Efim A Khazanov, and Aleksandr M Sergeev. Horizons of petawatt laser technology. *Physics-Uspekhi*, 54(1):9, 2011.

[6] G. Laurent, W. Cao, H. Li, Z. Wang, I. Ben-Itzhak, and C. L. Cocke. Attosecond control of orbital parity mix interferences and the relative phase of even and odd harmonics in an attosecond pulse train. *Phys. Rev. Lett.*, 109:083001, Aug 2012.

[7] G. Mourou D. Strickland. Compression of amplified chirped optical pulses. *Optics Communication*, 56:219–221, 1985.

[8] Geoffrey H. C. New Ian N. Ross, Pavel Matousek and Karoly Osvay. Analysis and optimization of optical parametric chirped pulse amplification. *J. Opt. Soc. Am. B*, 19:2945–2956, 2002.

[9] M. D. Perry, D. Pennington, B. C. Stuart, G. Tietbohl, J. A. Britten, C. Brown, S. Herman,

B. Golick, M. Kartz, J. Miller, H. T. Powell, M. Vergino, and V. Yanovsky. Petawatt laser pulses. *Opt. Lett.*, 24(3):160–162, Feb 1999.

[10] A. Dubietis, R. Butkus, and A.P. Piskarskas. Trends in chirped pulse optical parametric amplification. *Selected Topics in Quantum Electronics, IEEE Journal of*, 12(2):163–172, 2006.

[11] Audrius Zaukevičius, Vytautas Jukna, Roman Antipenkov, Vilija Martinenaite, Arunas Varanavičius, Algis Piskarskas, and Gintaras Valiulis. Spatial chirp and angular dispersion dynamics in femtosecond noncollinear opcpa. In *Lasers, Sources, and Related Photonic Devices*, page AM4A.28. Optical Society of America, 2012.

[12] Luis Cardoso and Goncalo Figueira. Broadband amplification in non-linear crystals using controlled angular dispersion of signal beam. *Optics Communications*, 251:405–414, 2005.

[13] Luis Cardoso and Goncalo Figueira. Bandwidth increase by controlled angular dispersion of signal beam in optical parametric amplification. *Optics Express*, 12:3108, 2004.

[14] K. Yamane, T. Tanigawa, T. Sekikawa, and M. Yamashita. Angularly-dispersed optical parametric amplification of optical pulses with one-octave bandwidth toward monocycle regime. *Opt. Express*, 16(22):18345–18353, Oct 2008.

[15] Gunnar Arisholm, Jens Biegert, Philip Schlup, Christoph Hauri, and Ursula Keller. Ultra-broadband chirped-pulse optical parametric amplifier with angularly dispersed beams. *Opt. Express*, 12(3):518–530, Feb 2004.

[16] http://www.coherent.com/downloader/?DLID=6627.

[17] http://en.wikipedia.org/wiki/Ti sapphire_laser.

[18] Rudiger Paschotta. http://www.rp-photonics.com/titanium_sapphire_lasers.html.

[19] P. N. Kean D. E. Spence and W. Sibbett. 60-fsec pulse generation from a self-mode-locked ti:sapphire laser. *Optics Letters*, 16:42–44, 1991.

[20] Lu Wei K. M. Yoo Xing Qi-rong, Zhang Wei-li and J. Lueng. Experimental study on the self-mode-locked ti:sapphire laser. *Acta Physica Sinica (Overseas Edition)*, 5(1):39, 1996.

[21] Liu Hua-Gang, Hu Ming-Lie, Song You-Jian, Li Yan-Feng, Chai Lu, and Wang Ching-Yue. Operation of kerr-lens mode-locked ti:sapphire laser in the non-soliton regime. *Chinese Physics B*, 19(1):014215, 2010.

[22] G. Cerullo, S. De Silvestri, and V. Magni. Self-starting kerr-lens mode locking of a ti:sapphire laser. *Opt. Lett.*, 19(14):1040–1042, Jul 1994.

[23] Szuyuan Chen and Jyhpyng Wang. Self-starting issues of passive self-focusing mode locking.

Opt. Lett., 16(21):1689–1691, Nov 1991.

[24] Uwe Morgner Christian Jirauschek and Franz X. Kartner. Spatiotemporal gaussian pulse dynamics in kerr-lens mode-locked lasers. *J. Opt. Soc. Am. B*, 20:1356, 2003.

[25] Ivan P. Christov and Vency D. Stoev. Kerr-lens mode-locked laser model: role of space time effects. *J. Opt. Soc. Am. B*, 15(7):1960–1966, Jul 1998.

[26] Jeff Chen Cristian Antonelli and Franz X. Kartner. Intracavity pulse dynamics and stability for passively mode-locked lasers. *Opt. Express*, 15:5919, 2007.

[27] Charles G. Durfee, Tristan Storz, Jonathan Garlick, Steven Hill, Jeff A. Squier, Matthew Kirchner, Greg Taft, Kevin Shea, Henry Kapteyn, Margaret Murnane, and Sterling Backus. Direct diode-pumped kerr-lens mode-locked ti:sapphire laser. *Opt. Express*, 20(13):13677–13683, Jun 2012.

[28] F. W. Helbing, G. Steinmeyer, U. Keller, R. S. Windeler, J. Stenger, and H. R. Telle. Carrier-envelope offset dynamics of mode-locked lasers. *Opt. Lett.*, 27(3):194–196, Feb 2002.

[29] U. Keller, G. W 'tHooft, W. H. Knox, and J. E. Cunningham. Femtosecond pulses from a continuously self-starting passively mode-locked ti:sapphire laser. *Opt. Lett.*, 16(13):1022–1024, Jul 1991.

[30] Y. M. Liu, K. W. Sun, P. R. Prucnal, and S. A. Lyon. Simple method to start and maintain self-mode-locking of a ti:sapphire laser. *Opt. Lett.*, 17(17):1219–1221, Sep 1992.

[31] Michel Piché and François Salin. Self-mode locking of solid-state lasers without apertures. *Opt. Lett.*, 18(13):1041–1043, Jul 1993.

[32] Jonathan R. Birge. *Methods for Engineering Sub-Two-Cycle Mode-Locked Lasers*. PhD thesis, MIT, 2009.

[33] Li jin Chen. *Design, optimization, and applications of few-cycle Ti:Sapphire lasers*. PhD thesis, Massachusetts Institute of Technology. Dept. of Electrical Engineering and Computer Science., 2012.

[34] Rick Trebino. *Frequency-Resolved Optical Gating: The Measurement of Ultrashort Laser Pulses*. Spring, 2002.

[35] Rick Trebino and Daniel J. Kane. Using phase retrieval to measure the intensity and phase of ultrashort pulses: frequency-resolved optical gating. *J. Opt. Soc. Am. A*, 10:1101, 1993.

[36] Rick Trebino. *Frequency-Resolved Optical Gating: The Measurement of Ultrashort Laser Pulses*. Springer, 2000.

[37] N. Matuschek G. Steinmeyer U. Keller C. Iaconis L. Gallmann, D. H. Sutter and I. A.

Walmsley. Chracterization of sub-6-fs optical pulses with spectral phase interferometry for direct electric-field reconstruction. *Optics Letters*, 24:1314–1316, 1999.

[38] C. Iaconis and I.A. Walmsley. Self-referencing spectral interferometry for measuring ultrashort optical pulses. *Quantum Electronics, IEEE Journal of*, 35(4):501–509, 1999.

[39] Miguel Miranda, Thomas Fordell, Cord Arnold, Anne L'Huillier, and Helder Crespo. Simultaneous compression and characterization of ultrashort laser pulses using chirped mirrors and glass wedges. *Opt. Express*, 20:688–697, 2012.

[40] R A Smith S Luan, M H R Hutchinson and F Zhou. High dynamic range third-order correlation measurement of picosecond laser pulse shapes. *Meas Sci. Technol.*, 4:1426–1429, 1993.

[41] J.A. Nees E. Power G.A. Mourou K.-H. Hong, B. Hou. Generation and measurement of >1e8 intensity contrast ratio in a relativistic khz chirped-pulse amplified laser. *Appl. Phys. B*, 81:447–457, 2005.

[42] Delmar photonics, 4119 Twilight Ridge, San Diego, CA 92130 USA. *Third-order cross-correlator MODEL Rincon 800-5 Instruction manual Version 2.3*, July 2008.

[43] N. Forget V. Bagnoud, J. D. Zuegel and C. Le Blanc. High-dynamic-range temporal measurements of short pulses amplified by opcpa. *Optics Express*, 15:5504–5511, 2007.

[44] Nguyen Xuan Truong. Setup and characterization of a high-dynamic-range third-order correlator for 1 khz laser system. Master's thesis, Friedrich-Schiller-Universitat Jena, 2004.

[45] J. A. Armstrong. Measurement of picosecond laser pulse widths. *Applied Physics Letters*, 10(1):16–18, 1967.

[46] Ian C. McMichael Jean-Claude M. Diels, Joel J. Fontaine and Francesco Simoni. Control and measurement of ultrashort pulse shapes (in amplitude and phase) with femtosecond accuracy. *Appl. Opt.*, 24:1270, 1985.

[47] H. Yamada K. Naganuma, K. Mogi. General method for ultrashort light pulse chirp measurement. *IEEE J. Quant. Electron.*, 25:1225, 1989.

[48] A. M. Weiner J. Chung. Ambiguity of ultrashort pulse shapes retrieved from the intensity autocorrelation and the power spectrum. *IEEE J. Select. Top. Quant. Electron.*, 7:656, 2001.

[49] M. Sheik-Bahae T. Hirayama. Real-time chirp diagnostic for ultrashort laser pulses. *Opt. Lett.*, 27:860, 2002.

[50] Wolfgang Rudolph Jean-Claude Diels. *Ultrashort laser pulse phenomena: fundamentals, techniques, and applications on a femtosecond time scale*. Academic Press, 1996.

[51] http://www.coherent.com/products/?731/Single Shot-Autocorrelator-SSA.

[52] International journal of swarm intelligence.

[53] An-Chun Tien Jerome Faure Daniel Kaplan Marcel Bouvier Takashi Buma Paul Van Rompay John Nees Peter P. Pronko Donald Umstadter Marc Nantel, Jiro Itatani and Gerard A. Mourou. Temporal contrast in ti:sapphire lasers: Characterization and control. *IEEE Journal of selected topics in Quantum Eletronics*, 4:449–458, 1998.

[54] H. Cheng G. Mourou D. Kopf I. D. Jung K. J. Weingarten A. Braun, J. V. Rudd and U. Keller. Characterization of short-pulse oscillators by means of a high-dynamic-range autocorrelation measurement. *Optics Letters*, 20:1889–1891, 1995.

[55] R.N. Gyuzalian J. Janszky, G. Corradi. On a possibility of analysing the temporal characteristics of short light pulses. *Optics Communications*, 23:293–298, 77.

[56] P A Naik P D Gupta M Raghuramaiah, A K Sharma and R A Ganeev. A second-order autocorrelator for single-shot measurement of femtosecond laser pulse durations. *Sadhana*, 26:603–611, 2001.

[57] R. Allott C. Danson J. Collier, C. Hernandez-Gomez and A. Hall. A single-shot third-order autocorrelator for pulse contrast and pulse shape measurements. *Laser and Particle Beams*, 19:231–235, 2001.

[58] Michael Gerrity. Single-shot third-order autocorrelator for measuring prepulses on ultrafast high intensity lasers. Department of Physics, University of Texas at Austin, May 2007.

[59] C. Haefner M. Shverdin M. Taranowski I. Jovanovic, C. Brown and C. P. J. Barty. High-dynamic-range, 200-ps window, single-shot crosscorrelator for ultrahigh intensity laser characterization. OSA JThD137, 2007. OSA 1-55752-834-9.

[60] Csaba Toth Catalin V. Filip and Wim P. Leemans. Optical cross-correlator based on supercontinuum generation. *Optics Express*, 14:2512–2519, 2006.

[61] J. Bromage C. Dorrer and J. D. Zuegel. High-dynamic-range, single-shot cross-correlator using a pulse replicator. In *CLEO/QELS*, 2008.

[62] Jake Bromage Christophe Dorrer and J. D. Zuegel. High-dynamic-range single-shot cross-correlator based on an optical pulse replicator. *Optics Express*, 16:13534–13544, 2008.

[63] A.V. Konyashchenko V.V. Lozhkarev G.A. Luchinin G.A. Lutsenko S.Yu. Mironov E.A. Khazanov I.V. Yakovlev V.N. Ginzburg, N.V. Didenko. Third-order correlator for measuring the time profile of petawatt laser pulses. *Quantum Electronics*, 38:1027–1032, 2008.

[64] Robert W. Boyd. *Nonlinear Optics*. Elsevier, 2008.

[65] V. I. Karpman and E. M. Krushkal. Modulated waves in nonlinear dispersive media. *Soviet Physics JETP*, 28:1969, 1969.

Bibliography

[66] Gilles Cheriaux. *Influences des distorsions de phase sur le profil d impulsions femtosecondes dans l amplification a derive de frequences.* PhD thesis, Universite Paris XI, 1997.

[67] Catherine Le Blanc. Principes et realisation d'une chaine laser femtoseconde haute intensite basee sur le saphir dope au titane. *Annales de Physique*, 1:1–157, 1994.

[68] V.M. Malkin Z. Toroker E.A. Khazanov A.M. Sergeev T. Tajima G.A. Mourou, N.J. Fisch and B. Le Garrec. Exawatt-zettawatt pulse generation and applications. *Optics Communications*, 285:720–724, 2012.

[69] Nicolas Forget. *Des amplificateurs laser aux amplificateurs parametriques : etudes de l'amplification parametrique a derive de frequence et du blocage de modes dans les oscillateurs parametriques optiques.* PhD thesis, Ecole polytechnique, 2005.

[70] Amandine Renault. *Etude et realisation de la pre-amplification d impulsions a derive de frequence par amplification parametrique optique.* PhD thesis, Ecole Polytechnique, 2006.

[71] Philip Kevin Bates. *Optical Parametric Chirped Pulse Amplification in the Few-Cycle Regime.* PhD thesis, Imperial College, University of London, 2007.

[72] I. Jovanovic. *Optical Parametric Amplification for High Peak and Average Power.* PhD thesis, University of California, Berkeley, 2001.

[73] J. Ducuing J. A. Armstrong, N. Bloembergen and P.S. Pershan. Interactions between light waves in a nonlinear dielectric. *Phys. Rev.*, 127:1918–1939, 1962.

[74] T. Fuji A. Baltuska and T. Kobayashi. Visible pulse compression to 4 fs by optical parametric amplification and programmable dispersion control. *Optics Letters*, 27:306–308, 2002.

[75] Alfred Cardew Dixon. *The elementary properties of the elliptic functions.* Macmillan and Co. and New York, 1894.

[76] Irene A. Stegun Milton Abramowitz, editor. *Handbook of Mathematical Functions: with Formulas, Graphs, and Mathematical Tables, pag.589-590.* Dover Books on Mathematics, 1972.

[77] G. Jonusauskas A. Dubietis and A. Piskarskas. Powerful femtosecond pulse generation by chirped and stretched pulse parametric amplification in a bbo crystal. *Optics Communications*, 88:437440, 1992.

[78] M. Towrie A. J. Langley J. L. Collier I. N. Ross, P.Matousek. The prospects for ultrashort pulse duration and ultrahigh intensity using optical parametric chirped pulse amplifiers. *Optics Communications*, 114:125 – 133, 1997.

[79] Yunpei Deng Xun Gu Hanieh Fattahi Thomas Metzger Marcus Ossiander Ferenc Krausz Alexander Schwarz, Moritz Ueffing and Reinhard Kienberger. Active stabilization for

optically synchronized optical parametric chirped pulse amplification. *Opt Express.*, 20:5557–5565, 2012.

[80] Franz Tavella. *Multiterawatt few-cycle pulse OPCPA for applications in high field physics.* PhD thesis, Ludwig-Maximilians Universitat, 2007.

[81] Alexandra Agra Amorim. *High-power and tuneable ultrashort laser pulses in the sub-two-cycle regime: towards novel light sources.* PhD thesis, Faculdade de Ciencias, Universidade do Porto, 2012.

[82] J. Limpert, F. Roser, D.N. Schimpf, E. Seise, T. Eidam, S. Hadrich, J. Rothhardt, C.J. Misas, and Andreas Tunnermann. High repetition rate gigawatt peak power fiber laser systems: Challenges, design, and experiment. *Selected Topics in Quantum Electronics, IEEE Journal of*, 15:159–169, 2009.

[83] S. Hadrich F.Roser J. Limpert A. Tunnermann D. N. Schimpf, D. Muller. High quality fiber cpa-system at a b-integral of 16. In *CLEO/QELS Conference: May 6-11*, 2007.

[84] A Frackiewicz M Galimberti S Hancock R Heathcote C Hernandez-Gomez P Holligan A Kidd IO Musgrave D Pepler W Shaikh TB Winstone, S Blake. Vulcan 10pw project : Design of the long pulse pump laser.

[85] G.A. Mourou, N.J. Fisch, V.M. Malkin, Z. Toroker, E.A. Khazanov, A.M. Sergeev, T. Tajima, and B. Le Garrec. Exawatt-zettawatt pulse generation and applications. *Optics Communications*, 285(5):720 – 724, 2012.

[86] Gerard A. Mourou, Toshiki Tajima, and Sergei V. Bulanov. Optics in the relativistic regime. *Rev. Mod. Phys.*, 78:309–371, Apr 2006.

[87] Giulio Cerullo and Sandro De Silvestri. Ultrafast optical parametric amplifiers. *Review of Scientific Instruments*, 74(1):1–18, 2003.

[88] R. Ell, U. Morgner, F. X. Kartner, J. G. Fujimoto, E. P. Ippen, V. Scheuer, G. Angelow, T. Tschudi, M. J. Lederer, A. Boiko, and B. Luther-Davies. Generation of 5-fs pulses and octave-spanning spectra directly from a ti:sapphire laser. *Opt. Lett.*, 26(6):373–375, Mar 2001.

[89] Stefan Rausch, Thomas Binhammer, Anne Harth, Jungwon Kim, Richard Ell, Franz X. Kartner, and Uwe Morgner. Controlled waveforms on the single-cycle scale from a femtosecond oscillator. *Opt. Express*, 16(13):9739–9745, Jun 2008.

[90] O. Albert and G. Mourou. Single optical cycle laser pulse in the visible and near-infrared spectral range. *Applied Physics B: Lasers and Optics*, 69:207–209, 1999. 10.1007/s003400050795.

[91] M. Wegener. *Extreme nonlinear optics - pag.18.* Springer, 2005.

[92] Helder Crespo. *Cascaded four-wave mixing processes and laser pulse generation in ultrafast nonlinear optics.* PhD thesis, Universidade Tecnica de Lisboa, Instituto Superior Tecnico, 2006.

[93] Franz X. Kartner. Ultrafast optics, mit open courseware, spring 2005.

[94] Thomas Brabec and Ferenc Krausz. Intense few-cycle laser fields: Frontiers of nonlinear optics. *Rev. Mod. Phys.*, 72:545–591, 2000.

[95] A. Bartels L. Robertsson M. Zucco R. S. Windeler-G.Wilpers C. Oates L. Hollberg S. A. Diddams L.-S. Ma, Z. Bi. Optical frequency synthesis and comparison with uncertainty at the 1e-19 level. *Science*, 303:1843–1845, 2004.

[96] D. C. Yost M. J. Martin A. Marcinkeviius M. E. Fermann T. R. Schibli, I. Hartl and J. Ye. Optical frequency comb with submillihertz linewidth and more than 10 w average power. *Nature Photonics*, 2:355–359, 2008.

[97] L. Dahlstram. Passive mode-locking and q-switching of high power lasers by means of the optical kerr effect. *Optics Communications*, 5(3):157 – 162, 1972.

[98] M. Richardson K. Sala and N. Isenor. Passive mode locking of lasers with the optical kerr effect modulator. *IEEE Journal of Quantum Electronics*, 13:915–924, 1977.

[99] E G Lariontsev and Vladimir N Serkin. Possibility of using self-focusing for increasing contrast and narrowing of ultrashort light pulses. *Soviet Journal of Quantum Electronics*, 5(7):796, 1975.

[100] P. F. Moulton. Spectroscopic and laser characteristics of ti:al2o3. *J. Opt. Soc. Am. B*, 3(1):125–133, Jan 1986.

[101] Milton Birnbaum and Alexander J. Pertica. Laser material characteristics of ti:al2o3. *J. Opt. Soc. Am. B*, 4(9):1434, Sep 1987.

[102] François Salin, Jeff Squier, and Michel Piche. Mode locking of ti:ai2o3 lasers and self-focusing: a gaussian approximation. *Opt. Lett.*, 16(21):1674–1676, Nov 1991.

[103] H. A. Haus and E. P. Ippen. Self-starting of passively mode-locked lasers. *Opt. Lett.*, 16(17):1331–1333, Sep 1991.

[104] Nobuhiko Sarukura, Yuzo Ishida, and Hidetoshi Nakano. Generation of 50-fsec pulses from a pulse-compressed, cw, passively mode-locked ti:sapphire laser. *Opt. Lett.*, 16(3):153–155, Feb 1991.

[105] Rudiger Paschotta. www.rp-photonics.com.

[106] Pedro Oliveira Rosa Weinegard Helder Crespo, Miguel Miranda. Broadband 5.9 fs ti:sapphire

laser characterized using the dispertion-scan technique. Optics Letters, To be submitted.

[107] G. Cerullo, S. De Silvestri, and V. Magni. Self-starting kerr-lens mode locking of a ti:sapphire laser. *Opt. Lett.*, 19(14):1040–1042, Jul 1994.

[108] Gary W. Pearson Czeslaw Radzewicz and Jerzy S. Krasinski. Use of zns as an additional highly nonlinear intracavity self-focusing element in a ti sapphire self-modelocked laser. *Optics Communications*, 102:464–468, 1993.

[109] Robert Szipöcs, Kárpát Ferencz, Christian Spielmann, and Ferenc Krausz. Chirped multilayer coatings for broadband dispersion control in femtosecond lasers. *Opt. Lett.*, 19(3):201–203, Feb 1994.

[110] A. Stingl, M. Lenzner, Ch. Spielmann, F. Krausz, and R. Szipöcs. Sub-10-fs mirror-dispersion-controlled ti:sapphire laser. *Opt. Lett.*, 20(6):602–604, Mar 1995.

[111] Michelle Y. Sander, Jonathan Birge, Andrew Benedick, Helder M. Crespo, and Franz X. Kärtner. Dynamics of dispersion managed octave-spanning titanium:sapphire lasers. *J. Opt. Soc. Am. B*, 26(4):743–749, Apr 2009.

[112] E.J Grace, A Ritsataki, P.M.W French, and G.H.C New. New optimization criteria for slit-apertured and gain-apertured klm all-solid-state lasers. *Optics Communications*, 183:249 – 264, 2000.

[113] Fabio Giambruno. *New perspectives in Ultrashort Laser Pulse Amplification*. PhD thesis, Palermo University, 2009.

[114] H. KOGELNIK and T. LI. Laser beams and resonators. *Appl. Opt.*, 5(10):1550–1567, Oct 1966.

[115] A. E. Siegman. *Lasers*. University Science Books, 1986.

[116] W. Koechner. Thermal lensing in a nd:yag laser rod. *Appl. Opt.*, 9(11):2548–2553, Nov 1970.

[117] M. E. Innocenzi, H. T. Yura, C. L. Fincher, and R. A. Fields. Thermal modeling of continuous-wave end-pumped solid-state lasers. *Applied Physics Letters*, 56(19):1831–1833, 1990.

[118] S. Ito, H. Nagaoka, T. Miura, K. Kobayashi, A. Endo, and K. Torizuka. Measurement of thermal lensing in a power amplifier of a terawatt ti:sapphire laser. *Applied Physics B: Lasers and Optics*, 74:343–347, 2002. 10.1007/s003400200812.

[119] H. P. Weber S . Merazzi C. Pfistner, R. Weber and R. Gruber. Thermal beam distortions in end-pumped nd: Yag, nd: Gsgg, and nd : Ylf rods. *IEEE Journal of Quantum Electronics*, 30:1605–1615, 1994.

[120] M. Sparks. Optical distortion by heated windows in high-power laser systems. *Journal of*

Applied Physics, 42(12):5029–5046, 1971.

[121] Shuzhen Fan, Xingyu Zhang, Qingpu Wang, Shutao Li, Shuanghong Ding, and Fufang Su. More precise determination of thermal lens focal length for end-pumped solid-state lasers. *Optics Communications*, 266:620 – 626, 2006.

[122] A. A. Andrade, T. Catunda, I. Bodnar, J. Mura, and M. L. Baesso. Thermal lens determination of the temperature coefficient of optical path length in optical materials. *Review of Scientific Instruments*, 74:877–880, 2003.

[123] H. Eilers, E. Strauss, and W. M. Yen. Photoelastic effect in ti^{3+}-doped sapphire. *Phys. Rev. B*, 45:9604–9610, May 1992.

[124] Wei Zheng and Gunter Lüpke. Photoelastic lensing effect in ti:sapphire crystal pumped by high-energy pulses. *Appl. Opt.*, 51(12):1945–1949, Apr 2012.

[125] J. Reintjes and M. B. Schulz. Photoelastic constants of selected ultrasonic delay-line crystals. *Journal of Applied Physics*, 39(11):5254–5258, 1968.

[126] Gerd Wagner, Max Shiler, and Volker Wulfmeyer. Simulations of thermal lensing of a ti:sapphire crystal end-pumped with high average power. *Opt. Express*, 13:8045–8055, 2005.

[127] SeongKu Lee TaeJun Yu IlWoo Choi JaeHee Sung, TaeMoon Jeong and Jongmin Lee. Analysis of thermal aberrations in the power amplifiers of a10-hz 100-tw ti:sapphire laser. *J. Korean Phys.Soc.*, 55:495–500, 2009.

[128] Mladen Franko and Chieu D. Tran. Analytical thermal lens instrumentation. *Review of Scientific Instruments*, 67(1):1–18, 1996.

[129] N. Rimington, S. Schieffer, W. Schroeder, and Brian Brickeen. Thermal lens shaping in brewster gain media: A high-power, diode-pumped nd:gdvo4 laser. *Opt. Express*, 12(7):1426–1436, Apr 2004.

[130] Vidya Ramanathan, Jinho Lee, Shengbo Xu, Xiaoming Wang, Luke Williams, William Malphurs, and D. H. Reitze. Analysis of thermal aberrations in a high average power single-stage ti:sapphire regenerative chirped pulse amplifier: Simulation and experiment. *Review of Scientific Instruments*, 77:103103, 2006.

[131] mt berlin. http://www.mt-berlin.com/.

[132] Ltd. Full Range Enterprise Co. http://www.chinasupply.net/optical/product/crystals/tisapphire.pdf.

[133] David M. Gaudiosi, Etienne Gagnon, Amy L. Lytle, Julie L. Fiore, Emily A. Gibson, Steve Kane, Jeff Squier, Margaret M. Murnane, Henry C. Kapteyn, Ralph Jimenez, and Sterling Backus. Multi-kilohertz repetition rate ti:sapphire amplifier based on down-chirped pulse amplification. *Opt. Express*, 14(20):9277–9283, Oct 2006.

[134] precision micro optics.

[135] M. Grinberg and A. Mandelis. Non-radiative fast processes and quantum efficiency of transition metal ions in soloids. *Journal of Luminescence*, 58:307 – 310, 1994.

[136] Jianping Zhou, Greg Taft, Chung-Po Huang, Margaret M. Murnane, Henry C. Kapteyn, and Ivan P. Christov. Pulse evolution in a broad-bandwidth ti:sapphire laser. *Opt. Lett.*, 19(15):1149–1151, Aug 1994.

[137] Yong Ho Cha Yong Joo Rhee Byoung Chul Lee Yong Woo Lee, Jong Hoon Yi and Byung Duk Yoo. Numerical analysis of soft-aperture kerr-lens mode locking in ti:sapphire laser cavities by using nonlinear abcd matrices. *Journal of the Korean Physical Society*, 46:1131–1136, 2005.

[138] Vadim I. Smirnov Leonid B. Glebov Andrey V. Okishev, Christophe Dorrer and Jonathan D. Zuegel. Spectral filtering in a diode-pumped nd:ylf regenerative amplifier using a volume bragg grating. *Optics Express*, 15:8197–8202, 2007.

[139] I. A. Begishev J. D. Zuegel V. I. Smirnov C. Dorrer, A. V. Okishev and L. B. Glebov. Optical parametric chirped-pulse-amplification contrast enhancement by regenerative pump spectral filtering. *Optics Letters*, 32:2378–2380, 2007.

[140] A. Offner. Unit power imaging catoptric anastigmat, 1973.

[141] F. Salin J. P. Chambaret Barry Walker G. Cheriaux, P. Rousseau and L. F. Dimauro. Aberration-free stretcher design for ultrashort-pulse amplification. *Optics Letters*, 21:414–416, 1996.

[142] T G Dubrovina M D Mikhailov E G Sall Aleksandr V Charukhchev V D Vinokurova, R R Gerke and V E Yashin. Metallised holographic diffraction gratings with the enhanced radiation resistance for laser pulse compression systems. *Quantum Electronics*, 35:569–572, 2005.

[143] J. H. Seldin and J. R. Fienup. Numerical investigation of the uniqueness of phase retrieval. *J. Opt. Soc. Am. A*, 7(3):412–427, Mar 1990.

[144] J. R. Fienup. Phase retrieval using boundary conditions. *J. Opt. Soc. Am. A*, 3(2):284–288, Feb 1986.

[145] Femtolasers. Femtolasers rainbow.

[146] M. S. Pshenichnikov D. A. Weirsma A. Baltuska, Z. Wei and R. Szipocs. All solid-state cavity dumped sub-5-fs laser. *Appl. Phys. B*, 65:175, 1997.

[147] E. I. Blount and J. R. Klaudder. Recovery of laser intensity from correlation data. *Journal of Applied Physics*, 40:2874–2875, 1969.

[148] S.T. Eng T. Andersson. Determination of the pulse response from intensity autocorrelation measurements of ultrashort laser pulses. *Opt. Comm.*, 47:288, 1983.

[149] et al. J. Peatross. Temporal decorrelation of short laser pulses. *J. Opt. Soc. Am. B*, 15:216, 1998.

[150] H. Yamada K. Naganuma, K. Mogi. General method for ultrashort light pulse chirp measurement. *IEEE J. Quant. Electron.*, 25:1225, 1989.

[151] Gerd Weigelt Adolf W. Lohmann and Bernhard Wirnitzer. Speckle masking in astronomy: triple correlation theory and applications. *Applied optics*, 22:4028–4037, 1983.

[152] R. Sauerbrey T. Feurer, S. Niedermeier. Measuring the temporal intensity of ultrashort laser pulses by triple correlation. *Appl. Phys. B*, 66:163–168, 1998.

[153] Gia-Wei Chern Kung-Hsuan Lin Chih-Jie Lee Yu-Chueh Hung Tzu-Ming Liu, Yin-Chieh Huang and Chi-Kuang Suna. Triple-optical autocorrelation for direct optical pulse-shape measurement. *Appl. Phys. Lett.*, 81:1402–1404, 2002.

[154] Gia-Wei Chern Kung-Hsuan Lin Yu-Chueh Hung Chih-Jie Lee Tzu-Ming Liu, Yin-Chieh Huang and Chi-Kuang Sun. Characterization of ultrashort optical pulses with third-harmonic-generation based triple autocorrelation. *IEEE Journal of Quantum Eletronics*, 38:1529–1535, 2002.

[155] I N Ross E J Divall. Construction and testing of an optical parametric amplifier correlator. Technical report, Central Laser Facility Annual Report, CCLRC Rutherford Appleton Laboratory, 2002/2003.

[156] I Ross E Divall. Design and construction of an optical parametric correlator (opac). Technical report, Central Laser Facility Annual Report, CCLRC Rutherford Appleton Laboratory, 2003/2004.

[157] Edwin J. Divall and Ian N. Ross. High dynamic range contrast measurements by use of an optical parametric amplifier correlator. *Optics Letters*, 29:2273–2275, 2004.

[158] V.I. Redkorechev J. Tummler P.V. Nickles G. Priebe, K.A. Janulewicz. Pulse shape measurement by a non-collinear third-order correlation technique. *Optics Communications*, 259:848–851, 2006.

[159] T. Shimada R.C. Shah, R.P. Johnsona and B.M. Hegelich. Large temporal window contrast measurement using optical parametric amplification and low-sensitivity detectors. *Eur. Phys. J. D*, 55:305–309, 2009.

[160] M. Horowitz Y. Barad, H. Eisenberg and Y. Silberberg. Nonlinear scanning laser microscopy by third harmonic generation. *Appl. Phys. Lett.*, 70:922–924, 1997.

[161] L. Sarger R. Barille, L. Canioni and G. Rivoire. Nonlinearity measurements of thin films by third-harmonic-generation microscopy. *Physical Review E*, 66:067602, 2002.

[162] Gary C. Bjorklund. Effects of focusing on third-order nonlinear processes in isotropic media. *IEEE J. Quant. Electron.*, 11:287, 1975.

[163] Thomas Y. F. Tsang. Optical third harmonic generation at the interfaces. *Physical Review A*, 52:4116–4125, 1995.

[164] I. Bugar F. Uherek E. E. Serebryannikov S. O. Konorov M. V. Alfimov D. Chorvat A. A. Ivanov, D. Lorenc and A. M. Zheltikov. Multimode anharmonic third-order harmonic generation in a photonic-crystal fiber. *Physical Review E*, 73:016610, 2006.

[165] A. Becker M. Scalora S. L. Chin N. Aközbek, A. Iwasaki and C.M. Bowden. Third-harmonic generation and self-channeling in air using high-power femtosecond laser pulses. *Physical Review Letters*, 89:143901, 2002.

[166] Rajesh Sreedharanpillai. *Third-Harmonic Generation from Isotropic and Anisotropic Media Using Focused Laser Beams*. PhD thesis, Universiteit van Amsterdam, 2007.

[167] Aurelie Jullien. *Generation D'impulsions Laser Ultra-breves et Ultra-intense a Contraste Temporel Eleve*. PhD thesis, Ecole Polytechnique, 2006.

[168] J. Stewart Aitchison Arkady Major, Fumiyo Yoshino and Peter W. E. Smith. Wide spectral range third-order autocorrelator based on ultrafast nonresonant nonlinear refraction. *Optics Letters*, 29:1945–1947, 2004.

[169] V. Kabelka and A.V. Masalov. Angularly resolved autocorrelation for single-shot time-frequency imaging of ultrashort light pulse. *Optics Communications*, 121:141 – 148, 1995.

[170] Amandine Renault, Frederika Auge-Rochereau, Thomas Planchon, Pascal D Oliveira, Thierry Auguste, Gilles Cheriaux, and Jean-Paul Chambaret. {ASE} contrast improvement with a non-linear filtering sagnac interferometer. *Optics Communications*, 248:535 – 541, 2005.

[171] L. Canova, M. Merano, A. Jullien, G. Cheriaux, R. Lopez Martens, O. Albert, N. Forget, S. Kourtev, N. Minkovski, and S.M. Saltiel. Coherent contrast improvement by cross-polarized wave generation. In *Lasers and Electro-Optics, 2007. CLEO 2007. Conference on*, pages 1–2, 2007.

[172] F.J. Harris. On the use of windows for harmonic analysis with the discrete fourier transform. *Proceedings of the IEEE*, 66(1):51–83, 1978.

[173] E. W. Van Stryland. J.-C. Diels and D. Gold. Investigation of the parameters affecting subpicosecond pulse durations in passively modelocked dye lasers. In Springer-Verlag, editor, *Picosecond phenomena*, page 117, Berlin, West Germany:, 1978.

[174] R. Morita K. Yamane, T. Kito and M. Yamashita. Experimental and theoretical demonstration of validity and limitations in fringe-resolved autocorrelation measurements for pulses of few optical cycles. *Optics Express*, 12:2762, 2004.

[175] C. E. Shannon. Communication in the presence of noise. *Classic paper in: Proc. IEEE*, 86:447, 1998.

[176] P. Oliveira J. L. Silva L. M. Bernardo F. X. Kärtner A. A. Amorim, M. V. Tognetti and H. M. Crespo. Sub-two-cycle pulses by soliton self-compression in highly nonlinear photonic crystal fibers. *Optics Letters*, 34:3851–3853, 2009.

[177] Andrius Baltuska Maxim S. Pshenichnikov Jinendra K. Ranka, Alexander L. Gaeta and Douwe A. Wiersma. Autocorrelation measurement of 6-fs pulses based on the two-photon-induced photocurrent in a gaasp photodiode. *Opt. Lett.*, 22:1344, 1997.

[178] J.M. Dudley L.P. Barry B. Thomsen D.T. Reid, W. Sibbett and J.D. Harvey. Commercial semiconductor devices for two photon absorption autocorrelation of ultrashort light pulses. *Applied Optics*, 37:8142, 1998.

[179] M. Sheik-Bahae. Femtosecond kerr-lens autocorrelation. *Opt. Lett.*, 22:399, 1997.

[180] Michael P. Hasselbeck Daniel A. Bender and Mansoor Sheik-Bahae. Sensitive ultrashort pulse chirp measurement. *Opt. Lett.*, 31:122, 2006.

[181] Daniel A. Bender and Mansoor Sheik-Bahae. Modified spectrum autointerferometric correlation (mosaic) for single-shot pulse characterization. *Opt. Lett.*, 32:2822, 2007.

[182] Prasad Anant Naik Avnish Kumar Sharma and Parshotam Dass Gupta. Simple and sensitive method for visual detection of temporal asymmetry of ultrashort laser pulses. *Opt. Express*, 12:1389, 2004.

[183] W. O. Saxton R. W. Gerchberg. A practical algorithm for the determination of the phase from image and diffraction plane pictures. *Optik*, 35:237, 1972.

[184] John P. Boyd. *Chebyshev and Fourier Spectral Methods*. DOVER Publications, 2000.

[185] Qun Zhao Jason Langley. Unwrapping magnetic resonance phase maps with chebyshev polynomials. *Magnetic Resonance Imaging*, 27:1293, 2009.

[186] J. A. Nelder and R. Mead. A simplex method for function minimization. *Computer Journal*, 7:308, 1965.

[187] Margaret H. Wright Jeffrey C. Lagarias, James A. Reeds and Paul E. Wright. Convergence properties of the nelder-mead simplex method in low dimensions. *SIAM J. Optim.*, 9:112, 1998.

[188] K.I.M. McKinnon. Convergence of the nelder-mead simplex method to a non-stationary point. *SIAM J. Optim.*, 9:148, 1998.

[189] Nils Aall Barricelli. Esempi numerici di processi di evoluzione. *Methodos*, -:45, 1954.

[190] N. A. Barricelli. Symbiogenetic evolution processes realized by artificial methods. *Methodos*, 9:152, 1957.

[191] Nils Aall Barricell. Numerical testing of evolution theories. *Journal of Statistical Computation and Simulation*, 1:97, 1972.

[192] George Box. Evolutionary operation: A method for increasing industrial productivity. *Applied Statistics*, 6:2:81, 1957.

[193] John Holland. *Adaptation in Natural and Artificial Systems: An Introductory Analysis with Applications to Biology, Control, and Artificial Intelligence*. University of Michigan Press, 1975.

[194] G. Rudolph. Convergence analysis of canonical genetic algorithms. *IEEE Trans. Neural Networks*, 5:1:96, 1994.

[195] D.B. Fogel. Asymptotic convergence properties of genetic algorithms and evolutionary programming. *Cybernetics and Systems*, 25:389, 1994.

[196] Nikolaus Hansen. *The CMA Evolution Strategy: A Tutorial*, April 2008.

[197] Randy L. Haupt. Optimum population size and mutation rate for a simple real genetic algorithm that optimizes array factors. In *Antennas and Propagation Society International Symposium, 2000. IEEE*, 2000.

[198] Jung Y. Huang Ching-Wei Chen and Ci-Ling Pan. Pulse retrieval from interferometric autocorrelation measurement by use of the population-split genetic algorithm. *Opt. Express*, 14:10930, 2006.

[199] Chang Hee Nam Kyung Han Hong, Yong Soo Leeb. Electric-field reconstruction of femtosecond laser pulses from interferometric autocorrelation using an evolutionary algorithm. *Opt. Comm.*, 271:169, 2007.

[200] James Strohaber Alexandre Kolomenski Hans Schuessler George Kattawar Wenlong Yang, Matthew Springer and Alexei Sokolov. Spectral phase retrieval from interferometric autocorrelation by a combination of graduated optimization and genetic algorithms. *Opt. Express*, 18:15028, 2010.

[201] P. Oliveira L. M. Bernardo F. X. Kartner H. Crespo A. A. Amorim, M. Tognetti. Experimental demonstration of sub-two-cycle soliton-effect pulse compression in a photonic crystal fiber. In *CLEO-EQEC 2009 Conference Digest*, 2009.

Bibliography

[202] Martin Schutz Thomas Back. Intelligent mutation rate control in canonical genetic algorithms. In *Foundation of Intelligent Systems 9th International Symposium, ISMIS '96*, 1996.

[203] Russell Eberhart James Kennedy. Particle swarm optimization. In *Proceedings of IEEE International Conference on Neural Networks. IV.*, page 1942, 1995.

[204] Rene Thomsen Jakob VesterstrÃž. A comparative study of differential evolution, particle swarm optimization, and evolutionary algorithms on numerical benchmark problems. In *Proc. IEEE congr. Evolutionary Computation*, page 1980, 2004.

[205] Magnus Erik and Hvass Pedersen. Good parameters for particle swarm optimization. Technical report, Hvass Laboratories, 2010.

[206] Jacques Riget and Jakob S. Vesterstrom. A diversity-guided particle swarm optimizer - the arpso. Technical report, EVALife Project Group, Department of Computer Science, Aarhus Universitet,, 2002.

[207] Riccardo Poli. An analysis of publications on particle swarm optimisation applications. Technical report, Department of Computer Science University of Essex, 2007.

[208] Harald Gerhardt Peter Simon and Sandor Szatmari. A single-shot autocorrelator for uv femtosecond pulses. *Meas. Sci. Technol.*, 1:637–639, 1990.

[209] Yu Oishi Pengqian Wang Keigo Nagasaka Katsutoshi Takatoi, Akira Suda and Katsumi Midorikawa. A single-shot transient-grating autocorrelator for the measurement of femtosecond laser pulses in the ultraviolet. *Japanese Journal of Applied Physics*, 43:993–996, 2004.

[210] E. T. J. Nibbering A. Kummrow M. Rini T. Elsaesser V. Kebbel H.-J. Hartmann R. Grunwald, U. Griebner and W. Juptner. Spatially resolved small-angle noncollinear interferometric autocorrelation of ultrashort pulses with microaxicon arrays. *J. Opt. Soc. Am. A*, 18:2923–2931, 2001.

[211] Nelson Lopes Goncalo Figueira, Luis Cardoso and Joao Wemans. Mirrorless single-shot tilted-pulse-front autocorrelator. *J. Opt. Soc. Am. B*, 22:2709–2714, 2005.

[212] Xun Gu Patrick O Shea, Mark Kimmel and Rick Trebino. Highly simplified device for ultrashort-pulse measurement. *Optics Letters*, 26:932–934, 2001.

[213] Christophe Dorrer Doug French and Igor Jovanovic. Two-beam spider for dual-pulse single-shot characterization. *Optics Letters*, 34:3415–3417, 2009.

[214] S. L. Chin F. Theberge, S. M. Sharifi and H. Schroder. Simple 3-d characterization of ultrashort laser pulses. *Optics Express*, 14:10125–10131, 2006.

[215] Pablo Gabolde. *Measurements of the Spatio-Temporal Profiles of Femtosecond Laser Pulses*. PhD thesis, Georgia Institute of Technology, 2007.

[216] Hans Sigg Daniel Erni Heinz Jackel Axel Murk Daniel Sutterlin, Volker Schlott. Spatial auto-correlation interferometer with single shot capbility using coherent transition radiation. In *Proceedings of DIPAC*, 2005.

[217] David Mendlovic Haldun M. Ozaktas. Fractional fourier transform as a tool for analyzing beam propagation and spherical mirror resonators. *Optics Letters*, 19:1678–1680, 1994.

[218] Marco V. Tognetti and Helder M. Crespo. Sub-two-cycle soliton-effect pulse compression at 800 nm in photonic crystal fibers. *J. Opt. Soc. Am. B*, 24(6):1410–1415, Jun 2007.

[219] C.E. Wayne T. Schafer. Propagation of ultra-short optical pulses in cubic nonlinear media. *Physica D*, 196:90–105, 2004.

[220] I. Chaperot E. Dauler S. Guerin G. Jaeger A. Muller A. Migdall N. Boeuf, D. Branning. Calculating characteristics of noncollinear phase matching in uniaxial and biaxial crystals. *Opt. Eng.*, 39:1016–1024, 2000.

[221] Joseph W. Goodman. *Introduction to Fourier Optics*. McGraw-Hill, 1996.

[222] Norman Morrison. *Introduction to Fourier Analysis*. Wiley-Interscience, 1994.

[223] Wolfgang Rudolph Jean-Claude Diels. *Ultrashort laser pulse phenomena: fundamentals, techniques, and applications on a femtosecond time scale*. Academic Press, 1996.

Appendices

A. Appendix for chapter 1

Fourier transform definition

As usual we define the Fourier transform of $f(\vec{r},t)$ as:

$$\mathscr{F}\{f(\vec{r},t)\}\left(\vec{k},\omega\right) = \int\int f(\vec{r},t)e^{i\left[\omega t - \vec{k}.\vec{r}\right]}d\vec{r}dt \qquad (A.1)$$

If we are only treating the temporal aspects of a function we get:

$$\mathscr{F}\{f(t)\}(\omega) = \int\int f(t)e^{i\omega t}dt \qquad (A.2)$$

On the SVE approximation

The SVE approximation used here is sometimes not enough to characterize the pulse evolution thoroughly, in this case we need to use the backward propagation and the second order derivative that we neglected in the when analyzing the propagation equation in linear media. In this case we have to had the term that is propagating backwards which we can incorporate into the equation using the following term:

However we note that the SVE approximation was used to simulate several ultrashort pulse oscillators that had a duration of $8\,fs$ inside the cavity ($800\,nm$ central wavelength) [33], or to simulate generation of sub-two-cycle laser pulses from PCF solitonic compression [218], work that has been confirmed experimentally [176].

It is rather obvious that we can have other approaches which are more correct to sub-two-cycles pulse propagation, in [219] T. Schäfer and C.E. Wayne create a short pulse equation appropriated to such pulses, in this case instead of dividing the electric (optical) field in an amplitude and a carrier wave, the field is decomposed in a different fields with several scales of pulse duration, the first order of this approximation is taken to constitute the short pulse equation, also in this model the refraction index is taken to be given by the formula $n = n_0 - a\lambda^2$. However the applicability of this equation for fields with more than 3 or 4 optical cycles is not known (or media which refraction index cannot be

reproduced by the formula above). In reality even for pulses which spectral shape and bandwidth that would allow a sub-two-cycle pulses, during propagation through a dispersive medium only locally the field would be short enough to require the use of the second order derivative to explain the pulse behavior, in other words only locally the pulse would be sub-two-cycle.

Normalizations

We use the auxiliary constants like:

$$
\begin{aligned}
\beta_0 &= \frac{\omega_1 \omega_2 \chi_{eff}^{(2)}}{2c^2 \sqrt{k_1 k_2}} \\
\beta_1 &= \frac{\omega_0 \omega_2 \chi_{eff}^{(2)}}{2c^2 \sqrt{k_0 k_2}} \\
\beta_2 &= \frac{\omega_1 \omega_0 \chi_{eff}^{(2)}}{2c^2 \sqrt{k_1 k_0}} \\
\Pi^2 &= \beta_0 \beta_1 \beta_2
\end{aligned}
\tag{A.3}
$$

Using these variables we may input them onto the coupled equations:

$$
\begin{aligned}
\frac{\partial A_0}{\partial z} &= i \left[\frac{\Pi}{\beta_0} \right]^2 A_1 A_2 \; e^{-i\Delta kz} \\
\frac{\partial A_1}{\partial z} &= i \left[\frac{\Pi}{\beta_1} \right]^2 A_0 \overline{A_2} \; e^{i\Delta kz} \\
\frac{\partial A_2}{\partial z} &= i \left[\frac{\Pi}{\beta_2} \right]^2 A_0 \overline{A_1} \; e^{i\Delta kz}
\end{aligned}
\tag{A.4}
$$

From here we get directly:

$$
\begin{aligned}
B_0 &= \beta_0 A_0 \\
B_1 &= \beta_1 A_1 \\
B_2 &= \beta_2 A_2
\end{aligned}
\tag{A.5}
$$

It is possible to transform B_0 to be $B_0 = \beta_0 A_0 \exp(i\Delta kz)$ to eliminate the phase-matching exponential.

Parametric equations resolutions

Low pump depletion:

Consider $|B_0|$ constant and the coupled equations in the following form:

$$
\begin{aligned}
\frac{\partial B_1}{\partial z} &= i \; B_0 \overline{B_2} \; \exp\left(-i\Delta kz\right) \\
\frac{\partial \overline{B_2}}{\partial z} &= -i \; \overline{B_0} B_1 \; \exp\left(i\Delta kz\right)
\end{aligned}
\tag{A.6}
$$

We expose the dependence in $\exp(-i\Delta kz)$ just to let B_0 independent on z, $B_0 = L_{NL}^{-1}$, however B_0 a free constant phase is indifferent for our problem. We make a variable shift to $b_{1,2} = B_{1,2} \exp\left(-i\frac{\Delta kz}{2}\right)$ and obtain a linear system that can be treated classically [64], with the initial conditions that $B_2(0) = 0, B_1(0) \neq 0, \frac{\partial B_1(0)}{\partial z} = 0, \frac{\partial B_2(0)}{\partial z} = i\ B_0\overline{B}_1(0)$ we get:

$$\frac{\partial}{\partial z}\begin{bmatrix} b_1 \\ b_2 \end{bmatrix} = i\begin{bmatrix} -\frac{\Delta k}{2} & L_{NL}^{-1} \\ L_{NL}^{-1} & \frac{\Delta k}{2} \end{bmatrix}\begin{bmatrix} b_1 \\ b_2 \end{bmatrix} \tag{A.7}$$

With this we get a propagation factor $\gamma = \sqrt{L_{NL}^{-2} - \left(\frac{\Delta k}{2}\right)}$ and a solution like:

$$B_1(z) = B_1(0)\left[\cosh(\gamma z) + i\frac{\Delta k}{2\gamma}\sinh(\gamma z)\right]e^{i\frac{\Delta kz}{2}}$$
$$B_2(z) = i\overline{B}_1(0)\frac{\Delta k}{2\gamma}\sinh(\gamma z)e^{i\frac{\Delta kz}{2}} \tag{A.8}$$

Resolution of the coupled equations

$$\frac{\partial B_0}{\partial z} = i\ B_1 B_2\ \exp(-i\Delta kz)$$
$$\frac{\partial B_1}{\partial z} = i\ B_0\overline{B}_2\ \exp(i\Delta kz)$$
$$\frac{\partial B_2}{\partial z} = i\ B_0\overline{B}_1\ \exp(i\Delta kz) \tag{A.9}$$

This resolution by several authors since it's first resolution by Armstrong et al. [73]. The Manley-Rowe relations can be done by writing the derivative equations $\frac{\partial |B_i|^2}{\partial z}$, and we obtain:

$$\frac{\partial |B_0|^2}{\partial z} = 2|B_0||B_1||B_2|\sin(\Theta)$$
$$\frac{\partial |B_1|^2}{\partial z} = -2|B_0||B_1||B_2|\sin(\Theta)$$
$$\frac{\partial |B_2|^2}{\partial z} = -2|B_0||B_1||B_2|\sin(\Theta) \tag{A.10}$$

where $\Theta = \phi_0 - \phi_1 - \phi_2 + \Delta kz$. From this we get three propagation constants:

$$m_0 = |B_1|^2 - |B_2|^2$$
$$m_1 = |B_0|^2 + |B_2|^2$$
$$m_2 = |B_0|^2 + |B_1|^2 \tag{A.11}$$

The last constant will be deduced from the propagation equation of the field phases:

$$\frac{\partial \phi_0}{\partial z} = \frac{|B_1||B_2|}{|B_0|}\cos(\Theta)$$
$$\frac{\partial \phi_1}{\partial z} = \frac{|B_0||B_2|}{|B_1|}\cos(\Theta)$$
$$\frac{\partial \phi_2}{\partial z} = \frac{|B_0||B_1|}{|B_2|}\cos(\Theta) \tag{A.12}$$

A. Appendix for chapter 1

The derivative of Θ is going to be given by:

$$\frac{\partial \Theta}{\partial z} = \left[\frac{|B_1||B_2|}{|B_0|} - \frac{|B_0||B_2|}{|B_1|} - \frac{|B_0||B_1|}{|B_2|} \right] \cos(\Theta) + \Delta k \qquad (A.13)$$

which using the absolute field propagation equations:

$$\begin{aligned}
\frac{\partial \Theta}{\partial z} &= \left[\frac{1}{|B_0|} \frac{\partial |B_0|}{\partial z} + \frac{1}{|B_1|} \frac{\partial |B_1|}{\partial z} + \frac{1}{|B_2|} \frac{\partial |B_2|}{\partial z} \right] \cot(\Theta) + \Delta k \\
&- \frac{\partial \ln(\cos \Theta)}{\partial z} = \left[\frac{\partial \ln(|B_0||B_1||B_2|)}{\partial z} \right] + \Delta k \tan(\Theta) \\
\left[\frac{\partial \ln(|B_0||B_1||B_2|\cos \Theta)}{\partial z} \right] &+ \Delta k \frac{\partial |B_0|^2}{\partial z} \frac{1}{2|B_0||B_1||B_2|\cos \Theta} = 0 \\
\frac{\partial}{\partial z} \left[|B_0||B_1||B_2| \cos \Theta + \tfrac{\Delta k}{2} |B_0|^2 \right] &= 0
\end{aligned} \qquad (A.14)$$

And so the constants arise:

$$\begin{aligned}
\Gamma_0 &= |B_0||B_1||B_2| \cos \Theta + \tfrac{\Delta k}{2} |B_0|^2 \\
\Gamma_1 &= |B_0||B_1||B_2| \cos \Theta - \tfrac{\Delta k}{2} |B_1|^2 \\
\Gamma_2 &= |B_0||B_1||B_2| \cos \Theta - \tfrac{\Delta k}{2} |B_2|^2
\end{aligned} \qquad (A.15)$$

No idler input and no phase mismatch

Let us imagine that the longest wavelength is not inputted in the nonlinear medium, in this case the phase matching is calculated as seen in Sub-Sec. (1.5.1). If the amplitude B_2 is zero, $\Gamma_2 = 0$, $\Gamma_0 = -\frac{\Delta k}{2} |B_0(0)|^2$, if the phase matching is perfect we obtain $\Gamma_i = 0\, i = 0, 1, 2$ the resulting equations become:

$$\begin{aligned}
\left(\frac{\partial |B_0|}{\partial z} \right)^2 &= (m_2 - |B_0|^2)(m_1 - |B_0|^2) \\
\left(\frac{\partial |B_1|}{\partial z} \right)^2 &= (m_2 - |B_1|^2)(|B_1|^2 - m_0) \\
\left(\frac{\partial |B_2|}{\partial z} \right)^2 &= (m_1 - |B_2|^2)(m_0 + |B_2|^2)
\end{aligned} \qquad (A.16)$$

The resolution of the amplitude evolution equations using the constants above $\Gamma_2 = \Gamma_1 = \Gamma_0 = 0$, which results in $\cos \Theta = 0$ for any $|B_2| \neq 0$, this is the same to say that the B_2 beam is created in such a way that $\Theta = \pi/2$. The equations above transform themselves in:

$$\begin{aligned}
\left(\frac{\partial |B_0|}{\partial z} \right)^2 &= (m_2 - |B_0|^2)(m_1 - |B_0|^2) \\
\left(\frac{\partial |B_1|}{\partial z} \right)^2 &= (m_2 - |B_1|^2)(|B_1|^2 - m_0) \\
\left(\frac{\partial |B_2|}{\partial z} \right)^2 &= (m_1 - |B_2|^2)(m_0 + |B_2|^2)
\end{aligned} \qquad (A.17)$$

The first equation we may use it to obtain ($y^2 = \frac{|B_0|^2}{m_1}$):

$$\left(\frac{\partial |B_0|}{\partial z}\right)^2 = (m_2 - |B_0|^2)(m_1 - |B_0|^2)$$
$$\left(\frac{\partial y}{\partial \sqrt{m_2} z}\right)^2 = (1 - y^2)(1 - \frac{m_1}{m_2} y^2) \tag{A.18}$$
$$y = sn(\sqrt{m_2}(z - z_0)|\frac{m_1}{m_2})$$

by the definition of Jacobi sine *sn*. We obtain the other amplitudes simply using the definition of the Manley Morley constants.

$|B_1|^2 = m_2 - |B_0|^2$ and $|B_2|^2 = m_1 - |B_0|^2$. The amplitude can also be solved using the B_2 evolution equation.

$$\left(\frac{\partial |B_2|}{\partial z}\right)^2 = (m_1 - |B_2|^2)(m_2 - m_1 + |B_2|^2)$$
$$\left(\frac{\partial |B_2|}{\partial z}\right)^2 = m_1 m_2 (1 - \frac{|B_2|^2}{m_1})(1 - \frac{m_1}{m_2} + \frac{1}{m_2}|B_2|^2) \tag{A.19}$$
$$\left(\frac{\partial y}{\partial \sqrt{m_2} z}\right)^2 = (1 - y^2)(1 - \frac{m_1}{m_2} + \frac{m_1}{m_2} y^2)$$
$$y = cn(\sqrt{m_2}(z - z_0)|\frac{m_1}{m_2})$$

by definition of Jacobi cosine, *cn*.

$$|B_0| = |B_0(0)||sn(\frac{|B_0(0)|}{\sqrt{\gamma}} z - K(\gamma)|\gamma)|$$
$$|B_1| = |B_0(0)|\sqrt{\delta + cn^2(\frac{|B_0(0)|}{\sqrt{\gamma}} z - K(\gamma)|\gamma)}$$
$$|B_2| = |B_0(0)||cn(\frac{|B_0(0)|}{\sqrt{\gamma}} z - K(\gamma)|\gamma)| \tag{A.20}$$
$$\delta = \left|\frac{B_1(0)}{B_0(0)}\right|^2$$
$$\gamma = \frac{1}{1+\delta}$$

Where *sn* and *cn* are sinus and co-sinus Jacobi elliptical functions. We notice that for $|B_1| \ll |B_0|$, $\frac{m_2}{m_1} \simeq 1$, the elliptic functions transform themselves in tanh and *sech* for *sn* and *cn* correspondingly. However if we apply this approximations blindly we get a problem concerning the initial value because $K(1) \to \infty$.

In fact, using $\frac{m_2}{m_1} = 1$, we obtain $B_1(0) = 0$, only one beam exists, we are in a situation where the production of photons at λ_1, λ_2 can only be done by parametric fluorescence [220]. We may give approximate values for the amplitudes when we are working with small δ values, however beware that $K(\gamma)$ (or its inverse) cannot be approximated by a Taylor series around one. We will calculate it's values and obtain:

$$|B_0| = |B_0(0)||\tanh(\frac{|B_0(0)|}{\sqrt{\gamma}}z - K(\gamma)) + \alpha|$$
$$|B_1| = |B_0(0)|\sqrt{\delta + \sec h^2(\frac{|B_0(0)|}{\sqrt{\gamma}}z - K(\gamma)) + \beta}$$
$$|B_2| = |B_0(0)||\sec h(\frac{|B_0(0)|}{\sqrt{\gamma}}z - K(\gamma)) + \eta| \qquad (A.21)$$
$$\alpha = \tanh(K(\gamma)) + 1$$
$$\beta = -\sec h^2(K(\gamma))$$
$$\eta = -\sec h(K(\gamma))$$

Notice that $[\alpha - 1, \beta, \eta] \to [0, 0, 0]$ for $\gamma \to 1$ and so this terms can be negligible. If we have $\gamma \to 0$ the Jacobi sinus and co-sinus would be transformed in simple sin and cos functions, for big values of δ the amplitudes will evolve as sin and cos functions. From the expressions above we obtain a new nonlinear length that is given by:

$$L_{NL}^{(b)} = \frac{\sqrt{\gamma}}{|B_0|} = \frac{1}{\sqrt{|B_0(0)|^2 + |B_1(0)|^2}} \qquad (A.22)$$

This nonlinear length is a small correction to the expressions given in Sec. (1.2) .

The fields phases can also be evaluated using:

$$\frac{\partial \phi_0}{\partial z} = \frac{|B_1||B_2|}{|B_0|}\cos(\Theta)$$
$$\frac{\partial \phi_1}{\partial z} = \frac{|B_0||B_2|}{|B_1|}\cos(\Theta) \qquad (A.23)$$
$$\frac{\partial \phi_2}{\partial z} = \frac{|B_0||B_1|}{|B_2|}\cos(\Theta)$$

From Eq. (1.25) we see that, if in the initial conditions we have no idler (the idler is only created due to the TWM) and no phase mismatch every Γ_i is null. Moreover, from Eq. (A.20) makes clear that in general $|B_0|, |B_1|, |B_2|$ are different from zero, which means that $\cos(\Theta) = 0$.

The three phases will be constant and its difference will also be constant $\phi_0 - \phi_1 - \phi_2 = \pi/2$, this is considering that the idler wave is created by the propagation. However, if we have three waves at the input, no phase mismatch and the phase difference between beams is $\pi/2$, Γ_i will also be equal to zero and $\phi_0 - \phi_1 - \phi_2 = \pi/2$.

In Fig. (A.1) we notice that when δ increases the evolution looks like a sinus function. We need to realize that amplitude square is not the same as the intensity. In order to evaluate the intensity and therefore the energy of the beams, we have to calculate quantum efficiency for each beam (λ_1/λ_0 or λ_2/λ_0), which is not accounted for in these pictures.
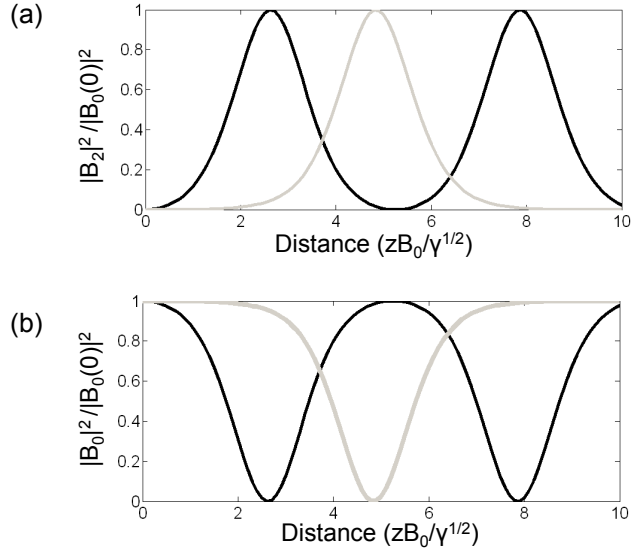
Figure A.1.: Evolution of the idler amplitude square (a) when $\delta = 0.1$ (black line) and $\delta = 1e-3$ (gray line). (b) Evolution of the pump amplitude square for the same conditions.
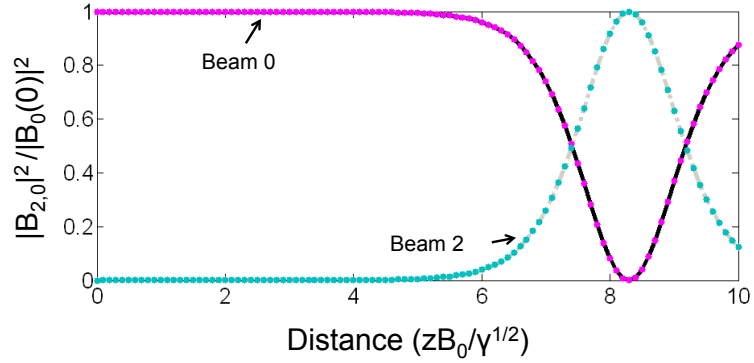

Figure A.2.: Evolution of the idler amplitude square (gray line starting at zero) and for the pump amplitude square (black line starting at 1) compared with the approximations to the hyperbolic functions given by the points, magenta for the pump and turquoise for the idler.

No idler input When we have some phase-mismatch however, only $\Gamma_2 = 0$. We use the amplitude evolution equation for B_2

$$\left(\frac{\partial |B_2|}{\partial z}\right)^2 = (m_1 - |B_2|^2)(m_0 + |B_2|^2) - \left(\frac{\Delta k}{2}\right)^2 |B_2|^2$$

$$\left(\frac{\partial |B_2|}{\partial z}\right)^2 = (\gamma \gamma_1 - |B_2|^2)(\gamma \gamma_2 + |B_2|^2) \tag{A.24}$$

To make this step we may solve the equation in x $(m_1 - x)(m_0 + x) - \left(\frac{\Delta k}{2}\right)^2 x = 0$

$$\gamma\gamma_1 = \frac{m_1 - m_0 - \left(\frac{\Delta k}{2}\right)^2}{2} + \sqrt{\left(\frac{m_1 - m_0 - \left(\frac{\Delta k}{2}\right)^2}{2}\right)^2 + m_1 m_0}$$

$$\gamma\gamma_2 = -\frac{m_1 - m_0 - \left(\frac{\Delta k}{2}\right)^2}{2} + \sqrt{\left(\frac{m_1 - m_0 - \left(\frac{\Delta k}{2}\right)^2}{2}\right)^2 + m_1 m_0} \tag{A.25}$$

We have the same resolution has above, with: $y^2 = \frac{|B_2|^2}{\gamma\gamma_1}$:

$$\left(\frac{\partial |B_2|}{\partial z}\right)^2 = \gamma\gamma_1(\gamma\gamma_2 + \gamma\gamma_1)(1 - y^2)\left(1 - \frac{\gamma\gamma_1}{\gamma\gamma_2 + \gamma\gamma_1} + \frac{\gamma\gamma_1}{\gamma\gamma_2 + \gamma\gamma_1}y^2\right)$$

$$y = cn\left(\alpha(z - z_0)\left|\frac{\gamma\gamma_1}{\gamma\gamma_2 + \gamma\gamma_1}\right.\right)$$

$$\alpha = \sqrt{(\gamma\gamma_2 + \gamma\gamma_1)} \tag{A.26}$$

We may use Eq. (A.11) to obtain the B_1 and B_0 equations.

General case

In a general case we have to be aware that the coefficients used can originate complex values that are not easy to quantify. However we will give the general solution of the propagation equations. The solution to this problem are given without any considerations on the features of the pulses' evolution, because this will be highly dependent on the TWM initial values. The Jacobi elliptical function can be similar to sinusoidal functions or hyperbolic functions, and in general Jacobi function can have quite different behaviors.

Using a phase mismatch and a nonzero Γ_i constant the evolution equation of $|B_0|^2$ becomes (the derivative of $|B_1|^2$ and $|B_2|^2$ is symmetric) :

$$\left(\frac{\partial |B_0|^2}{\partial z}\right)^2 = 2|B_0|^2(m_2 - |B_0|^2)(m_1 - |B_0|^2) - 2(\Gamma_0 - \tfrac{\Delta k}{2}|B_0|^2)^2 \tag{A.27}$$

This can be rewritten as:

$$\tfrac{1}{2}\left(\frac{\partial Z}{\partial z}\right)^2 = (Z - Z_0)(Z - Z_1)(Z - Z_2) \tag{A.28}$$

Where $Z = |B_0|^2$. In order to go from Eq. (A.27) to Eq. (A.35), we have to obtain the roots of the expression in Eq. (A.27).

With the polynomial equation given by:

$$Z^3 - bZ^2 + cZ - \Gamma_0^2 = 0 \tag{A.29}$$

The second and third coefficients of the third order equation can be given by:

$$b = \left(m_1 + m_2 - \frac{\Delta k^2}{4} \right)$$
$$c = m_1 m_2 + \Delta k \Gamma_0 \tag{A.30}$$

We can obtain three real roots only if $\Delta > 0$. Where Δ is given by:

$$\Delta = 18bc\Gamma_0^2 - 4b^3\Gamma_0^2 + b^2 c^2 \tag{A.31}$$

If $\Delta = 0$, the polynomial has multiple roots, in which case it is very easy to obtain the evolution equations. Considering that we have multiple real roots[1] in Eq. (A.35) are given by:

$$Z_0 = \frac{b}{3} - \frac{1}{3}\left[\sqrt[3]{\frac{1}{2}[q+p]} + \sqrt[3]{\frac{1}{2}[q-p]} \right]$$
$$Z_1 = \frac{b}{3} + \frac{1+i\sqrt{3}}{6}\sqrt[3]{\frac{1}{2}[q+p]} + \frac{1-i\sqrt{3}}{6}\sqrt[3]{\frac{1}{2}[q-p]} \tag{A.32}$$
$$Z_2 = \frac{b}{3} + \frac{1-i\sqrt{3}}{6}\sqrt[3]{\frac{1}{2}[q+p]} + \frac{1+i\sqrt{3}}{6}\sqrt[3]{\frac{1}{2}[q-p]}$$

Where:

$$q = 9bc - 2b^3 - 27\Gamma_0^2$$
$$p = \sqrt{q^2 - 4(b^2 - 3c)^3} \tag{A.33}$$

After this we transform Eq. (A.35) with the following variable transform:

$$y^2 = \frac{Z - Z_0}{Z_1 - Z_0}$$
$$m = \frac{Z_1 - Z_0}{Z_2 - Z_0} \tag{A.34}$$

Obtaining:

$$\frac{1}{2}\left(\frac{\partial y}{\partial \sqrt{Z_2 - Z_0}z} \right)^2 = (1 - y^2)(1 - my^2) \tag{A.35}$$

Which give automatically that:

$$y = sn\left(\sqrt{Z_2 - Z_0}(z - z_0)|m \right) \tag{A.36}$$

Or for the fields square amplitude:

---

[1]In reality if the roots are not real the calculations stay the same but the Jacobi sinusoidal function will have complex arguments.

$$|B_0|^2 = Z_0 + (Z_1 - Z_0)\, sn^2\left(\sqrt{Z_2 - Z_0}(z - z_0)|m\right)$$
$$|B_1|^2 = m_2 - Z_0 - (Z_1 - Z_0)\, sn^2\left(\sqrt{Z_2 - Z_0}(z - z_0)|m\right) \quad\quad \text{(A.37)}$$
$$|B_2|^2 = m_1 - Z_0 - (Z_1 - Z_0)\, sn^2\left(\sqrt{Z_2 - Z_0}(z - z_0)|m\right)$$

The initial value can be determined by:

$$z_0 = -\frac{1}{\sqrt{Z_2 - Z_0}} F\left(\sqrt{\frac{|B_0|^2 - Z_0}{Z_1 - Z_0}}\,\bigg|\, m\right) \quad\quad \text{(A.38)}$$

Where $F(u|m)$ is the first order incomplete integral. The phase of the pulses is governed by the equations:

$$\frac{\partial \phi_0}{\partial z} = \frac{\Gamma_0}{|B_0|^2} - \frac{\Delta k}{2}$$
$$\frac{\partial \phi_1}{\partial z} = \frac{\Gamma_1}{|B_1|^2} - \frac{\Delta k}{2} \quad\quad \text{(A.39)}$$
$$\frac{\partial \phi_2}{\partial z} = \frac{\Gamma_2}{|B_2|^2} - \frac{\Delta k}{2}$$

Which results in:

$$\phi_0 = -\frac{\Delta k}{2} z + \frac{\Gamma_0}{Z_0 \sqrt{Z_2 - Z_0}} \Pi\left(1 - \frac{Z_1}{Z_0}; am(\sqrt{Z_2 - Z_0}(z - z_0|m)|m\right)$$
$$\phi_1 = \frac{\Delta k}{2} z + \frac{\Gamma_1}{(m_2 - Z_0)\sqrt{Z_2 - Z_0}} \Pi\left(\frac{Z_1 - Z_0}{m_2 - Z_0}; am(\sqrt{Z_2 - Z_0}(z - z_0|m)|m\right) \quad\quad \text{(A.40)}$$
$$\phi_2 = \frac{\Delta k}{2} z + \frac{\Gamma_1}{(m_1 - Z_0)\sqrt{Z_2 - Z_0}} \Pi\left(\frac{Z_1 - Z_0}{m_1 - Z_0}; am(\sqrt{Z_2 - Z_0}(z - z_0|m)|m\right)$$

B. Appendix for chapter 2

First oscillator data

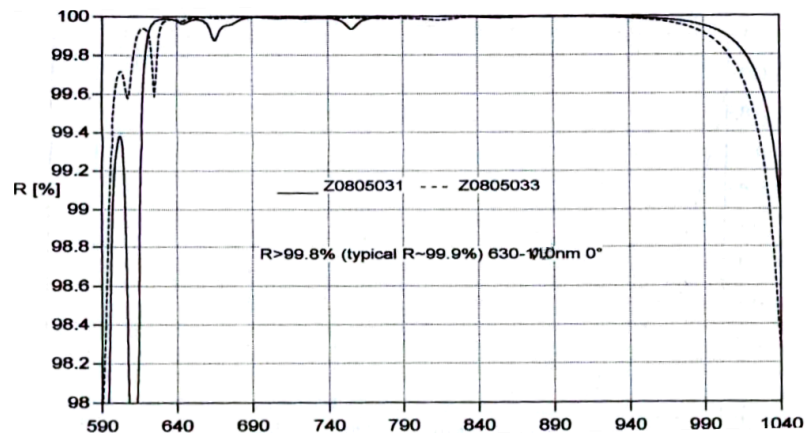The curved mirrors of the sub-cavity values of reflectance and GDD:

Figure B.1.: Reflectivity curves for the curved mirrors inside the cavity as a function of the wavelength, MC1 (Z0805033) and MC2 (Z0805031).
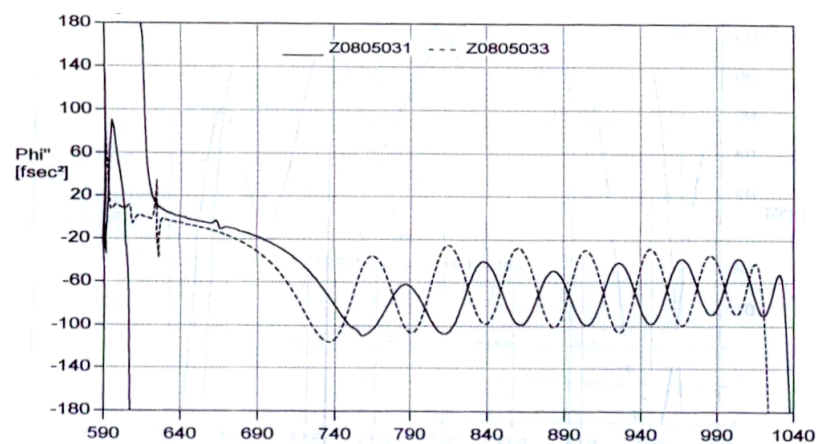

Figure B.2.: Second derivative of the spectral phase variation with the wavelength in nanometers, MC1 (Z0805033) and MC2 (Z0805031).
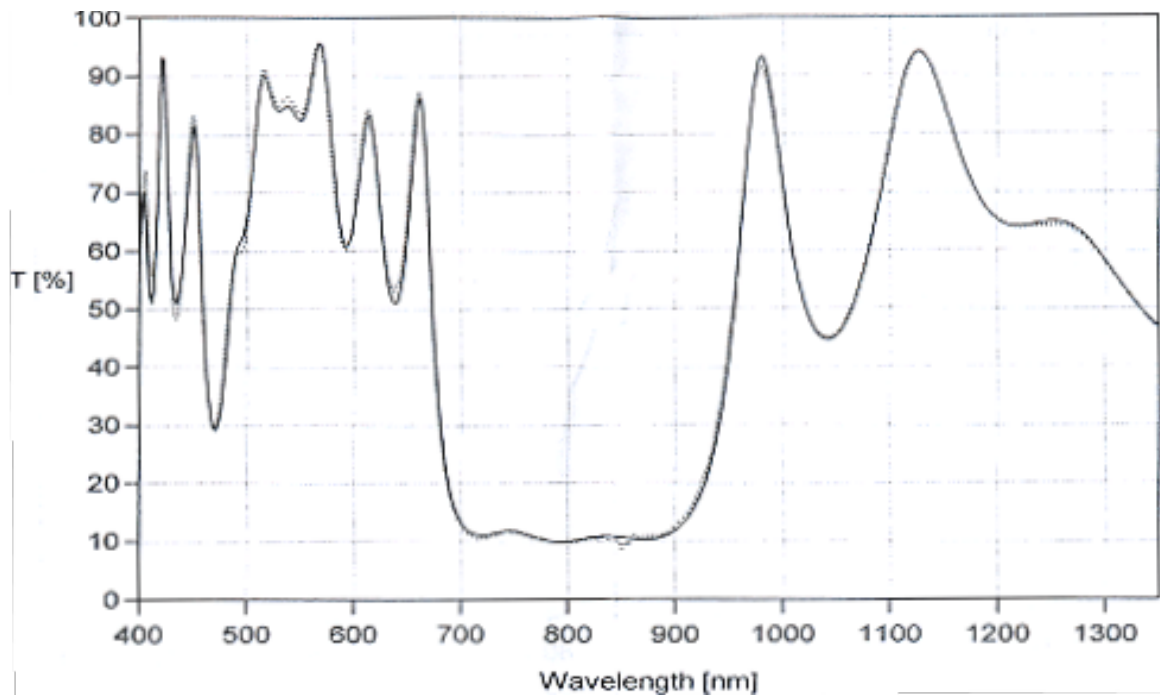
The transmission and GDD curve of the output coupler:

Figure B.3.: Output coupler transmission coefficients.
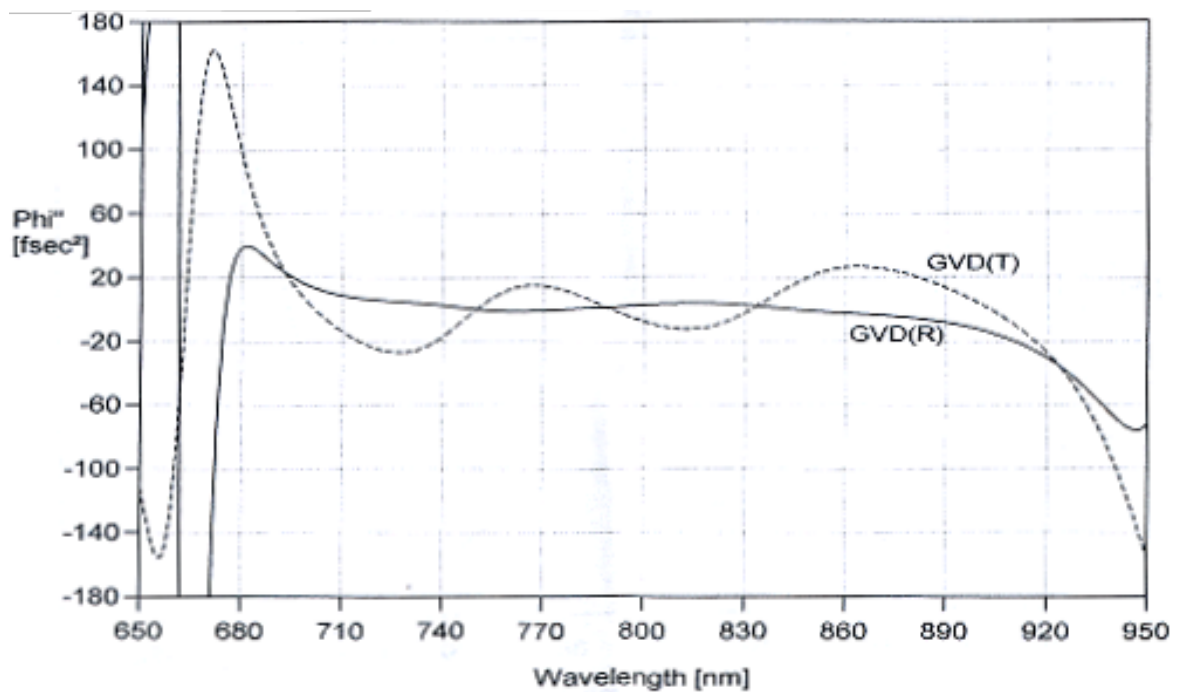
Figure B.4.: GDD values introduced by the output coupler, for the transmitted beam GVD(T) and for the reflected one GVD(R).

254

The data for the Z mirrors on the side of the output coupler:
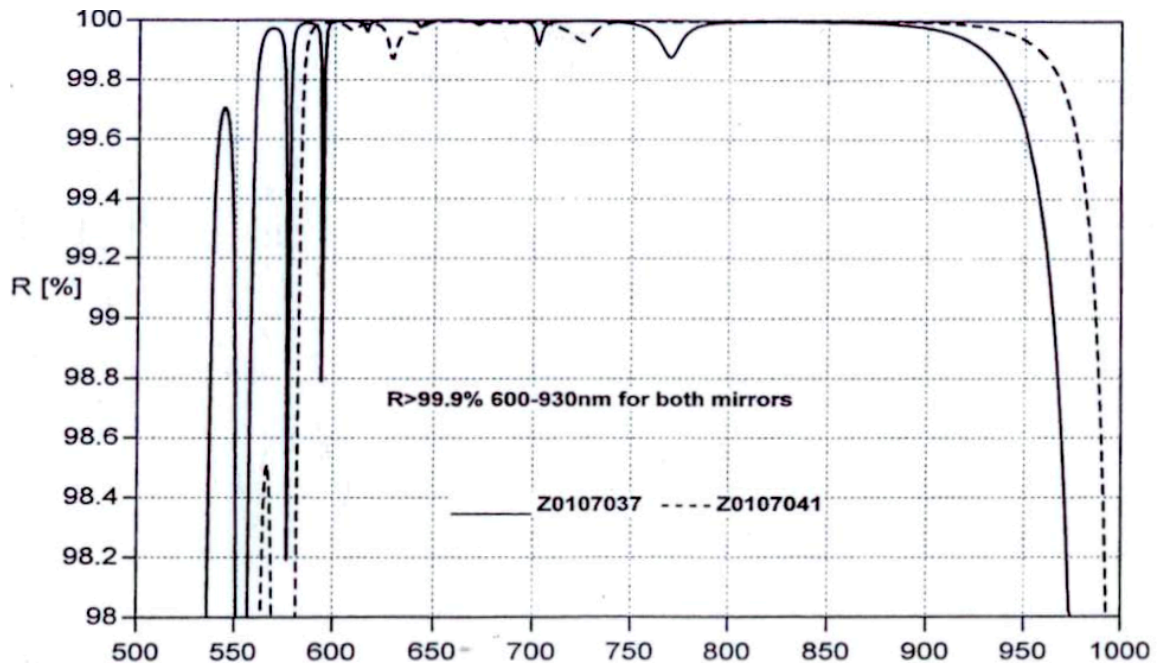
Figure B.5.: Zero degree incidence reflective coefficients, for M1 (Z0102037) and M2 (Z0102041).
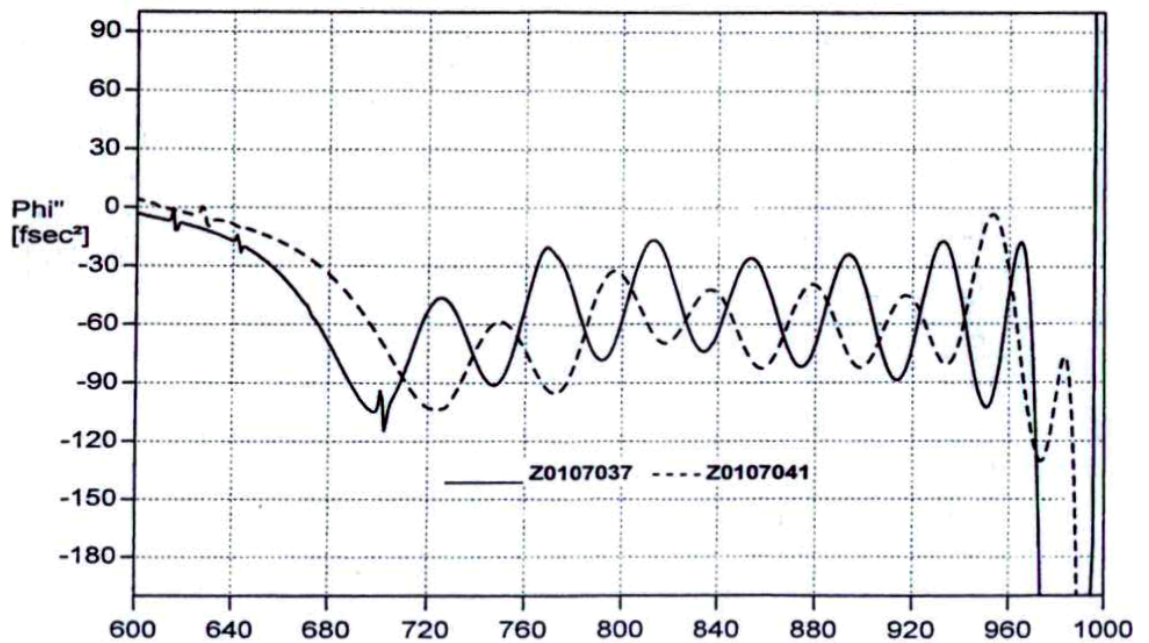

Figure B.6.: GDD values introduced by the output coupler, for the transmitted beam GVD(T) and for the reflected one GVD(R). M1 (Z0102037) and M2 (Z0102041).

B. Appendix for chapter 2

For the mirrors on big arm that has the prisms, we have the reflectance for 0° incidence and 10°
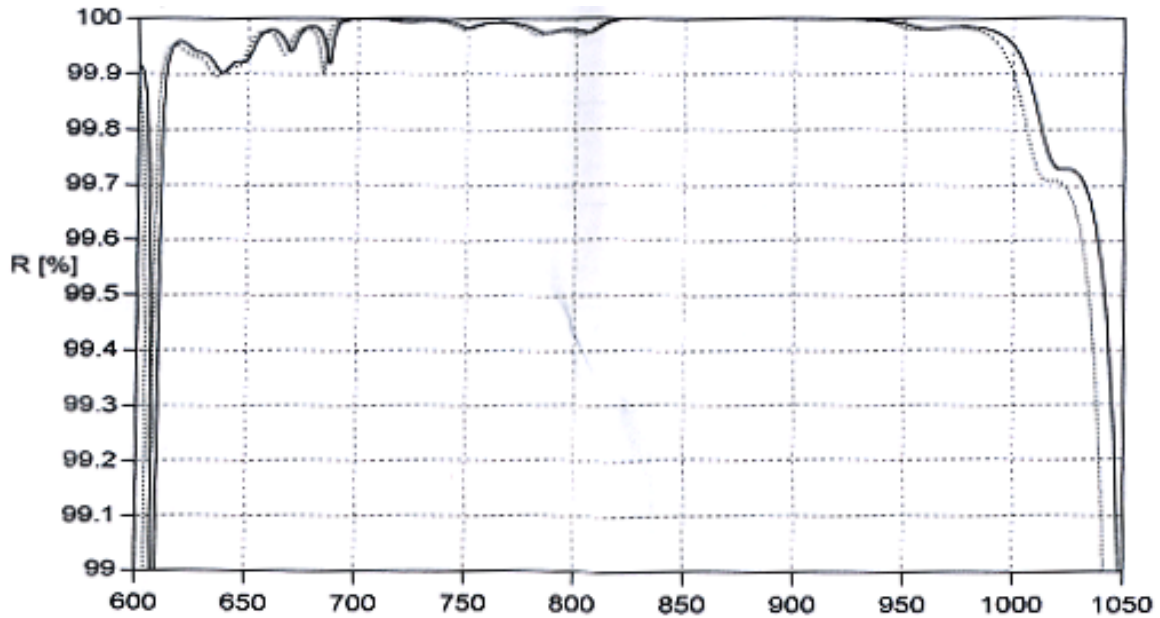incidence:

Figure B.7.: Reflective coefficient for the back-end mirror M4 (G0304008). The continuous line is at 0°
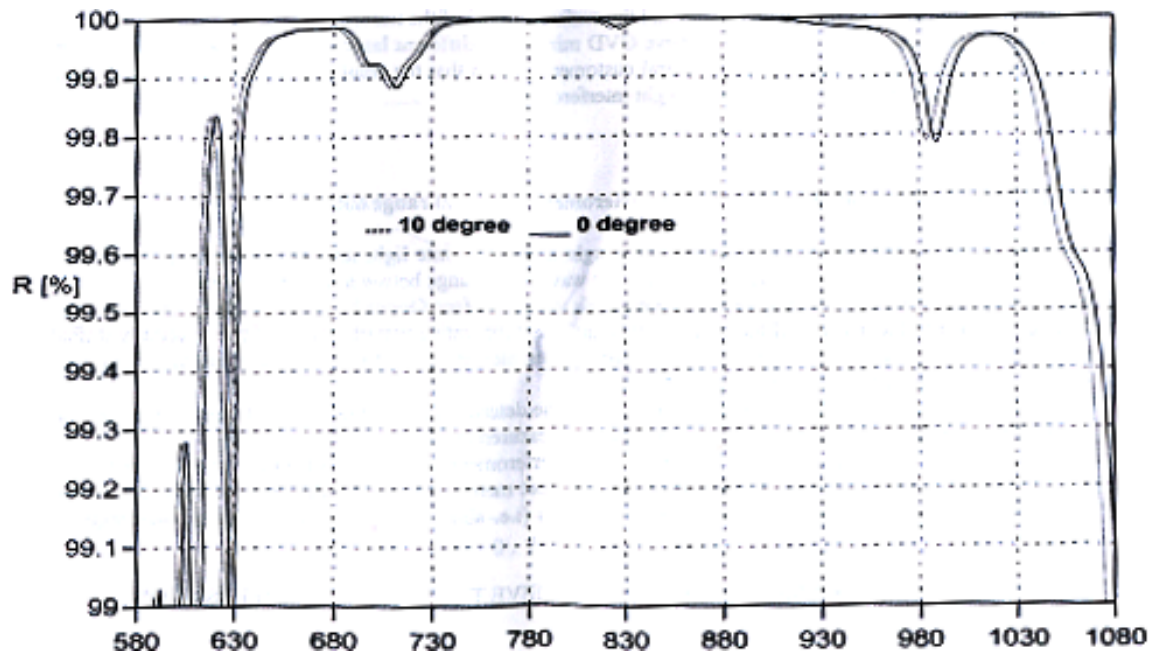incidence and the traced line for 10° incident angle.

Figure B.8.: Reflectance values for M3 (G1003015) mirror for 0 and 10 degrees.
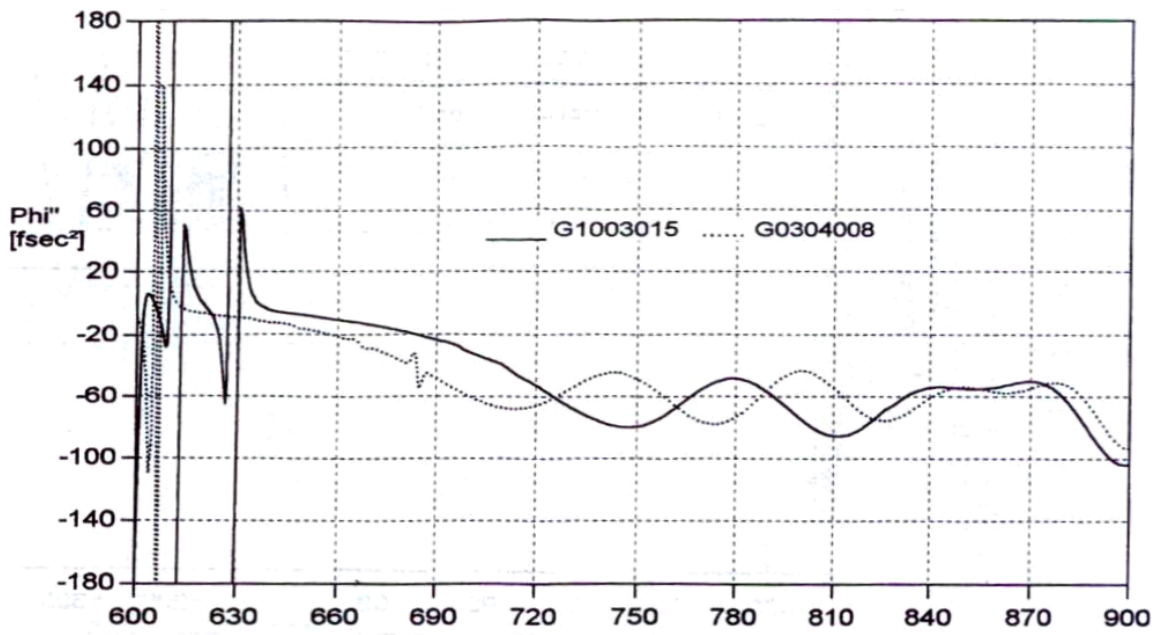
Figure B.9.: GDD values for M3 (G1003015) and M4 (G0304008).

The possible spectrum that had a linear FWHM smaller profile but a bigger logarithmic one.
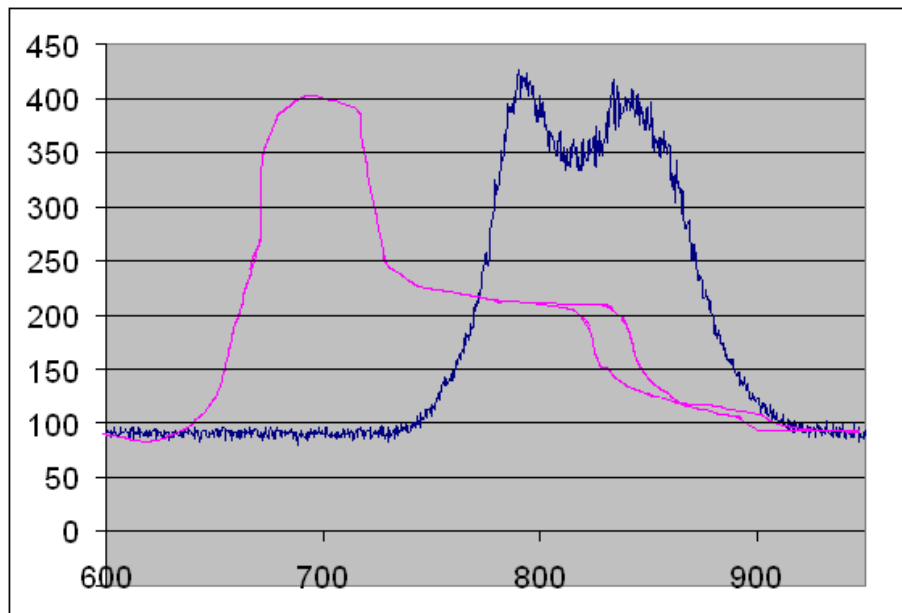

Figure B.10.: Spectral intensity, actual intensity profile in blue and a possible spectral shape with a larger spectral bandwidth in a log scale but not on a linear scale in red.

ABCD matrix propagation

Half a crystal will be represented in the sagittal plane by the matrix:

$$[CR_S] = \begin{bmatrix} \cos\left(\frac{\gamma_s L}{2}\right) & \frac{\sin\left(\frac{\gamma_s L}{2}\right)}{n\gamma_s} \\ -n\gamma_s \sin\left(\frac{\gamma_s L}{2}\right) & \cos\left(\frac{\gamma_s L}{2}\right) \end{bmatrix} \tag{B.1}$$

In the tangential plane by:

$$[CR_t] = \begin{bmatrix} \cos\left(\frac{\gamma_t L}{2}\right) & \frac{\sin\left(\frac{\gamma_t L}{2}\right)}{n^3\gamma_t} \\ -n^3\gamma_t \sin\left(\frac{\gamma_t L}{2}\right) & \cos\left(\frac{\gamma_t L}{2}\right) \end{bmatrix} \tag{B.2}$$

No matter the axis the simple propagation through a distance d is represented by:

$$[P(d)] = \begin{bmatrix} 1 & d \\ 0 & 1 \end{bmatrix} \tag{B.3}$$

For the sagittal plane the bounce in a θ incidence in a curved mirror (focal distance f) is given by:

$$[CM_s] = \begin{bmatrix} 1 & 0 \\ -\frac{\cos(\theta)}{f} & 1 \end{bmatrix} \tag{B.4}$$

For the tangential place:

$$[CM_t] = \begin{bmatrix} 1 & 0 \\ -\frac{1}{f\cos(\theta)} & 1 \end{bmatrix} \tag{B.5}$$

The stability is calculated from the ABCD matrix by:

$$S_i = 1 - \frac{(A_i + D_i)^2}{2} \tag{B.6}$$

and the beam curvature radius and the beam size is calculated by:

$$R = \frac{2B}{D - A} \tag{B.7}$$

$$w_i = \sqrt{\frac{\lambda |B_i|}{\pi\sqrt{S_i}}} \tag{B.8}$$

C. Appendix for chapter 3

Gerchberg-Saxton algorithm

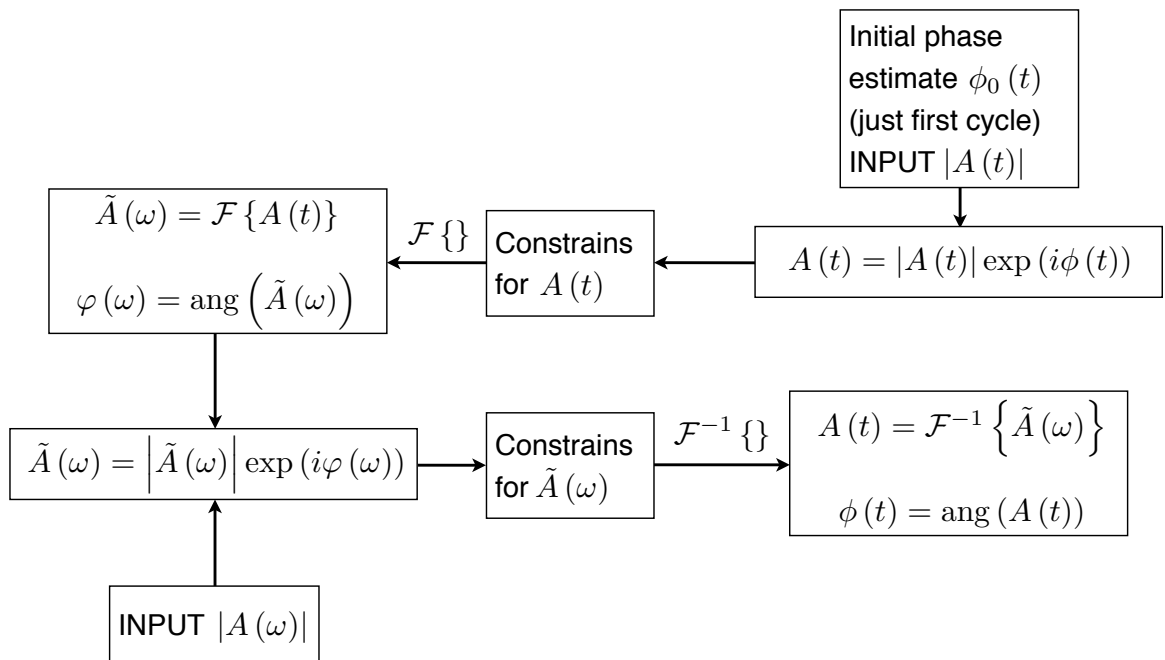A schematic representation of the Gerchberg-Saxton algorithm may be seen in Fig. (C.1).

Figure C.1.: GS like algorithm. It's a fast convergency algorithm.

D. Appendix for chapter 4

D.1. Dispersion of ultrafast waves, Fourier approach

Let us consider a medium that responds linearly to an applied EM field and an optical field that can be decomposed in its Fourier transform:

$$\widetilde{E}(\vec{k}, \omega) = F\{E(\vec{r}, t)\}. \tag{D.1}$$

This is actually a good description of the phase and amplitude of an ultrashort pulse, due to the fact that the linear response of a material has eigenfunctions that are plane waves, makes the decomposition in Fourier components the ideal way to predict the behavior of ultrafast pulses in a linear material. A known Fourier transform property is the limitation of the product of the variances, $\triangle$, of conjugated functions (also known as the Heisenberg uncertainty principle) [221, 222].

$$\triangle_{\widetilde{E}} \triangle_E > \frac{1}{2} \tag{D.2}$$

Let us assume for simplicity that the field is normalized, i.e., we can write $\int |\widetilde{E}(\vec{k}, \omega)|^2 d\vec{k} d\omega = 1$ and $\int |E(\vec{r}, t)|^2 d\vec{r} dt = 1$. From Eq. (D.2) we see that in order for the pulse to be short in time, which means a small $\triangle_E$, the spectrum has to be wide and so $\triangle_{\widetilde{E}}$ has to be large[1].

The actual value of the variance product is going to depend on the pulse phase and shape [36, 223]. For Gaussian pulses the FWHM product is given by:

$$\triangle \omega_{\frac{1}{2}} \triangle \tau_{\frac{1}{2}} = 4 \ln(2) \sqrt{1 + a^2} \tag{D.3}$$

In which the parameter a is a chirp in time: $A(\tau) = C \exp\left[-(1 - ia) \frac{\tau^2}{2 \ln(2) \tau_{1/2}^2}\right]$.

This means that for a Gaussian pulse to be 5 fs FWHM in duration we have to have at least 88 THz, or 188 nm@800 nm.

---

[1]The exact minimum time bandwidth product might depend on the exact definition of Fourier transform, in some definitions this value can be $\frac{1}{16\pi^2}$ instead of $\frac{1}{2}$.

D. Appendix for chapter 4

The linear propagation can be represented by Fig. (D.1). The output field in time can be determined by:

$$E(\vec{r},t)|_B = F^{-1}\left\{exp(i\mathbf{k}.\vec{r})F\left\{E(\vec{r},t)|_A\right\}\right\} \tag{D.4}$$

or if the propagation direction is z with a defined refraction index $n(\omega)$ it results in:

$$E(\vec{r},t)|_B = F^{-1}\left\{exp(i\frac{2\pi n(\omega)}{\lambda}z)F\left\{E(\vec{r},t)|_A\right\}\right\}, \tag{D.5}$$

where λ is the wavelength. The phase (and delay) of each of these Fourier components is going to be different but easily calculated by $\frac{2\pi n(\omega)}{\lambda}$. This makes the Fourier space the ideal space to treat the linear propagation not the direct space.
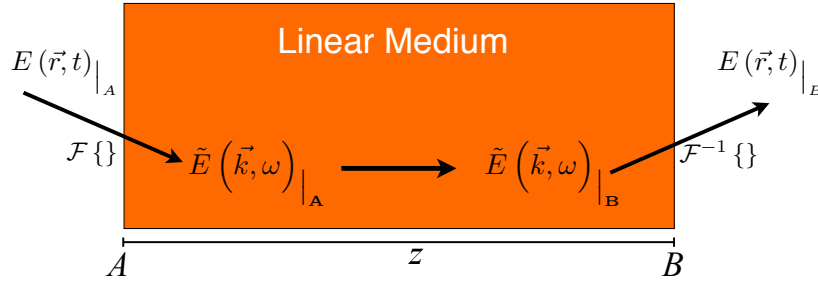

Figure D.1.: Propagation throughout a linear medium with length z from a plane A to a plane B.

Let us consider only a second order expansion of the wave vector in such a way that we can consider it to be $k(\omega) = \frac{1}{2}\left.\frac{d^2k_0}{d\omega^2}\right|_{\omega_0}(\omega-\omega_0)^2$, $k_0^" = \left.\frac{d^2k_0}{d\omega^2}\right|_{\omega_0}$.

The Gaussian pulse will change its time bandwidth product. With some simple arithmetic we obtain the following expression:

$$\triangle\omega_{\frac{1}{2}}\triangle\tau_{\frac{1}{2}} = 4\ln(2)\sqrt{1+\left(a+\frac{k_0^"z\Delta\omega_{\frac{1}{2}}^2}{4\ln(2)}\right)^2} \tag{D.6}$$

This will shorten or increase pulse duration depending on whether we have positive or negative chirp to begin with. The second order dispersion for several materials is given in Tab. (D.1). From Eq. (D.6) we see that for large values of dispersion the pulse duration will be proportional to it.

Material	$\frac{d^2 k_0}{d\omega^2}\Big|_{\omega_0}$ (fs^2/mm)
Dry air	2.13E-2
Fused silica	36.1
BK7	44.6
Ti:Sapphire (e-axis)	56.6
Ti:Sapphire (o-axis)	58.0
SF1	148
SF57	223
LaK14	72.1

Table D.1.: Wave vector second derivative $\frac{d^2 k_0}{d\omega^2}\Big|_{\omega_0}$ for several materials. The values are given in fs^2/mm with a central wavelength of 800 nm.

D.2. Defining a time window in a time frequency method

There are several processes that work both in direct and indirect space. To do this it is important to find an optimal time/frequency window. Furthermore the method of transporting from one space to the other the Fourier transform is done using Fast Fourier transform (FFT), which is faster then discrete Fourier transform by a factor of $N/\ln(N)$, where N is the number of points used in the discretization.

If we want to operate in both the direct space and the reciprocal space or frequency space, it is imperative to have a good representation of the pulse in both spaces. In order to do that we have to be pretty conscious on how to distribute the points of the function on both spaces, so that one of the spaces is not overly defined (oversampled) at the expense of the other space being under-sampled.

In Fig. (D.2) we give an example of a bad increase in the number of sampled points, if we just increase the number of points leaving the time window as it is, the step will be smaller in the time domain but not in the frequency domain, we will be mapping unnecessary territory in the frequency domain without any advantage in the time domain. The inverse can also happen, a sampling problem in the frequency domain won't be solved just by increasing the number of points in the time domain.

In order to solve this we may use a semi-analytical method to have the same number of points in the zone of interest for the time and frequency domain. We recall Eq. (D.3) for Gaussian pulses and Eq. (D.2) for general pulses to understand that, the zone of interest product is constant, it will depend on the shape of the pulse and the phase it has, the more spectral phase (chirp) it has the bigger is the time frequency product, and so we can consider that

$$\Delta_i \omega \Delta_i t = C \qquad (D.7)$$

where $\Delta_i\omega, \Delta_i t$ is the electric field zone of interest, in frequency and in time. Its definition does not concern us. Knowing this, the number of points in the zone of interest in time is given by:

$$N_t = \frac{\Delta_i t}{\Delta t} N \tag{D.8}$$

Similarly in the frequency domain we get:

$$N_\omega = \frac{\Delta_i \omega}{\Delta \omega} N \tag{D.9}$$

Where N is the total number of points. $\Delta\omega, \Delta t$ are the frequency and time windows in general. Considering that ideally, the number of points in the interest zone has to be the same in both domains. We obtain the following definition for the time window and for the frequency window:

$$\begin{aligned} \Delta\omega = \frac{\Delta_i \omega}{\sqrt{C}}\sqrt{N} & \quad \Delta t = \frac{\sqrt{C}}{\Delta_i \omega}\sqrt{N} \\ \Delta t = \frac{\Delta_i t}{\sqrt{C}}\sqrt{N} & \quad \Delta\omega = \frac{\sqrt{C}}{\Delta_i t}\sqrt{N} \end{aligned} \tag{D.10}$$

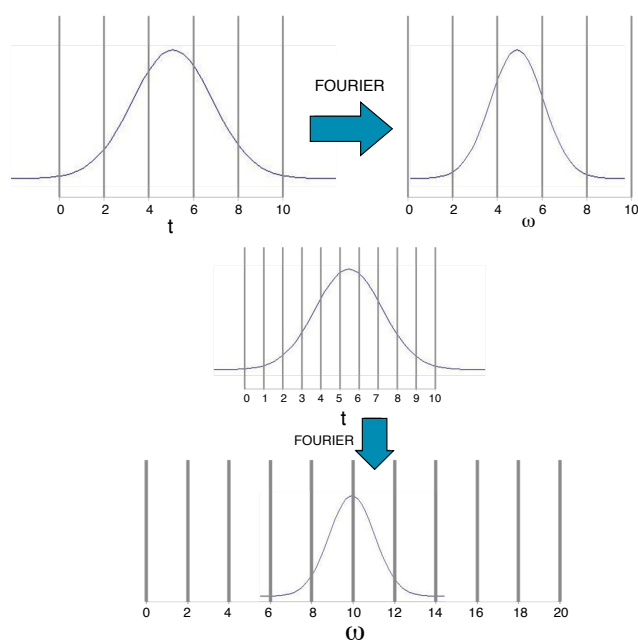The discretization intervals are given by $1/N$ of the values above.

Figure D.2.: (top) Relation between the points in time and in the Fourier domain. Increasing the definition in the time domain (middle) will not give us a better definition in the Fourier domain (bottom) but only an increase of the Fourier window; the frequency definition will remain unchanged.

Despite the considerations above for highly chirped pulses interpolation at each step might be needed

to allow for a reasonable computing time.

For a Gaussian beam we obtain a constant C that is given by (see Eq. (D.3)):

$$C_g = 4\ln(2)\sqrt{1+a^2} \tag{D.11}$$

where a is a chirp parameter.

For Fourier limited for $sech^2$ pulse the constant we obtain:

$$C_{sech^2} \simeq 2 \tag{D.12}$$